Spring 2015

Elastic Waves Along a Fracture Intersection

Bradley C. Abell
Purdue University

Graduate School Form 30
Updated 1/15/2015

PURDUE UNIVERSITY
GRADUATE SCHOOL
Thesis/Dissertation Acceptance

This is to certify that the thesis/dissertation prepared

By Bradley Charles Abell

Entitled

Elastic Waves along a Fracture Intersection

For the degree of Doctor of Philosophy

Is approved by the final examining committee:

Laura Pyrak-Nolte Chair	Antonio Bobet
Maarten De Hoop	
Henry Melosh	
David Nolte	

To the best of my knowledge and as understood by the student in the Thesis/Dissertation Agreement, Publication Delay, and Certification Disclaimer (Graduate School Form 32), this thesis/dissertation adheres to the provisions of Purdue University's "Policy of Integrity in Research" and the use of copyright material.

Approved by Major Professor(s): Laura Pyrak-Nolte

Approved by: Mark Haugan 4/10/2015

Head of the Departmental Graduate Program Date

ELASTIC WAVES ALONG A FRACTURE INTERSECTION

A Dissertation

Submitted to the Faculty

of

Purdue University

by

Bradley Charles Abell

In Partial Fulfillment of the

Requirements for the Degree

of

Doctor of Philosophy

May 2015

Purdue University

West Lafayette, Indiana

To my wife, my family, and all those who have given me their time and effort.

ACKNOWLEDGMENTS

Professor Pyrak-Nolte, five years ago I walked into your office and asked if you had a project that I could work on. You told me, "There may be something interesting that happens at fracture intersections; you should look into it." At the time I didn't even know what a fracture was, and five years later here I am writing an entire dissertation on the subject. Professor Pyrak-Nolte, your guidance, patience, support, intelligence, and effort to understand the science is unmatched. You taught me to *listen to the data* and determine from the theory what was happening physically. Thank you for everything you have shown me these past five years. Without your guidance, this work would not exist.

To my committee members, you have given me guidance in times of uncertainty and lead me to solutions when no answer seemed available. Professor Bobet, you helped me to think logically and practically, which allowed my successful construction of the biaxial load frame in your lab. Thank you for allowing me to use your equipment and expertise. Professor Nolte, you helped me focus on what a physicist should think about. Without your guidance, I never would have looked into group theory, which has now become the foundation of this work. Professor Melosh, although our contact was short, you expressed how important understanding the properties of specific stiffness were. Finally, Professor De Hoop, your practical approach to non trivial problems has guided me through the past few years. Thank you for always making the time in your schedule to meet with me and share your always interesting stories. Your tireless pursuit to build the Geomathematical Imaging Group (GMIG) at Purdue is appreciated, not only for the financial support during my time here but also the vast knowledge it provided the imaging community.

This endeavor would never have been possible on my own. As with any project, many hands make light work. I must thank Professor Andreas Mayer at Hochschule

Offenburg, Germany. You provided me theoretical guidance for the foundation of coupling waves. Although we have never met in person, your advice and insight was more valuable than you could imagine.

I am indebted to my fellow graduate students during the course of this project: Chris Petrovitch, Eric Boomsma, Siyi Shao, WeiWei Li, Min-Kwang Choi, Ahmadreza Heyadat, Xuhui Zhou, Anahita Modiriasari, Amanda Dye, Leila Sadeghi, and Zhenyu Xu. Your advice, help in setting up experiments, paper edits, discussions during group meetings, and general friendliness have been fundamental to my work and positive experience in graduate school. I must also thank the undergraduate students who I have had the pleasure of working alongside: Josh Knobloch, Tressa Mackin, Matthew Smith, Nolan Teasdale, Bill Watterson, Kevin Nejman, Colton Brown, Jack Conrad, and Michael McCann. You both trained me and allowed me the pleasure of being your mentors.

Within Purdue University I have been able to save a dramatic amount of time and effort in constructing and troubleshooting my experiments thanks in part to the individuals on the staff within the physics department and the university as a whole. I would like to especially thank Mark Smith for always being willing to help me troubleshoot electronic circuits, Thomas Halsmer for lending me his decades of expertise on machining and general mechanical knowledge, James Corwin for teaching me how to use the machine shop, and Aamer Mahmood for his help in fabricating micromodels; although nothing came of the project I learned a dramatic amount about fabrication thanks to you. I would also like to thank the secretarial staff within the physics department. Sandy, Linda, Janice, Nancy, Carol, and Pam, your friendliness and willingness to drop everything to help, listen, or share your stories was greatly appreciated; it does not go unnoticed.

My love of physics started at my undergraduate institution, Gustavus Adolphus College in St. Peter, Minnesota. The professors at Gustavus taught me how enjoyable physics could be and lead me on the path to graduate school. I am especially indebted to Professor Huber. Professor, you provided my first opportunity to perform

experimental physics research in your lab and helped me become a useful and practical physicist. My fellow research student the first summer, Dan Mellema, you allowed me to bounce ideas off of you and helped me to truly fall in love with experimental work, thank you.

None of this would have been possible without my loving family. My parents, Carol and Alan, who have been my greatest supporters throughout my life. Dad, you once told me, "Do what you love, don't worry about the money; it always has a way of working itself out." That advice allowed me to pursue my dream of getting a Ph.D. in physics. Mom, you always made sure I remembered the people in addition to the science. You helped me become a personable physicist and more approachable scientist. Mom and Dad, without your sound advice, guidance, support, encouragement, and amazing love, none of this would have been possible. To my siblings, Laura and Julia, you are the best sisters I could ask for. Thank you for listening to your nerdy brother all of these years.

Finally, to my wife, Kayla; you are my drive in life. You moved to Indiana with me to let me pursue my dream of becoming a Ph.D. graduate. You put up with my "science talk" for years and are always willing to listen to me. You have dealt with all of my traveling, late night working, and are always happy to be my audience for practice presentations. No matter how frustrated, excited, bummed out, tired, or absentminded I feel, I know you are always waiting for me at the end of the day. Kayla, you are my best friend, and I am the luckiest man in the world to have an amazing woman like you to share my life with. I love you, and I cannot wait to start the next chapter of our lives together.

TABLE OF CONTENTS

Page

LIST OF TABLES

LIST OF FIGURES

Figure Page

Figure Page

Figure Page

SYMBOLS

A	area
A_0	amplitude
a_{mn}	expansion coefficients in displacement
B_i	vector space
C_n^k	operation of C_n repeated k times
$C_{\alpha,\beta,\mu,\nu}$	elastic moduli
C_Ψ	admissibility constant
D	derivative operator
E	identity operator
E_{avg}	energy density
f	frequency
$f(x,t)$	plane wave function
G	generic group
$\bar{\mathbf{G}}$	matrix relating the elastic constants to the geometry
$\bar{\mathbf{H}}$	Stress at the interface between media 3 and 4
h	standard deviation in asperity height
$\bar{\mathbf{I}}$	identity matrix
i	$\sqrt{-1}$
J	Rayleigh wave displacement parallel to surface
j, m, n	index counters for sums
k	wavenumber
$\mathbf{k}$	wave vector
l_i	dimension of i^{th} IR
L	length
$L_a(x)$	Laguerre polynomial

$\bar{\mathbf{M}}$	matrix relating the elastic constants to the coupling
N_c	number of classes
N_k	number of elements in the k^{th} class
n^α	number of times the IR occurs along Γ
$\bar{\mathbf{n}}$	normal direction unit vector
P_{avg}	power flow density
P	Cauchy principle value
p	expansion terms
$\bar{\mathbf{Q}}$	unitary matrix of eigenvectors ($V_{m,n}$)
q	translation of window
R	stiffness ratio ($\frac{\kappa_{shear}}{\kappa_{normal}}$)
$\bar{\mathbf{r}}$	displacement vector
S_n	improper rotation
s	harmonic number, scale
$\bar{\mathbf{s}}$	unit vector parallel to surface
$\bar{\mathbf{T}}$	stress field
$\tilde{T}$	stress amplitude
t	time
$\bar{\mathbf{t}}$	traction
$\tilde{U}$	displacement amplitude
$\bar{\mathbf{U}} = U_n^{\alpha,\eta}$	displacement at the interface
u	displacement
$\hat{u}$	displacement in transformed coordinate system
$\bar{\mathbf{V}}$	arbitrary column vector
v_{energy}	energy velocity
v_{group}	group velocity
v_{phase}	phase velocity
$V_{m,n}$	eigenvectors of matrix $\bar{\mathbf{M}}$
v	velocity

v_P	P-wave velocity
v_S	S-wave velocity
v_R	Rayleigh velocity
W	Rayleigh wave displacement normal to surface
x	position or direction
y	position or direction
Z	impedance
z	position or direction
α, β, μ, ν	coordinate directions
$\propto$	proportional to
δ	fracture deformation
δ_m	maximum joint closure
δ_{ab}	Kronecker delta function
$\epsilon_{\mu,\nu}$	strain
θ	transducer polarization angle
$\theta^{'}$	phase angle
Θ	Heaviside step function
κ	fracture specific stiffness
κ_c	critical specific stiffness
κ_n	normal specific stiffness
κ_o	specific stiffness at zero stress
κ_{spring}	stiffness of a spring
$\bar{\mathbf{\Lambda}}$	diagonal matrix of eigenvalues
λ_L	Lamé's first constant
λ_w	wavelength
λ	eigenvalues of matrix $\bar{\mathbf{M}}$
μ_L	Lamé's second constant (shear modulus)
ρ	density
σ	reflection operator

$\sigma_{\alpha,\beta}$	stress component
ς	normal stress
$\bar{\sigma}$	stress at the interface between media 2 and 3
$\boldsymbol{\tau}$	stress at the interface between media 1 and 2
$\phi^{'}$	group angle
$\phi_m(x)$	weighted Laguerre function
ψ	apex angle
Ψ	transforming function (i.e., mother wavelet)
ω	angular frequency
ν	Poisson's ratio
η	medium label
χ_k^{Γ}	character of the k^{th} class or IR Γ
ξ	generic vector
Γ	representation
$\bar{\gamma}$	stress at the interface between media 1 and 4
Σ	sum
*	complex conjugate, conjugate transpose
$\cdot$	dot product
$\int$	integral
∂	partial derivative
∞	infinity
$[A, B]$	commuting matrices
$\{A, B\}$	set of operators A,B
$A \in G$	A is an element in the set of G
A^T	transpose of A
$'$	derivative

ABBREVIATIONS

CWW	Coupled Wedge Wave
DD	Displacement Discontinuity
DIC	Digital Image Correlation
dof	degrees of freedom
FT	Fourier transformation
IR	Irreducible representation
lhs	left hand side
P-waves	Compressional waves
rhs	right hand side
RS	Rayleigh Stoneley Wave
S-waves	Shear waves
TI	Transversely Isotropic
WT	Wavelet Transformation
WW	Wedge Wave

ABSTRACT

Abell, Bradley Charles Ph.D., Purdue University, May 2015. Elastic waves along a fracture intersection . Major Professor: Laura J. Pyrak-Nolte.

Fractures and fracture networks play a significant role in the subsurface hydraulic connectivity within the Earth. While a significant amount of research has been performed on the seismic response of single fractures and sets of fractures, few studies have examined the effect of fracture intersections on elastic wave propagation. Intersections play a key role in the connectivity of a fracture network that ultimately affects the hydraulic integrity of a rock mass. In this dissertation two new types of coupled waves are examined that propagate along intersections. 1) A coupled wedge wave that propagates along a surface fracture with particle motion highly localized to the intersection of a fracture with a free surface, and 2) fracture intersection waves that propagate along the intersection between two orthogonal fractures. Theoretical formulations were derived to determine the particle motion and velocity of intersection waves. Vibrational modes calculated from the theoretical formulation match those predicted by group theory based on the symmetry of the problem.

For the coupled wedge wave, two vibrational modes exist that range in velocity between the wedge wave and Rayleigh wave velocity and exhibit either wagging or breathing motion depending on the Poisson's ratio. For the intersection waves, the observed modes depend on the properties of the fractures forming the intersection. If both fractures have equal stiffness four modes exist, two with wagging and two with breathing motion. If the fractures have unequal stiffness, four modes also exist, but the motion depends on the Poisson's ratio.

The velocity of intersection waves depends on the coupling or stiffness of the intersection and frequency of the signal. In general, the different modes travel with

speeds between the wedge wave and bulk shear wave velocity. Laboratory experiments were performed on isotropic and anisotropic samples to verify the existence of these waves. For both waves, the observed signals were determined to depend on the applied load, which affects the stiffness of the fractures.

These results have significant implications for fracture network characterization using remote techniques in both the laboratory and the field. The coupling parameter used in this discussion, i.e., specific stiffness, is a potential parameter to link the hydraulic properties of the fracture intersections to their seismic response. These results are a first step towards remote characterization to determine the hydraulic connectivity of fracture networks.

1. Introduction

Discontinuities in rock, such as fractures and joints [1], are observed all over the surface and subsurface of the Earth's crust. Throughout history, scientists and engineers have studied fractures, in nearly every geographic location on Earth, for various reasons (e.g., mining, gas, oil). Across all areas of study, the impact fractures play in understanding the Earth has been significant in many aspects [2]. It is a goal of this work to further advance this knowledge into orthogonal fracture intersections.

Fractures, which are defined as any discontinuity between two adjacent materials in partial contact, can exist in isolation, as sets, and intersecting other fractures. The presence of discontinuities in rock affects the stability and transport properties of the rock mass. One goal is to use geophysical methods (e.g., seismic waves) to locate fractures and remotely characterize their properties, extent, and connectivity. The effects of isolated and parallel sets of fractures on seismic wave transmission and reflection have been studied theoretically, numerically, and experimentally [3–11]. These results indicated that fractures give rise to converted modes, cause anisotropy, and can produce guided-modes [4,12–17]. Although extensive research on the seismic response of single fractures has been conducted, the effect of fracture intersections on elastic wave propagation has been largely ignored.

A logical progression when studying fractures is to start with an isolated fracture, build up to parallel sets, then to networks. In nearly all geographic locations on Earth fractures occur in networks, which are made up of intersecting fractures, with interconnected paths that can either hinder or facilitate flow [18–20]. As with single fractures, the hydraulic properties of fracture networks are dominated by the

[1]One of the first references to a joint in the Earth was from Pliny's Natural History (circa 77 AD) translated in 1601 by Holland. Pliny used the Latin word 'commissuris', which was translated as joint, to describe the area he was studying [1].

mechanical properties (e.g., connectivity, specific stiffness, density, symmetry orientation, etc.) [19, 21–24].

Fracture intersections and networks have been a focus of scientific study since the early nineteenth century. Some of the earliest examples of fracture intersections in scientific literature were written by English geologists who tried to develop a mathematical model for the formation of fracture intersections [25]. Since these early studies, relatively little work has been done on analyzing the role of intersections in geophysical interpretations, and virtually nothing has been done to seismically/acoustically characterize an intersection. Several groups have studied, theoretically, the effects of fracture network spacing, formation, aperture, seismic attenuation, thermal variations, boreholes, stress, and orientation in fracture networks in rock [20, 26–32]. Attempts have even been made to study effective media approaches and to study intersecting cracks [33–36]. However, these theoretical studies did not take into account the interaction between the fracture planes, and found no significant effects of the intersection. Computationally, researchers have found that fractures do in fact intersect often and in many geometries, indicating a further need for laboratory and field studies on the effects intersections have on seismic wave propagation [37–39].

For this reason, fracture networks are a major concern in the isolation of underground storage sites, such as nuclear waste or ammunition, mining, fault mechanics, petroleum engineering, construction, ground water flow, and CO_2 sequestration [19–21, 26, 40–43]. Fracture intersections have even been used as a tool to remotely investigate geologic and stress history of celestial bodies [44–48]. Until recently, the tendency in the petroleum industry was to ignore the effects of fractures in the field production history, which lead to a loss in profits, unnecessary drilling, and loss of recovery [19, 31, 49].

In addition to the above reasons, the hydraulic properties of intersections have been a topic of interest within the hydrology community [50–59]. Nevertheless, most of the focus on fracture intersections has centered on their genesis (i.e., formation) [22,28,38,43–47,60–67]. Genesis studies determined that fracture intersection patterns

found in nature (see Table H.1) were caused by local stress history and a possible reversal (by 90°) of the stress field. They found that 1) fractures tend to propagate across other fractures only if the older fracture was sealed [28], 2) a local stress reversal (by 90°) can occur when the spacing to layer thickness ratio changed from greater to less than a critical ratio, which is a function of the horizontal stress [38], 3) secondary fractures are generally created from visco-elastic effects or from loading conditions [61], and 4) intersections are found in all types of geologic settings at various scales [19, 20, 22, 26, 28, 38, 43–46, 60–65, 68, 69].

Intersections observed in the field, either at the surface or subsurface, are found to have relatively small variations in geometry within a given rock mass. In the petroleum industry the fracture orientation is found 1) to be consistent within 15°-20° in extended areas and 2) to develop in orthogonal sets, which are hypothesized to be caused by the loading and unloading history [19]. Others have made classifications of intersections as orthogonal and nonorthogonal, depending upon the angle in which the two fractures meet, classifying them as "+" or "X". If only one fracture is continuous, the intersection forms a "⊤", or a curved "⊤". Finally, triple intersections are defined as "Y" shaped where the angles between the fractures are near 120° [42, 43, 46]. For additional examples see [20, 25, 26, 30, 44, 47, 48, 62, 64, 66, 67, 70, 71] along with the table of each type of fracture intersection shown in Table H.1.

The goal of this study, is to develop a method for characterizing a single fracture intersection using elastic waves. This project seeks to develop a mathematical formulation for elastic waves that propagate along the intersection of two fractures and to demonstrate the existence of intersection waves through laboratory experiments. The need for this study arises from the lack of understanding and information regarding wave propagation near intersections.

The conceptual framework of this dissertation is represented visually in Fig. 1.1. The intersection is analyzed by first studying the wedge wave (WW) (chapter 4), the WWs are then combined to understand a surface fracture wave, i.e., coupled wedge wave (CWW) (chapter 5) and then four WWs are coupled together to model

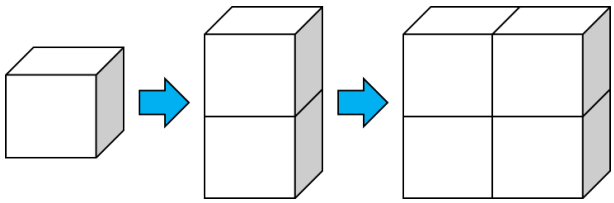

Figure 1.1. Conceptual approach to analyzing a fracture intersection used in this document. The intersection is made up of corners (i.e., wedges) in partial contact.

intersection waves (chapter 6). It is the goal of this work to build up the reader's understanding from a single wedge to the full orthogonal intersection. To achieve this, the dissertation is ordered as described below.

This dissertation begins with a review of elasticity and anisotropy to familiarize the reader with the topic and to provide a theoretical framework for wave propagation. Chapter 3 reviews different types of elastic waves that propagate through the body or bulk of a medium, along the surface of a medium, and along a single fracture plane. The full theoretical derivations of these types of waves is left to the extensive reference list, but the main properties are discussed here.

The less familiar wedge wave (WW) is introduced separately, with the aid of group theory, in chapter 4. Group theory analysis is provided in explicit detail for the WW, and in later chapters for other types of coupled waves. The use of group theory is paramount to predicting the unique vibrational modes of the waves discussed here. The theoretical foundations of group theory are rather tedious and can mask the important information it provides. For this reason only the required theorems, without proof, are discussed.

Chapter 5 introduces coupled wedge waves (CWW) that propagates along a surface fracture meeting a free surface and were newly discovered by this author. A similar group theory analysis is used to predict two vibrational modes for the CWW under any given set of material parameters. Using the predicted results as a guide, the full theoretical derivation of the CWW is explicitly provided, along with numeri-

cal calculations of the expected wave speeds and vibrational modes, which are found to agree with the group theory results. Finally, an experimental verification of this wave is shown for both isotropic and anisotropic media.

The final chapter of this dissertation, chapter 6, follows the same format as the previous two chapters in analyzing the orthogonal intersection under equal and unequal loading conditions. It builds on the knowledge gained in studying the WW and CWW. The theoretical results are discussed in detail and experimentally verified for both isotropic and anisotropic media.

2. Elasticity Theory

Laboratory experiments are essential in understanding physical phenomenon and characterizing rocks found in the field. Although an entire rock mass cannot be easily sampled, small cores from the field help to understand layering, fractures, mineral content and most importantly, anisotropy of a rock. Anisotropy is a measure of the variation in rock properties as a function of direction. Typically, these are the three orthogonal directions from Cartesian coordinates and are often taken with the coordinates aligned parallel and orthogonal to any layering present.

In the following chapter a discussion of anisotropic symmetry groups is given. Measurement techniques, as well as symmetry classes, are presented, and the theoretical relationships between the measured velocities and elasticity tensor are derived. Special emphasis is given to the types of velocities typically encountered in the theory and experimental measurements.

2.1 Anisotropy

The theory of anisotropy was developed nearly two centuries ago to understand crystals, the elastic ether, light propagation and metals [72]. Anisotropy assumes that the material under study is different along different orthogonal directions. These variations depend upon the material symmetries within the sample. The following derivation discusses the relationships between the anisotropic parameters and the different material symmetries that are possible. In the geo-sciences, especially seismology, the assumption that rocks are isotropic, i.e., the same in all directions, was and is still assumed in a large majority of research [72]. Unfortunately, rocks are almost never isotropic. They possess micro-cracks, mineral deposits, density variations, etc. that all impact the isotropic assumption.

Extensive research on anisotropy has been done in the areas of: seismology [72–74], phonons [75], metals [76], wood [77, 78], and even industrial applications like musical instruments and brake pads [79, 80]. The measurement of the anisotropy is perhaps the most complicated step to determine the elastic constants that characterize the material. Although the techniques to measure elastic constants are important, the reader is left to the references for a full description of the various measurement techniques [81–83].

2.2 Elastic Constant Relations

To fully define the anisotropy of a sample, a tensor of the elastic constants is derived and presented for different material symmetries. The derivation of the elastic tensor, which relates stress to strain, originates from the generalized Hooke's Law [73, 84]

$$\sigma_{\alpha\beta} = C_{\alpha\beta\mu\nu}\epsilon_{\mu\nu}, \tag{2.1}$$

where $\sigma_{\alpha\beta}$ is the stress and $\epsilon_{\mu\nu}$ is the strain. The elastic tensor, $C_{\alpha\beta\mu\nu}$, is a second rank tensor that can have up to 36 independent values:

$$C_{\alpha\beta\mu\nu} = \begin{pmatrix} C_{11} & C_{12} & C_{13} & C_{14} & C_{15} & C_{16} \\ C_{21} & C_{22} & C_{23} & C_{24} & C_{25} & C_{26} \\ C_{31} & C_{32} & C_{33} & C_{34} & C_{35} & C_{36} \\ C_{41} & C_{42} & C_{43} & C_{44} & C_{45} & C_{46} \\ C_{51} & C_{52} & C_{53} & C_{54} & C_{55} & C_{56} \\ C_{61} & C_{62} & C_{63} & C_{64} & C_{65} & C_{66} \end{pmatrix}. \tag{2.2}$$

The Voigt notation has been used in Eqn. 2.2 to simplify the tensor notation, i.e., tensor to matrix. The Voigt notation condenses the first two ($\alpha\beta$) and last two ($\mu\nu$) terms together using the following notation,

$$\alpha\beta = \begin{cases} 11 \rightarrow 1 \\ 22 \rightarrow 2 \\ 33 \rightarrow 3 \\ 23 = 32 \rightarrow 4 \\ 13 = 31 \rightarrow 5 \\ 12 = 21 \rightarrow 6 \end{cases} . \tag{2.3}$$

However, these independent values have a high amount of degeneracy because of the material symmetries that are present in nearly every material. The most common symmetry classes are discussed below in section 2.3.

The value of the elastic constants are calculated from elastic wave velocities measured along orthogonal directions in a sample. Whenever these velocities are equal for a given plane (e.g., the same velocity in the x and y direction, but not the z direction) this plane is said to be a *symmetry plane*. Group theory (see chapter 4) can also be applied to these symmetry planes to derive the relationships below [85]. Once these planes are known, the samples are usually cut aligned with the symmetry plane or at a known angle to it. The orientation and number of these symmetry planes determines the class of anisotropy for a sample.

Both compressional (P) and shear (S) wave velocities measured along the symmetry planes are required to determine the elastic constants in Eqn. 2.2. The P-wave velocities are labeled v_{pxyz}, where xyz are the components of the velocity in those directions. As long as the symmetry planes are aligned with the coordinate system, the P-wave velocities are visualized as shown in Fig. 2.1. From the measured P-wave phase velocities, the following relationships apply for the elastic constants [84]

$$C_{11} = \rho v_{p100}^2, \tag{2.4}$$

$$C_{22} = \rho v_{p010}^2, \tag{2.5}$$

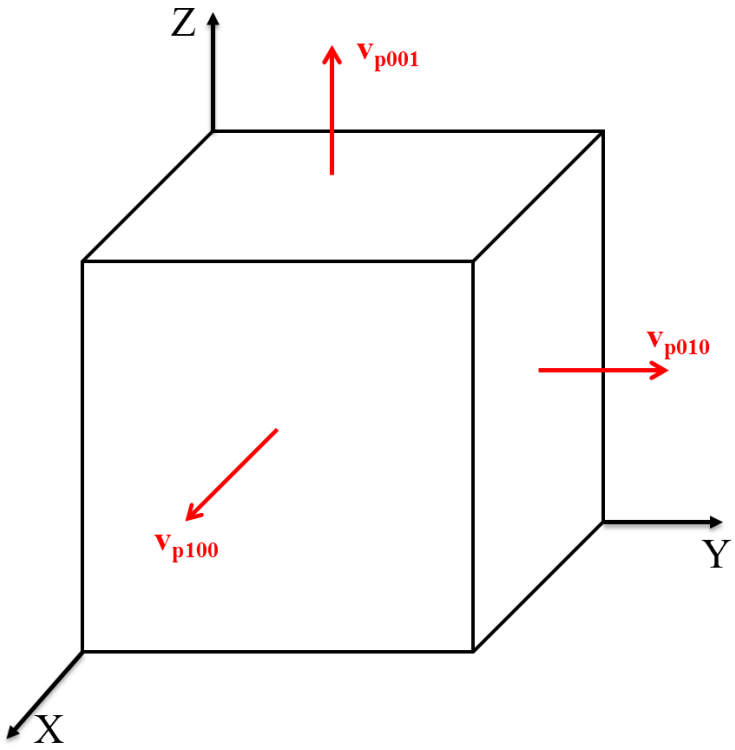

Figure 2.1. Labeling for P-waves propagating along symmetry planes that are aligned with the axes. The subscript numbers represent the direction of propagation (i.e., x,y,z).

$$C_{33} = \rho v_{p001}^2. \tag{2.6}$$

where ρ is the density of the sample.

For S-waves, there are two polarizations that must be measured in each direction (e.g., propagating in x, polarized in y and z). The six required waves are shown, along with their polarization, in Fig. 2.2. Depending on the symmetry of the material (e.g., transversely isotropic), these velocities are used to find the remaining diagonal elastic constants. Using Voigt notation (see Eqn. 2.3) the following relationships are found

$$C_{44} = \rho v_{s23}^2, \tag{2.7}$$

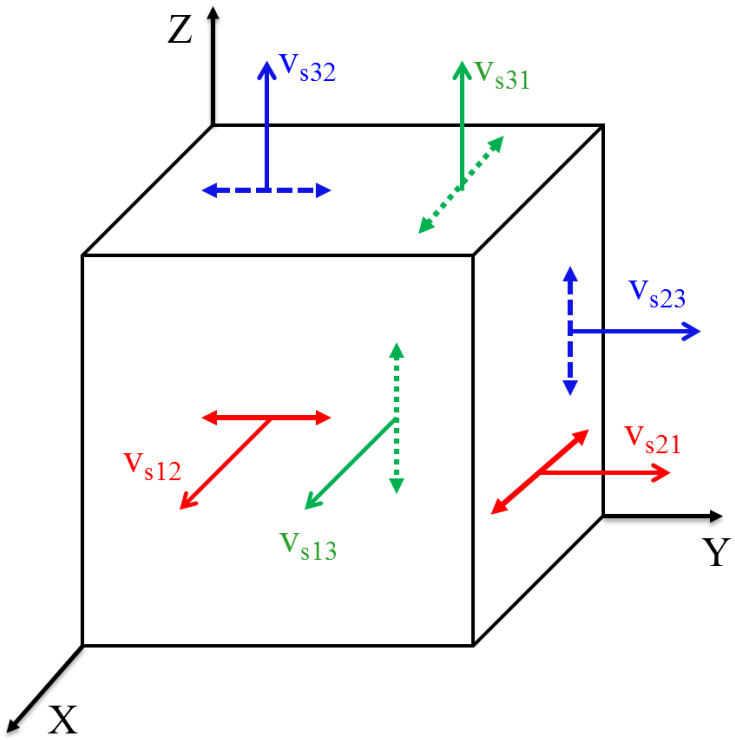

Figure 2.2. S-wave velocities propagating along the symmetry directions that are aligned with the coordinate axes. The first subscript is the direction of propagation (i.e., x,y,z = 1,2,3, respectively) and the second subscript is the polarization of the wave. Note that the double sided arrows represent the polarization of the waveform and the single sided arrows are the direction of propagation.

$$C_{55} = \rho v_{s13}^2, \tag{2.8}$$

$$C_{66} = \rho v_{s12}^2. \tag{2.9}$$

These equations define the diagonal elastic constants in Eqn. 2.2. The off diagonal elastic constants (e.g., C_{13}) are discussed in detail below for various symmetries.

2.3 Material Symmetries

2.3.1 Orthorhombic

When there are three independent symmetry planes (i.e., each Cartesian direction has a unique P-wave velocity and S-wave velocity making three unique symmetry planes), the material is said to have orthorhombic symmetry (e.g., Olivine). This is the lowest (i.e., most anisotropic) symmetry class that will be explicitly discussed in this work.

The elastic tensor (in Eqn. 2.2), written in Voigt notation (Eqn. 2.3), for orthorhombic symmetry is expressed as

$$C_{\alpha\beta\mu\nu} = \begin{pmatrix} C_{11} & C_{12} & C_{13} & 0 & 0 & 0 \\ C_{12} & C_{22} & C_{23} & 0 & 0 & 0 \\ C_{13} & C_{23} & C_{33} & 0 & 0 & 0 \\ 0 & 0 & 0 & C_{44} & 0 & 0 \\ 0 & 0 & 0 & 0 & C_{55} & 0 \\ 0 & 0 & 0 & 0 & 0 & C_{66} \end{pmatrix}. \tag{2.10}$$

Note that the diagonal components are all independent, and the off diagonal components ($C_{12},\ C_{13},\ C_{23}$) are all different. The diagonal components are calculated as described above, and the off diagonal components are determined from velocity measurements made at some non-orthogonal angle with respect to the symmetry planes [77]. For the C_{12} component, a P wave velocity measurement made at a non-orthogonal angle (typically 45° with respect to the x and y symmetry planes) must be taken. This wave is defined as v_{p110}, and is used to determine C_{12} from the following relationship

$$\rho v_{p110}^2 = \frac{C_{66}}{2} + \frac{C_{11} + C_{22}}{4} + \frac{\left[(C_{11} - C_{22})^2 + 4(C_{12} + C_{66})^2\right]^{\frac{1}{2}}}{4}. \tag{2.11}$$

In a similar way, the C_{13} term is determined from off angle P-wave measurements with respect to the x and z symmetry planes. If this is measured at 45°, the relationship between the velocity, v_{p101}, and the elastic constants is

$$\rho v_{p101}^2 = \frac{C_{55}}{2} + \frac{C_{11}+C_{33}}{4} + \frac{\left[(C_{11}-C_{33})^2 + 4(C_{13}+C_{55})^2\right]^{\frac{1}{2}}}{4}. \tag{2.12}$$

Finally, the C_{23} term is determined from a P wave velocity measurement, v_{p011}, with respect to the y and z symmetry planes. The relationship between this velocity and the elastic constants is

$$\rho v_{p011}^2 = \frac{C_{44}}{2} + \frac{C_{33}+C_{22}}{4} + \frac{\left[(C_{33}-C_{22})^2 + 4(C_{23}+C_{44})^2\right]^{\frac{1}{2}}}{4}. \tag{2.13}$$

Similar relationships can be derived for velocities not measured at 45° using the Christoffel equations found in most references on elasticity [77, 84]. It should also be mentioned that work by this author [83] and others [77, 78, 81, 86–96] have found other techniques to measure the off-diagonal elastic constants.

2.3.2 Transverse Isotropy

Transversely isotropic (TI) media is common in geologic formations (e.g., shales [97] and sandstone [98]) due to both layering and the applied stress in the crust of the Earth [97]. Earth's upper crust is often modeled as TI media because the symmetry planes are typically parallel to the free surface of the Earth. TI media have one direction, usually aligned with the z axis, that is different than the other two. For the P-wave velocities in Fig. 2.1, TI media have $v_{p100} = v_{p010}$ and for the S-wave velocities in Fig. 2.2, $v_{s\alpha\beta} = v_{s\beta\alpha},\ \alpha(\beta) = 1, 2, 3$. The elasticity matrix (Eqn. 2.2) is simplified for TI media to

$$C_{\alpha\beta\mu\nu} = \begin{pmatrix} C_{11} & C_{12} & C_{13} & 0 & 0 & 0 \\ C_{12} & C_{11} & C_{13} & 0 & 0 & 0 \\ C_{13} & C_{13} & C_{33} & 0 & 0 & 0 \\ 0 & 0 & 0 & C_{44} & 0 & 0 \\ 0 & 0 & 0 & 0 & C_{44} & 0 \\ 0 & 0 & 0 & 0 & 0 & C_{66} \end{pmatrix}. \tag{2.14}$$

One special identity for the off diagonal term C_{12}, for this material symmetry and higher, is

$$C_{12} = C_{11} - 2C_{66}. \tag{2.15}$$

The C_{13} term is the same as Eqn. 2.12.

2.3.3 Cubic

Cubic media (e.g., rocksalt) has three independent velocities that must be measured to obtain the full elastic tensor. The P-wave velocity in cubic media is the same in every direction (i.e., $v_{p100} = v_{p010} = v_{p001}$), while the S-wave velocity varies, but only v_{s13} or v_{s12} are necessary to obtain C_{44} (see Eqn. 2.7). The full elastic tensor (Eqn. 2.2) for cubic media is expressed as

$$C_{\alpha\beta\mu\nu} = \begin{pmatrix} C_{11} & C_{12} & C_{12} & 0 & 0 & 0 \\ C_{12} & C_{11} & C_{12} & 0 & 0 & 0 \\ C_{12} & C_{12} & C_{11} & 0 & 0 & 0 \\ 0 & 0 & 0 & C_{44} & 0 & 0 \\ 0 & 0 & 0 & 0 & C_{44} & 0 \\ 0 & 0 & 0 & 0 & 0 & C_{44} \end{pmatrix}. \tag{2.16}$$

The measurement of C_{12} requires an off diagonal velocity measurement, typically done at 45°, with respect to the coordinate axes [73, 84]. For any measurement at 45°, C_{12} is calculated from:

$$\begin{aligned} \rho v_{pc}^2 &= \frac{1}{2}\left(C_{11} + C_{12} + 2C_{44}\right), \\ v_{pc} &= v_{p110} = v_{p101} = v_{p011}. \end{aligned} \tag{2.17}$$

2.3.4 Isotropic

The highest symmetry possible is called isotropic symmetry. Isotropic media have the same P- and S-wave velocities in every direction, both on and off axis (e.g., some glass and metals). Although this symmetry is typically assumed for many models and analysis tools, it is rarely observed in real materials found in the Earth.

The two independent velocities are expressed as

$$v_{p100} = v_{p010} = v_{p001} = v_P, \tag{2.18}$$

and

$$v_{s12} = v_{s21} = v_{s13} = v_{s31} = v_{s23} = v_{s32} = v_S. \tag{2.19}$$

These velocities are related to the well known Lamé constants, λ_L and μ_L [99,100] by the relations

$$v_P = \sqrt{\frac{2\mu_L + \lambda_L}{\rho}} = \sqrt{\frac{C_{11}}{\rho}}, \tag{2.20}$$

and

$$v_S = \sqrt{\frac{\mu_L}{\rho}} = \sqrt{\frac{C_{11} - C_{12}}{2\rho}} = \sqrt{\frac{C_{66}}{\rho}}. \tag{2.21}$$

With these relationships, and Eqn. 2.15, the elastic tensor (Eqn. 2.2) for isotropic media becomes

$$
\begin{aligned}
C_{\alpha\beta\mu\nu} &= \begin{pmatrix}
C_{11} & C_{12} & C_{12} & 0 & 0 & 0 \\
C_{12} & C_{11} & C_{12} & 0 & 0 & 0 \\
C_{12} & C_{12} & C_{11} & 0 & 0 & 0 \\
0 & 0 & 0 & C_{66} & 0 & 0 \\
0 & 0 & 0 & 0 & C_{66} & 0 \\
0 & 0 & 0 & 0 & 0 & C_{66}
\end{pmatrix} \\
&= \begin{pmatrix}
\lambda_L + 2\mu_L & \lambda_L & \lambda_L & 0 & 0 & 0 \\
\lambda_L & \lambda_L + 2\mu_L & \lambda_L & 0 & 0 & 0 \\
\lambda_L & \lambda_L & \lambda_L + 2\mu_L & 0 & 0 & 0 \\
0 & 0 & 0 & \mu_L & 0 & 0 \\
0 & 0 & 0 & 0 & \mu_L & 0 \\
0 & 0 & 0 & 0 & 0 & \mu_L
\end{pmatrix}.
\end{aligned}
\tag{2.22}
$$

This concludes the discussion of anisotropy parameters and measurements for different symmetry classes.

2.4 Phase, Group, and Energy Velocity

Perhaps the most complicated and confusing issue regarding anisotropy is the difference between phase and group velocity. These velocities have a very basic theoretical definition, but can have different effects on experimental interpretation if they are not used correctly. In the following, the phase and group velocity are defined for a plane wave propagating through an elastic material. For further discussion and derivations see [84, 98, 99, 101].

2.4.1 Phase Velocity

When harmonic waves are propagated through an elastic medium, the monochromatic wavefronts have equal spacing in their phase. The velocity at which these

phase fronts (cophasal surfaces) arrive is called the *phase velocity*. To demonstrate this theoretically, a harmonic wave displacement is expressed. Typically, in the form

$$f(x,t) = A_0 cos(\mathbf{k}x \pm \omega t), \tag{2.23}$$

where A_0 is the amplitude, ω is the angular frequency, t is the time, $\mathbf{k}$ is the wave vector, and x is the position [84].

To determine the phase velocity, it is necessary to find the function $f(x,t)$ equal at two positions (x,t) and $(x+dx, t+dt)$. This can be thought of as the wave at two adjacent peaks. The velocity that the wave propagates from one position (x,t) to another $(x+dx, t+dt)$ is defined as the phase velocity. Since this definition must apply at any x and t, the choice of $x=0$ and $t=0$ is made for simplicity. Applied to Eqn. 2.23, this yields

$$\begin{aligned} &\mathbf{k}dx \pm \omega dt = 0, \\ &\frac{dx}{dt} = \pm\frac{\omega}{\mathbf{k}} = v_{phase}. \end{aligned} \tag{2.24}$$

Equation 2.24 is the theoretical definition of the phase velocity for any plane wave with frequency ω, traveling along wave vector $\mathbf{k}$. For this reason, the phase velocity is also measured along the direction of $\mathbf{k}$.

In anisotropic media, the wavefront vector can be complicated depending on the type and orientation of the anisotropy. It is generally defined with respect to an angle, named the phase angle (θ'), which is made between the plane of the source and the normal to the wavefront (see Thomsen (1986) [98] for a full description). This angle is used to define several relationships, which are discussed below, for both phase and group velocity (Fig. 2.3).

2.4.2 Group Velocity

For waves propagated through an elastic sample in the laboratory or for rock in the field, the transducers or seismic sources that create the waves are usually not

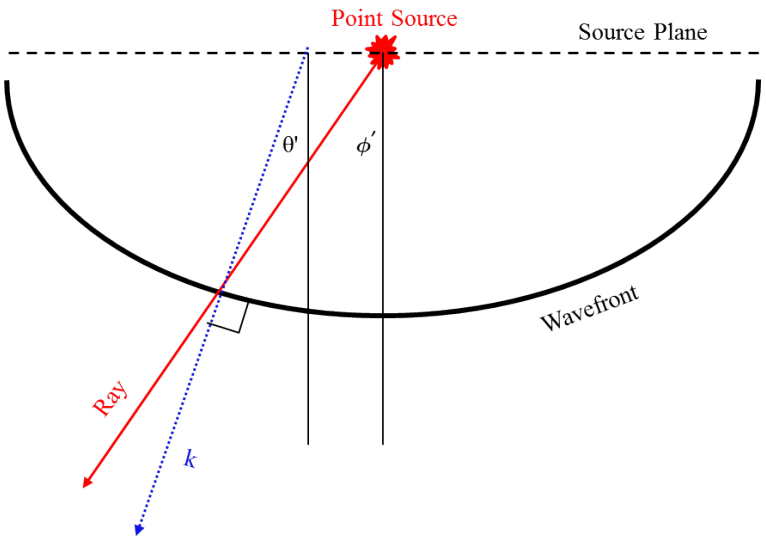

Figure 2.3. Schematic based on Fig. 1 of Thomsen (1986) [98] demonstrating the difference between phase and group angles for a wavefront propagating through an anisotropic material. The phase velocity and phase angle (θ') are measured using the path length normal to the wavefront (dashed arrow marked **k**), while the group velocity and group angle (ϕ') are measured from the ray path that goes from the source directly to the receiver (solid arrow marked **ray**).

monochromatic. The resulting wave propagates at several frequencies and may even exhibit dispersion in frequency or direction. This dispersion leads to wave packets (Fig. 2.4) that travel, in most cases, at a velocity different than the phase velocity.

The wave packets travel at the group velocity, which is defined as the derivative of the phase velocity, such that

$$\begin{aligned} v_{group} = \frac{\partial \omega}{\partial \mathbf{k}} = \frac{\partial(\frac{2\pi v_{phase}}{\lambda_w})}{\partial(\frac{2\pi}{\lambda_w})} = v_{phase} + \lambda_w^{-1} \frac{\partial v_{phase}}{\partial \lambda_w^{-1}} \frac{\partial \lambda_w}{\partial \lambda_w} \\ = v_{phase} - \lambda_w \frac{dv_{phase}}{d\lambda_w} = v_{phase} + k \frac{dv_{phase}}{d\mathbf{k}}, \end{aligned} \tag{2.25}$$

where λ_w is the wavelength. From Eqn. 2.25 whenever the phase velocity, v_{phase}, is frequency or directionally dependent (i.e., $\frac{dv_{phase}}{d\mathbf{k}} \neq 0$), the phase velocity is different than the group velocity [84].

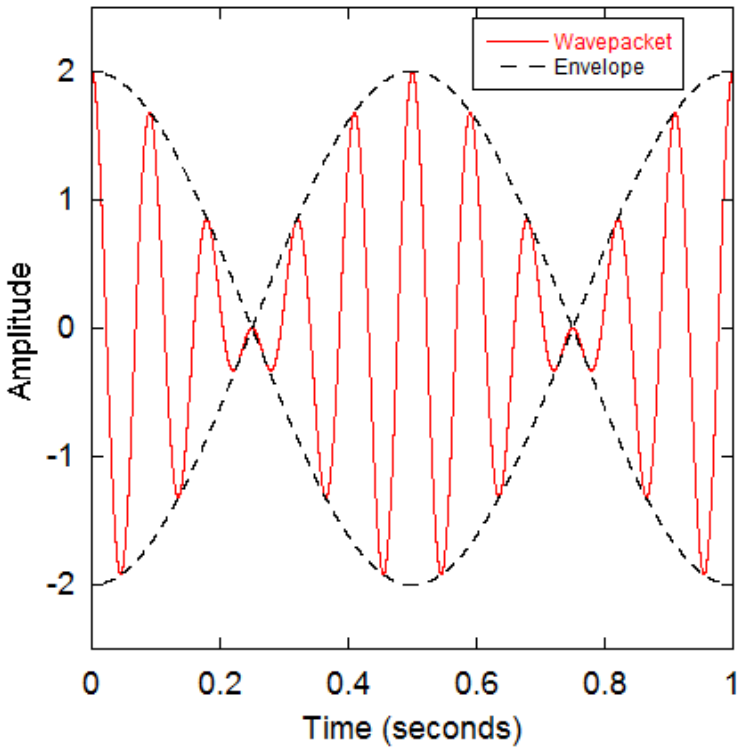

Figure 2.4. An example of a wave packet with a 2 Hz frequency. The envelope of this wave packet moves with the group velocity, while the wave itself moves at the phase velocity.

In an experiment, the *group velocity* is the velocity at which the wavefront propagates from a direct ray connecting the source and receiver (solid red arrow in Fig. 2.3). Note that this does not usually correspond to the same ray made by the phase velocity (dashed blue arrow in Fig. 2.3), because the wavefront is not always spherical. The angle made with this ray and the plane of the source is defined as the group angle (ϕ') (Fig. 2.3) [98]. The difference between the group and phase velocity is shown using a wave packet in Fig. 2.4. The wave packet (solid red lines in Fig. 2.4) moves with the phase velocity (fast) while the envelope (dashed lines in Fig. 2.4) moves at the group velocity (slow). Although in general the components of the packet are allowed to have different (phase) velocities, for homogeneous elastic media they are equal, i.e., frequency independent.

For elastic media, the phase and group velocities are related using the phase and group angles as [98]

$$v_{group}^2(\phi^{'}) = v_{phase}^2(\theta^{'}) + \left(\frac{dv_{phase}}{d\theta^{'}}\right)^2. \tag{2.26}$$

It should be mentioned that the definition in Eqn. 2.26 does not hold in attenuating media. For attenuating media Eqn. 2.26 is commonly referred to as the envelope velocity [101].

Note that at $\theta^{'} = 0°$ and $\theta^{'} = 90°$, the derivative in Eqn. 2.26 goes to zero and the group and phase velocity are equal. This is in agreement with the fact that along orthogonal symmetry planes the phase velocity is identical to the group velocity. The difficulty in calculating Eqn. 2.26 arises from the partial derivative, because it is difficult to make enough measurements at various angles to obtain a smooth derivative, making the analysis cumbersome.

2.4.3 Energy Velocity

Along with the concepts of both phase and group velocities arises the question: what velocity does the energy of the wave propagate at? This is called the *energy velocity* and is defined as the ratio of the time averaged power flow density, i.e., power flux, P_{avg}, to the total energy density, E_{avg} [84, 101]. The formal derivation of the energy velocity is rather lengthy and the reader is directed to the references for the details [84, 99, 101]. The results are shown here.

As mentioned above, the energy velocity is defined as

$$v_{energy} = \frac{P_{avg}}{E_{avg}}. \tag{2.27}$$

For elastic media, the phase and energy velocity are related by [101]

$$\mathbf{k} \cdot v_{energy} = v_{phase}, \tag{2.28}$$

where $\cdot$ is the dot product of the wave vector with the energy velocity vector.

Equation 2.28 indicates that in elastic media, the phase velocity is the projection of the energy velocity along the wavefront direction.

For elastic, lossless media, it is found that the group and energy velocity are equal, i.e., $v_{energy} = v_{group}$ [84, 101]. Consequently, these are also equal to the envelope velocity in elastic media, as discussed above.

Although not discussed here, viscoelastic solids, which have time dependent responses to vibrations, have different relationships between these velocities. The phase and group velocity, although defined the same way, have subtle differences that are beyond the scope of this discussion [101]. For viscoelastic media it is found that the phase and energy velocities are identical (in 1D) and for certain situations in 2D and 3D. The group velocity in these types of materials has no physical significance because the dispersion of the harmonic signals causes the definition to be changed and become no longer relevant.

For lossless media, the relationship between the phase and energy velocity (Eqn. 2.28) remains, as long as the media is homogeneous. The group velocity for low-loss media has physical meaning, but is no longer equal to the energy velocity, at least in general [101].

2.5 Summary

Basic elasticity theory has been presented to help discern the different types of symmetries and anisotropies present in rock. A brief overview of the relationships between velocity and the elastic stiffness terms (C_{ijkl}) for various symmetry groups was presented. In addition to the anisotropy discussion, an overview of the difficulty in discerning the type of velocity was also presented. With this fundamental description of anisotropy, a theoretical analysis can now be carried out using these definitions.

These results are used in the remaining chapters to derive the coupled wedge wave (CWW) and intersection wave for various anisotropy classes. For the remainder of this report, the phase, group, and energy velocities are equal because all measurements

are made along symmetry planes. The type of velocity measured will not be indicated unless necessary to the discussion.

3. Elastic Wave Propagation

3.1 Introduction

This chapter will discuss body, surface, and coupled waves that are used in seismology to measure properties in rock and other materials in science and engineering. A general description of each type of wave will be given, but the reader is left to the references for a full mathematical derivation for each wave. The wedge wave, which is a type of surface wave, will be discussed in more detail in chapter 4.

3.2 Body Waves

Body waves are elastic waves that propagate through the bulk material of an object [100]. The equations of motion lead to three types of body waves: compressional (P) waves and two polarizations of shear (S) waves.

The P-wave is a longitudinal wave whose particle motion is in the direction of wave propagation. The two S-waves, sometimes labeled SV and SH for shear vertical and horizontal, are transverse waves with particle motion perpendicular to the propagation direction. Typically, the polarization of these waves is represented by an arrow as shown in Fig. 3.1. Figure 3.1 illustrates the velocity differences for the P, S, Rayleigh, wedge, and non-wedge type waves propagated through an isotropic aluminum sample (Table H.3). The P-wave arrives first, as expected, followed by the large amplitude bulk S-wave, then Rayleigh and wedge waves arrive. The wedge wave (WW) (discussed in chapter 4) is excited by polarizing an S-wave transducer perpendicular to the half angle bisecting the corner (see inset). The non-wedge wave is excited by an S-wave source polarized perpendicular to the WW excitation geometry (see inset in Fig. 3.1). Note that the non-wedge arrives at the Rayleigh velocity but

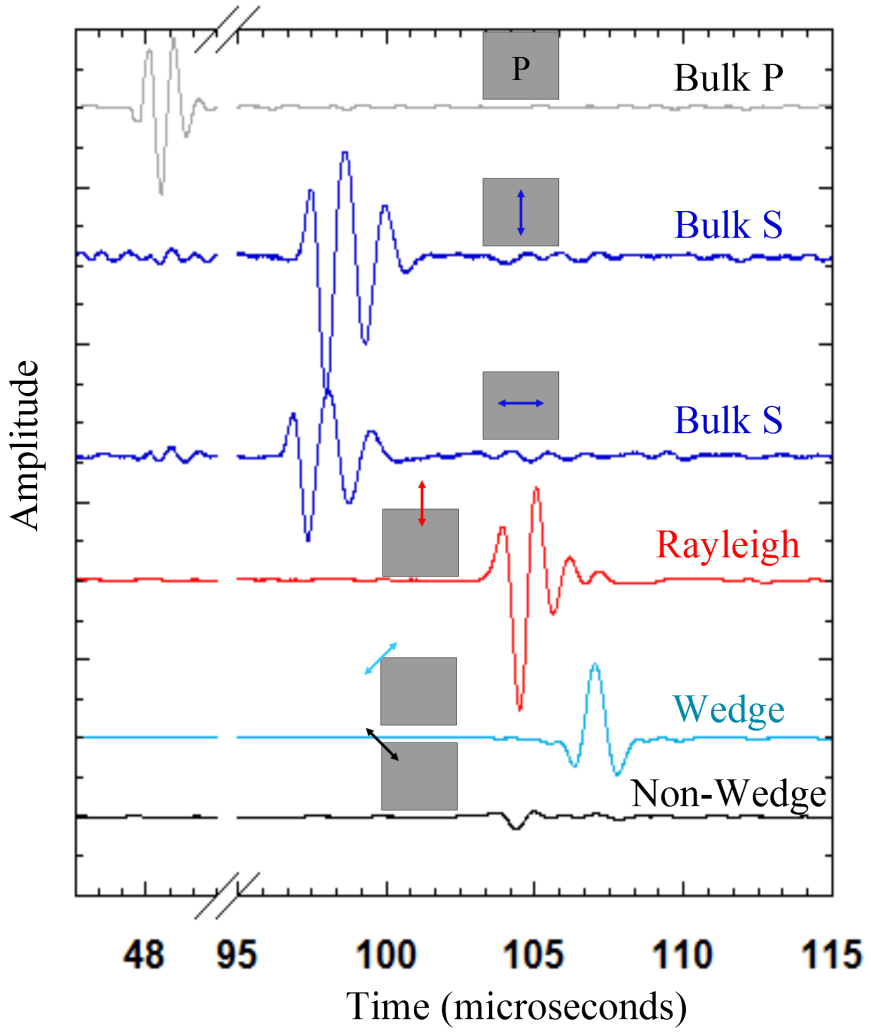

Figure 3.1. Different types of bulk and surface waves propagating through and along an isotropic aluminum sample (Fig. 5.19). The inset figures indicate the polarization (arrows) of the S-wave transducers.

with much lower amplitude. This is because the non-wedge polarization delocalizes the WW into Rayleigh waves on both free surfaces that are only partially excited, meaning neither are fully amplified. The receiver, located at the corner is not measuring the full Rayleigh wave on either surface, causing the small amplitude in Fig. 3.1.

For isotropic media (chapter 2), the two shear waves travel at the same velocity in any given direction and the P-wave travels faster than the S-waves (see Fig. 3.1). For anisotropic media, the P-wave is still faster than either S-wave, but the velocity of each wave may be different in any direction depending on the level of anisotropy and the symmetry within the matrix material. An example of this is shown in Fig. 3.2 for a sample of garolite.

Garolite (G10) is a synthetic, layered, epoxy, laminate material that simulates the anisotropy commonly found within layered rock. As Fig. 3.2 demonstrates, the P-wave always arrives prior to the S-wave, but the two S-wave polarizations are shifted, here by ~ 10 microseconds. The sample was a 10.1 cm cube with TI symmetry [83].

It was observed by Tsvankin (1997) that most shales exhibit transverse isotropy (section 2.3.2) [97]. That is, they have a plane where the velocities (P, S) are the same in either orthogonal direction. However, other media possess higher or lower anisotropy [84]. For example, Thomsen (1986) showed that most media possess $< 20\%$ anisotropy and can thus be represented by the linear terms in a Taylor expansion of the full anisotropic solution [98]. This was later extended to transversely isotropic and orthorhombic media [97, 102].

Although much work has been done to address the issues caused by anisotropy both acoustically and mathematically, many models still use isotropic assumptions and thus miss the effects of anisotropy, which can significantly affect elastic waves [72, 103].

3.3 Surface Waves

3.3.1 Rayleigh Waves

The most widely studied type of surface wave is the Rayleigh wave, which propagates along a free surface of a material with longitudinal and transverse (shear) motion perpendicular to the free surface, i.e., elliptical retrograde particle motion [104]. The Rayleigh wave was originally derived by Lord Rayleigh (1885) and was later extended

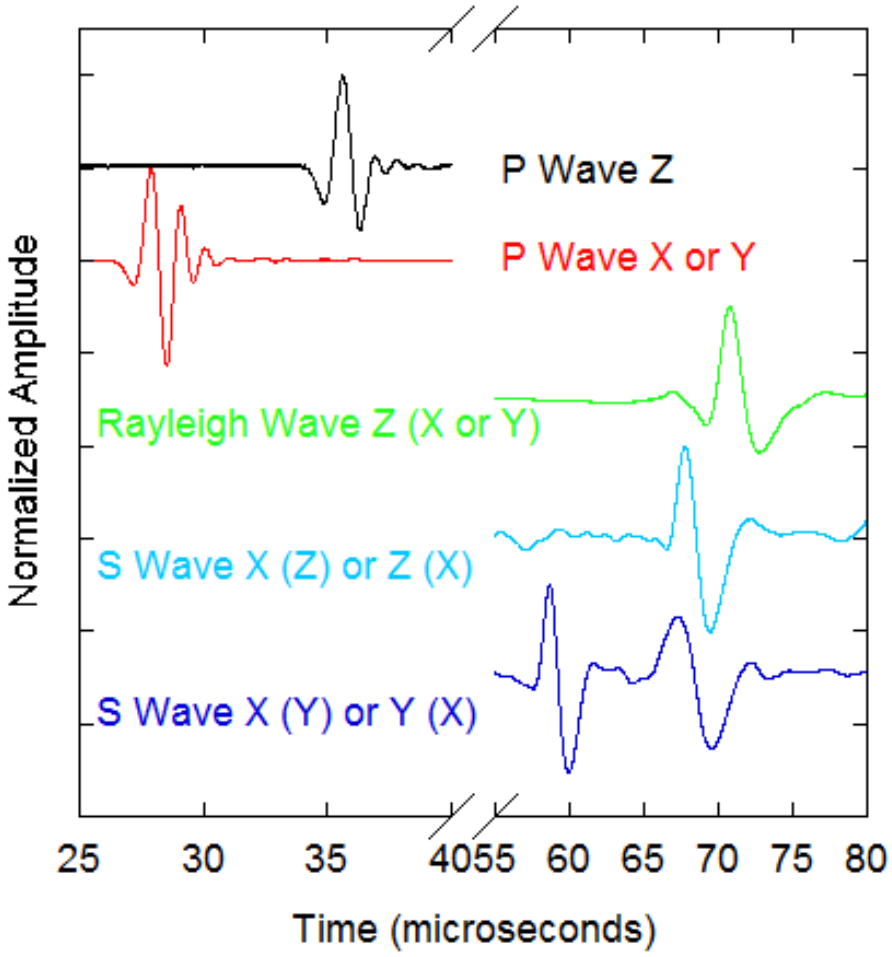

Figure 3.2. Different types of bulk and surface waves propagating through and along an anisotropic (garolite) sample. The first letter represents the direction of propagation and the parenthesis is the polarization direction.

to analytic solutions for isotropic and anisotropic media as a function of the material parameters [104–111]. The range of existence for the Rayleigh wave is also very large, and thus is highly applicable to most materials [112].

The anisotropic solution for a Rayleigh wave was derived using general orthotropic symmetry [107, 108] (section 2.3.1) (i.e., three independent, orthogonal symmetry planes) but can be converted to other symmetries using the formulation set forth by Chadwick (1976) [113].

Jaeger et al. (2007) derived equations for the displacement of Rayleigh waves for both the normal (W) and parallel (J) directions to the free surface as [99]

$$W = -kA_0 \left[\sqrt{(1-\alpha^2 r^2)} e^{-\sqrt{(1-\alpha^2 r^2)}kz} - \frac{\left[1 - \left(\frac{r^2}{2}\right)\right]}{\sqrt{(1-r^2)}} e^{-\sqrt{(1-r^2)}kz} \right] cos(k(x - v_R t)), \tag{3.1}$$

and

$$J = -kA_0 \left[e^{-\sqrt{(1-\alpha^2 r^2)}kz} - \left[1 - \left(\frac{r^2}{2}\right)\right] e^{-\sqrt{(1-r^2)}kz} \right] sin(k(x - v_R t)), \tag{3.2}$$

where A_0 is the amplitude, k is the wavenumber, t is time, v_R is the Rayleigh velocity, z is the direction normal to the interface, x is parallel to the interface and

$$\begin{aligned} r &= \frac{v_R}{v_P}, \\ \alpha &= \frac{v_P}{v_S}, \end{aligned} \tag{3.3}$$

where v_S is the S wave velocity and v_P is the P wave velocity.

For the isotropic Rayleigh wave as a function of depth (Eqns. 3.1 and 3.2), the displacement amplitude quickly decays to zero (i.e., within a few wavelengths). As an example, the normalized displacement for a surface with a Poisson's ratio of 0.25 is shown in Fig. 3.3. For the direction normal (W) to the free surface (Eqn. 3.1) the amplitude increases slightly and then drops to zero within $2\lambda_w$. For the direction parallel (J) to the free surface (Eqn. 3.2), the amplitude changes sign prior to $0.5\lambda_w$ and then decays back to zero within $2\lambda_w$, indicating a flip of the particle's elliptical trajectory (see Fig. 3.3).

The Poisson's ratio, ν, is a parameter that indicates the ratio of transverse to axial strain undergone by a body in a given direction [99]. For isotropic materials, only one Poisson's ratio is necessary to describe the material. A positive ν indicates that under compression the body expands in the transverse direction, the regime

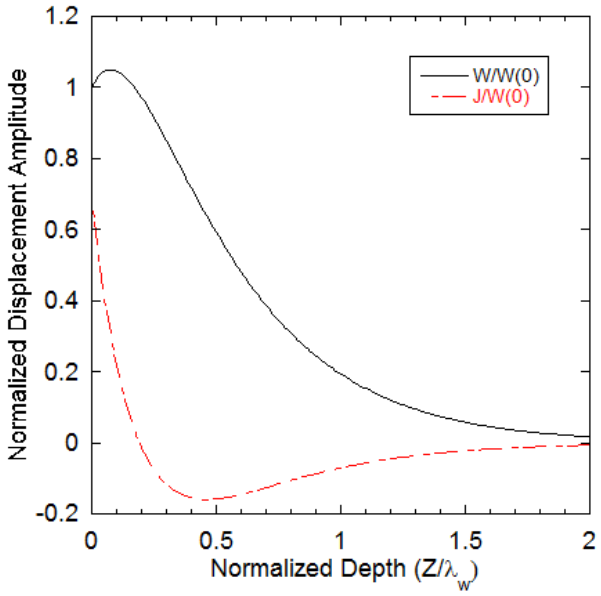

Figure 3.3. Normalized decay of the Rayleigh wave amplitude from Eqns. 3.1 and 3.2 with a Poisson's ratio of 0.25. The amplitudes are normalized by Eqn. 3.1 at $z = 0$ (i.e., $W(0)$). The depth is normalized by the wavelength, λ_w.

in which most materials exist. A negative ν indicates that under compression the transverse directions contract. Many negative ν materials are man made and a whole area of materials engineering is devoted to the study of negative ν materials or auxetic materials [114].

The Rayleigh wave velocity is slower than the bulk S-wave (Fig. 3.1) and is a function of Poisson's ratio, ν. The relationship between ν and the velocity of the Rayleigh wave is given in Fig. 3.4 and indicates a slightly faster velocity for positive ν than negative ν. A full description of this relationship and derivation can be found in the references [105, 106].

The particle motion of the Rayleigh wave is elliptical retrograde (shown in Fig. 3.5). As the Rayleigh wave propagates in the x direction, the motion is elliptical and rotates in the -x direction, i.e., counterclockwise, which arises from the trigonometric functions in Eqns. 3.1 and 3.2.

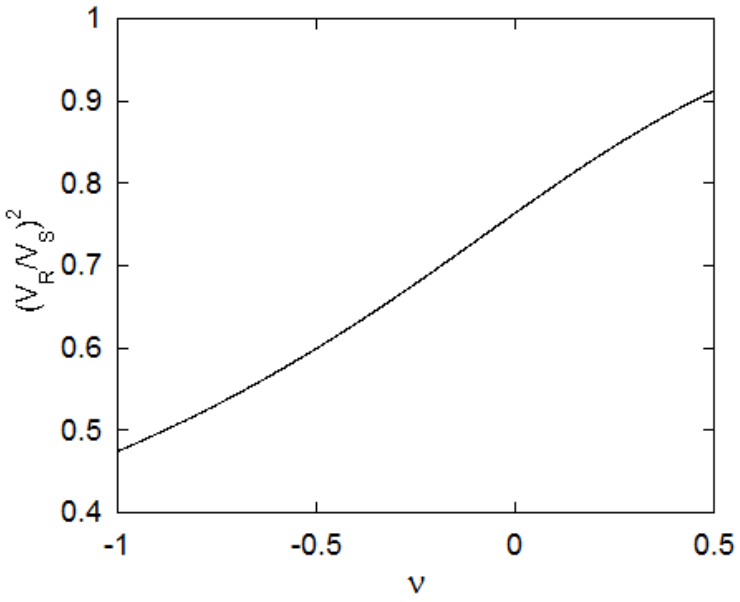

Figure 3.4. Rayleigh wave velocity as a function of Poisson's ratio (ν), based on the analytic solution from Rahman et al. (1995) [105]. v_R and v_S are the Rayleigh and bulk S-wave velocities, respectively.

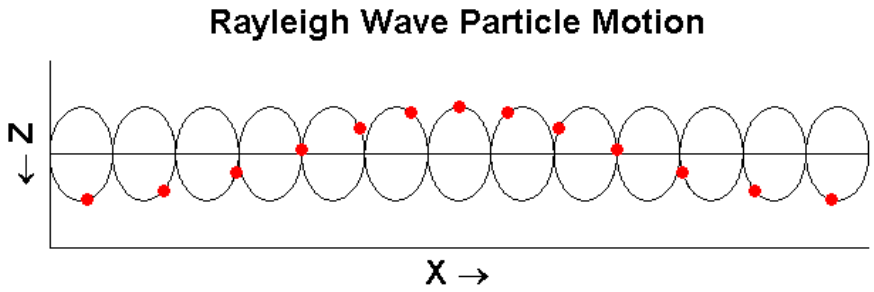

Figure 3.5. Particle motion for a Rayleigh wave propagating along the X direction. The parameters used were $v_P = 6000\ \frac{m}{s}$, $v_S = 3464\ \frac{m}{s}$, $v_R = 3184.9\ \frac{m}{s}$, and a frequency of $f = 1\ MHz$.

3.4 Coupled Surface Waves

Soon after the discovery of surface waves, several groups began coupling them to develop more complex applications for surface waves. Several of these waves are discussed here.

3.4.1 Stoneley Waves

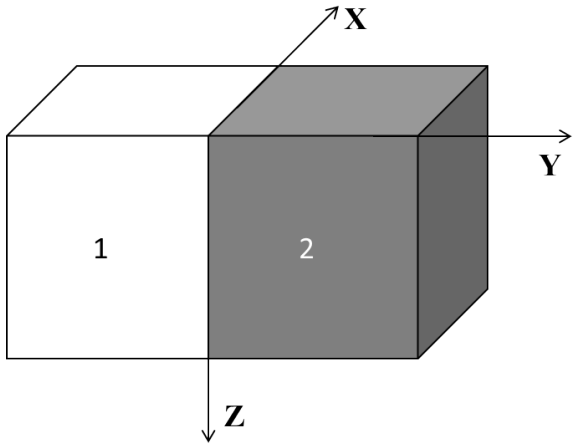

Figure 3.6. Geometry for exciting a Stoneley wave. The Stoneley wave exists along the fracture plane between two *different* media, labeled 1 and 2.

When two Rayleigh waves are propagated along the free surfaces between two *different* media, and coupled using continuous stress and continuous displacement boundary conditions, a Stoneley wave is supported that propagates in the x direction of Fig. 3.6 [115]. A Stoneley wave has a range of existence for various values of the material properties (density, ρ, and shear modulus, μ_L) (Fig. 3.7) [112, 116]. The Stoneley wave region of existence is between the two curves (i.e., hashed region) shown in Fig. 3.7, but not outside of this region. When the material parameters are outside of this region Stoneley waves delocalize to bulk waves. No Stoneley wave exists when the media are the same ($\frac{\mu_L}{\mu_L} = \frac{\rho}{\rho} = 1$ in Fig. 3.7); thus, it has limited applications to fractured media, because the media on either side of a fracture tend to be identical. Stoneley waves were also expanded to include anisotropy [117, 118], analytic solutions [119], and loosely bonded contacts with continuous displacements [120], but still require different media.

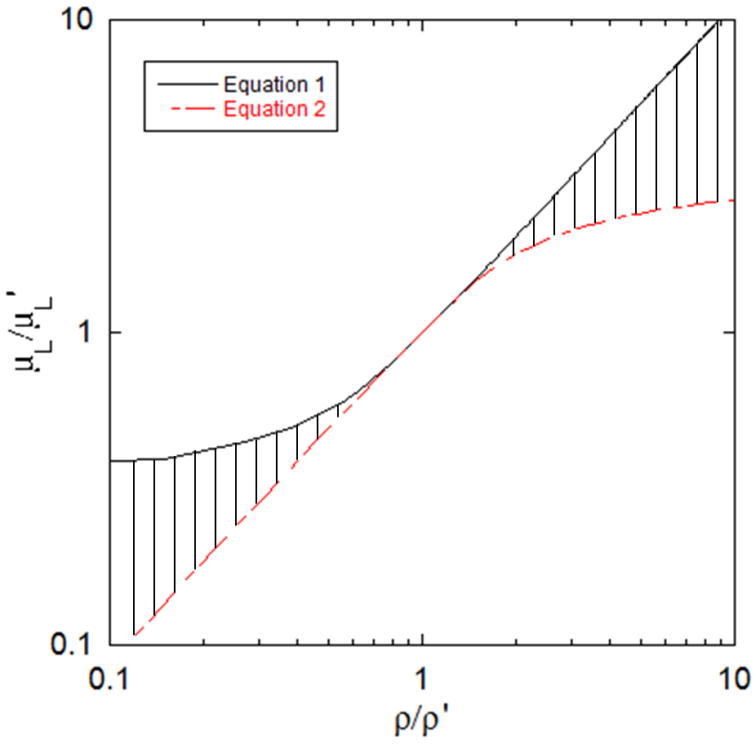

Figure 3.7. The range of existence for Stoneley waves falls within the hashed region. The lines are based upon Eqns. 1 and 2 of Scholte (1947) [112] for a Poisson's ratio of $\frac{1}{3}$. μ_L and $\mu_L^{'}$ are the bulk modulus of the two media, and ρ and $\rho^{'}$ are the densities of the same two media.

3.4.2 Interface Waves

Using an approach analogous to Stoneley waves, several authors independently derived a dispersive wave, called an interface wave, that arose by coupling two Rayleigh waves through continuous stress [121] and discontinuous displacement boundary conditions [12,122–125] (which is discussed in section 5.3.6). A similar approach analyzed a three layer model in which the middle layer went to zero thickness [13, 126–128]. These interface waves were predicted to exist along the plane formed by two elastic, isotropic half spaces in contact. The continuous stress and displacement discontinuity (DD) boundary conditions yield a waveform that is dispersive in both frequency, and specific stiffness, κ, of the fracture (Fig 3.8).

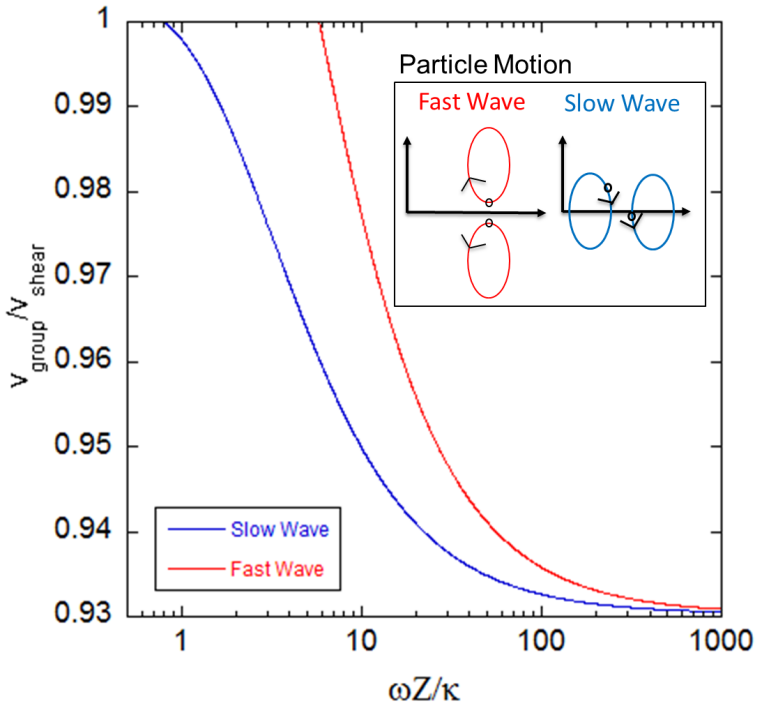

Figure 3.8. Normalized interface wave group velocity, v_{group}, as a function of normalized stiffness. ω is the frequency, κ is the specific stiffness, and Z is the impedance (ρv_S). The insets shows the particle motion of the fast wave and slow wave and the transducer polarization required to excite an interface wave.

There are two types of interface waves: symmetric and antisymmetric (i.e., fast and slow, respectively) shown in the inset of Fig 3.8. Although some experimental evidence has pointed towards a compressional interface wave mode, no theory has been presented [129]. The two types are so named based on the relationship between the phase of their particle motion, shown in the inset of Fig. 3.8. The existence of these waveforms, either individually or together, depends upon the physical properties of the two media that make up the fracture (see Fig. 5 of Pyrak-Nolte et al. (1987)). For two materials with a Poisson's ratio of 0.25, and a wavenumber of 5600, the existence region is shown in Fig. 5 of Pyrak-Nolte et al. (1987). Note that the slow wave exists everywhere for these parameters, but the fast wave only exists in the shaded region.

Later experimental and numerical work demonstrated the existence of interface waves [2, 4, 5, 7, 9, 13–15, 130–134], and more recently demonstrated their behavior in anisotropic media [16]. Initial attempts at understanding intersection waves looked at the possibility of coupled interface waves interacting at the fracture intersection, but this was determined to not be the case due to the range of velocities observed in the experiments.

Although most of the studies on interface waves ignore the effect of cross coupling specific stiffnesses, i.e., only the diagonal stiffness terms (Eqn. 3.4) are applied, Nakagawa et al. [130,135] tackled the problem of using cross coupling stiffnesses. The cross coupling specific stiffnesses are the off diagonal terms in the κ tensor of DD theory (see Eqn. 3.4). Nakagawa et al. (2000) applied DD boundary conditions, including these off diagonal stiffness components, such that DD equations became

$$\begin{pmatrix} \sigma_{zx} \\ \sigma_{zy} \\ \sigma_{zz} \end{pmatrix} = \begin{pmatrix} \kappa_{xx} & \kappa_{xy} & \kappa_{xz} \\ \kappa_{yx} & \kappa_{yy} & \kappa_{yz} \\ \kappa_{zx} & \kappa_{zy} & \kappa_{zz} \end{pmatrix} \begin{pmatrix} u_{2x} - u_{1x} \\ u_{2y} - u_{1y} \\ u_{2z} - u_{1z} \end{pmatrix} \tag{3.4}$$

where σ_{zi} are the components of the stress tensor, κ_{ij} are the specific stiffness components and u_{mj} are the displacements in medium m, in the j direction. Prior to this work, only the diagonal stiffness terms were used.

When the full stiffness tensor was applied to elastic waves propagating along a sheared fracture, the predicted interface waves (shown in Fig. 9.3 of Nakagawa (1998)) differed only slightly from those without the cross-coupling stiffness terms (compare Figs. 3.8 and 9.3 of Nakagawa (1998)).

Nakagawa (1998) determined that an increase in the cross coupling κ caused a decrease in the antisymmetric (slow) interface wave velocity, and an even smaller increase in the symmetric (fast) interface wave velocity compared to the original results without cross coupling κ. The range of velocities did not vary with this addition of cross coupling, but the analysis of κ for a given interface wave velocity changed under this interpretation (Fig. 9.3 of Nakagawa (1998)).

Nakagawa also analyzed the affect that cross coupling κ had on the particle motion of interface waves. As described above (Fig. 3.8), interface waves with no cross coupling κ exhibit either symmetric or antisymmetric particle motion, in an elliptical retrograde tendency, similar to the Rayleigh wave (Fig. 3.5). For low off diagonal κ terms, little effect on the particle motion shape was observed (Fig. 9.4a of Nakagawa (1998)). As κ increases, the antisymmetric wave's ellipticity becomes narrower in the direction normal to the fracture, becoming similar to the particle motion of a bulk S-wave (Fig. 9.4b of Nakagawa (1998)). At high κ the symmetric wave became a leaky P-wave, indicated by horizontal particle motion (Fig. 9.4a of Nakagawa (1998)). Although these changes are small, Nakagawa commented that the most significant difference is the altering of the phase between the particle motion on both surfaces of the fracture. When there is no cross coupling κ (i.e., $\kappa_{ij} = 0,\ i \neq j$), the particle motion in the two media are perfectly symmetric (or antisymmetric). As the cross coupling κ is increased, this symmetry (or anti-symmetry) breaks down, causing the two media to display a phase shift.

3.4.3 Rayleigh Stoneley Waves

Wedge waves (chapter 4) were also coupled, using continuous boundary conditions, by several groups [136–138]. The coupling done by Sokolova et al. (2012) lead to the prediction of a Rayleigh-Stoneley (RS) wave that propagates along the coupled tips of two isotropic, orthogonal wedges in welded contact [138]. It is essentially a Stoneley type wave propagating along a welded surface fracture (Fig. 3.6).

The RS wave gives insight into the limiting behavior for coupled wedge waves (see section 5.3.7), but the range of existence only extends from 0 to 0.3 for ratios of shear modulus ($\frac{\mu 2}{\mu 1}$) and densities ($\frac{\rho 2}{\rho 1}$) and does not exist when the two media are the same, shown in Fig. 2 of Sokolova et al., (2012) [138]. This existence range severely limits the materials that could support this wave and prevents easy verification in the laboratory or field of its existence.

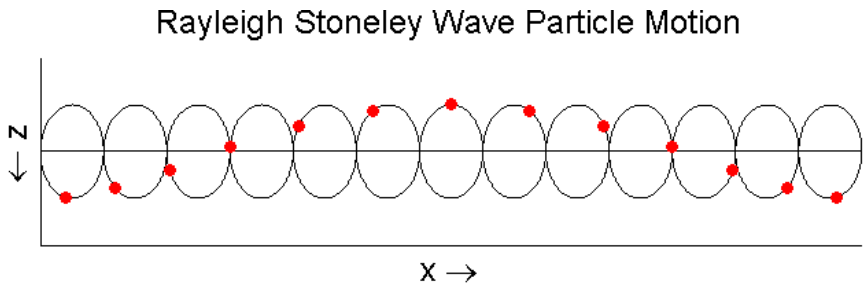

Figure 3.9. Rayleigh-Stoneley (RS) wave particle motion propagating in the x direction. Note that the waveform is propagated to the right and that the particle motion is prograde elliptical. The same parameters as Fig. 3.5 were used.

The particle motion of the RS waves is prograde elliptical (Fig. 3.9), opposite that of the Rayleigh wave (Fig. 3.5). As the wave propagates along the x direction, the particle motion is in the x-z plane, but the particle motion is rotating clockwise in the positive x direction. This is shown as snapshots in time in Fig. 3.9.

To calculate the displacement along the fracture plane (i.e., z direction in Fig. 3.6), the velocity of the RS wave was used to determine the eigenvectors of the secular equation for RS waves (Eqn. 17 in Sokolova et al. (2012) [138]) corresponding to an eigenvalue of 0. Then, these eigenvectors were used to calculate the displacements. The results are shown in Fig. 3.10 for all three displacement directions using $\frac{\rho_2}{\rho_1} = 0.08$ and $\frac{\mu_2}{\mu_1} = 0.1$ for the material properties.

RS waves also decay in a fashion similar to Rayleigh waves (compare Figs. 3.10 and 3.3). The x- component of the RS wave decays quickly, and flips sign prior to a depth of one wavelength before asymptoting to 0 amplitude along the free surface (solid line in Fig. 3.10). The y component decays roughly exponentially within a few wavelengths (large dashed line in Fig. 3.10) and the z component decays even closer, indicating a high localization of the RS wave to the free surface (small dashed line in Fig. 3.10).

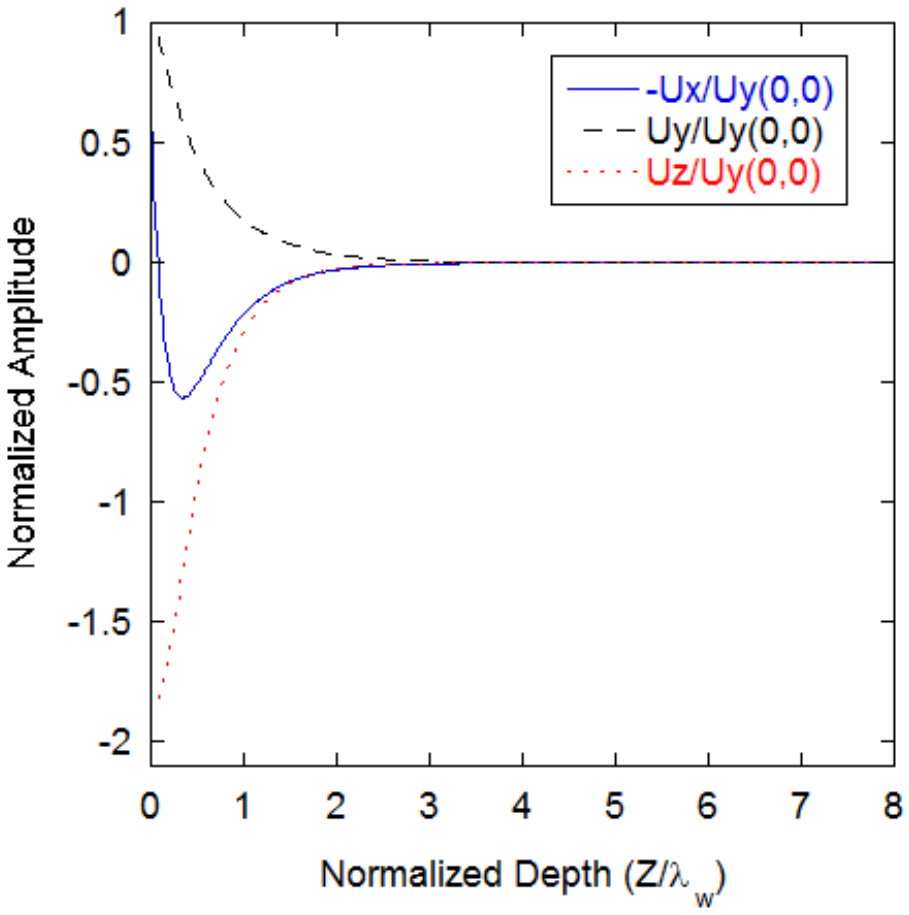

Figure 3.10. Rayleigh-Stoneley (RS) wave decay, based on Fig. 4b of Sokolova et al. (2012) [138]. The displacements have been normalized by the displacement in the y direction (Fig. 3.6) and shown to decay as a function of wavelength. Note that the displacement in all directions has basically gone to zero by 3 wavelengths (λ_w).

3.5 Summary

In this chapter, the existence and properties of bulk, surface, and coupled waves were presented for several geometries, as well as background discussions on previous work done to understand these waves. These waves have all played an important role in non-destructive testing of samples, both in the laboratory and in the field.

The coupled waves presented in this chapter, especially interface waves, have been used extensively as a probe in measuring the κ of fractures. This is a key physical

parameter for inferring the hydraulic characteristics of a fracture. The goal is to couple waves in a way that allows a fracture intersection to be characterized and described theoretically and experimentally with applications to the field.

4. Group Theory and Wedge Waves

4.1 Introduction

This chapter introduces group theory analysis for application to waves localized near corners. The formulation presented in this chapter is required for the analysis in chapters 5 and 6. An example of the application of group theory to a wedge wave (WW) is given and compared to the literature results.

Group theory provides the mathematical formulation to interpret symmetry, and the physical implications of the symmetry. Group theory has been applied to many problems (e.g., vibrational modes of water), and has provided deep physical insight into problems in quantum mechanics and chemistry. This chapter contains an in depth discussion on basic group theory terminology and usage, followed by the application of group theory to the study of WWs. Several sources were used for this derivation, of which Joshi (1973) [139] and Wolfram et al. (2014) [140] were the easiest to understand.

Although a group theory analysis of WWs has been previously carried out [141, 142], the tools required to apply group theory to other vibrational problems are discussed here for use in later chapters. For the WW and other coupled waves, group theory was required to predict and verify the number and types of vibrational modes for the waves considered in this work; thus, a full discussion is given.

In the following analysis, a brief overview of some terminology and notation used in group theory, followed by a simple example involving the transformation of a hand is shown to get familiar with the topic. Each step of the analysis is described below from the formulation of Wolfram et al. (2014) [140].

Although many texts begin by deriving several fundamental theorems in group theory followed by examples, this chapter will focus on the WW problem and provide

Table 4.1
Mulliken symbol definitions [143].

Symbol	**Property**
A	Symmetric under lowest n-fold rotation in group
B	Anti-symmetric under lowest n-fold rotation in group
ε	Two dimensional (i.e., doubly degenerate)
T	Three dimensional (i.e., triply degenerate)

the necessary theorems when they arise in the discussion. For additional information and formal proofs of the theorems the reader is referred to the references.

Table 4.2
Mulliken symbol subscripts and superscripts [143].

Index	**Position**	**Property**
1	subscript	Symmetric under σ_v, or C_2 perpendicular to C_n
2	subscript	Anti-symmetric under σ_v, or C_2 perpendicular to C_n
g	subscript	Symmetric under inversion (i)
u	subscript	Antisymmetric under inversion (i)
’	superscript	Symmetric under σ_h if i is not present
”	superscript	Antisymmetric under σ_h if i is not present
+	superscript	Symmetric under σ_v in $D_{\infty h}$
-	superscript	Antisymmetric under σ_v in $D_{\infty h}$

4.1.1 Notation

Several types of notation are used in texts on group theory. The notation used in this work are highlighted here. Tables 4.1-4.2 list the symbol, subscript, and

superscript definitions, respectively. This set of symbols is called *Mulliken Notation*, and is used to define the modes of vibration.

Other notation used includes:

- G denotes a generic group.
- $A \in G$ means that A is an element (operator) in the set of G. Sometimes it is said that, "A belongs to G".
- $|G|$ is the order of the group. Sometimes represented by a lowercase symbol (e.g., $|G| = g$).
- C_n^k denotes the operation of C_n repeated k times (e.g. $C_4^3 = C_4C_4C_4$).
- $[A, B] = AB - BA = 0$ is the notation for commuting operators.
- E is the identity operator.

4.1.2 Groups and Theorems

A *Group*, G, is defined as a *set* of elements (sometimes called operators) denoted $\{R, S, T, ...\}$. In general, elements of the set do not commute (i.e., $[R, S] \neq 0$). These elements are called a group if a multiplication rule is defined for any two elements so that the product RS has a definite meaning and the following four postulates apply. [144].

Postulate 1 (Closure) *If R and S belong to the set of operators within group G (i.e., $R \in G$ and $S \in G$), then RS also belongs to this set (i.e., $RS \in G$).*

Postulate 2 (Associative law) *The following rule must apply for operators R, S, $T \in G$: $R(ST) = (RS)T$.*

Postulate 3 (Identity) *There exists the identity operator, E, such that $AE = EA = A$ for any A belonging to the set of operators.*

Postulate 4 (Inverse) *There exists an inverse element for each element within the set such that* $AB = BA = E$ *where* $B = A^{-1}$ *and* B *is called the inverse of* A*.*

Examples of Groups

- All integers under addition. These form a discrete group.
- Complex numbers form a group of order 4. They are: 1, $i, 1$, and $-i$ under multiplication.
- Group of order two consisting of the real numbers: $1, -1$, with ordinary multiplication as the law of composition.

4.1.3 Terminology

Group theory involves several uncommon terms which are used throughout this dissertation. A list of common terminology used in group theory analysis is presented here to aid in the comprehension of the derivations [139, 140, 143, 144].

Table 4.3: Terminology used in group theory [139, 140, 143, 144].

Term	**Definition**
Abelian Group	A group where all the elements commute (i.e., $[R, S] = 0$).
Active View-Point	Operations which transform the object and leave the coordinate system fixed.
Characters	The sum of all the diagonal elements of a matrix (i.e., the trace). Typically χ is the symbol used.

continued on next page

Table 4.3: *continued*

Term	**Definition**
Classes	Sets within a group of elements $\{A, B, C, ...\}$ which can be split into smaller sets such that all the elements of the smaller set are conjugate to each other, but no two elements belonging to different smaller sets are conjugate.
Conjugate Elements	Two elements that follow a similarity transformation. (e.g., $A^{-1}BA = C$ and $A^{-1}CA = B$ means that B and C are conjugate elements).
Covering Operation	Rotation or reflection of an object into an indistinguishable configuration.
Equivalent	When things exchange positions under a symmetry operation (e.g., atoms in a molecule).
Finite Group	A group that has a finite number of elements.
Improper Rotation	Rotation about an axis by some angle $\frac{2\pi}{n}$ followed by a reflection in a plane containing that axis. This operation is labeled S_n.
n-fold symmetry axis	An axis about which a rotation of $\frac{2\pi}{n}$, (n=positive integer) leaves the system invariant. Typically denoted as C_n.
Order of the Group	The total number of elements in the set.
Passive View-Point	Operations that transform the coordinate system and leaves the object fixed.
Point Groups	A symmetry group of a finite system in which all symmetry operations leave at least one point of the system unmoved.
Proper Rotation	Rotation about an axis by some angle $\frac{2\pi}{n}$, labeled C_n.
Proper Subgroup	A subgroup of G and $\neq G$.

continued on next page

Table 4.3: *continued*

Term	**Definition**
Subgroup	A set H is a subgroup of G if H is itself a group and if all the elements of H are also in G. Every group, G, has at least two trivial subgroups E (identity) and G (the group itself). This differs from a class because a class is not a group, in general.
Symmetry Groups	Groups in which the operations leave a system unchanged.
Symmetry Operation	An operation which brings a system into a position indistinguishable from that which it originally occupied. It does not change the distance between any two points inside of the system.
Vibrational Normal Modes	Vibrations which leave the center of mass stationary ($\sum_i m_i \mathbf{r}_i = 0$) [140]. If the object or molecule is set vibrating in one of these modes, it will remain in this mode alone, and other modes will not be excited, i.e., it is independent.

4.1.4 Transformations

There are several fundamental transformations that can occur in analyzing the symmetry of a given problem. These are: *identity, reflection, rotation about an axis, inversion,* and an *improper rotation.* The best way to describe these transformations is by example. The operations (i.e., transformations) are applied to a right hand to demonstrate their effect and are shown in Fig. 4.1. It is observed that reflection, inversion, and improper rotation change a right hand into a left hand. The other operations alter the right hand, but keep it as a right hand. Point groups are formed

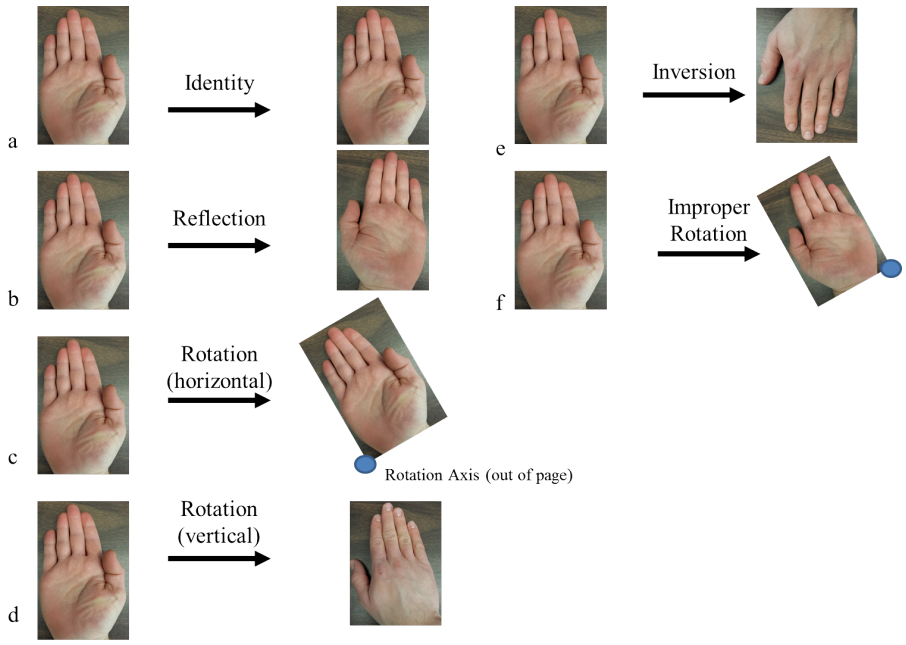

Figure 4.1. Transformations on a right hand. a) Identity (E) does nothing. b) Reflection, sometimes called a mirror reflection, makes a right hand to a left hand. c) Rotation (horizontal) is a rotation about an axis out of the page. d) Rotation (vertical) is a rotation about an axis in the plane of the page typically vertical (usually called z axis). e) Inversion, flips hand over and changes it to a left hand. f) Improper rotation switches to a left hand and rotates. These are based on Fig. 1.6.a.ii-1 of Mirman [85].

from reflections, inversions, and rotations only. Space groups (not discussed here) come from the addition of translations.

4.1.5 Representations

Let $G = \{E, A, B, ...\}$ be a finite group of order g. Let $W = \{W(E), W(A), W(B), ...\}$ be a set of square matrices, all of the same order, with the property: $W(A)W(B) = W(AB)$ such that if $AB = C$ in the group G, then $W(A)W(B) = W(C)$. If this is true, then the set W is said to be a *representation of the group* G. The order of W is the *dimension of the representation*. Note that W does not need to be a group. [139]

Representations of a specific group can be reduced using mathematical properties. Eventually to a point that they are an *Irreducible Representation (IR).*

Lemma 4.1.1 *Schur Lemma 1*

If $\Gamma^{(i)}$ *is an IR of a group,* G*, and if a matrix,* P*, commutes with all the matrices of* $\Gamma^{(i)}$*, then* P *must be a constant matrix (i.e.,* $P = cE$*) [139, 140, 143].*

Lemma 4.1.2 *Schur Lemma 2*

If $\Gamma^{(i)}$ *and* $\Gamma^{(j)}$ *are two IRs of dimensions* l_i *and* l_j*, respectively, of a group* G *and if a matrix* $\bar{\mathbf{N}}$ *(order* l_i *x* l_j*) satisfies:* $\Gamma^{(i)}(A)\bar{\mathbf{N}} = \bar{\mathbf{N}}\Gamma^{(j)}(A)$ *for all* $A \in G$*, then either* $\bar{\mathbf{N}} = 0$ *or* $|\bar{\mathbf{N}}| \neq 0$*, in which case* $\Gamma^{(i)}$ *and* $\Gamma^{(j)}$ *are equivalent representations. Note: if* $l_i \neq l_j$ *then* $\bar{\mathbf{N}} = 0$ *is the only possibility [139, 140, 143].*

If there exists a vector space B_n which is used to create a representation of the group G, then the following can be said: for every element $A \in G$, and every vector $\xi \in B_n$, $A\xi$ also belongs to B_n. This is described as, "*The vector space* B_n *is invariant under the transformations of* G *(i.e., invariant under* G*)*" [139].

The vector space B_m is a *subspace* of another vector space B_n if every vector of B_m is also contained within B_n. BL_m is called a *proper subspace* of B_n if the vectors of B_m do not exhaust the space B_n. This means that B_n is a subspace of itself, but is not proper with respect to itself.

A representation is said to be *reducible* if the corresponding spaces B_m contain additional invariant proper subspaces within them. The process of reduction is continued until the final form of all the matrices of the representation are diagonal and are fully reduced, leading to an IR [139]. See section 3.6 of Joshi for details on how to reduce a representation [139].

4.2 Group Theory Analysis of Wedge Waves

Group theory analysis is applied to the well known wedge wave (WW) to demonstrate the method for predicting vibrational modes. As mentioned in the introduction,

the group theory analysis for the WW has been done, but is demonstrated here to help introduce the ideas and steps necessary to carry out group theory analysis. The same analysis is applied to the coupled wedge wave (chapter 5), intersection wave (chapter 6), and the Rayleigh-Stoneley wave (Appendix C.1).

4.2.1 Step 1: Identify the point group and its symmetry operations

For many group theory problems, several symmetry operations are possible that maintain at least one point unaltered after the operation is applied. For the WW, these operations need to leave the tip of the wedge unaltered. This corresponds to the point $x = y = z = 0$ that is unchanged after the operation is applied. The WW geometry and coordinate system used in this analysis are shown in Fig. 4.2. The wave propagates along the tip (x=y=0) in the z direction.

The symmetry operators, which preserve the point group symmetry of the wedge, are the identity, E, and reflection along the $y = x$ plane, σ. These two operators form the point group C_s. C_s is a nonaxial, cyclic, order 2, Abelian group which has no proper or improper rotation axes. Other names exist for this group including: C_{1h}, S_1, and C_{2i}, but in this discussion the C_s notation is used.

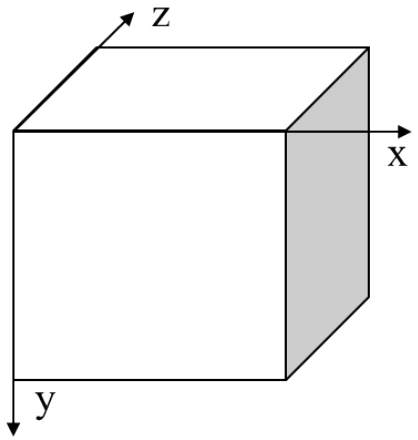

Figure 4.2. Geometry used in the group theory analysis of the WW.

Table 4.4
Action table for the WW analysis.

	E	σ
r_x	r_x	r_y
r_y	r_y	r_x
r_z	r_z	r_z

4.2.2 Step 2: Specify the coordinate system and basis functions

The coordinate system used for the WW analysis is the Cartesian coordinate system shown in Fig. 4.2. This coordinate system, located at the tip of the wedge, is used to define the displacement vectors, which are used as basis functions. It should be mentioned that the basis functions are not attached to the wedge, i.e., this is an active view-point.

4.2.3 Step 3: Determine the effects of the symmetry operations on the basis functions

Consider some vector, $\bar{\mathbf{r}}$, which is located on the wedge. After operating on this vector with one of the symmetry operators, $\bar{\mathbf{r}}$ may be changed. The effects of the symmetry operators on this vector are written symbolically as

$$\begin{aligned} &\Gamma(E)r_x \rightarrow r_x,\ \Gamma(E)r_y \rightarrow r_y,\ \Gamma(E)r_z \rightarrow r_z, \\ &\Gamma(\sigma)r_x \rightarrow r_y,\ \Gamma(\sigma)r_y \rightarrow r_x,\ \Gamma(\sigma)r_z \rightarrow r_z, \end{aligned} \tag{4.1}$$

and are used to form an action table (Table 4.4).

The action table allows a quick visual interpretation of Eqn. 4.1. Acting the representations of the operators in the top row on the vectors in the first column. The results are shown in the corresponding box within the table.

4.2.4 Step 4: Construct a matrix representation for each element using the basis functions

The next step is to determine which matrix can operate on a vector of basis functions to yield the resulting vectors in the action table (Table 4.4). If the basis function vector is defined as

$$[r] = \begin{bmatrix} r_x \\ r_y \\ r_z \end{bmatrix}, \tag{4.2}$$

then the matrix representation of the operators in C_s are

$$\Gamma(E) = \begin{bmatrix} 1 & 0 & 0 \\ 0 & 1 & 0 \\ 0 & 0 & 1 \end{bmatrix}, \tag{4.3}$$

and

$$\Gamma(\sigma) = \begin{bmatrix} 0 & 1 & 0 \\ 1 & 0 & 0 \\ 0 & 0 & 1 \end{bmatrix}. \tag{4.4}$$

Compare the results of $\Gamma(E)[r]$ and $\Gamma(\sigma)[r]$ to Table 4.4 to verify.

4.2.5 Step 5: Determine the number and type of irreducible representations

The classes of the C_s group must be determined to continue analyzing the vibrational modes of the WW. In general, the classes are found by applying the products $O_i A O_i^{-1}$, where A is the operator to determine the class of the group, and O_i are all the other operators in the group. The identity operator (E) is in a class of its own because it commutes with all other operators, in this group or any other. A class is represented by the notation $\{E\}$. Because there are only two operators in the C_s class, σ must also be in a class by itself, i.e., $\{\sigma\}$. The properties of these classes are shown through a character table.

Character tables are used to predict vibrations and other properties of the object under investigation. These tables are derived in many references on group theory. Their derivation is rather lengthy, but they come from several basic theorems. The theorems are discussed in this section and are taken from the references [139,140,143].

Theorem 4.2.1 *The characters of all operations in the same class are equal in each given irreducible (or reducible) representation [139, 140, 143].*

Theorem 4.2.2 *The point product of the characters of any two IRs is 0. This theorem can be stated in terms of orthogonality as: the characters of the IRs of a group are orthogonal to one another [140]. In equation form*

$$\frac{1}{h}\sum_{i=1}^{h}\left(\chi_i^{\alpha}\right)^{*}\chi_i^{\beta}=\delta_{\alpha\beta}, \tag{4.5}$$

where χ_i^{α} is the character of the representation $\Gamma^{\alpha}(O_i)$, $\delta_{\alpha\beta}$ is the Kronecker delta function, and h is the number of elements in the group.

As an example, check the C_{3v} character table 4.5

$$\begin{aligned}
&\Gamma_{A1} * \Gamma_{A2} = (1)(1)+(1)(1)+(1)(1)+(1)(-1)+(1)(-1)+(1)(-1)=0,\\
&\Gamma_{A2} * \Gamma_{\varepsilon} = (1)(2)+(1)(-1)+(1)(-1)+(-1)(0)+(-1)(0)+(-1)(0)=0,\\
&\Gamma_{A1} * \Gamma_{\varepsilon} = (1)(2)+(1)(-1)+(1)(-1)+(1)(0)+(1)(0)+(1)(0)=0.
\end{aligned} \tag{4.6}$$

Theorem 4.2.3 *The sum of the squares of all characters (i.e., all the dimensions) in any IR is equal to the order of the group. The order of the group is the number of symmetry operators. This is expressed as*

$$\sum_{i=1}^{N_c} l_i^2 = h, \tag{4.7}$$

where l_i is the dimension of the ith IR and h is the number of elements in the group [140].

As an example, look at the character table (Table 4.5) for C_{3v} which is order 6. For A_1 Eqn. 4.7 becomes: $1^2 + 1^2 + 1^2 + 1^2 + 1^2 + 1^2 = 6$, for A_2: $1^2 + 1^2 + 1^2 + (-1)^2 + (-1)^2 + (-1)^2 = 6$, and for E: $2^2 + (-1)^2 + (-1)^2 + 0^2 + 0^2 + 0^2 = 6$. There are six operators: $E,\ C_3,\ C_3^2,\ \sigma_v,\ \sigma_v^{'}$, and $\sigma_v^{''}$.

Table 4.5
Character table for the point group C_{3v}.

C_{3v}	E	C_3	C_3^2	σ_v	$\sigma_v^{'}$	$\sigma_v^{''}$
A_1	1	1	1	1	1	1
A_2	1	1	1	-1	-1	-1
ε	2	-1	-1	0	0	0

=

C_{3v}	E	$2C_3$	$3\sigma_v$
A_1	1	1	1
A_2	1	1	-1
ε	2	-1	0

Theorem 4.2.4 *The number of IRs of a group is equal to the number of classes in the group. As an example, the group C_{3v} has three classes: $\{C_3, C_3^2\}$, $\{\sigma_v, \sigma_v^{'}, \sigma_v^{''}\}$, and $\{E\}$. This means that the group C_{3v} has three IRs ($A_1,\ A_2,\ \varepsilon$) [139, 140, 143].*

In a character table, the operators in the same class are only displayed in one column, but labeled with a coefficient that represents how many operators are in that class. For example, the $\{C_3, C_3^2\}$ class is represented by $2C_3$ in the character table (top row in Table 4.5) representing 2 operators in the same class as C_3. Although this does not apply to the C_s point group discussed in this chapter, it does apply to the intersection wave discussed in chapter 6.

The character table for the C_s point group is shown in Table 4.6. The difference in the rows with the representation characters arises from the difference in the effect of the operators on a given geometry. For the wedge, the σ operator switches the x and y components, but not the medium or the z component. This leaves a different set of characters for the z component because neither operator affects the z coordinate.

Table 4.6
Character table for the point group C_s used in the WW analysis.

C_s	E	σ
$A^{'}$	1	1
$A^{''}$	1	-1
Γ^{xy}	2	0
Γ^{z}	1	1

The next step in the analysis is to determine the decomposition of each Γ into the IRs. To do this, look at the dimensionality of each IR. From theorem 4.2.3 the $\{E\}$ class is examined from the character table for C_s (Table 4.6). Since E is in a class by itself, the dimensionality of each IR is the character. The same can be said for the $\{\sigma\}$ class.

To determine the type and number of IRs in the representation, Γ, a similarity transformation (Appendix D) is used to represent the block-diagonal form of Γ with the IRs along the diagonal and the use of theorem 4.2.4 [140]. The similarity transformation is of the form $S^{-1}\Gamma(O_i)S = \Gamma^{'}(O_i)$. It can be shown, from Eqn. 4.5 [140], that n^{α}, the number of times the IR occurs along the diagonal blocks of $\Gamma^{'}(O_i)$, is

$$n^{\alpha} = \frac{1}{h}\sum_{k=1}^{N_c} N_k(\chi_k^{\alpha})^{*}\chi_k^{\Gamma}, \tag{4.8}$$

where N_k is the number of elements in the kth class, N_c is the number of classes, χ_k^{Γ} is the character of the kth class of Γ (Table 4.6), and χ_k^{α} is the character of the kth class of the αth IR [140].

The number of times each IR occurs is derived from Eqn. 4.8 leaving

$$n^{\alpha} = \frac{1}{2}\left[\chi_E^{*}\chi_E^{\alpha} + \chi_{\sigma}^{*}\chi_{\sigma}^{\alpha}\right], \tag{4.9}$$

such that for the wedge

$$n_{xy}^{A'} = \frac{1}{2}\left[(2)(1) + (0)(1)\right] = 1, \tag{4.10a}$$

$$n_{xy}^{A''} = \frac{1}{2}\left[(2)(1) + (0)(1)\right] = 1, \tag{4.10b}$$

$$n_{z}^{A'} = \frac{1}{2}\left[(1)(1) + (1)(1)\right] = 1, \tag{4.10c}$$

$$n_{z}^{A''} = \frac{1}{2}\left[(1)(1) + (1)(-1)\right] = 0. \tag{4.10d}$$

4.2.6 Step 6: Analyze the information in the decomposition

Using the n^{α} terms (Eqn. 4.10) the decomposition of Γ into IRs for the $x-y$ and z directions is represented as

$$\Gamma^{xy} = \Gamma^{A'} + \Gamma^{A''}, \tag{4.11a}$$

$$\Gamma^{z} = \Gamma^{A'}. \tag{4.11b}$$

The xy component has two degrees of freedom (dof) (2(1-D)=2) and the z component has only 1 dof (1(1-D)=1).

4.2.7 Step 7: Determine the symmetry functions

The use of the projection operator must be discussed before continuing the final symmetry analysis.

Theorem 4.2.5 *(***Projection Operator***)*
Let $\bar{\mathbf{V}}$ *be an arbitrary column vector and generate the vector* $\bar{\mathbf{V}}_m^{\alpha}$ *according to*

$$\bar{\mathbf{V}}_m^{\alpha} = \sum_{k=1}^{h} \Gamma_{mm}^{\alpha}(O_k)\left[\Gamma(O_k)\bar{\mathbf{V}}\right]. \tag{4.12}$$

where $\Gamma_{mm}^{\alpha}(O_k)$ *is the* m*th diagonal element of the* α*th IR for the* k*th operator of the group and* $\Gamma(O_k)\bar{\mathbf{V}}$ *is the function obtained by multiplying the function* $\bar{\mathbf{V}}$ *with*

the matrix $\Gamma(O_k)$. *Then* $\bar{\mathbf{V}}_m^{\alpha}$ *is a basis function for row* m *of the* α*th IR or a null vector [140].*

It should be mentioned that up to this point the entire analysis could have been carried out using 2-D coordinates (i.e., only x-y) without any loss of generality because the third dimension, z does not mix with the other two. This can be seen in the matrix elements of Eqns. 4.3-4.4. Because the z coordinate is independent, two arbitrary vectors must be used based on theorem 4.2.5 to get a full 3-D analysis. These two vectors are

$$\bar{\mathbf{V}}_x = [1\ 0\ 0\ 0\ 0\ 0]^T, \tag{4.13a}$$

$$\bar{\mathbf{V}}_z = [0\ 0\ 1\ 0\ 0\ 0]^T. \tag{4.13b}$$

These vectors are used to generate the relations

$$\bar{\mathbf{V}}^{A'} \propto [\Gamma(E) + \Gamma(\sigma)]\, \bar{\mathbf{V}}, \tag{4.14a}$$

$$\bar{\mathbf{V}}^{A''} \propto [\Gamma(E) - \Gamma(\sigma)]\, \bar{\mathbf{V}}. \tag{4.14b}$$

Using the results from Eqns. 4.3 and 4.4 along with the above vectors the symmetry functions for the WW, after normalizing, are

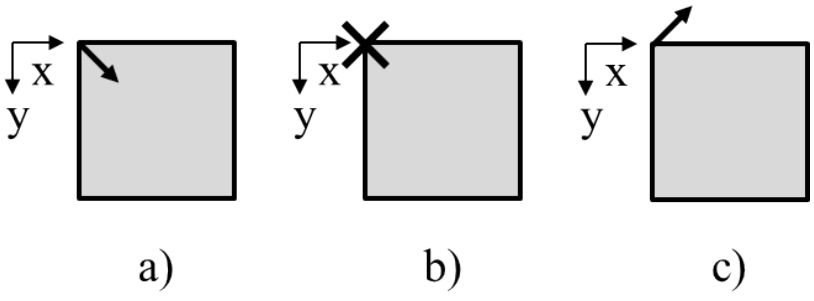

Figure 4.3. Components of the a) x-y and b) z components A' and the c) x-y components of A'' vibrational modes for the wedge.

$$\bar{\mathbf{V}}_{xy}^{A'} = \frac{1}{\sqrt{2}} \begin{pmatrix} 1 \\ 1 \\ 0 \end{pmatrix}, \qquad \bar{\mathbf{V}}_{z}^{A'} = \begin{pmatrix} 0 \\ 0 \\ 1 \end{pmatrix}, \tag{4.15}$$

and

$$\bar{\mathbf{V}}_{xy}^{A''} = \frac{1}{\sqrt{2}} \begin{pmatrix} 1 \\ -1 \\ 0 \end{pmatrix}. \tag{4.16}$$

These modes are shown in Fig. 4.3 and correspond to the *breathing* (Fig. 4.3a) and *wagging* (Fig. 4.3c) WWs [142]. Since Fig. 4.3b is pure translation, it is disregarded leaving two possible modes for the WW, in agreement with the previously derived results [141, 142]. The terms breathing and wagging represent the type of oscillations present at the tip of the wedge, as indicated in Fig. 4.3. The breathing mode expands and contracts both surfaces together, much like a bellows, while the wagging mode twists the corner in such a way as to appear to be wagging back and forth like a dog's tail. Group theory does not determine what velocity or material parameters are necessary to excite the breathing and wagging modes. The necessary material properties to excite these two modes is explained in later sections of this chapter. This ends the group theory analysis of the WW and matches the literature results on WW [141, 142].

4.3 Wedge Wave Discussion

4.3.1 Introduction

When elastic waves are propagated along the wedge formed by the intersection of two free surfaces (Fig. 4.4), a WW is excited. WWs were originally predicted to exist by Ash et al. (1969) [145]. Although no formal derivation or theoretical framework was laid out in this work, the authors used physical arguments of effective elastic constants and forces to predict that a WW should be supported and have velocities

slower than the Rayleigh wave. Thoeretically, WWs were first studied for use as a dispersion free waveguide by Lagasse et al. [146–148]. They used a finite element analysis to explore the velocity of WWs as a function of wedge apex angle, ψ (see Fig. 9 of Lagasse et al. (1973) [147]). This study indicated that the wedge motion was highly localized to the tip, that several modes (i.e., harmonics) existed at small ($\psi < 60°$) apex angles (Fig. 4.4), and both a symmetric and antisymmetric mode exist [147].

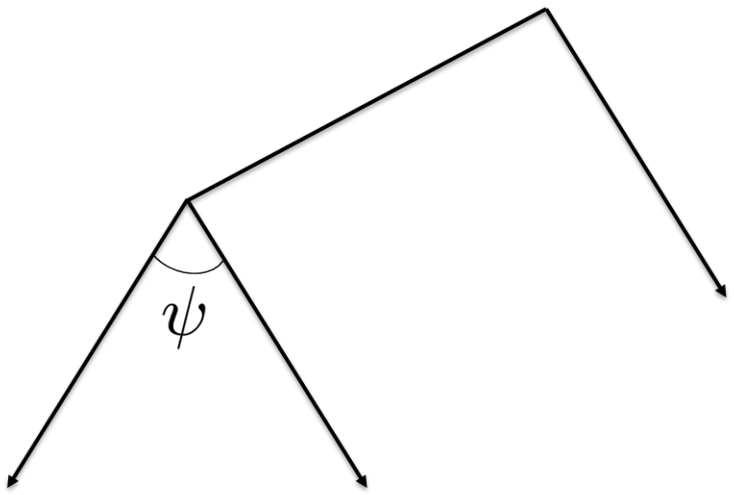

Figure 4.4. Geometry of a wedge that supports WWs. ψ is the apex angle which defines the wedge geometry.

Lagasse later expanded this work and found an empirical relationship between velocity and apex angle [1] [149]

$$v = v_R sin(s\psi), \quad s = 1, 2, 3, ... \quad s\psi < 90° \tag{4.17}$$

where v_R is the Rayleigh wave velocity, s is the harmonic, and ψ is the apex angle. Although this formulation held for small angles ($\psi < 30°$) and small s, it was found to be less accurate at higher angles [141, 150].

[1]This equation first appeared in Lagasse's 1972 IEEE symposium paper [149], and did not appear in the more widely known paper [146].

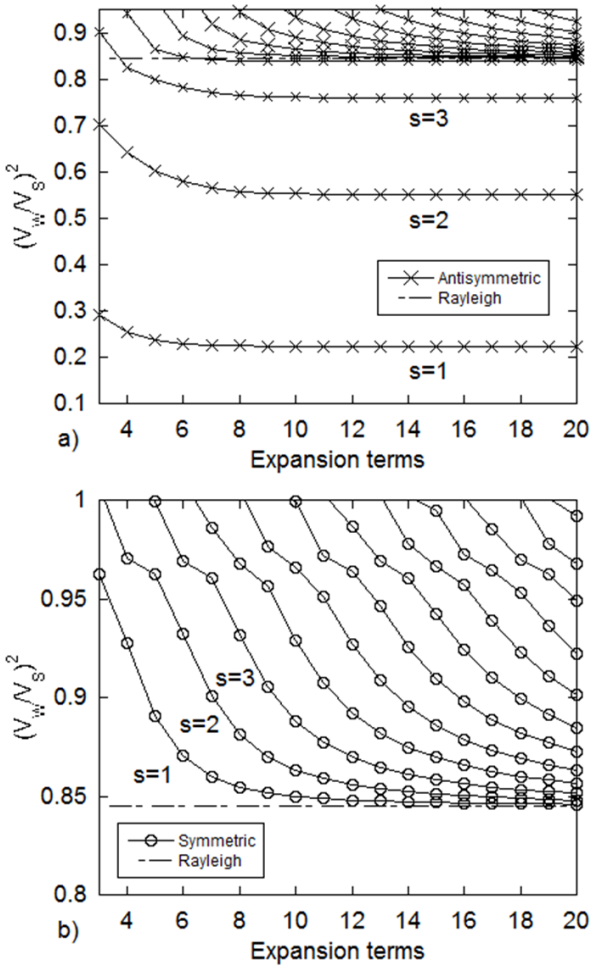

Figure 4.5. Velocity convergence of the $\psi = 30°$ isotropic WW as a function of the expansion terms for medium with ν =0.25. Note the rapid convergence for the first several a) antisymmetric modes (n=1,2,3). The b) symmetric mode converges slower and does not exist for an isotropic wedge with this angle and material properties, and thus the velocity is above the Rayleigh velocity (dashed line).

A mathematical derivation for the WW was performed by Maradudin et al. (1973) on orthogonal wedges ($\psi = 90°$) and Moss et al. (1974) for any angle [141,142]. Their derivations utilized position dependent elastic constants [151] and a linear expansion in Laguerre functions to represent the displacement along the wedge. Laguerre functions were selected because of their orthogonality over the wedge geometry (i.e., Laguerre functions are orthogonal and complete from $[0, \infty)$). See Appendix B for

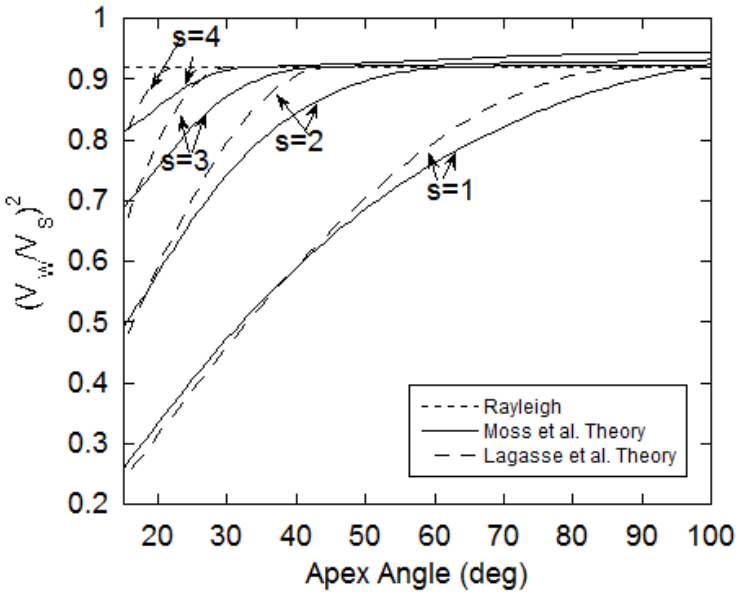

Figure 4.6. Results based on Moss et al. [141] showing the velocity of wagging mode WWs as a function of apex angle, ψ, for different modes, compared to the empirical relationship (Eqn. 4.17) set forth by Lagasse et al. [149]. Note that the velocity exceeds the Rayleigh velocity for $\psi > 90°$.

further discussion of Laguerre functions. This derivation resulted in an eigenvalue problem whose accuracy increased with the number of expansion terms used. As an example of the convergence for the WW, the symmetric and antisymmetric modes for a medium with Poisson's ratio of 0.25 and apex angle of 30° are displayed in Fig. 4.5.

The antisymmetric (wagging) mode, which has motion localized near the wedge tip for these materials, converges after $\sim$ 5 expansion terms (Fig. 4.5a). The symmetric (breathing) mode, which is delocalized for this Poisson's ratio and angle, also converges, but to a velocity at (or above) the Rayleigh wave velocity (Fig. 4.5b).

The numerical results from these studies agreed with Lagasse's modeling and extended the range and number of harmonics that were not initially observed in the finite element study [142]. The theoretical derivation, which included any apex angle, utilized a coordinate transformation that allowed the same displacement expansion

in Laguerre functions to be utilized [141]. As an example, the wagging WW velocity was calculated at several angles and is shown in Fig. 4.6, compared with Lagasse's empirical relationship for apex angles from $\psi = 10 - 100^{\circ}$ (Eqn. 4.17). Note that at low angles the two solutions agree rather well, but as the apex angle is increased, the deviation between the two solutions increases (Fig. 4.6).

4.3.2 Wedge Wave Modes

The study by Maradudin et al. [142] discovered a second type of WW mode, which was named the symmetric mode. This symmetric mode has breathing type motion, while the antisymmetric mode has wagging type motion. Throughout the remainder of this document the terms breathing and wagging will be used to describe these two modes.

An example of the wagging mode is shown in Fig. 4.7. The breathing mode, which is less common, is shown in Fig. 4.8 for several different isotropic materials. Note that both the wagging and breathing modes have larger amplitude for larger absolute value of the Poisson's ratio. The material properties necessary to support these two modes is described in the following section.

It should be mentioned here that these calculated (and later experimentally verified) modes agree exactly with those predicted by group theory in Fig. 4.3. The wagging mode exhibits the oscillatory behavior in a shearing type motion along the wedge, while the breathing mode (Fig. 4.8) expands and contracts as expected.

4.3.3 Wedge Wave Existence

Rigorous mathematical proofs on the existence of WWs were derived much later. Kamotskii (2009) [152] mathematically verified the existence of WWs for acute angle wedges by reducing the problem to studying the spectrum of a self-adjoint operator in the $L_2(\Omega)$ Hilbert space (Ω is an angle in R^2). Kamotskii verified that the operator had at least one point on the discrete spectrum coinciding with the ray $[V_R^2 k^2, +\infty)$

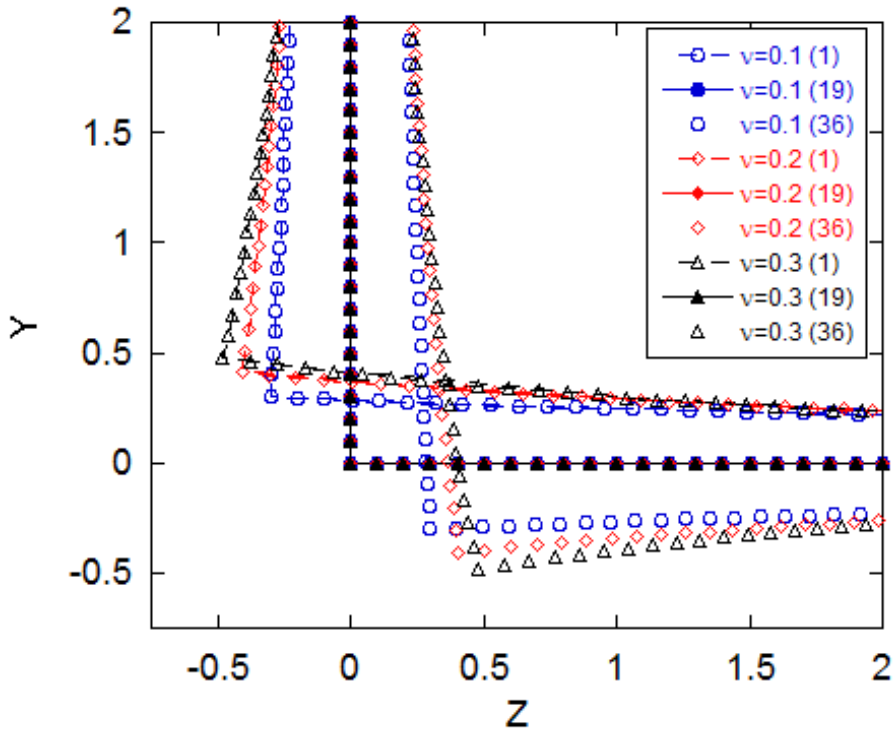

Figure 4.7. Wagging mode for the orthogonal WW based on the theoretical formulation of Moss et al. [141]. The wagging mode for three different materials, with Poisson's ratio of +0.1, +0.2, and +0.3, are shown at three different snapshots in time.

which proved the existence of a WW. No value of the WW velocity was obtained here, simply a mathematical proof of its existence. This rigorous proof was later extended to other apex angles by Zavorokhin and Nazarov (2011) [153]. They derived a sufficient condition for the existence of waveguide modes (i.e., regions where the breathing, wagging, or both could exist) as a function of the apex angle and Poisson's ratio (Fig. 4.9).

Their results demonstrate that there are three unique regions for WWs to exist. Labeled regions I, II, and III in Fig. 4.9, where the wagging, breathing, or both are found, respectively. The results are shown as a function of Poisson's ratio (ν) and indicate that the breathing mode only exists for materials with negative ν. As mentioned above, negative ν values are rarely found in nature, and so it is more likely

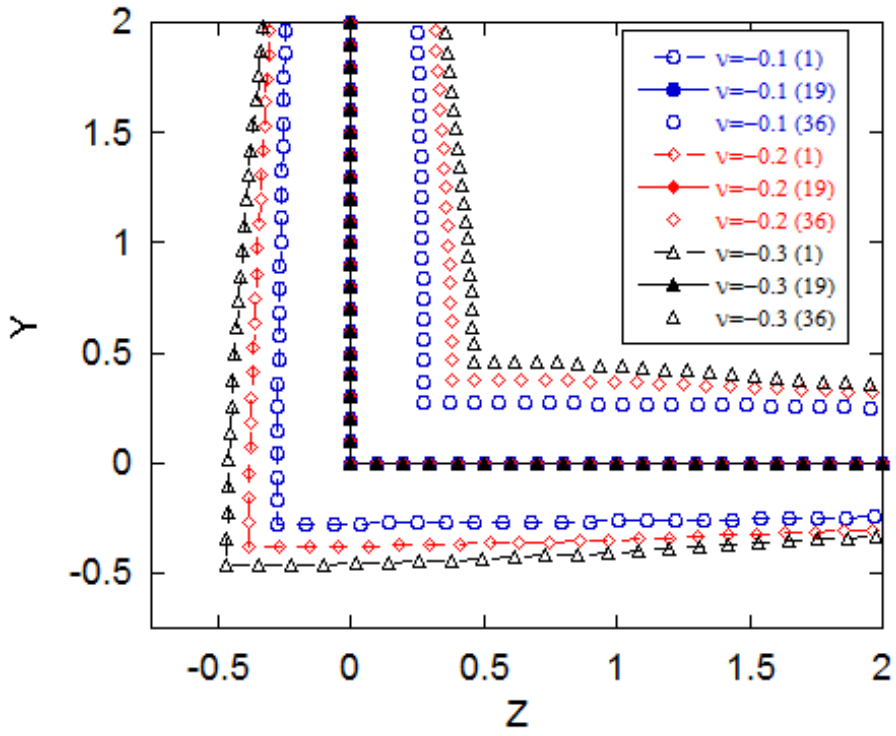

Figure 4.8. Breathing mode for the orthogonal WW based on the theoretical formulation of Moss et al. [141]. The breathing mode for three different materials, with Poisson's ratio of -0.1, -0.2, and -0.3, are shown at three different snapshots in time.

that the wagging mode is observed (region I in Fig. 4.9). It is also interesting to note that the wagging mode is restricted to angles less than $\sim 101°$, but can exist in all types of materials.

Later, experimental work by DeBilly and others [154–158] verified the existence of WWs using S-wave contact transducers [154, 159]. Several examples of the velocity measurements are shown in Fig. 4.10. Their work demonstrated that the amplitude of the WW was largest when polarized perpendicularly to the bisecting line of the apex angle. Recall Fig. 3.1, which demonstrates the difference between polarizations at the corner of a sample.

Other experimental work on WWs revealed that the dispersion was a function of the wedge imperfection [160–162]. These results were compared with the the-

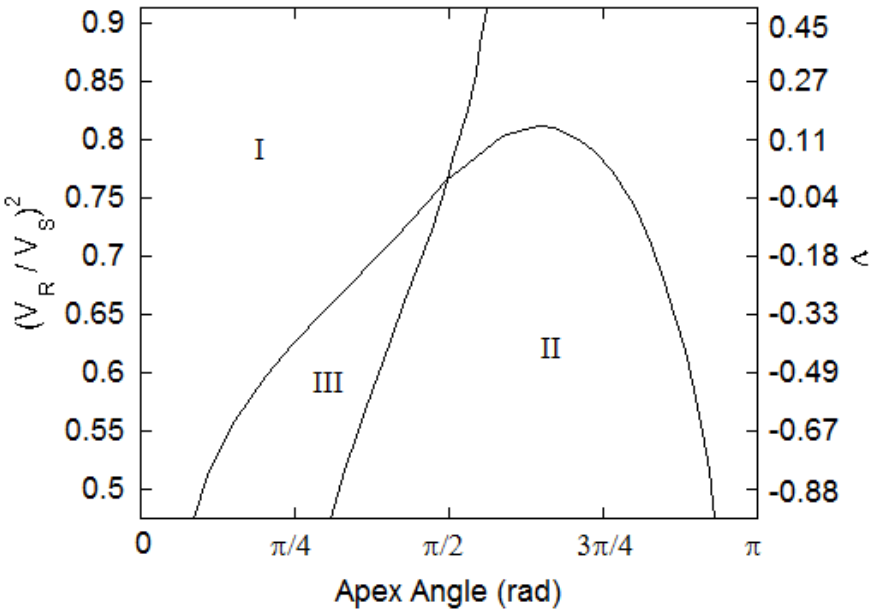

Figure 4.9. Regions of existence for the wagging (I) and breathing (II) WW modes as a function of the velocity and apex angle in isotropic media. Region III is where both modes can exist. Based on Fig. 2 of Zavorokhin et al. [153].

ory [141] and found to be in good agreement. Different techniques were used to verify the existence of WWs, including laser ultrasonics [163–171] and water loaded wedges [172–174]. Other mathematical approaches were also utilized including plate theory studies [175,176], asymptotics [177], nonlinearity theory [166,178,179], Fourier integrals [180], Lagrangian analysis [181], and finite element [182, 183]. The theoretical methods were expanded to include other wedge type geometries [148, 184–191], wedge diffraction [192], scattering [193], dispersion [176], anisotropy [194, 195], electrostatic wave theories [196–201], and smaller angle wedges [202, 203]. Several very nice, in-depth summaries on WWs have also been published [150, 204–207] as well as attempts to use the localization of WWs for industrial applications [165, 208–211].

Throughout all of these studies, no single analytic expression for the WW velocity was derived that could extend over the whole range of apex angles [206]. For this

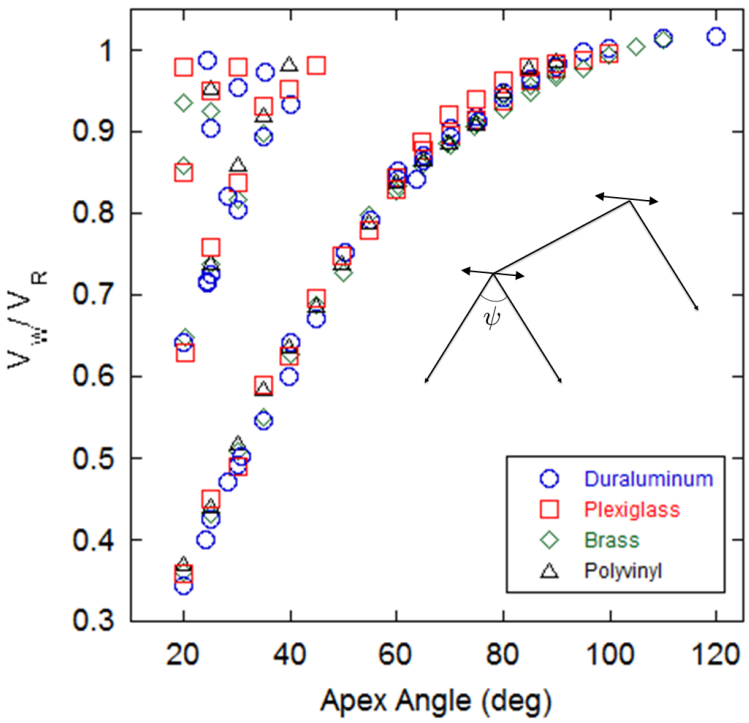

Figure 4.10. Experimental measurements of the first three antisymmetric wedge wave modes measured using contact [154, 159] and inter digital transducers [149] in several materials. Inset shows S-wave source transducer polarization.

reason, the numerical approach set forth by Maradudin et al. (1973) will be used as the foundation for the coupling of WWs to form a surface fracture and intersection [142].

4.4 Summary

Group theory analysis was introduced in this chapter, and the formulation was presented that predicts the vibrational modes for oscillating problems. The analysis was applied to the WW, in agreement with previous group theory analysis techniques, resulting in the prediction of two vibrational modes (breathing and wagging modes) localized to the wedge tip. It should be mentioned that although group theory does

not predict the velocity or material properties necessary to support such modes, without it, the breathing mode would likely not have been discovered, because it exists mainly for negative Poisson's ratio materials.

Much work has been done to predict, characterize, measure, and derive analytical expressions for the WW. Experimental investigations, using both contact and non-contact methods, were presented and have verified the existence of the WW, in agreement with the theoretical formulation.

The results of this chapter set the foundation for the following chapters, which focus on coupling the aforementioned WWs at surface fractures and fracture intersections. A similar group theory formulation will be used to analyze these new modes and predict the number and types of vibrational modes supported by these new geometries. The terms breathing and wagging will continue to be used throughout this work.

5. Coupled Wedge Waves

5.1 Introduction

This chapter presents the derivation of coupled wedge waves (CWWs) that propagate along a surface fracture. Using group theory, two modes are predicted for the CWW, similar to the wedge wave (WW) of the previous chapter. A theoretical derivation is given that couples two wedges using displacement discontinuity boundary conditions. The secular equation is then used to predict the velocity and particle motion of the CWW. Finally, an experimental test of the CWW is performed and used to verify its existence.

5.2 Group Theory Analysis of Coupled Wedge Waves

The analysis of the CWW's vibrational modes is derived here using a similar formulation to the WW vibrational modes given in chapter 4.

5.2.1 Step 1: Identify the point group and its symmetry operations

A CWW propagates along the intersection of a fracture and a free surface, formed by two media in partial contact, as shown in Fig. 5.1. The geometry is made up of two media, labeled 1 and 2 in Fig. 5.1. The media are in contact along the z-x plane at y=0, and a free surface exists along the y-x plane at z=0. The wave propagates in the x direction localized near the free surface and interface between the media.

For this group theory analysis, the two media are assumed to be identical. The symmetry operators allowed for this geometry are the identity (E) and the reflection operator about the z-x plane (σ). Together, these two operators form the point group C_s, the same as the WW in chapter 4.

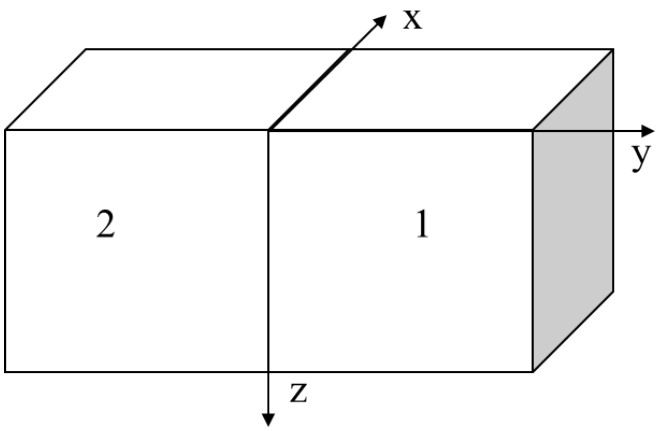

Figure 5.1. Geometry of the CWW with the two media in partial contact along the z-x plane and the y-x plane forming a free surface.

5.2.2 Step 2: Specify the coordinate system and basis functions

The Cartesian coordinate systems, which is located at the tips of the two media ($x = y = z = 0$ in Fig. 5.1), are used to define the displacements in the two media that are used as the basis functions for this analysis. Here again, an active view-point is used (see section 4.1.3 for a description).

5.2.3 Step 3: Determine the effects of the symmetry operations on the basis functions

Consider the vector $\bar{\mathbf{r}}$ (section 4.2.3) and the effects of the symmetry operators in this group acting on it. The two operators of this point group have the effect

$$\begin{aligned}
&\Gamma(E)r_x(1) \to r_x(1),\ \Gamma(E)r_y(1) \to r_y(1),\ \Gamma(E)r_z(1) \to r_z(1),\\
&\Gamma(E)r_x(2) \to r_x(2),\ \Gamma(E)r_y(2) \to r_y(2),\ \Gamma(E)r_z(2) \to r_z(2),\\
&\Gamma(\sigma)r_x(1) \to r_x(2),\ \Gamma(\sigma)r_y(1) \to -r_y(2),\ \Gamma(\sigma)r_z(1) \to r_z(2),\\
&\Gamma(\sigma)r_x(2) \to r_x(1),\ \Gamma(\sigma)r_y(2) \to -r_y(1),\ \Gamma(\sigma)r_z(2) \to r_z(1).
\end{aligned} \tag{5.1}$$

where the 1 and 2 represent the media.

Table 5.1
Action table for the CWW.

	E	σ
r_x	r_x	r_x
r_y	r_y	$-r_y$
r_z	r_z	r_z
1	1	2
2	2	1

The symmetry relationships are summarized in action table 5.1. The action table has the addition of the media labels, where the WW action table (Table 4.4) only had one medium, and a label was not necessary.

5.2.4 Step 4: Construct a matrix representation for each element using the basis functions

To determine the matrix representation of the elements the basis functions, E, and σ are put into matrix form as

$$[r(i)] = \begin{bmatrix} r_x(1) & r_y(1) & r_z(1) & r_x(2) & r_y(2) & r_z(2) \end{bmatrix}^T, \tag{5.2}$$

$$\Gamma(E) = \begin{bmatrix} 1 & 0 & 0 & 0 & 0 & 0 \\ 0 & 1 & 0 & 0 & 0 & 0 \\ 0 & 0 & 1 & 0 & 0 & 0 \\ 0 & 0 & 0 & 1 & 0 & 0 \\ 0 & 0 & 0 & 0 & 1 & 0 \\ 0 & 0 & 0 & 0 & 0 & 1 \end{bmatrix}, \tag{5.3}$$

and

$$\Gamma(\sigma) = \begin{bmatrix} 0 & 0 & 0 & 1 & 0 & 0 \\ 0 & 0 & 0 & 0 & -1 & 0 \\ 0 & 0 & 0 & 0 & 0 & 1 \\ 1 & 0 & 0 & 0 & 0 & 0 \\ 0 & -1 & 0 & 0 & 0 & 0 \\ 0 & 0 & 1 & 0 & 0 & 0 \end{bmatrix}, \tag{5.4}$$

where ^{T} represents the transpose.

This is verified by comparing

$$\begin{aligned} \Gamma(E)[r(i)] &= [r(f)], \\ \Gamma(\sigma)[r(i)] &= [r(f)], \end{aligned} \tag{5.5}$$

to Table 5.1, where i and f are the initial and final media labels, respectively.

5.2.5 Step 5: Determine the number and type of irreducible representations

Table 5.2
Character table for the point group C_s used in the CWW analysis.

C_s	E	σ
A'	1	1
A''	1	-1
Γ^x	2	0
Γ^y	2	0
Γ^z	2	0

The only class possible is $\{\sigma\}$ because the operator E is always in a class by itself (i.e., $\{E\}$) (see section 4.2.5). These classes and their characters are shown in the character table (Table 5.2). Recall the Mulliken notation from Tables 4.1 - 4.2.

For the two irreducible representations (IRs) in the C_s class, this leaves

$$n_\beta^\alpha = \frac{1}{2}\left[\chi_E^* \chi_E^\alpha + \chi_\sigma^* \chi_\sigma^\alpha\right], \tag{5.6a}$$

$$n_\beta^{A'} = \frac{1}{2}\left[(2)(1) + (0)(1)\right] = 1,\ \beta = x, y, z, \tag{5.6b}$$

$$n_\beta^{A''} = \frac{1}{2}\left[(2)(1) + (0)(-1)\right] = 1,\ \beta = x, y, z. \tag{5.6c}$$

5.2.6 Step 6: Analyze the information in the decomposition

The results of Eqn. 5.6 are used to decompose the representation as

$$\Gamma^x = \Gamma^y = \Gamma^z = (1)\Gamma^{A'} + (1)\Gamma^{A''}. \tag{5.7}$$

For all three directions there are two degrees of freedom (dof) (2(1-D)=2).

5.2.7 Step 7: Determine the symmetry functions

Using the character table for the CWW (Table 5.2) and theorem 4.2.5 results in the relationship

$$\bar{\mathbf{V}}^{A'} \propto \left[\Gamma(E) + \Gamma(\sigma)\right]\bar{\mathbf{V}}, \tag{5.8a}$$

$$\bar{\mathbf{V}}^{A''} \propto \left[\Gamma(E) - \Gamma(\sigma)\right]\bar{\mathbf{V}}. \tag{5.8b}$$

Using Eqns. 5.3 and 5.4 along with the $\bar{\mathbf{V}}$ vectors

$$\bar{\mathbf{V}}_x = \left[1\ 0\ 0\ 0\ 0\ 0\right]^T, \tag{5.9a}$$

$$\bar{\mathbf{V}}_y = \left[0\ 1\ 0\ 0\ 0\ 0\right]^T, \tag{5.9b}$$

$$\bar{\mathbf{V}}_z = \left[0\ 0\ 1\ 0\ 0\ 0\right]^T, \tag{5.9c}$$

the symmetry functions for the CWW, after normalizing, are

$$\bar{\mathbf{V}}_x^{A'} = \frac{1}{\sqrt{2}} \begin{pmatrix} 1 \\ 0 \\ 0 \\ 1 \\ 0 \\ 0 \end{pmatrix}, \qquad \bar{\mathbf{V}}_y^{A'} = \frac{1}{\sqrt{2}} \begin{pmatrix} 0 \\ 1 \\ 0 \\ 0 \\ -1 \\ 0 \end{pmatrix}, \qquad \bar{\mathbf{V}}_z^{A'} = \frac{1}{\sqrt{2}} \begin{pmatrix} 0 \\ 0 \\ 1 \\ 0 \\ 0 \\ 1 \end{pmatrix}, \tag{5.10}$$

$$\bar{\mathbf{V}}_x^{A''} = \frac{1}{\sqrt{2}} \begin{pmatrix} 1 \\ 0 \\ 0 \\ -1 \\ 0 \\ 0 \end{pmatrix}, \qquad \bar{\mathbf{V}}_y^{A''} = \frac{1}{\sqrt{2}} \begin{pmatrix} 0 \\ 1 \\ 0 \\ 0 \\ 1 \\ 0 \end{pmatrix}, \qquad \bar{\mathbf{V}}_z^{A''} = \frac{1}{\sqrt{2}} \begin{pmatrix} 0 \\ 0 \\ 1 \\ 0 \\ 0 \\ -1 \end{pmatrix}. \tag{5.11}$$

Equations 5.10-5.11 are visualized in Figs. 5.2-5.3. Note that the x and z components in Eqn. 5.10 and the y component in Eqn. 5.11 are all translation modes. For a translational mode, the center of mass is not stationary, and thus a pure translational mode cannot be supported. However, since these are only the individual components, they are not pure translational modes. They are combined to form the vibrational modes of the CWW, discussed below. Note that the 'x' symbol means into the page and 'o' symbol means out of the page.

The components are combined to form four possible vibrational modes, depending on the phase of the vibrations in each component, resulting in two breathing (Fig. 5.4a and Fig. 5.5a) and two wagging modes (Fig. 5.4b and Fig. 5.5b) for the CWW. Based on the analysis of the WW modes in chapter 4, it is most likely that the breathing modes exist only for negative Poisson's ratios while the wagging modes exist for positive Poisson's ratio materials. This will be explored in a parameter study later in this chapter. Based on this argument, it is predicted that only two modes exist under a given set of material parameters.

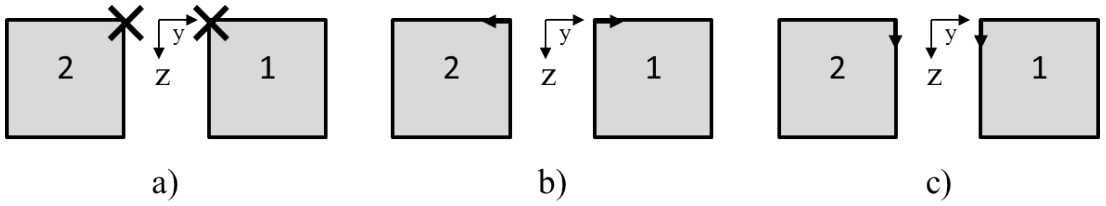

Figure 5.2. Components of the $A^{'}$ vibrational modes for the CWW. The a) x-components, b) y-components, and c) z-components.

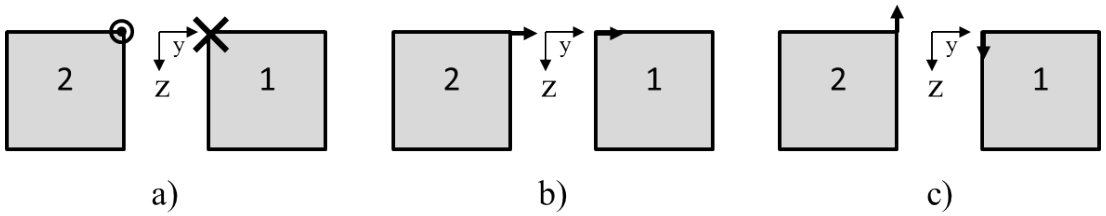

Figure 5.3. Components of the $A^{''}$ vibrational modes for the CWW. The a) x-components, b) y-components, and c) z-components.

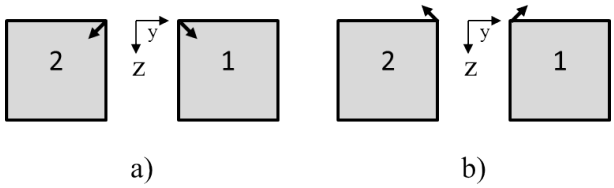

Figure 5.4. The $A^{'}$ vibrational modes for the CWW. The a) breathing and b) wagging modes.

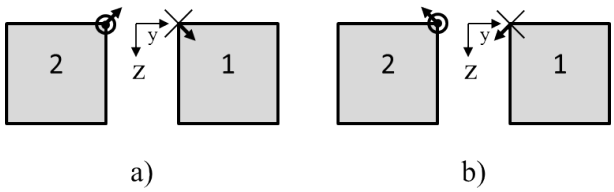

Figure 5.5. The $A^{''}$ vibrational modes for the CWW. The a) breathing and b) wagging modes.

Summary

The results presented in the above section predict that the CWW should have two unique solutions for any given set of material parameters, as long as both media are the same. These two modes have wagging or breathing type motion, depending on the parameters used. Analogous to the WW case, this derivation provides no insight into the velocity or materials necessary to support such a mode.

5.3 Theoretical Derivation of Coupled Wedge Waves

5.3.1 Introduction

Using elasticity theory (chapter 2) along with displacement discontinuity (DD) boundary conditions, a new type of coupled wave is derived [103]. The theoretical derivation for coupled wedge waves (CWWs) is explicitly described in this section. The problem geometry, expansions, boundary conditions, and results are discussed for the CWW in both isotropic and anisotropic media.

5.3.2 Problem Geometry

In this derivation the media are defined such that a fracture exists on the $x-z$ plane between two media that is assumed smooth along $z>0$ (Fig. 5.6). Medium 1 exists in the region $x>0, y>0, z>0$ and medium 2 exists in the region $x>0, y<0, z>0$. A free surface exists on the $x-y$ plane at $z=0$. Medium η has mass density $\rho^{(\eta)}$, and elastic moduli $C^{(\eta)}_{\alpha,\beta,\mu,\nu}$. The lower-case Greek letters indicate the Cartesian indices (i.e., $\alpha=1,2,3$ is the x,y,z direction). In the following derivation the general case of the two media being different is presented, although the CWW can exist when the two media are the same.

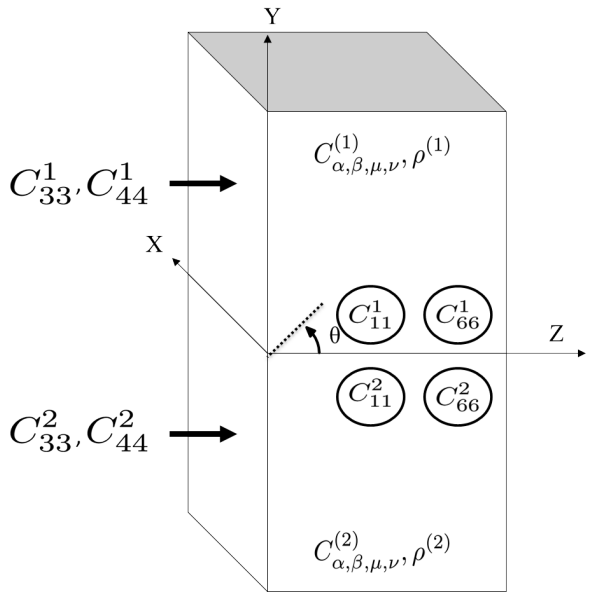

Figure 5.6. Geometry of the CWW. The superscript represents the medium, θ is the polarization angle of the transducer, C_{ij} represent the direction the elastic constants are measured, and ρ is the density of the medium.

5.3.3 Problem Definition

This derivation is closely based on the work by Sokolova et al. (2012) [138]. For waves propagating along the intersection in the x direction, the following assumption is made for the displacement, u, and stress, T, fields.

$$u_\alpha(x,y,z;t) = e^{i(kx-wt)}\tilde{U}_\alpha(y,z) + e^{-i(kx-wt)}\tilde{U}^*_\alpha(y,z), \tag{5.12}$$

$$T_{\alpha,\beta}(x,y,z;t) = e^{i(kx-wt)}\tilde{T}_{\alpha,\beta}(y,z) + e^{-i(kx-wt)}\tilde{T}^*_{\alpha,\beta}(y,z), \tag{5.13}$$

where k is the wave vector, related to the frequency by $w = vk$, v is the phase velocity, t is time, $\tilde{T}_{\alpha,\beta}$ is the stress amplitude, $\tilde{U}_\alpha$ is the displacement amplitude and * means complex conjugate. The equation of motion is written in terms of these fields as

$$\rho \frac{\partial^2 u_\alpha}{\partial \mathrm{t}^2} = \sum_{\beta=1}^{3} \frac{\partial T_{\alpha\beta}}{\partial \mathrm{x}_\beta}, \tag{5.14}$$

where ρ is the density. Applying Eqns. 5.12 and 5.13 to Eqn. 5.14 yields

$$-\rho\omega^2 u_\alpha = ikT_{\alpha,1} + \frac{\partial}{\partial \mathrm{y}} T_{\alpha,2} + \frac{\partial}{\partial \mathrm{z}} T_{\alpha,3}. \tag{5.15}$$

The stress tensor is defined by the strain as

$$T_{\alpha\beta} = \sum_{\mu\nu=1}^{3} C_{\alpha,\beta,\mu,\nu} \frac{1}{2} \left(\frac{\partial u_\mu}{\partial \mathrm{x}_\nu} + \frac{\partial u_\nu}{\partial \mathrm{x}_\mu} \right), \tag{5.16}$$

which is simplified, for media with symmetric elastic stiffness matrices, to

$$\tilde{T}^{(1/2)}_{\alpha\beta}(y,z) = \sum_{\mu,\nu=1}^{3} C^{(1/2)}_{\alpha,\beta,\mu,\nu} D_\nu(k) \tilde{U}^{(1/2)}_\mu(y,z), \tag{5.17}$$

where the operators D are defined for the above geometry as:

$$D_1(k) \equiv ik, \;\; D_2(k) \equiv \frac{\partial}{\partial \mathrm{y}}, \;\; D_3(k) \equiv \frac{\partial}{\partial \mathrm{z}}. \tag{5.18}$$

Applying Eqns. 5.17 and 5.18 to Eqn. 5.14 and canceling the exponential terms leaves

$$-\rho\omega^2 \tilde{U}_\alpha = \sum_{\beta,\mu,\nu=1}^{3} D_\beta(k) C_{\alpha,\beta,\mu,\nu} D_\nu(k) \tilde{U}_\mu. \tag{5.19}$$

The displacement amplitudes are now expanded in a linear series of Laguerre functions for each media as

$$\tilde{U}^{(1/2)}_\alpha(y,z) = \sum_{m,n=0}^{\infty} a^{(\alpha,1/2)}_{mn} \phi_m(\pm ky) \phi_n(kz), \tag{5.20}$$

where the top sign corresponds to medium 1 and the bottom to medium 2.

The ϕ functions are defined in terms of the Laguerre polynomials ($L_a(x)$) as (see Appendix A):

$$\phi_b(x) = e^{-\frac{x}{2}} \frac{L_b(x)}{b!},\ L_b(x) = e^x \frac{\mathrm{d}^b}{\mathrm{dx^b}}\big(e^{-x}x^b\big), \tag{5.21}$$

where

$$\phi_b(0) = 1,\ b = 0, 1, 2, \ldots. \tag{5.22}$$

Because a wedge occupies the region from 0 to ∞, and the Laguerre polynomials, ϕ, are orthonormal and complete from $[0, \infty)$, they are well suited to model the problem geometry. For a further explanation of Laguerre polynomials see Appendix A.

The goal of this derivation is to solve for the coefficients, a_{mn}, in the expansion. To do this, substitute the expansion (Eqn. 5.20) into the equation of motion (Eqn. 5.19) leaving

$$\begin{gathered} -\rho^{(1/2)}\omega^2 \sum_{m,n=0}^{\infty} a_{m,n}^{(\alpha,1/2)} \phi_m(\pm ky)\phi_n(kz) = \\ \sum_{\beta,\mu,\nu=1}^{3} D_\beta C_{\alpha,\beta,\mu,\nu}^{(1/2)} D_\nu \sum_{m,n=0}^{\infty} a_{m,n}^{(\mu,1/2)} \phi_m(\pm ky)\phi_n(kz). \end{gathered} \tag{5.23}$$

Both sides of Eqn. 5.23 are multiplied by $\phi_p(\pm ky)\phi_q(kz)$ and integrated over the quarter space for each medium. This leads to the following for the left hand side (lhs) of Eqn. 5.23

$$\begin{gathered} lhs^{(1/2)} = \mp \int_0^{\infty} \int_0^{\pm\infty} \int_0^{\infty} \rho^{(1/2)}\omega^2 \\ \sum_{m,n=0}^{\infty} a_{m,n}^{(\alpha,1/2)} \phi_m(\pm ky)\phi_n(kz)\phi_p(\pm ky)\phi_q(kz)\mathrm{d}x\mathrm{d}y\mathrm{d}z. \end{gathered} \tag{5.24}$$

The $\mp$ sign arises from the change in the limits of the y integral. Note that the integral over x cancels with the right hand side (rhs) of Eqn. 5.23. Using the relation

$$\int_0^{\pm\infty} \phi_\mathrm{a}(\pm ky)\phi_b(\pm ky)\mathrm{d}y = \pm\frac{\delta_{ab}}{k}, \tag{5.25}$$

where δ is the Kronecker delta symbol

$$\delta_{ab} = \left\{ \begin{array}{ll} 1 & \text{if } a = b \\ 0 & \text{if } a \neq b \end{array} \right\}, \tag{5.26}$$

the lhs is

$$lhs^{(1/2)} = -\rho^{(1/2)}\omega^2 \sum_{m,n=0}^{\infty} a_{m,n}^{(\alpha,1/2)} \frac{\delta_{pm}}{k} \frac{\delta_{qn}}{k}, \tag{5.27}$$

which is simplified to

$$lhs^{(1/2)} = -\rho^{(1/2)}v^2 \sum_{m,n=0}^{\infty} a_{m,n}^{(\alpha,1/2)} \delta_{pm}\delta_{qn}. \tag{5.28}$$

For the rhs (Eqn. 5.23)

$$\begin{aligned} rhs^{(1/2)} = \pm \int_0^{\infty} \int_0^{\pm\infty} \sum_{\beta,\mu,\nu=1}^{3} D_\beta C_{\alpha,\beta,\mu,\nu}^{(1/2)} D_\nu \\ \sum_{m,n=0}^{\infty} a_{m,n}^{(\mu,1/2)} \phi_m(\pm ky)\phi_n(kz)\phi_p(\pm ky)\phi_q(kz)\mathrm{d}y\mathrm{d}z. \end{aligned} \tag{5.29}$$

Equation 5.17 substituted in 5.29 yields

$$rhs^{(1/2)} = \pm \sum_{\beta=1}^{3} D_\beta \int_0^{\infty} \int_0^{\pm\infty} \tilde{T}_{\alpha,\beta}^{(1/2)}(y,z)\phi_p(\pm ky)\phi_q(kz)\mathrm{d}y\mathrm{d}z. \tag{5.30}$$

The sum over β is expanded into three terms

$$\begin{aligned} rhs^{(1/2)} = \pm ik \int_0^{\infty} \int_0^{\pm\infty} \tilde{T}_{\alpha,1}(y,z)\phi_p(\pm ky)\phi_q(kz)\mathrm{d}y\mathrm{d}z \\ \pm \frac{\partial}{\partial \mathrm{y}} \int_0^{\infty} \int_0^{\pm\infty} \tilde{T}_{\alpha,2}(y,z)\phi_p(\pm ky)\phi_q(kz)\mathrm{d}y\mathrm{d}z \\ \pm \frac{\partial}{\partial \mathrm{z}} \int_0^{\infty} \int_0^{\pm\infty} \tilde{T}_{\alpha,3}(y,z)\phi_p(\pm ky)\phi_q(kz)\mathrm{d}y\mathrm{d}z. \end{aligned} \tag{5.31}$$

The second term in Eqn. 5.31 is integrated by parts $\int uv'\mathrm{d}y = uv - \int vu'\mathrm{d}y$ and renamed $B^{(\eta)}$ where

$$B^{(1)} = [\phi_p(ky) \int_0^\infty \tilde{T}_{\alpha,2}(y,z)\phi_q(kz)\mathrm{d}z]_0^{y=\infty} - \int_0^\infty \int_0^\infty \tilde{T}_{\alpha,2}(y,z)\phi_q(kz)\frac{\mathrm{d}\phi_p(ky)}{\mathrm{d}y}\mathrm{d}y\mathrm{d}z, \tag{5.32}$$

$$B^{(1)} = -\phi_p(0) \int_0^\infty \tilde{T}_{\alpha,2}(0,z)\phi_q(kz)\mathrm{d}z - \int_0^\infty \int_0^\infty \tilde{T}_{\alpha,2}(y,z)\phi_q(kz)\frac{\mathrm{d}\phi_p(ky)}{\mathrm{d}y}\mathrm{d}y\mathrm{d}z, \tag{5.33}$$

$$B^{(2)} = [\phi_p(-ky) \int_0^\infty \tilde{T}_{\alpha,2}(y,z)\phi_q(kz)\mathrm{d}z]_{-\infty}^{y=0} - \int_0^\infty \int_{-\infty}^0 \tilde{T}_{\alpha,2}(y,z)\phi_q(kz)\frac{\mathrm{d}\phi_p(-ky)}{\mathrm{d}y}\mathrm{d}y\mathrm{d}z, \tag{5.34}$$

$$B^{(2)} = \phi_p(0) \int_0^\infty \tilde{T}_{\alpha,2}(0,z)\phi_q(kz)\mathrm{d}z - \int_0^\infty \int_{-\infty}^0 \tilde{T}_{\alpha,2}(y,z)\phi_q(kz)\frac{\mathrm{d}\phi_p(-ky)}{\mathrm{d}y}\mathrm{d}y\mathrm{d}z. \tag{5.35}$$

The stress at the interface between media 1 and 2 is defined as

$$\tau_n^{(\alpha)} \equiv \int_0^\infty \phi_n(kz)\tilde{T}_{\alpha,2}(0,z)\mathrm{d}z, \tag{5.36}$$

and is applied to Eqns. 5.32 - 5.35 yielding

$$B^{(1)} = -\phi_p(0)\tau_q^{(\alpha,1)} - \int_0^\infty \int_0^\infty \tilde{T}_{\alpha,2}(y,z)\phi_q(kz)\frac{\mathrm{d}\phi_p(ky)}{\mathrm{d}y}\mathrm{d}y\mathrm{d}z, \tag{5.37}$$

$$B^{(2)} = \phi_p(0)\tau_q^{(\alpha,2)} - \int_0^\infty \int_{-\infty}^0 \tilde{T}_{\alpha,2}(y,z)\phi_q(kz)\frac{\mathrm{d}\phi_p(-ky)}{\mathrm{d}y}\mathrm{d}y\mathrm{d}z. \tag{5.38}$$

The third term in Eqn. 5.31 is integrated by parts again, and labeled $C^{(\eta)}$ where

$$C^{(1)} = [\phi_q(kz) \int_0^\infty \tilde{T}_{\alpha,3}(y,z)\phi_p(ky)\mathrm{d}y]_0^{z=\infty} - \int_0^\infty \int_0^\infty \tilde{T}_{\alpha,3}(y,z)\phi_p(ky)\frac{\mathrm{d}\phi_q(kz)}{\mathrm{d}z}\mathrm{d}y\mathrm{d}z, \tag{5.39}$$

$$C^{(1)} = -\phi_q(0)\int_0^\infty \tilde{T}_{\alpha,3}(y,0)\phi_p(ky)\mathrm{d}y - \int_0^\infty\int_0^\infty \tilde{T}_{\alpha,3}(y,z)\phi_p(ky)\frac{\mathrm{d}\phi_q(kz)}{\mathrm{d}z}\mathrm{d}y\mathrm{d}z, \tag{5.40}$$

$$C^{(1)} = -\int_0^\infty\int_0^\infty \tilde{T}_{\alpha,3}(y,z)\phi_p(ky)\frac{\mathrm{d}\phi_q(kz)}{\mathrm{d}z}\mathrm{d}y\mathrm{d}z, \tag{5.41}$$

$$C^{(2)} = [\phi_q(kz)\int_{-\infty}^0 \tilde{T}_{\alpha,3}(y,z)\phi_p(-ky)\mathrm{d}y]_0^{z=\infty} - \int_0^\infty\int_{-\infty}^0 \tilde{T}_{\alpha,3}(y,z)\phi_p(-ky)\frac{\mathrm{d}\phi_q(kz)}{\mathrm{d}z}\mathrm{d}y\mathrm{d}z, \tag{5.42}$$

$$C^{(2)} = -\phi_q(0)\int_{-\infty}^0 \tilde{T}_{\alpha,3}(y,0)\phi_p(-ky)\mathrm{d}y - \int_0^\infty\int_{-\infty}^0 \tilde{T}_{\alpha,3}(y,z)\phi_p(-ky)\frac{\mathrm{d}\phi_q(kz)}{\mathrm{d}z}\mathrm{d}y\mathrm{d}z, \tag{5.43}$$

$$C^{(2)} = -\int_0^\infty\int_{-\infty}^0 \tilde{T}_{\alpha,3}(y,z)\phi_p(-ky)\frac{\mathrm{d}\phi_q(kz)}{\mathrm{d}z}\mathrm{d}y\mathrm{d}z. \tag{5.44}$$

Equations 5.37, 5.38, 5.41, and 5.44 are placed back into Eqn. 5.31, yielding

$$\begin{aligned} rhs^{(1)} = {} & ik\int_0^\infty\int_0^\infty \tilde{T}_{\alpha,1}(y,z)\phi_p(ky)\phi_q(kz)\mathrm{d}y\mathrm{d}z \\ & - \phi_p(0)\tau_q^{(\alpha,1)} - \int_0^\infty\int_0^\infty \tilde{T}_{\alpha,2}(y,z)\phi_q(kz)\frac{\mathrm{d}\phi_p(ky)}{\mathrm{d}y}\mathrm{d}y\mathrm{d}z \\ & - \int_0^\infty\int_0^\infty \tilde{T}_{\alpha,3}(y,z)\phi_p(ky)\frac{\mathrm{d}\phi_q(kz)}{\mathrm{d}z}\mathrm{d}y\mathrm{d}z, \end{aligned} \tag{5.45}$$

for medium 1, and

$$\begin{aligned} rhs^{(2)} = {} & ik\int_0^\infty\int_{-\infty}^0 \tilde{T}_{\alpha,1}(y,z)\phi_p(-ky)\phi_q(kz)\mathrm{d}y\mathrm{d}z \\ & + \phi_p(0)\tau_q^{(\alpha,2)} - \int_0^\infty\int_{-\infty}^0 \tilde{T}_{\alpha,2}(y,z)\phi_q(kz)\frac{\mathrm{d}\phi_p(-ky)}{\mathrm{d}y}\mathrm{d}y\mathrm{d}z \\ & - \int_0^\infty\int_{-\infty}^0 \tilde{T}_{\alpha,3}(y,z)\phi_p(-ky)\frac{\mathrm{d}\phi_q(kz)}{\mathrm{d}z}\mathrm{d}y\mathrm{d}z, \end{aligned} \tag{5.46}$$

for medium 2. The three remaining integrals in Eqns. 5.45 and 5.46 are combined to form

$$\sum_{\mu=1}^{3}\sum_{m,n=0}^{\infty} -a_{m,n}^{(\mu,1)} M_{p,q,m,n}^{(\alpha,\mu,1)}, \tag{5.47}$$

where $a_{m,n}$ was defined in Eqn. 5.20 and $\bar{\mathbf{M}}$ is defined as

$$\begin{aligned} M_{pq,mn}^{(\alpha,\mu,1/2)} = \pm \sum_{\beta,\nu=1}^{3} \int_0^{\infty}\int_0^{\pm\infty} \Big[D_\beta(k)\phi_p(\pm ky)\phi_q(kz)\Big]^* \\ C_{\alpha\beta\mu\nu}^{(1/2)}\Big[D_\nu(k)\phi_m(\pm ky)\phi_n(kz)\Big]\mathrm{d}y\mathrm{d}z. \end{aligned} \tag{5.48}$$

Here, $[D_\beta\phi_p\phi_q]^*$ in the first term of Eqn. 5.48 is from the sign difference between the real and imaginary parts of Eqns. 5.45 - 5.46. Applying the above notation, Eqns. 5.45 - 5.46 become

$$rhs^{(1)} = -\phi_p(0)\tau_q^{(\alpha,1)} - \sum_{\mu=1}^{3}\sum_{m,n=0}^{\infty} a_{mn}^{(\mu,1)} M_{p,q,m,n}^{(\alpha,\mu,1)}, \tag{5.49}$$

$$rhs^{(2)} = \phi_p(0)\tau_q^{(\alpha,2)} - \sum_{\mu=1}^{3}\sum_{m,n=0}^{\infty} a_{mn}^{(\mu,2)} M_{p,q,m,n}^{(\alpha,\mu,2)}. \tag{5.50}$$

Equation 5.28 is set equal to Eqns. 5.49 and 5.50 yielding

$$\sum_{\mu=1}^{3}\sum_{m,n=0}^{\infty} \left(M_{p,q,m,n}^{(\alpha,\mu,1)} - \rho^{(1)}v^2\delta_{\alpha\mu}\delta_{pm}\delta_{qn}\right) a_{mn}^{(\mu,1)} = -\phi_p(0)\tau_q^{(\alpha,1)}, \tag{5.51}$$

for medium 1 and

$$\sum_{\mu=1}^{3}\sum_{m,n=0}^{\infty} \left(M_{p,q,m,n}^{(\alpha,\mu,2)} - \rho^{(2)}v^2\delta_{\alpha\mu}\delta_{pm}\delta_{qn}\right) a_{mn}^{(\mu,2)} = \phi_p(0)\tau_q^{(\alpha,2)}, \tag{5.52}$$

for medium 2.

The equations of motion have now been determined for the two media, with waves propagating along the x direction, located at the intersection of the fracture with the free surface.

5.3.4 Solving Matrix $\bar{\mathbf{M}}$

Several relationships are required to solve the $\bar{\mathbf{M}}$ matrices in Eqn. 5.48. First, there are three possible integrals that could occur for the Laguerre functions (ϕ) in Eqn. 5.48. The three integrals are:

$$\int_0^{\pm\infty} \phi_{\mathrm{a}}(\pm ky)\phi_b(\pm ky)\mathrm{d}y = \pm\frac{\delta_{ab}}{k}, \tag{5.53}$$

$$\int_0^{\pm\infty} \phi_{\mathrm{a}}(\pm ky)\frac{\partial}{\partial \mathrm{y}}\phi_b(\pm ky)\mathrm{d}y = -\Theta(b-a) + \frac{\delta_{ab}}{2} \equiv \psi_{a,b}, \tag{5.54}$$

and

$$\int_0^{\pm\infty} \frac{\partial}{\partial \mathrm{y}}\big(\phi_{\mathrm{a}}(\pm ky)\big)\frac{\partial}{\partial \mathrm{y}}\big(\phi_b(\pm ky)\big)\mathrm{d}y = \pm k\left[min(a,b) + \frac{1}{2} - \frac{\delta_{ab}}{4}\right] \equiv \pm k\Gamma_{a,b}, \tag{5.55}$$

where Θ is a step function defined by

$$\Theta(f) = \left\{ \begin{array}{ll} 0 & \text{if } f < 0 \\ 1 & \text{if } f \geq 0 \end{array} \right\}. \tag{5.56}$$

The elastic stiffness matrix, $C^{(1/2)}_{\alpha\beta\mu\nu}$, depends upon the material symmetry (e.g., isotropic, transversely isotropic, etc.). The general orthorhombic elastic stiffness matrix (Eqn. 2.10) is used so that any higher symmetries can be applied by properly adjusting the elastic constants.

Applying Eqn. 2.10 to the definition of $\bar{\mathbf{M}}$ (Eqn. 5.48) the following relationships are found:

$$M^{(1,1,1/2)}_{pq,mn} = C^{(1/2)}_{11}\delta_{pm}\delta_{qn} + C^{(1/2)}_{66}\{\delta_{qn}\Gamma_{p,m}\} + C^{(1/2)}_{55}\{\delta_{pm}\Gamma_{q,n}\}, \tag{5.57}$$

$$M^{(1,2,1/2)}_{pq,mn} = \pm\Big[- iC^{(1/2)}_{12}\delta_{qn}\psi_{p,m} + iC^{(1/2)}_{66}\delta_{qn}\psi_{m,p}\Big], \tag{5.58}$$

$$M^{(1,3,1/2)}_{pq,mn} = -iC^{(1/2)}_{13}\delta_{pm}\psi_{q,n} + iC^{(1/2)}_{55}\delta_{pm}\psi_{n,q}, \tag{5.59}$$

$$M^{(2,1,1/2)}_{pq,mn} = \pm\Big[- iC^{(1/2)}_{66}\delta_{qn}\psi_{p,m} + iC^{(1/2)}_{12}\delta_{qn}\psi_{m,p}\Big], \tag{5.60}$$

$$M^{(2,2,1/2)}_{pq,mn} = C^{(1/2)}_{66}\delta_{pm}\delta_{qn} + C^{(1/2)}_{22}\delta_{qn}\Gamma_{m,p} + C^{(1/2)}_{44}\delta_{pm}\Gamma_{q,n}, \tag{5.61}$$

$$M^{(2,3,1/2)}_{pq,mn} = \pm\Bigg[C^{(1/2)}_{23}\psi_{m,p}\psi_{q,n} + C^{(1/2)}_{44}\psi_{p,m}\psi_{n,q}\Bigg], \tag{5.62}$$

$$M^{(3,1,1/2)}_{pq,mn} = -iC^{(1/2)}_{55}\delta_{pm}\psi_{q,n} + iC^{(1/2)}_{13}\delta_{pm}\psi_{n,q}, \tag{5.63}$$

$$M^{(3,2,1/2)}_{pq,mn} = \pm\Bigg[C^{(1/2)}_{44}\psi_{m,p}\psi_{q,n} + C^{(1/2)}_{23}\psi_{p,m}\psi_{n,q}\Bigg], \tag{5.64}$$

and

$$M^{(3,3,1/2)}_{pq,mn} = C^{(1/2)}_{55}\delta_{pm}\delta_{qn} + C^{(1/2)}_{44}\delta_{qn}\Gamma_{m,p} + C^{(1/2)}_{33}\delta_{pm}\Gamma_{n,q}. \tag{5.65}$$

When Eqns. 5.57 - 5.65 are combined to form matrix $\bar{\mathbf{M}}$, the result is a Hermitian ($\bar{\mathbf{M}} = \bar{\mathbf{M}}^{\dagger}$) matrix independent of k, the wavenumber.

5.3.5 Transformation

To calculate $\bar{\mathbf{M}}$ numerically, a transformation is required to move to another coordinate system, because the current formulation is in an imaginary space. Following the work of Maradudin et al. (1973) the following transformation is used [142]

$$\hat{u}_x = iu_x, \quad \hat{u}_y = u_y, \quad \hat{u}_z = u_z, \tag{5.66}$$

which is condensed to

$$\hat{u}_\alpha = u_\alpha \left(\delta_{\alpha,1} i + \delta_{\alpha,2} + \delta_{\alpha,3}\right). \tag{5.67}$$

Using this transformation, the matrix $\bar{\mathbf{M}}$ changes, such that for every $\alpha = 1$ an $+i = \sqrt{-1}$ must be inserted, and for every $\mu = 1$ an $-i$ must be inserted. That is

$$M^{12} \rightarrow iM^{12}, \tag{5.68}$$

$$M^{13} \rightarrow iM^{13}, \tag{5.69}$$

$$M^{21} \rightarrow -iM^{21}, \tag{5.70}$$

$$M^{31} \rightarrow -iM^{31}. \tag{5.71}$$

These are the only terms affected. Applying this transformation to Eqns. 5.57 - 5.65 yields

$$M^{(1,1,1/2)}_{pq,mn} = C^{(1/2)}_{11}\delta_{pm}\delta_{qn} + C^{(1/2)}_{66}\{\delta_{qn}\Gamma_{p,m}\} + C^{(1/2)}_{55}\{\delta_{pm}\Gamma_{q,n}\}, \tag{5.72}$$

$$M^{(1,2,1/2)}_{pq,mn} = \pm\Big[C^{(1/2)}_{12}\delta_{qn}\psi_{p,m} - C^{(1/2)}_{66}\delta_{qn}\psi_{m,p}\Big], \tag{5.73}$$

$$M^{(1,3,1/2)}_{pq,mn} = C^{(1/2)}_{13}\delta_{pm}\psi_{q,n} - C^{(1/2)}_{55}\delta_{pm}\psi_{n,q}, \tag{5.74}$$

$$M^{(2,1,1/2)}_{pq,mn} = \pm\Big[-C^{(1/2)}_{66}\delta_{qn}\psi_{p,m} + C^{(1/2)}_{12}\delta_{qn}\psi_{m,p}\Big], \tag{5.75}$$

$$M^{(2,2,1/2)}_{pq,mn} = C^{(1/2)}_{66}\delta_{pm}\delta_{qn} + C^{(1/2)}_{22}\delta_{qn}\Gamma_{m,p} + C^{(1/2)}_{44}\delta_{pm}\Gamma_{q,n}, \tag{5.76}$$

$$M^{(2,3,1/2)}_{pq,mn} = \pm\left[C^{(1/2)}_{23}\psi_{m,p}\psi_{q,n} + C^{(1/2)}_{44}\psi_{p,m}\psi_{n,q}\right], \tag{5.77}$$

$$M^{(3,1,1/2)}_{pq,mn} = -C^{(1/2)}_{55}\delta_{pm}\psi_{q,n} + C^{(1/2)}_{13}\delta_{pm}\psi_{n,q}, \tag{5.78}$$

$$M^{(3,2,1/2)}_{pq,mn} = \pm\left[C^{(1/2)}_{44}\psi_{m,p}\psi_{q,n} + C^{(1/2)}_{23}\psi_{p,m}\psi_{n,q}\right], \tag{5.79}$$

and

$$M^{(3,3,1/2)}_{pq,mn} = C^{(1/2)}_{55}\delta_{pm}\delta_{qn} + C^{(1/2)}_{44}\delta_{qn}\Gamma_{m,p} + C^{(1/2)}_{33}\delta_{pm}\Gamma_{n,q}. \tag{5.80}$$

An example of calculating the $\bar{\mathbf{M}}$ matrix, along with this transformation, is given in Appendix G.

5.3.6 Boundary Conditions

Previous theoretical work on coupling WWs assumed a welded (i.e., continuity of stress and displacement) contact between the two media [136–138,212]. Although this boundary condition leads to several interesting waveforms, many laboratory and field scale fracture studies have observed that fractures behave as non-welded contacts. It has been theoretically and experimentally verified that DD boundary conditions are more realistic and applicable to modeling the long wavelength behavior of fractures [33, 213]. In this work, interfaces are assumed to be non-welded, i.e., continuity in stress and a discontinuity in displacement. The discontinuity in displacement is assumed to be linearly proportional to the stress and inversely proportional to the specific stiffness (κ) of the fracture [12, 16, 122, 123, 214]. This type of boundary condition is often called the displacement discontinuity boundary condition (DD), sometimes called linear slip or non-welded interfaces.

Before applying the DD boundary conditions, the displacement at the interface will be defined as

$$U_n^{(\alpha,1/2)} \equiv k \int_0^\infty \phi_n(kz) \tilde{U}_\alpha^{(1/2)}(0,z) \mathrm{d}z. \tag{5.81}$$

Applying the expansion in Eqn. 5.20 gives

$$U_n^{(\alpha,1/2)} = k \int_0^\infty \phi_n(kz) \sum_{m,n=0}^{\infty} a_{m,n}^{(\alpha,1/2)} \phi_m(0) \phi_n(kz) \mathrm{d}z. \tag{5.82}$$

Using Eqn. 5.25, this is simplified to yield

$$U_n^{(\alpha,\eta)} = \sum_{m=0}^{\infty} a_{mn}^{(\alpha,\eta)}, \ \eta = 1, 2, \tag{5.83}$$

where η is the medium and a_{mn} are the expansion coefficients defined in Eqn. 5.20. Equation 5.83 is used to define the boundary conditions.

The DD boundary conditions along the fracture are defined for the problem geometry as

$$\tilde{U}_{\beta}^{(1)} - \tilde{U}_{\beta}^{(2)} = \frac{\tilde{T}_{\beta,y}^{(1)}}{\kappa_{\beta}},\ \beta = x, y, z. \tag{5.84}$$

Multiplying Eqn. 5.84 by $\phi_l(kz)$, applying the expansion in Eqn. 5.20, and integrating over the quarter space yields

$$\sum_{m,n=0}^{\infty} \left[\frac{a_{m,n}^{(\beta,1)}}{k} - \frac{a_{m,n}^{(\beta,2)}}{k}\right] = \frac{\tau_n^{(\beta,1)}}{\kappa_{\beta}}. \tag{5.85}$$

Equation 5.85 simplifies to

$$[U_n^{(\beta,1)} - U_n^{(\beta,2)}] = \frac{k}{\kappa_{\beta}} \tau_n^{(\beta,1)}. \tag{5.86}$$

The stress boundary condition is continuous across the interface and is given as

$$\tau_n^{(\beta,1)} = \tau_n^{(\beta,2)}. \tag{5.87}$$

Using Eqn. 5.51 above, the similarity transformation (see Appendix B) is applied to obtain

$$\bar{\mathbf{U}}^{(1)} = \bar{\mathbf{G}}^{(1)}(-\bar{\boldsymbol{\tau}}^{(1)}), \tag{5.88}$$

$$\bar{\mathbf{U}}^{(2)} = \bar{\mathbf{G}}^{(2)}(\bar{\boldsymbol{\tau}}^{(2)}), \tag{5.89}$$

where $\bar{\mathbf{G}}$ came from the similarity transformation $\bar{\mathbf{G}} = \bar{\mathbf{Q}}^{-1}\bar{\mathbf{A}}\bar{\mathbf{Q}}$ such that

$$G_{nq}^{(\alpha,\beta,1/2)} = \sum_{j=1}^{j_{max}} \frac{Q_n^{(\alpha,1/2)}(j) Q_q^{(\beta,1/2)*}(j)}{\lambda(j) - \rho^{(1/2)} v^2}, \tag{5.90}$$

where λ is the eigenvalue of $\bar{\mathbf{M}}$, and $\bar{\mathbf{Q}}$ is a unitary matrix (theorem 5 Appendix B) of size $[3(n_{max}+1)$ x $j_{max}]$. $\bar{\mathbf{Q}}$ is defined as

$$Q_n^{(\alpha,1-4)}(j) \equiv \sum_{m=0}^{m_{max}} V_{mn}^{(\alpha,1-4)}(j), \tag{5.91}$$

$$j_{max} = 3(m_{max}+1)(n_{max}+1), \tag{5.92}$$

where V_{mn} are the m, n components of the eigenvectors of $\bar{\mathbf{M}}$. See Appendix B for additional details on applying similarity transformations.

There are now 4 equations (Eqns. 5.86, 5.87, 6.112 and 5.89) and 4 unknowns ($\bar{\mathbf{U}}^{(1)}$, $\bar{\mathbf{U}}^{(2)}$, $\bar{\boldsymbol{\tau}}^{(1)}$ and $\bar{\boldsymbol{\tau}}^{(2)}$). Inserting Eqns. 5.88 and 5.89 into Eqn. 5.87 gives

$$-\bar{\mathbf{G}}^{-1\ (1)}\bar{\mathbf{U}}^{(1)} = \bar{\mathbf{G}}^{-1\ (2)}\bar{\mathbf{U}}^{(2)}, \tag{5.93}$$

where $\bar{\mathbf{G}}^{-1}$ is the inverse of $\bar{\mathbf{G}}$. Eliminating $\bar{\mathbf{U}}^{(1)}$ by applying Eqn. 5.86 yields

$$-\bar{\mathbf{G}}^{-1\ (1)}\big[\frac{k}{\kappa_\alpha}\bar{\boldsymbol{\tau}}^{(2)} + \bar{\mathbf{U}}^{(2)}\big] = \bar{\mathbf{G}}^{-1\ (2)}\bar{\mathbf{U}}^{(2)} \tag{5.94}$$

$$-\bar{\mathbf{G}}^{-1\ (1)}\frac{k}{\kappa_\alpha}\bar{\boldsymbol{\tau}}^{(2)} - \bar{\mathbf{G}}^{-1\ (1)}\bar{\mathbf{U}}^{(2)} = \bar{\mathbf{G}}^{-1\ (2)}\bar{\mathbf{U}}^{(2)} \tag{5.95}$$

$$-\bar{\mathbf{G}}^{-1\ (1)}\frac{k}{\kappa_\alpha}\big[\bar{\mathbf{G}}^{-1\ (2)}\bar{\mathbf{U}}^{(2)}\big] - \bar{\mathbf{G}}^{-1\ (1)}\bar{\mathbf{U}}^{(2)} = \bar{\mathbf{G}}^{-1\ (2)}\bar{\mathbf{U}}^{(2)} \tag{5.96}$$

$$\big[-\bar{\mathbf{G}}^{-1\ (1)}\frac{k}{\kappa_\alpha}\bar{\mathbf{G}}^{-1\ (2)} - \bar{\mathbf{G}}^{-1\ (1)} - \bar{\mathbf{G}}^{-1\ (2)}\big]\bar{\mathbf{U}}^{(2)} = 0 \tag{5.97}$$

This is an eigenvalue problem which has solutions when

$$det[\bar{\mathbf{G}}^{-1\ (1)}\frac{k}{\kappa_\alpha}\bar{\mathbf{G}}^{-1\ (2)} + \bar{\mathbf{G}}^{-1\ (1)} + \bar{\mathbf{G}}^{-1\ (2)}] = 0 \tag{5.98}$$

Equation 5.98[1] is a secular equation that relates the velocity, frequency, stress, and elastic constants for the problem geometry (Fig. 5.6) using DD boundary conditions.

5.3.7 Conditions for the Specific Stiffness

In this solution, the CWW (Eqn. 5.98) reverts to the RS wave (section 3.4.3) or Rayleigh wave when $\kappa_\alpha \to \infty$, as is required for welded interfaces, depending on the

[1]Eqn. 5.98 is the general solution for the CWW. The equation stated in Abell et al. 2013 [103] was for a specific case where all the stiffness components were equal, yielding a diagonal matrix for $\frac{k}{\kappa}$. The results in Eqn. 5.98 should be used instead of that specific case.

material parameters [138]. When $\kappa_\alpha \to 0$, which is a free surface boundary condition, $\bar{\mathbf{G}}^{-1\ (1)} \to 0$ while $\frac{1}{\kappa_\alpha} \to \infty$, canceling the first and second terms in Eqn. 5.98. This leaves the determinant $det[\bar{\mathbf{G}}^{-1\ (2)}] = 0$ which is the equation for a WW [142].

The CWW solution is a function of κ on the contact plane (i.e., $\kappa_x,\ \kappa_y,\ \kappa_z$) between the two surfaces. Previous studies on the shear to normal stiffness ratio ($R = \frac{\kappa_{shear}}{\kappa_{normal}}$) were performed on the laboratory and field scale for various rock types and fracture [132, 215–217]. Theoretical studies have generally used the value of 1 for this ratio, although this is typically only valid for extremely smooth fracture planes [217].

In this study, for simplicity in modeling, the ratio was also assumed to be 1, i.e., $\kappa_x = \kappa_y$. Due to the presence of the free surface in the z direction, the stiffness term, $\frac{k}{\kappa_z}$ is multiplied by zero stress, and thus the stiffness is set to $\kappa_3 = \infty$ to be consistent with the free surface.

5.3.8 Summary

The preceding section derived a mathematical formulation for a wave propagating along the coupled interface between two wedges, made of the same or different material. This model applied a linear expansion in Laguerre functions to the displacement amplitudes of the wave. After applying this expansion to the equations of motion, a secular equation for the CWW was obtained using a DD boundary condition. This result reverts to the previously obtained RS, WW, or Rayleigh wave solution when the proper stiffness and material conditions are used.

The following sections will discuss the numerical and experimental verification of the CWW for two media of the same material, a case not allowed by RS waves, as well as different materials. These results were performed on both isotropic and anisotropic samples under load, and were used to obtain an estimate for the specific stiffness for the surface fractures studied.

5.4 Numerical Analysis of the CWW

5.4.1 Introduction

In this section, the results of a parameter study on the existence, velocity, and particle motion of the CWW is presented. The parameters used in this section are based on the experimentally measured values for the isotropic and anisotropic samples used in this study (Tables H.2-H.3).

This numerical study was used to determine the range of existence and velocity of the CWW modes as a function of the frequency and specific stiffness, κ, of the fracture. A comparison with the group theory results in the earlier sections is also given.

5.4.2 Convergence

Prior to running numerical calculations, the number of expansion terms required to achieve good convergence must be determined. Recall for the WW this was around 5 terms (section 4.3.1). The number of expansion terms used in Eqn. 5.20 was chosen to be 15 based upon an analysis of the convergence rate. The convergence to the ideal value is shown in Fig. 5.7. The convergence in Fig. 5.7 is expressed so that a perfect convergence would be at 0 on the y-axis. By increasing the number of expansion terms, p, (x-axis) the convergence decreases exponentially, towards zero. The fit to the numerical data indicates that the obtained value is within 0.2% of the "perfect" value for 15 expansion terms, which is an acceptable convergence and is used for this section.

5.4.3 CWW in Isotropic Media

To begin the numerical analysis, the secular equation for the CWW (Eqn. 5.98) was used to calculate the velocity. Several cases were examined to determine the effects of material parameters, i.e., Poisson's ratio (ν), on the CWW velocity. The

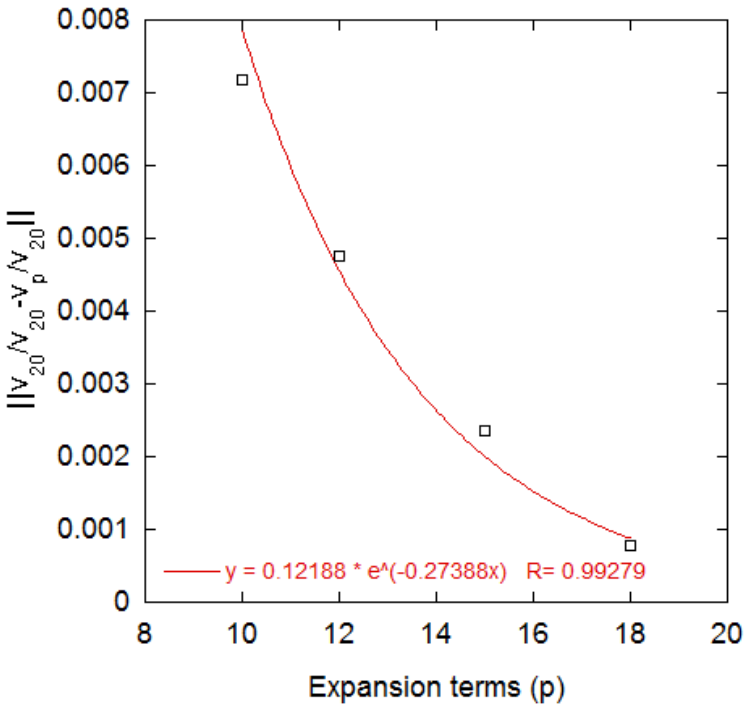

Figure 5.7. Normalized convergence for the isotropic CWW. The number of expansions, p, determines the rate of convergence to the perfect solution. For p=15, the case used in this study, the convergence is within 0.2% of the perfect (i.e., y-axis=0) solution.

results for three positive ν values (0.1, 0.2, 0.3) are shown in Fig. 5.8. As predicted by the group theory results in section 5.2, two modes were observed for each set of material parameters.

For all three values of the positive ν studied, two modes were found, which satisfied the secular equation. Mode 1, for each ν, exhibited the trend predicted in section 5.3.7 where at low stiffness (coupling), the velocity was at the WW velocity and as the stiffness increased, the velocity increased up to the Rayleigh velocity. The existence of mode 2 (Fig. 5.8) was more limited in terms of range of stiffness. It was only observed at low stiffnesses and cutoff as soon as the velocity reached the Rayleigh velocity. Once the velocity of mode 2 went above the Rayleigh wave velocity, the wave became delocalized and was no longer a guided mode, as required for the CWW solution.

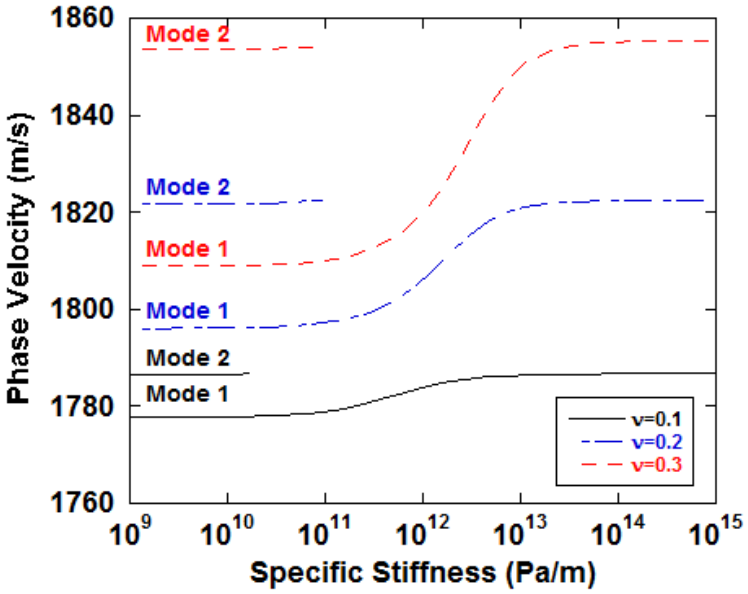

Figure 5.8. Numerical results of the CWW with different positive Poisson's ratio materials. Note that mode 2 cuts off near the Rayleigh velocity due to delocalization. Parameters used for the calculation were: $\rho = 2500\ \frac{kg}{m^3}$, $\mu = 1e10\ Pa$, and $p = 15$.

An analogous examination was given to negative ν materials. Again, two modes were observed and the results are shown in Fig. 5.9. Mode 1 had similar behavior to the positive ν results in that it had a velocity that ranged from the WW velocity to the Rayleigh wave velocity as a function of the specific stiffness. Mode 2 however, had a slightly larger range of existence, especially for large negative ν values, until it also became delocalized after exceeding the Rayleigh wave velocity. The particle motion will be examined to determine the difference between these modes in section 5.4.5.

5.4.4 CWW in Anisotropic Media

When the material parameters of a medium are anisotropic, the assumption of isotropy in velocity leads to a miscalculation of the velocity range as a function of κ. As an example, the velocities for two different directions in anisotropic aluminum

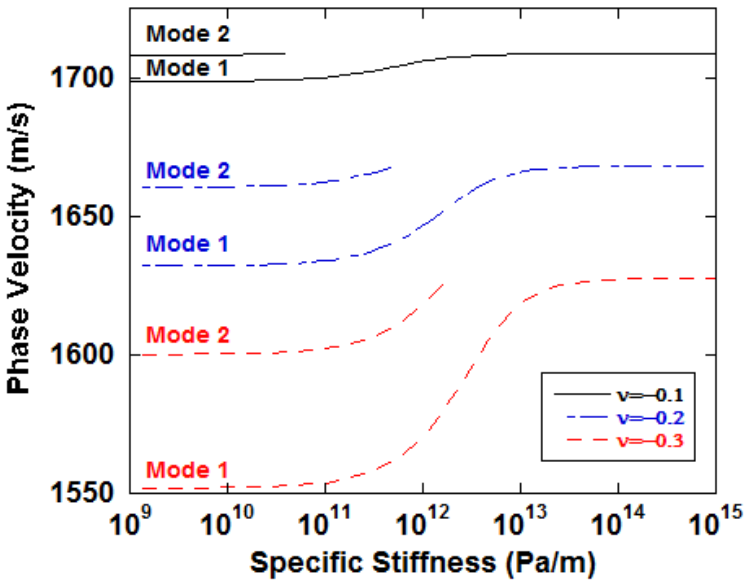

Figure 5.9. Numerical results of the CWW with different negative Poisson's ratio materials. Note that mode 2 cuts off near the Rayleigh velocity due to delocalization. Parameters used for the calculation were: $\rho = 2500\ \frac{kg}{m^3}$, $\mu = 1e10\ Pa$, and $p = 15$.

(Table H.3) are applied, separately, to the isotropic CWW theory. The S- and P-wave velocities from the x_1 direction of the anisotropic aluminum are applied to the isotropic CWW theory (Eqn. 5.98). This assumption results in a velocity range slightly lower to slightly higher than the WW velocity (partially dashed line in Fig. 5.10). When the other direction is used (x_2) in the isotropic theory, the velocity range is even lower (dashed line in Fig. 5.10). Note only mode 1 was analyzed here.

When the full anisotropic parameters are used (Table H.3) the expected velocity range, i.e., WW to Rayleigh wave velocity, is obtained for the CWW (solid line in Fig. 5.10). The anisotropic case is replotted in Fig. 5.11. Because this sample had only 4% anisotropy in S-wave velocity, this demonstrates the sensitivity of the CWW theory to anisotropic properties of the material.

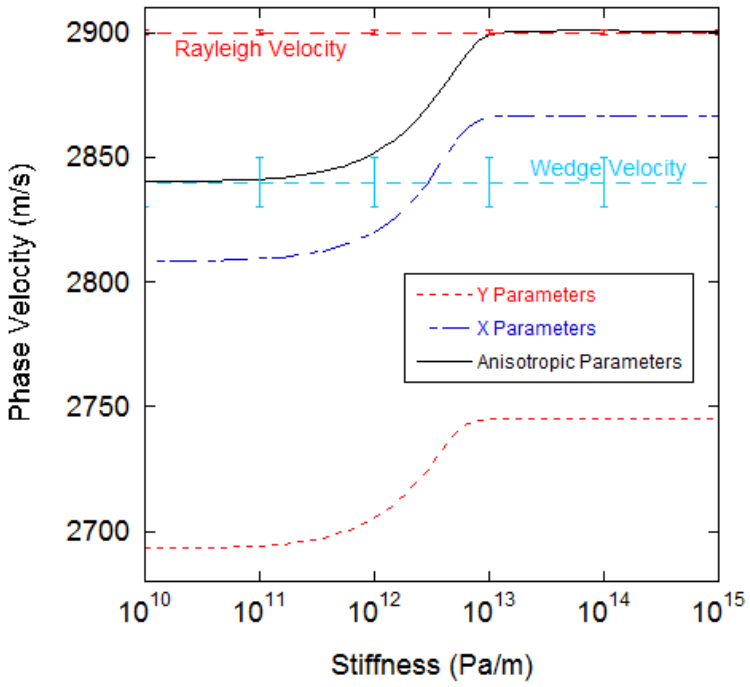

Figure 5.10. Numerical results comparing the mode 1 CWW using isotropic and anisotropic theory. The isotropic theory was applied to the X and Y direction parameters from Table H.3. This demonstrates the usefulness of taking into account the anisotropy, even when it is on the order of 5%.

5.4.5 Particle Motion

After solving the secular equation for the CWW (Eqn. 5.98), the results were used to obtain the displacements at various points within the sample. To calculate these displacements, the expansion coefficients (a_{mn}) were calculated using Eqns. 5.51-5.52. Note that the subscripts must be dealt with carefully as the $\phi_p(0)$ terms are each 1, but they add to the dimensionality of the matrices in these equations. Once the expansion coefficients were determined, they were used in Eqn. 5.20 to calculate the displacements in each media.

The analysis was performed on the isotropic results using $\nu = 0.1$ for both media. The results are shown in Fig. 5.12. The particle motion of mode 1 indicates that the vibrations are highly localized to the tips, as required, and that the two media are in

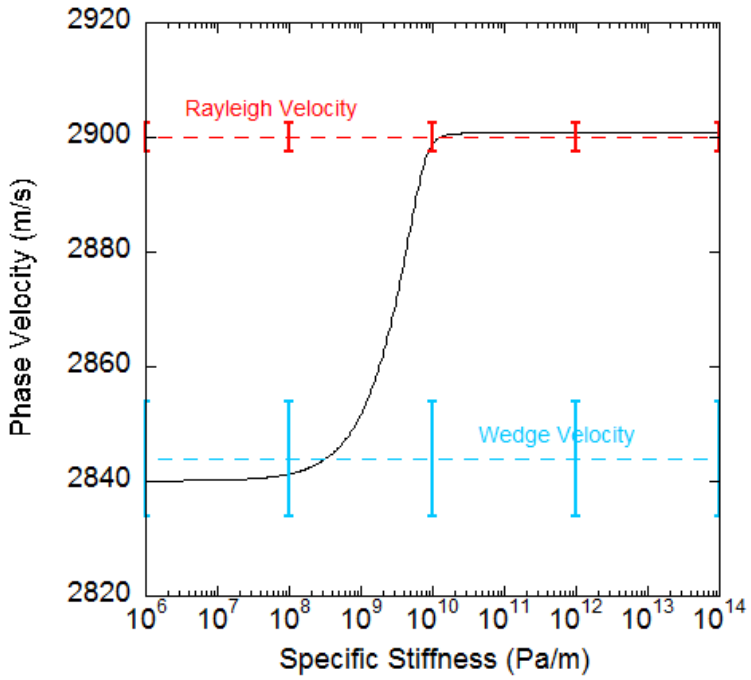

Figure 5.11. Anisotropic CWW theory. Mode 1 CWW phase velocity as a function of specific stiffness for the anisotropic aluminum parameters in Table H.3.

phase with each other. At low stiffness, the observed particle motion (Fig. 5.12a) is highly localized to the tips. At a higher stiffness (Fig. 5.12b), the CWW approaches a Rayleigh wave type mode and is no longer localized to the tip but instead to the surface. This motion matches the predicted motion from the $A^{'}$ mode shown in Fig. 5.4b from the group theory analysis.

Mode 2 exhibits a similar particle motion (Fig. 5.13a), with wagging near the tip, but with less amplitude than that of mode 1 (Fig. 5.12a) and out of phase motion. This mode matches the predicted motion of the $A^{''}$ mode from group theory analysis that was shown in Fig. 5.5b. At high values of stiffness, mode 2 becomes delocalized and the amplitude grows away from the tip (Fig. 5.13b). The amplitude of mode 2 is larger away from the interface, indicating a delocalization of this mode after $\sim 10\ \frac{GPa}{m}$ but the motion looks similar to Fig. 5.13a up to this stiffness.

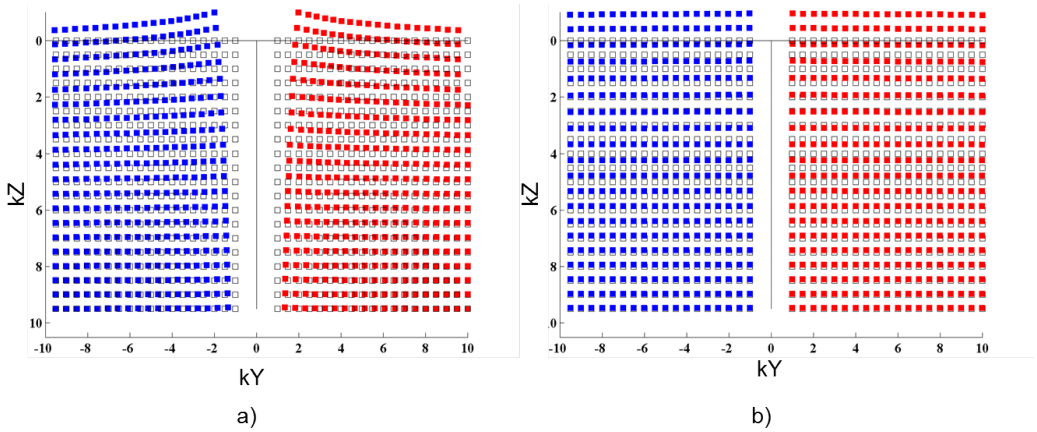

Figure 5.12. Particle motion of the mode 1 CWW at a specific stiffness of a) 1 $\frac{GPa}{m}$ and b) 79.1 $\frac{TPa}{m}$ for the $\nu = 0.1$ case shown in Fig. 5.8.

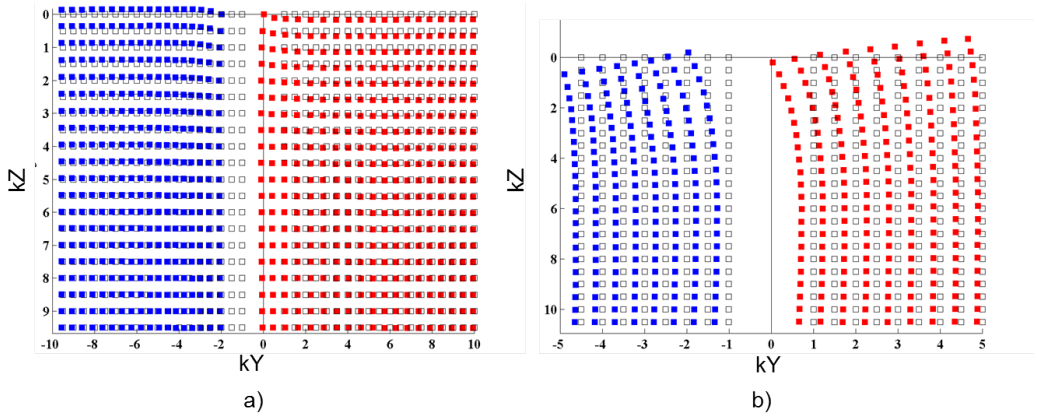

Figure 5.13. Particle motion of the mode 2 CWW at a specific stiffness of a) 1 $\frac{GPa}{m}$ and b) 79.1 $\frac{TPa}{m}$ for the $\nu = 0.1$ case shown in Fig. 5.8.

A similar analysis applies to the negative Poisson's ratio, ν, materials. For $\nu = -0.1$, which has velocity characteristics shown in Fig. 5.9, the particle motion for mode 1 was calculated and is shown in Fig. 5.14. Note that at low specific stiffness (Fig. 5.14a) the motion is a breathing type mode where the two media come together and then apart. For stronger coupling (i.e., higher stiffness), the media become welded and the observed motion couples to the Rayleigh wave mode, which is localized to

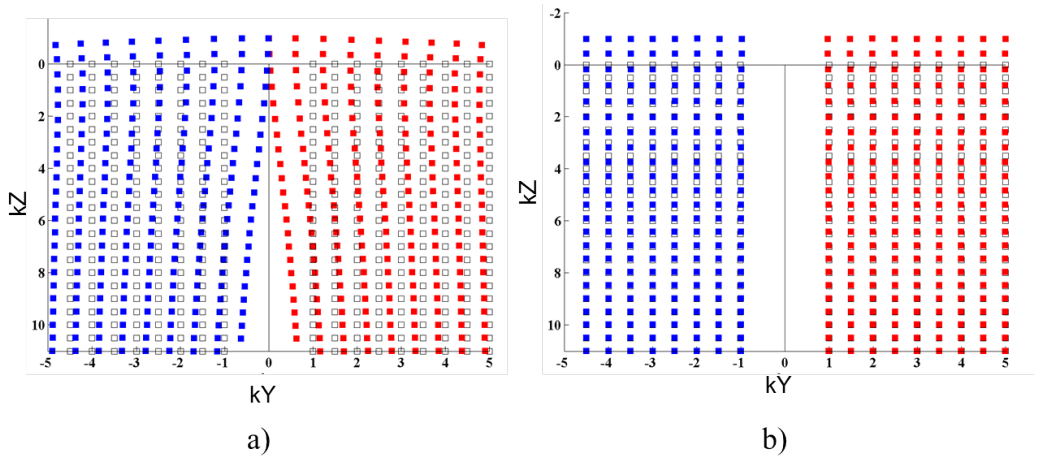

Figure 5.14. Particle motion of the mode 1 CWW with $\nu = -0.1$ at a specific stiffness of a) 1 $\frac{GPa}{m}$ and b) 79.1 $\frac{TPa}{m}$. The velocity is shown in Fig. 5.9.

the surface instead of the wedge tip. This is shown for a specific stiffness of 79.1 $\frac{TPa}{m}$ in Fig. 5.14b.

The particle motion for the CWW in mode 2 with $\nu = -0.1$ is shown in Fig. 5.15. At a specific stiffness of 1 $\frac{GPa}{m}$ the CWW again excites a breathing type mode, but for this mode, the motions are opposite. At high specific stiffness values the CWW becomes delocalized, as discussed above, and the guided CWW mode is no longer isolated to the surface or fracture.

5.4.6 Effect of Shear to Normal Stiffness Ratio

Although the shear to normal stiffness ratio was assumed to be 1 in the analysis of this study (section 5.3.7), the theoretical variations in the CWW velocity range, for different stiffness ratios, was explored. Figure 5.16 shows the velocity range for mode 1 CWW for different shear to normal stiffness ratios ($\frac{\kappa_x}{\kappa y}$). Note that for $\frac{\kappa_y}{\kappa_x} > 1$, the theoretical CWW velocity was partially below the WW velocity, indicating a slower wave than that propagating along the single wedge. For ratios of $\frac{\kappa_y}{\kappa_x} < 1$, the velocity values shifted in normalized frequency, but remained within the same velocity range

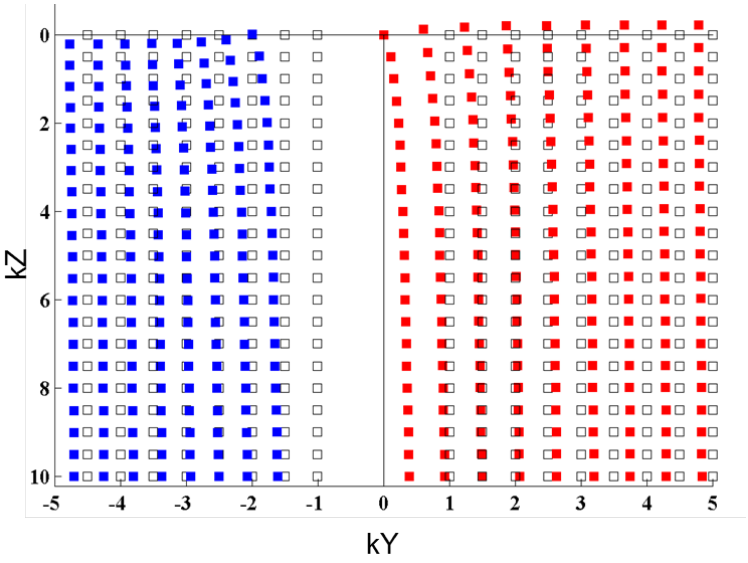

Figure 5.15. Particle motion of the mode 2 CWW with $\nu = -0.1$ at a specific stiffness of 1 $\frac{GPa}{m}$. The velocity is shown in Fig. 5.9.

(i.e., WW to Rayleigh wave velocity). Because the experimental results indicated a velocity range between the WW and Rayleigh wave velocity, the assumption of the stiffness ratio being 1 is reasonable and used here.

5.4.7 Existence of the CWW

Although the analysis was performed for a CWW in identical media, the results of an existence study are presented here for different media. The same numerical calculation discussed in the previous sections is performed but with the two media having different material parameters, and the same Poisson's ratio. The density, ρ, and shear modulus, μ_L, are changed so that the ratio of densities and moduli ranges between 0.05 and 3 for the two media in contact.

The results are shown in Fig. 5.17 for several different Poisson's ratio materials. Also shown in this figure are the existence regions for the Stoneley wave and interface wave (chapter 3) with the same material properties. As the Poisson's ratio increases the CWW range of existence also increases and even exceeds the regime expected for

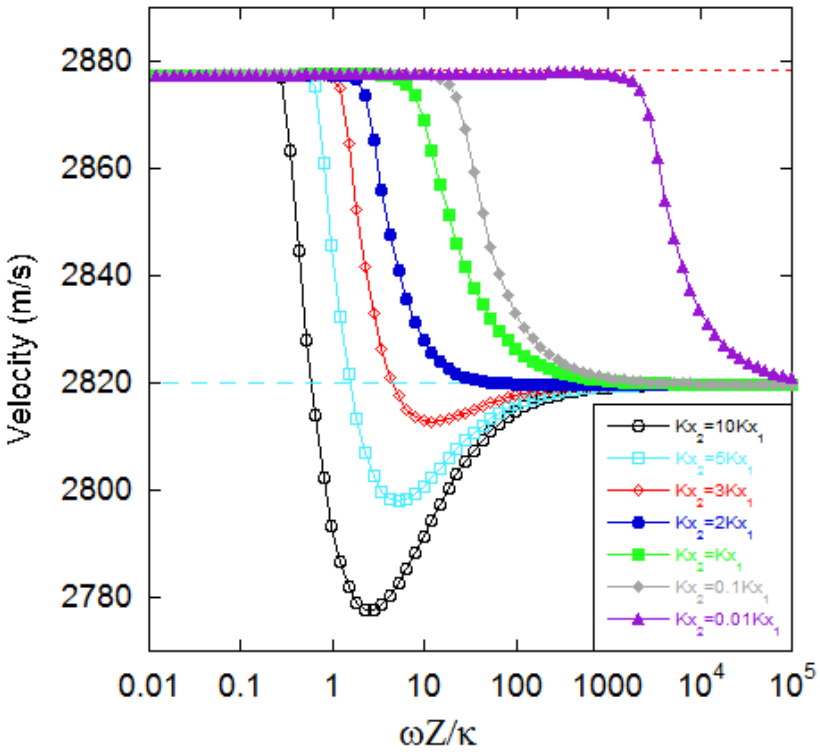

Figure 5.16. Numerical calculations of the mode 1 CWW for different ratios ($\frac{\kappa_y}{\kappa_x}$) of specific stiffness. Note for all values $\kappa_z = \infty$.

interface waves (Fig. 5.17d). The red symbols in Fig. 5.17 indicate where mode 2 was found to exist, and the blue symbols where mode 1 was found. Note that only along the line $\frac{\rho}{\rho'} = \frac{\mu}{\mu'}$ both modes 1 and 2 were found. Mode 2 was found outside of this regime (Fig. 5.17). This is due to the drop in symmetry when the media are away from this condition.

5.4.8 Summary

The numerical results discussed here agree well with the group theory analysis from section 5.2. Two modes were predicted for the CWW with particle motion in agreement with group theory. The effects of anisotropy, material properties, existence,

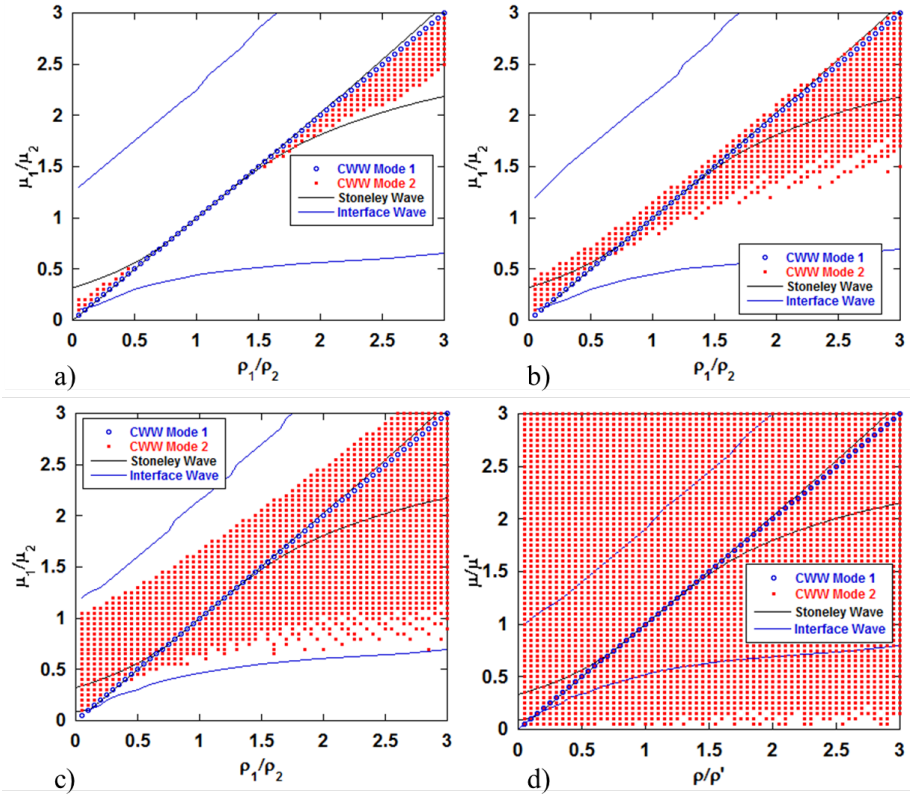

Figure 5.17. Existence plots for the CWW with different materials in contact. Each media had a Poisson's ratio of a) 0.075, b) 0.05, c) 0.1, and d) 0.2 but different μ_L and ρ values. Stoneley and interface wave existence curves are shown for comparison.

and shear to normal stiffness ratio were also presented and will be used to analyze the experimental results presented in the next section.

5.5 Experimental Verification of the CWW

5.5.1 Experimental Setup

Experimental studies were performed on isotropic and anisotropic aluminum samples to demonstrate the differences in the bulk, surface, and CWWs mentioned in the previous chapters. All of the experiments were performed using Olympus piezoelectric P (V-103) and S (V-153) contact transducers (centered at 1 MHz) to excite and detect

waves propagated through the samples (Fig. 5.18). The transducers were coupled to the samples using Busy Bee clover honey with 8.75% of the moisture evaporated through convection heating at $90°C$ for $\sim$ 120 minutes. A transducer is shown, from multiple perspectives, in Fig. 5.18.

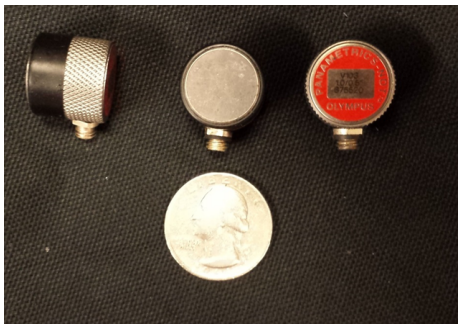

Figure 5.18. Image of piezoelectric contact transducers used to excite and receive ultrasonic waves. Quarter shown for scale.

The source transducer was excited using a 400V pulse with a 1 kHz repetition frequency from an Olympus 5077PR pulse generator. The waves were then propagated along, and through the samples, and the signals were recorded using a National Instruments PXI-1042 controller with a PXI-5122 digitizer and stored on a computer for analysis. A sampling rate of 100 $\frac{MS}{sec}$ and a record length of $10,000$ points were used in this study. A Labview code was created to efficiently switch the source/receiver pairs, average the signals, store the data, and apply the necessary software parameters to carry out the experiment.

5.5.2 Samples

The isotropic samples used in this study were aluminum cubes measuring $\sim$ 30 cm on a side (Table H.2). The anisotropic aluminum bars ($\sim$ 0.08m x 0.08m x 0.30m) used had TI symmetry. The elastic constants were calculated from the bulk wave velocities for these samples (chapter 2). An image of both samples is shown in Fig. 5.19

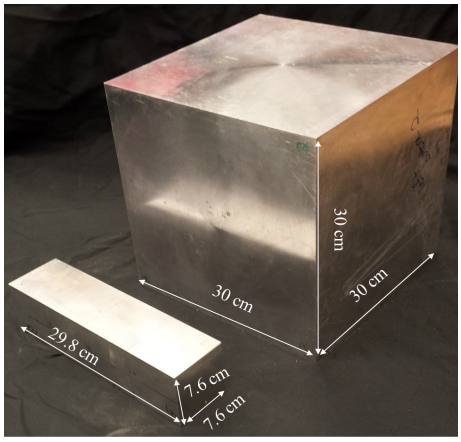

Figure 5.19. Isotropic aluminum cubes (big) and anisotropic aluminum bars (small) used in the experimental study.

From the recorded signals, the bulk P, bulk S, Rayleigh, WW, and CWW velocities were determined for each sample. The velocities were obtained from a Nolte-Hilbert wavelet analysis, for a frequency of 0.3 MHz, and are listed in Table H.3. 0.3 MHz was used because it was the peak in energy for the aluminum wavelet. These velocities are used in section 5.6 to compare the experimental results with the isotropic and anisotropic CWW theoretical predictions of section 5.4.

5.5.3 Load Frame Setup

The samples (see section 5.5.2) were placed inside a single axis Instron 444kN load frame, with an Instron model 59-R8100BTE controller running Bluehill 3 software. Experimental images of the isotropic and anisotropic samples inside the load frame are shown in Figs. 5.20a and 5.21a, respectively. The load frame was used to apply a normal load to the fracture plane, i.e., a load in the Y direction in Fig. 5.6. The load was applied in 2.22 kN increments from 0 to 400.3 kN . To evenly distribute the load an aluminum spacer was placed above the samples (see Figs 5.20 and 5.21). Once the load was applied, it was held constant while 30 signals were acquired and averaged at each transducer location.

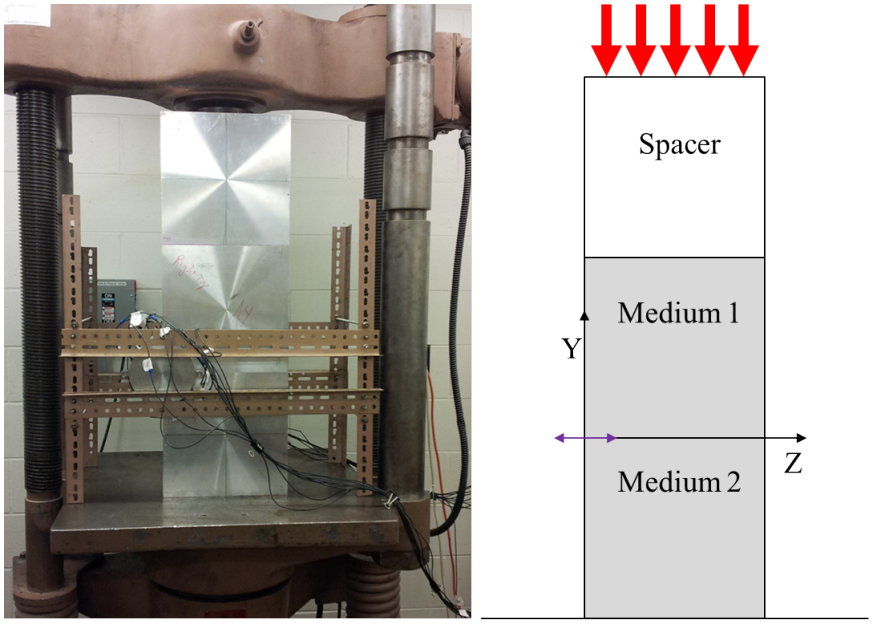

Figure 5.20. a) Isotropic aluminum cubes inside the Instron load frame. The top cube is used to evenly distribute the load throughout the fracture plane. The transducer housing and holder are seen on the left side of the samples. b) Pictorial sketch of the setup with the CWW transducer polarization and coordinate system indicated.

In order to sample the bulk material, single fractures, and surface fracture under the same loading conditions, two platens were used to hold multiple transducers in place on the sample (Fig. 5.22a). Nine transducers were contained in the receiver side and nine in the transmission side of each platen. The platens were machined such that the cables from the transducers are hidden and the platen is held flat against the samples. Thin shims and a washer were used below each transducer, in the holes, to elevate the transducers to the same height and thin Teflon sheets were applied to the surface to eliminate stress buildup on the metal face of the platen. The shims were 0.03 mm (0.0013 in.) thick and the washer was 0.86 mm (0.034 in.) thick. This is shown in Fig. 5.22b.

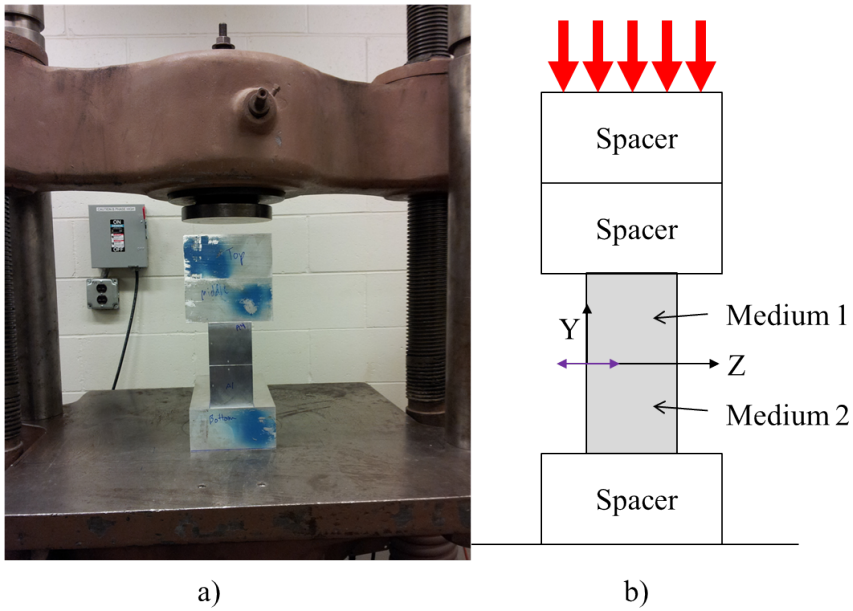

Figure 5.21. a) Anisotropic aluminum bars, with spacers above and below the sample, inside the Instron load frame. b) Pictorial sketch of the setup with the CWW transducer polarization and coordinate system indicated.

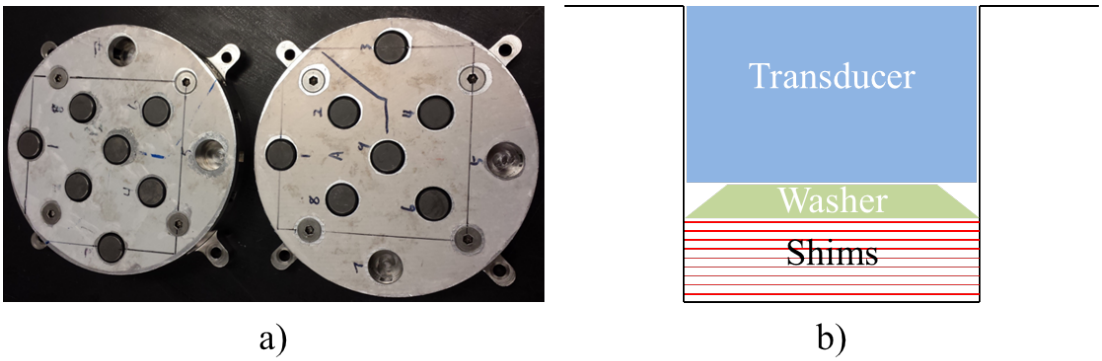

Figure 5.22. a) Array platens used to hold transducers onto samples and allow the fracture, surface fracture, and bulk to be sampled without removing the transducers. b) Side view of the array platens showing the shims and washer used to support the transducer to the correct height.

5.5.4 Digital Image Correlation

An image correlation technique was used to analyze the local displacements at the surface fracture during loading. Digital image correlation (DIC) has emerged as

a powerful tool for displacement and strain analysis. DIC is a particle tracking tool that uses small differences in images to calculate relative displacements on a surface, assuming a linear correspondence. Both 2-D and 3-D DIC methods exist and use relatively simple experimental setups for image collection [218]. The 2-D DIC only measures displacements in the plane of the image, and does not extract the out of plane deformation like the 3-D method does. However, the 3-D method requires two cameras while the 2-D method only requires one. For the analysis described here, only the 2-D method was used because the applied load was in the plane of the images and the samples (aluminum) have a large modulus, preventing large deformations out of plane. The basic outline of the DIC method and analysis are given here, but the details are left to the references (see chapter 5 of Ahmad Hedayat's Ph.D. dissertation [219]).

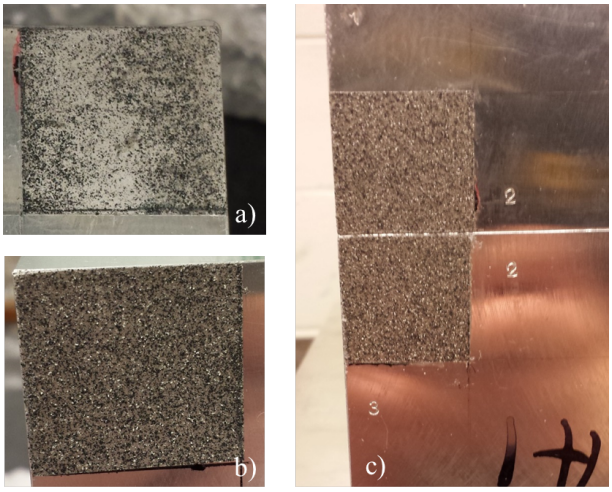

Figure 5.23. Examples of the speckle paint patterns used for DIC. When the paint is a) unevenly applied, the analysis is distorted. b) An even coating of speckle paint, shown in b), allows for the images to analyzed better. c) Each block was painted near the surface fracture.

DIC Setup

The images obtained from the DIC method must be unique at each loading step to calculate the differences in deformation. To do this, the surface is speckled to obtain a unique set of pixels for tracking displacements. Rustoleum multicolored textured spray paint was used for the DIC experiments described here. Speckle paint provided a speckled surface with unique patterns of pixels for correlation. The image window is relatively small (2.54 cm x 2.54 cm section on the corner of each sample shown in Fig. 5.23c) due to the camera used in this experiment. This was acceptable because the transducers (Fig. 5.18) used in these experiments only covered part of this window. In addition, if a larger window were used, the resolution would decrease. It was imperative that the speckle paint be applied uniformly as the analysis is affected by a poor speckle pattern. Examples of bad and good speckle patterns are shown in Fig. 5.23 a and b, respectively. To achieve good coverage over a desired region, shake the can for a few minutes, tape off the area of interest, hold the can upright (approximately 1 m away from the sample), and spray continuously, moving the can parallel to the face of the sample. A uniform speckle pattern is the desired goal. Once the paint has dried, remove the tape and the painted section should look like Fig. 5.23b.

After the speckle paint is applied, the samples are placed in the load frame. A Pointgrey CCD camera with a 50 mm focal length Fujinon lens (HF505A-1) was attached to a tripod and positioned such that the focal plane was at the speckle pattern on the sample (Fig. 5.24). To illuminate the samples uniformly a Fostec Ace I snake LED light was used (Fig. 5.24). One of the advantages of the 2-D DIC method is that it can use uniform light exposure instead of single point laser illumination. This is because the analysis uses a region of the speckle pattern to analyze instead of a single point. The correlation between images is unique for each region [218, 219] because each small region (typically square) has a unique pattern of pixels. Typically at least 3 pixels are required for each speckle point in the correlation.

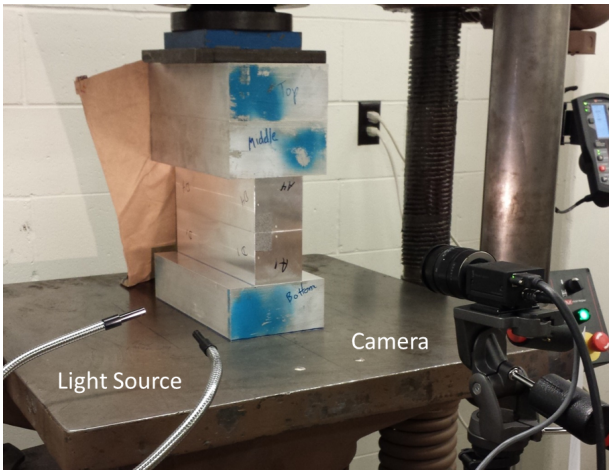

Figure 5.24. Setup of the digital image correlation used for analysis on the CWW. The light source and camera are shown in the image.

Once the setup was complete, images were captured at 1 frame every 2.15 seconds and stored on a computer using FLYCAP2 software. For the two blocks imaged here (Fig. 5.23c), the region of interest was 1120 x 1650 pixels.

The captured images were then analyzed using VIC-2D 2009 software by Correlated Solutions. This program analyzes the captured images and calculates the surface deformations from the images. For a detailed explanation of the analysis see chapter 5 of Ahmad Hedayat's dissertation [219]. The output files were then made into contour plots, after scaling by the proper pixel to length ratio for each run, and the horizontal and vertical displacements were analyzed.

5.6 Experimental Results and Discussion

5.6.1 Introduction

The experiments described above were performed on both the isotropic and anisotropic aluminum samples. The results from the DIC and elastic wave measurements are presented here.

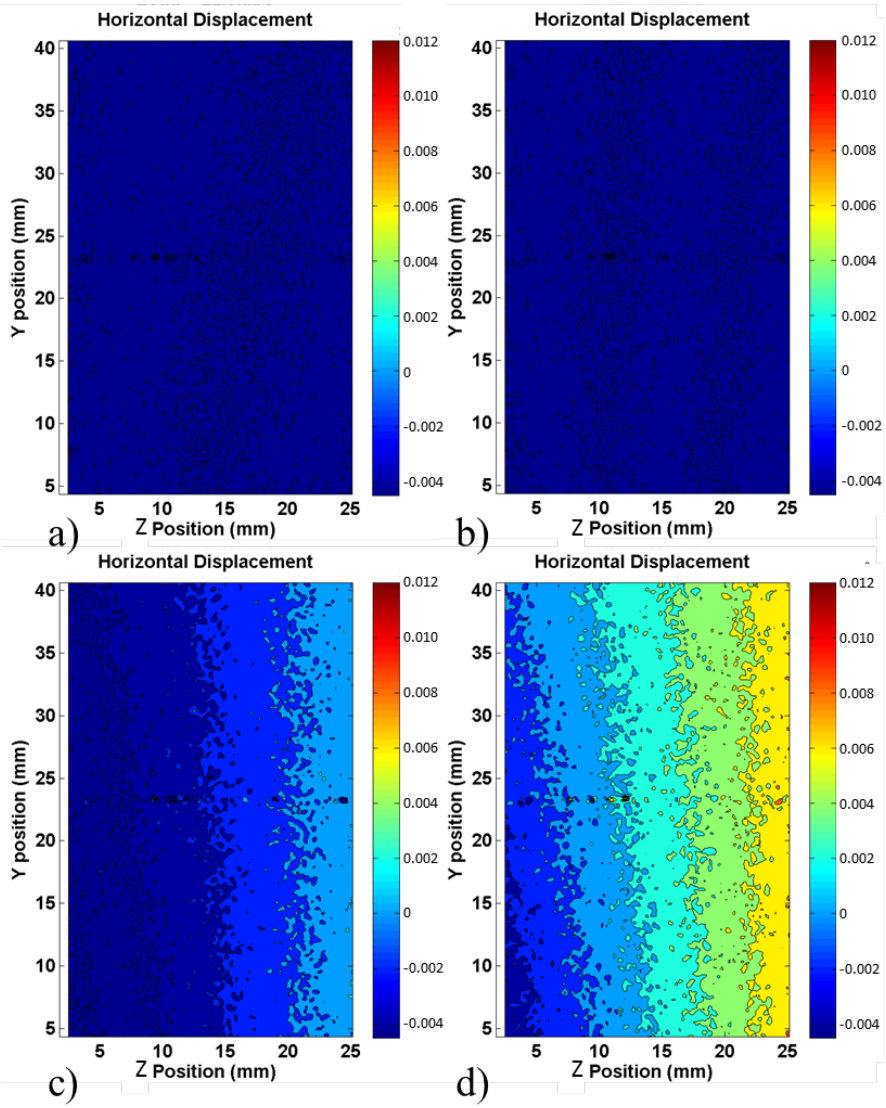

Figure 5.25. DIC results for the horizontal displacement of two aluminum bars under uniaxial loading conditions. Images are viewing the y-z plane (Fig. 5.6) The applied vertical loads were a) 100 kN, b) 200 kN, c) 300 kN, and d) 400 kN. The fracture is located near the Y position of 22.5 mm.

5.6.2 Digital Image Correlation

The horizontal displacements for the 2 block case are shown in Fig. 5.25. The image window shows only the speckled area, with the fracture located near 22.5 mm

on the y axis. As expected, the horizontal displacements are relatively small (note scale bar in Fig. 5.25), i.e., on the order of microns. For the first 200 kN of load, no horizontal displacement is observed in the sample. As the load was increased to 300 and 400 kN (Fig. 5.25c-d) the displacement increased slightly, but remained roughly uniform in both the top and bottom samples. This verifies that there was no build up of shear stress or displacement during the loading cycle due to the unconfined samples.

The vertical displacements for the 2 block analysis are shown in Fig. 5.26. As expected, the vertical displacements are larger, i.e. on the order of mm, because this direction was the direction of loading. As the applied load increased from 100 kN (Fig. 5.26a) up to 400 kN (Fig. 5.26d) the displacements increased but remained uniform throughout the entire region of interest. This demonstrated that, at least at the surface, the loading condition was uniform across and along the fracture plane near the free surface, indicating that there was no build up of stress along the fracture plane or at the tip of the free surface.

5.6.3 Signals and Analysis

The transmitted CWWs obtained as a function of applied load, in isotropic aluminum are show in Fig. 5.27 these plots show each signal offset vertically as a function of load. The signals from the anisotropic sample are shown in Fig. 5.28. At low load (0 kN), the signal arrives faster than the WW but slower than the Rayleigh wave indicating the fracture is only partially closed. As the load is increased (4.44 kN $\rightarrow$ 400 kN), the arrival time of the wave decreases continuously, until it is nearly at the Rayleigh wave velocity (top wave in Figs. 5.27 and 5.28). The same trend is observed in both the isotropic and anisotropic samples, as predicted by the numerical section above for the CWW (section 5.4).

As expected, the transducer polarization plays a significant role in the observed waveforms propagating along the surface fracture. The CWW propagates when the

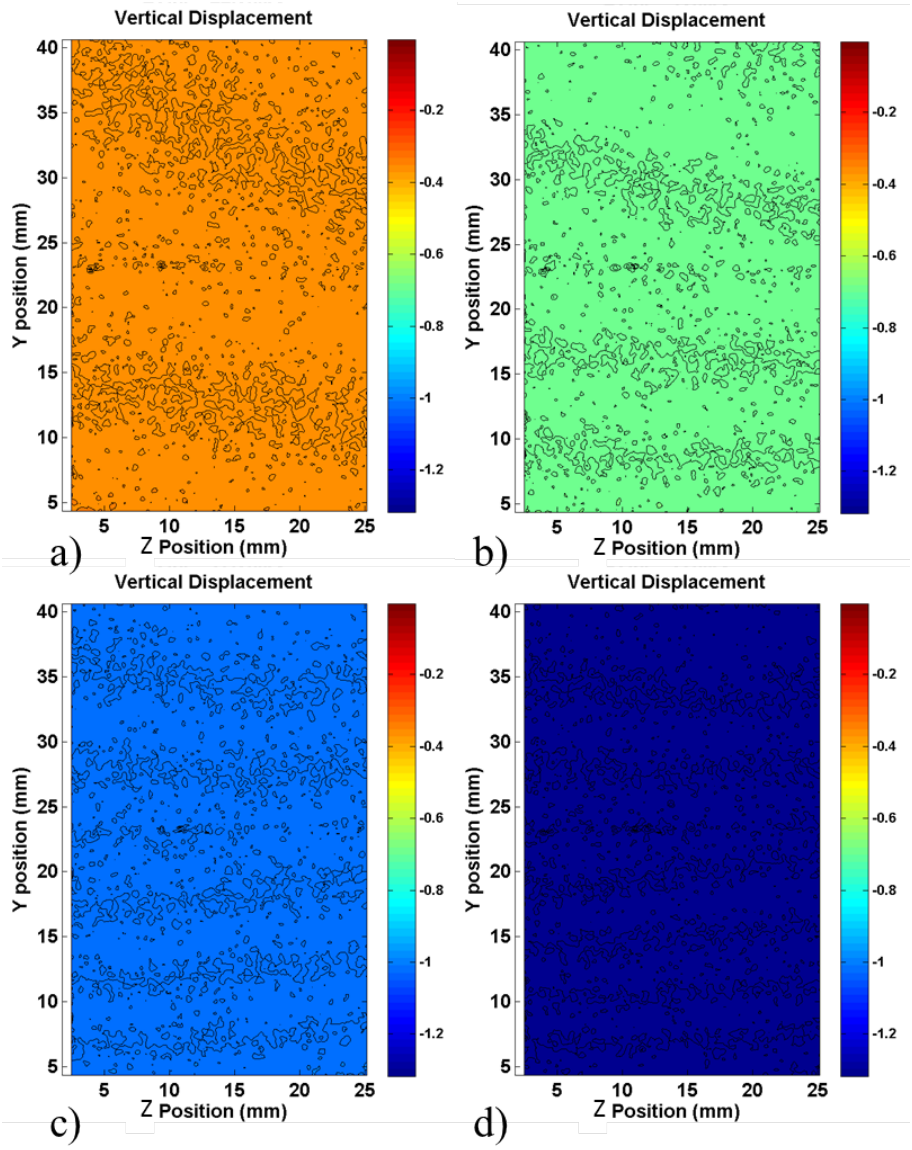

Figure 5.26. DIC results for the vertical displacement of two aluminum bars under uniaxial loading conditions. Images are viewing the y-z plane (Fig. 5.6) The applied vertical loads were a) 100 kN, b) 200 kN, c) 300 kN, and d) 400 kN. The fracture is located near the Y position of 22.5 mm.

S-wave transducer is polarized perpendicular to the free surface ($\theta = 0°$) shown in the insets of Fig. 5.27 or 5.28.

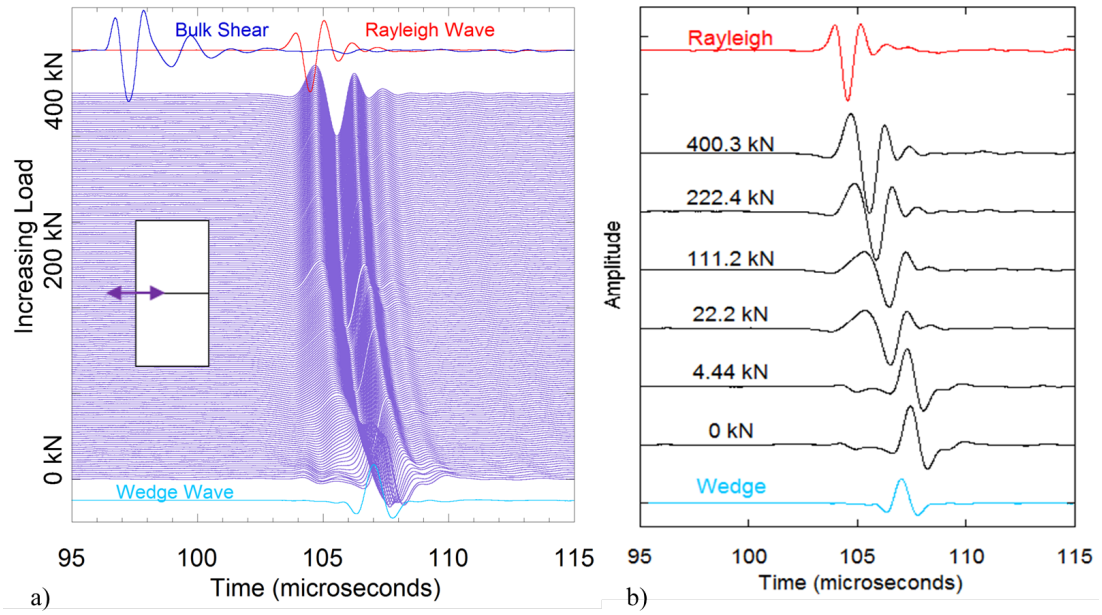

Figure 5.27. Waveforms through the isotropic aluminum cubes as a function of applied load, with the transducer polarized perpendicular to the free surface ($\theta = 0°$ in Fig. 5.6). a) Waveforms stacked to see the effects of increasing normal load, b) selected loads extracted from a. Inset shows transducer polarization.

When the polarization of the transducer is rotated so that the shear wave is parallel to the free surface ($\theta = 90°$), the observed waves exhibit interface wave type behavior. These signals, for both the isotropic and anisotropic samples are shown in Figs. 5.29 and 5.30. The isotropic sample, with the signal parallel ($\theta = 90°$) to the free surface, appear at first glance to be similar to the CWW in Fig. 5.27, but upon further inspection it is observed that the signal is arriving prior to the Rayleigh wave and is approaching the bulk S-wave arrival time. This is due to the types of motion excited by the source transducer polarization. Recall that the WW is excited at a polarization perpendicular to the bisecting line, and Rayleigh waves are excited at the wedge when the polarization is parallel to the bisecting angle (Fig. 3.1). Also, recall that Rayleigh waves are excited by S-wave sources normal to the free surface.

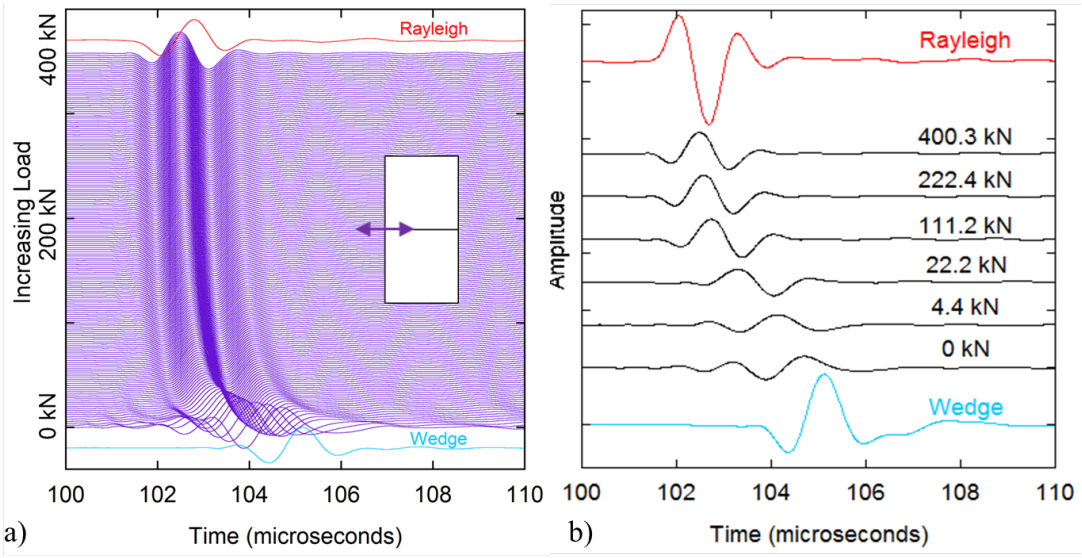

Figure 5.28. Waveforms through the anisotropic aluminum bars as a function of applied load, with the transducer polarized perpendicular to the free surface ($\theta = 0°$ in Fig. 5.6). a) Waveforms stacked to see the effects of increasing normal load, b) selected loads extracted from a. Inset shows transducer polarization.

For the $\theta = 0°$ polarization (Fig. 5.27 inset) the Rayleigh waves at the free surface and WWs are excited, causing the observed CWW. When the polarization is rotated to $\theta = 90°$ (Fig. 5.29 inset) the Rayleigh wave of each fracture is excited. These two Rayleigh waves couple and excite interface waves (section 3.4.2). The observed behavior in Figs. 5.29 and 5.30 is due to this interface wave excitation, due to the source polarization.

The anisotropic signals, for polarizations parallel to the free surface (Fig. 5.30 inset), demonstrate even stronger interface wave behavior. Since these samples are much smaller (Table H.3), the effect of the load is more dramatic than in the isotropic samples, and the observed signals change velocity, approaching the bulk S-wave arrival time. It is interesting to observe that there does appear to be more than one mode excited in the observed signals of Fig. 5.30, but the analysis is beyond the scope of this work.

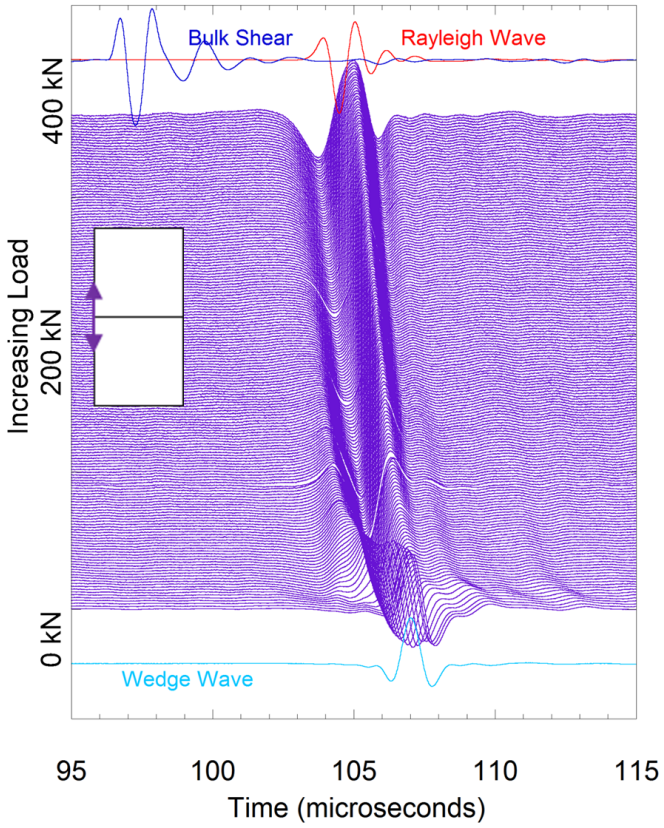

Figure 5.29. Waveforms through the isotropic aluminum cubes, with the transducer polarized parallel to the free surface ($\theta = 90°$ in Fig. 5.6). Note that although the trend appears similar to that for the perpendicular polarization in Fig. 5.27, the wave is actually going past the Rayleigh wave and heading towards the bulk S-wave.

5.6.4 Wavelet Analysis

Wavelet analysis (Appendix E), using a Nolte-Hilbert wavelet [220, 221], was performed on the CWW signals and used to calculate the group velocity at a frequency of 0.3 MHz, the peak frequency in the wavelet. The group velocity as a function of applied load, for both the isotropic and anisotropic samples, is shown in Fig. 5.31. The WW and Rayleigh wave velocity, for both the isotropic and anisotropic aluminum, are also shown in Fig. 5.31 at the same frequency. The error bars represent the range of velocities for all wedges and surfaces that were used in this study. Figure 5.31

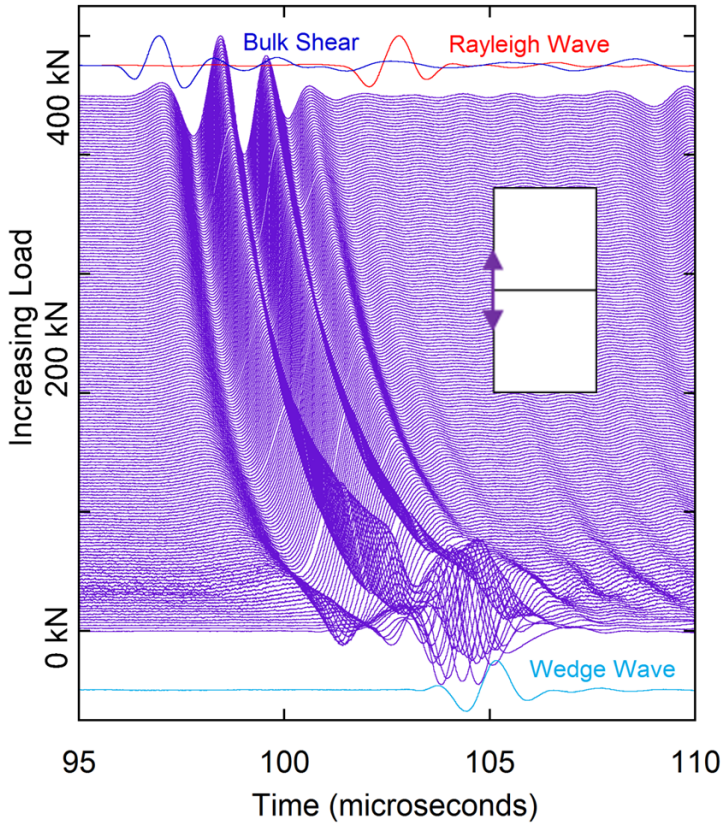

Figure 5.30. Waveforms through the anisotropic aluminum bars for the transducer polarized parallel to the free surface ($\theta = 90°$ shown in the inset). Note that this polarization picks up a wave similar to the interface wave, compared to the CWW observed in Fig. 5.28.

further demonstrates the trend exhibited in the stacked signals of Figs. 5.27-5.28. At low applied loads the CWW propagates near the WW velocity because each block is basically isolated due to a small amount of coupling between the samples. As the load increases, the coupling also increases and the observed signals change velocity until reaching the Rayleigh wave velocity, at which point the fracture has been closed (i.e., welded).

Using the CWW numerical results for mode 1 (see section 5.4), the calculated group velocities of Fig. 5.31 were analyzed to obtain an estimate of κ on the fracture plane, assuming $R = \frac{\kappa_x}{\kappa_y} = 1$. This calculated κ is shown, as a function of the applied load, for both the isotropic and anisotropic samples (Fig. 5.32). As the

coupling between the wedges increased, κ also increased, indicating that the contact area between the surfaces increased. The range of κ values obtained is within the previously observed range for aluminum samples measured using interface waves at high frequency [4]. Demonstrating the CWW's use for remotely estimating the specific stiffness along a surface fracture.

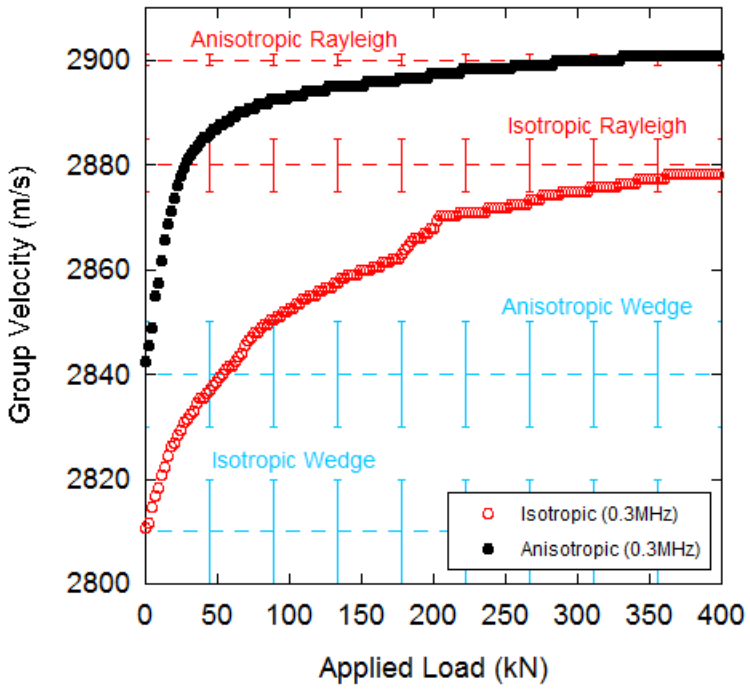

Figure 5.31. Group velocity of the isotropic (open circles) and anisotropic (filled circles) CWW as a function of applied load. All values are taken at 0.3 MHz.

5.7 Summary

The experimental study performed on both isotropic and anisotropic aluminum samples indicated a good agreement with the theoretically derived CWW. The CWW velocity was found to be a function of both frequency and stiffness, (i.e., dispersive) as expected for non-welded contacts. The velocity range of the observed signals was found to be within the theoretically predicted range. At low applied stress, the two

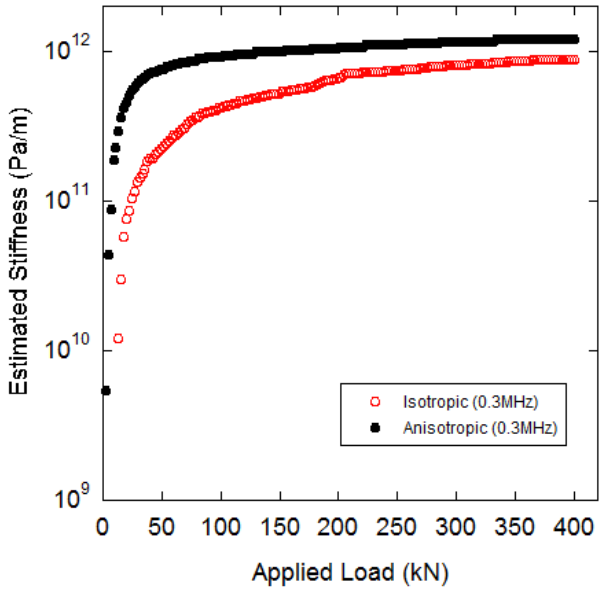

Figure 5.32. Estimated specific stiffness for the isotropic and anisotropic aluminum samples using the group velocity from the wavelet at 0.3 MHz and mode 1 CWW theory.

wedges are not coupled, giving rise to a single WW. As the applied stiffness of the fracture is increased, the two wedges couple and increase the CWW velocity, continuously, until the wedges are completely coupled in a welded interface, propagating at the Rayleigh wave velocity.

In this case, the welded interface gave rise to a Rayleigh wave; however, if the two media are within the range of existence for RS waves, the asymptotic behavior of the CWW velocity approaches that of the RS wave, not the single Rayleigh wave velocity. The experiments discussed in this section verified the existence of CWW when the two media are the same, a case not allowed in RS waves.

Group theory was used to predict the vibrational modes of the CWW, and indicated that two normal modes should exist for the CWW, depending on the material parameters. The theoretical results agreed with the group theory indicating that two modes for the CWW were supported. Mode 1 was found to propagate between the WW and Rayleigh wave velocity, while mode 2 propagated only slightly slower than

the Rayleigh wave velocity and after a relatively small coupling became delocalized. The experimental verification of the CWW determined that mode 1 did exist and exhibited the signatures expected. Mode 2 was not observed, and further work is needed to determine if this mode can be observed and under what conditions.

6. Intersection Waves

6.1 Introduction

This chapter contains the full intersection wave derivation, which is the pinnacle of this work. Similar to the previous two chapters, this chapter introduces the group theory analysis for an intersection under two different symmetry conditions and the results of these derivations. Next, a theoretical derivation is described to simulate waves isolated near the corners of a fracture intersection. The results are discussed and compared to the group theory analysis. Finally, experimental studies of intersection waves propagating along orthogonal fractures under uniaxial and biaxial loading conditions are described and analyzed.

6.2 Group Theory Analysis-Equal Stiffness

The group theory analysis here matches very closely to the format of the group theory analysis for the WW and CWW (chapters 4-5). Some differences, such as the presence of a 2D representation, are discussed, and the necessary theorems and derivations are also described here. Two cases are analyzed because the intersection geometry can have various types of stress conditions and materials. In the first case, the stiffnesses of each fracture are the same. In the second case, the stiffness of the vertical fracture differs from that of the horizontal. However, for each given fracture, the $\kappa_x,\ \kappa_y,\ \kappa_z$ terms are all equal.

The geometry of the problem analyzed in this section is shown in Fig. 6.1. The most symmetric case for an intersection geometry is when the specific stiffness (κ) along each fracture plane is set equal and the media are assumed to have the same

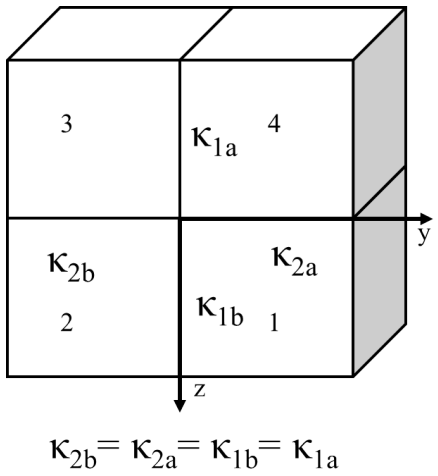

Figure 6.1. Geometry used in the intersection group theory analysis for both fracture planes having equal stiffness. The stiffness label on each fracture is shown.

material properties. The direction of propagation is in the x direction (i.e., into the page in Fig. 6.1).

6.2.1 Step 1: Identify the point group and its symmetry operations

Several symmetry operations are possible on the intersection geometry (Fig. 6.1) that maintain the point $x = y = z = 0$ after the operation is applied. These operations are identity (E), rotation ($C_4,\ C_2,\ C_4^3$), and reflection across mirror planes z-x, y-x, y=z, and y=-z ($\sigma_{v1},\ \sigma_{v2},\ \sigma_{d1},\ \sigma_{d2}$). Together, these operations form the group C_{4v}, which is a finite group, of order 8, and is non-Abelilan. This point group differs from the C_s point group analyzed for the WW and CWW.

6.2.2 Step 2: Specify the coordinate system and basis functions

The coordinate system used in this derivation is the Cartesian coordinate system centered at the fracture intersection with the y axis along the horizontal fracture, the z axis along the vertical fracture, and the x axis along the intersection (Fig.

6.1). Displacement vectors are used as the basis functions, which are located at the tips of each media using the same Cartesian coordinate system but individually represented for each media (i.e., $r_x(1)$, $i = 1, 2, 3, 4$). These basis functions are labeled r_α, $\alpha = x, y, z$. Note that the coordinate system is fixed and not attached to the geometry, i.e. an active view-point is used (Table 4.3).

6.2.3 Step 3: Determine the effects of the symmetry operations on the basis functions

Table 6.1
Action table for the C_{4v} point group.

	E	C_4	C_2	C_4^3	σ_{v1}	σ_{v2}	σ_{d1}	σ_{d2}
$r_x(i)$	$r_x(f)$	$r_x(f)$	$r_x(f)$	$r_x(f)$	$r_x(f)$	$r_x(f)$	$r_x(f)$	$r_x(f)$
$r_y(i)$	$r_y(f)$	$r_z(f)$	$-r_y(f)$	$-r_z(f)$	$-r_y(f)$	$r_y(f)$	$r_z(f)$	$-r_z(f)$
$r_z(i)$	$r_z(f)$	$-r_y(f)$	$-r_z(f)$	$r_y(f)$	$r_z(f)$	$-r_z(f)$	$r_y(f)$	$-r_y(f)$
1	1	2	3	4	2	4	1	3
2	2	3	4	1	1	3	4	2
3	3	4	1	2	4	2	3	1
4	4	1	2	3	3	1	2	4

Consider some vector, $\bar{\mathbf{r}}(1)$, located at the corner ($x = y = z = 0$) of block 1 (Fig. 6.1). After operating on this vector, say with C_4, $\bar{\mathbf{r}}(1)$ is rotated by 90° to block 2. This is written symbolically as

$$\Gamma(C_4) r_x(1) \rightarrow r_x(2), \tag{6.1a}$$

$$\Gamma(C_4) r_y(1) \rightarrow r_z(2), \tag{6.1b}$$

$$\Gamma(C_4) r_z(1) \rightarrow -r_y(2). \tag{6.1c}$$

A similar notation is used to represent rotation at each of the other corners, such that

$$\Gamma(C_4)r_x(i) \rightarrow r_x(f), \tag{6.2a}$$

$$\Gamma(C_4)r_y(i) \rightarrow r_z(f), \tag{6.2b}$$

$$\Gamma(C_4)r_z(i) \rightarrow -r_y(f), \tag{6.2c}$$

where i represents the initial media and f the final media after operating with C_4. Analyzing the effects of the other operators on all four corners leads to the construction of action table 6.1. See section 4.2.3 for details on action tables.

6.2.4 Step 4: Construct a matrix representation for each element using the basis functions

This step is used to determine the matrices that can operate on a set of basis functions to yield the resulting action table. An example of the C_4 operation is shown explicitly. If a vector $[r(i)]$ is defined as

$$[r(i)] = [r_x(1)\ r_y(1)\ r_z(1)\ r_x(2)\ r_y(2)\ r_z(2)\ r_x(3)\ r_y(3)\ r_z(3)\ r_x(4)\ r_y(4)\ r_z(4)]^T, \tag{6.3}$$

where ^{T} means the transpose, the matrix $\Gamma(C_4)$ operates on it to obtain another vector, $[r(f)]$, that has the corresponding result of the action table (Table 6.1). Written explicitly this is expressed as

$$\Gamma(C_4)[r(i)] = [r(f)]. \tag{6.4}$$

This requires that the representation $\Gamma(C_4)$ be a 12 x 12 matrix (4 media, 3 coordinates). Inspection of the action table yields

$$\Gamma(C_4) = \begin{bmatrix} 0 & 0 & 0 & 1 & 0 & 0 & 0 & 0 & 0 & 0 & 0 & 0 \\ 0 & 0 & 0 & 0 & 0 & 1 & 0 & 0 & 0 & 0 & 0 & 0 \\ 0 & 0 & 0 & 0 & -1 & 0 & 0 & 0 & 0 & 0 & 0 & 0 \\ 0 & 0 & 0 & 0 & 0 & 0 & 1 & 0 & 0 & 0 & 0 & 0 \\ 0 & 0 & 0 & 0 & 0 & 0 & 0 & 0 & 1 & 0 & 0 & 0 \\ 0 & 0 & 0 & 0 & 0 & 0 & 0 & -1 & 0 & 0 & 0 & 0 \\ 0 & 0 & 0 & 0 & 0 & 0 & 0 & 0 & 0 & 1 & 0 & 0 \\ 0 & 0 & 0 & 0 & 0 & 0 & 0 & 0 & 0 & 0 & 0 & 1 \\ 0 & 0 & 0 & 0 & 0 & 0 & 0 & 0 & 0 & 0 & -1 & 0 \\ 1 & 0 & 0 & 0 & 0 & 0 & 0 & 0 & 0 & 0 & 0 & 0 \\ 0 & 0 & 1 & 0 & 0 & 0 & 0 & 0 & 0 & 0 & 0 & 0 \\ 0 & -1 & 0 & 0 & 0 & 0 & 0 & 0 & 0 & 0 & 0 & 0 \end{bmatrix}. \tag{6.5}$$

A similar formulation follows for the other operators in the C_{4v} point group. Their matrix representations are

$$\Gamma(E) = \begin{bmatrix} 1 & 0 & 0 & 0 & 0 & 0 & 0 & 0 & 0 & 0 & 0 & 0 \\ 0 & 1 & 0 & 0 & 0 & 0 & 0 & 0 & 0 & 0 & 0 & 0 \\ 0 & 0 & 1 & 0 & 0 & 0 & 0 & 0 & 0 & 0 & 0 & 0 \\ 0 & 0 & 0 & 1 & 0 & 0 & 0 & 0 & 0 & 0 & 0 & 0 \\ 0 & 0 & 0 & 0 & 1 & 0 & 0 & 0 & 0 & 0 & 0 & 0 \\ 0 & 0 & 0 & 0 & 0 & 1 & 0 & 0 & 0 & 0 & 0 & 0 \\ 0 & 0 & 0 & 0 & 0 & 0 & 1 & 0 & 0 & 0 & 0 & 0 \\ 0 & 0 & 0 & 0 & 0 & 0 & 0 & 1 & 0 & 0 & 0 & 0 \\ 0 & 0 & 0 & 0 & 0 & 0 & 0 & 0 & 1 & 0 & 0 & 0 \\ 0 & 0 & 0 & 0 & 0 & 0 & 0 & 0 & 0 & 1 & 0 & 0 \\ 0 & 0 & 0 & 0 & 0 & 0 & 0 & 0 & 0 & 0 & 1 & 0 \\ 0 & 0 & 0 & 0 & 0 & 0 & 0 & 0 & 0 & 0 & 0 & 1 \end{bmatrix}, \tag{6.6}$$

$$\Gamma(C_4^3) = \begin{bmatrix} 0 & 0 & 0 & 0 & 0 & 0 & 0 & 0 & 0 & 1 & 0 & 0 \\ 0 & 0 & 0 & 0 & 0 & 0 & 0 & 0 & 0 & 0 & 0 & -1 \\ 0 & 0 & 0 & 0 & 0 & 0 & 0 & 0 & 0 & 0 & 1 & 0 \\ 1 & 0 & 0 & 0 & 0 & 0 & 0 & 0 & 0 & 0 & 0 & 0 \\ 0 & 0 & -1 & 0 & 0 & 0 & 0 & 0 & 0 & 0 & 0 & 0 \\ 0 & 1 & 0 & 0 & 0 & 0 & 0 & 0 & 0 & 0 & 0 & 0 \\ 0 & 0 & 0 & 1 & 0 & 0 & 0 & 0 & 0 & 0 & 0 & 0 \\ 0 & 0 & 0 & 0 & 0 & -1 & 0 & 0 & 0 & 0 & 0 & 0 \\ 0 & 0 & 0 & 0 & 1 & 0 & 0 & 0 & 0 & 0 & 0 & 0 \\ 0 & 0 & 0 & 0 & 0 & 0 & 1 & 0 & 0 & 0 & 0 & 0 \\ 0 & 0 & 0 & 0 & 0 & 0 & 0 & 0 & -1 & 0 & 0 & 0 \\ 0 & 0 & 0 & 0 & 0 & 0 & 0 & 1 & 0 & 0 & 0 & 0 \end{bmatrix}, \tag{6.7}$$

$$\Gamma(C_2) = \begin{bmatrix} 0 & 0 & 0 & 0 & 0 & 0 & 1 & 0 & 0 & 0 & 0 & 0 \\ 0 & 0 & 0 & 0 & 0 & 0 & 0 & -1 & 0 & 0 & 0 & 0 \\ 0 & 0 & 0 & 0 & 0 & 0 & 0 & 0 & -1 & 0 & 0 & 0 \\ 0 & 0 & 0 & 0 & 0 & 0 & 0 & 0 & 0 & 1 & 0 & 0 \\ 0 & 0 & 0 & 0 & 0 & 0 & 0 & 0 & 0 & 0 & -1 & 0 \\ 0 & 0 & 0 & 0 & 0 & 0 & 0 & 0 & 0 & 0 & 0 & -1 \\ 1 & 0 & 0 & 0 & 0 & 0 & 0 & 0 & 0 & 0 & 0 & 0 \\ 0 & -1 & 0 & 0 & 0 & 0 & 0 & 0 & 0 & 0 & 0 & 0 \\ 0 & 0 & -1 & 0 & 0 & 0 & 0 & 0 & 0 & 0 & 0 & 0 \\ 0 & 0 & 0 & 1 & 0 & 0 & 0 & 0 & 0 & 0 & 0 & 0 \\ 0 & 0 & 0 & 0 & -1 & 0 & 0 & 0 & 0 & 0 & 0 & 0 \\ 0 & 0 & 0 & 0 & 0 & -1 & 0 & 0 & 0 & 0 & 0 & 0 \end{bmatrix}, \tag{6.8}$$

$$\Gamma(\sigma_{d1}) = \begin{bmatrix} 1 & 0 & 0 & 0 & 0 & 0 & 0 & 0 & 0 & 0 & 0 & 0 \\ 0 & 0 & 1 & 0 & 0 & 0 & 0 & 0 & 0 & 0 & 0 & 0 \\ 0 & 1 & 0 & 0 & 0 & 0 & 0 & 0 & 0 & 0 & 0 & 0 \\ 0 & 0 & 0 & 0 & 0 & 0 & 0 & 0 & 0 & 1 & 0 & 0 \\ 0 & 0 & 0 & 0 & 0 & 0 & 0 & 0 & 0 & 0 & 0 & 1 \\ 0 & 0 & 0 & 0 & 0 & 0 & 0 & 0 & 0 & 0 & 1 & 0 \\ 0 & 0 & 0 & 0 & 0 & 0 & 1 & 0 & 0 & 0 & 0 & 0 \\ 0 & 0 & 0 & 0 & 0 & 0 & 0 & 0 & 1 & 0 & 0 & 0 \\ 0 & 0 & 0 & 0 & 0 & 0 & 0 & 1 & 0 & 0 & 0 & 0 \\ 0 & 0 & 0 & 1 & 0 & 0 & 0 & 0 & 0 & 0 & 0 & 0 \\ 0 & 0 & 0 & 0 & 0 & 1 & 0 & 0 & 0 & 0 & 0 & 0 \\ 0 & 0 & 0 & 0 & 1 & 0 & 0 & 0 & 0 & 0 & 0 & 0 \end{bmatrix}, \tag{6.9}$$

$$\Gamma(\sigma_{d2}) = \begin{bmatrix} 0 & 0 & 0 & 0 & 0 & 0 & 1 & 0 & 0 & 0 & 0 & 0 \\ 0 & 0 & 0 & 0 & 0 & 0 & 0 & 0 & -1 & 0 & 0 & 0 \\ 0 & 0 & 0 & 0 & 0 & 0 & 0 & -1 & 0 & 0 & 0 & 0 \\ 0 & 0 & 0 & 1 & 0 & 0 & 0 & 0 & 0 & 0 & 0 & 0 \\ 0 & 0 & 0 & 0 & 0 & -1 & 0 & 0 & 0 & 0 & 0 & 0 \\ 0 & 0 & 0 & 0 & -1 & 0 & 0 & 0 & 0 & 0 & 0 & 0 \\ 1 & 0 & 0 & 0 & 0 & 0 & 0 & 0 & 0 & 0 & 0 & 0 \\ 0 & 0 & -1 & 0 & 0 & 0 & 0 & 0 & 0 & 0 & 0 & 0 \\ 0 & -1 & 0 & 0 & 0 & 0 & 0 & 0 & 0 & 0 & 0 & 0 \\ 0 & 0 & 0 & 0 & 0 & 0 & 0 & 0 & 0 & 1 & 0 & 0 \\ 0 & 0 & 0 & 0 & 0 & 0 & 0 & 0 & 0 & 0 & 0 & -1 \\ 0 & 0 & 0 & 0 & 0 & 0 & 0 & 0 & 0 & 0 & -1 & 0 \end{bmatrix}, \tag{6.10}$$

$$\Gamma(\sigma_{v1}) = \begin{bmatrix} 0 & 0 & 0 & 1 & 0 & 0 & 0 & 0 & 0 & 0 & 0 & 0 \\ 0 & 0 & 0 & 0 & -1 & 0 & 0 & 0 & 0 & 0 & 0 & 0 \\ 0 & 0 & 0 & 0 & 0 & 1 & 0 & 0 & 0 & 0 & 0 & 0 \\ 1 & 0 & 0 & 0 & 0 & 0 & 0 & 0 & 0 & 0 & 0 & 0 \\ 0 & -1 & 0 & 0 & 0 & 0 & 0 & 0 & 0 & 0 & 0 & 0 \\ 0 & 0 & 1 & 0 & 0 & 0 & 0 & 0 & 0 & 0 & 0 & 0 \\ 0 & 0 & 0 & 0 & 0 & 0 & 0 & 0 & 0 & 1 & 0 & 0 \\ 0 & 0 & 0 & 0 & 0 & 0 & 0 & 0 & 0 & 0 & -1 & 0 \\ 0 & 0 & 0 & 0 & 0 & 0 & 0 & 0 & 0 & 0 & 0 & 1 \\ 0 & 0 & 0 & 0 & 0 & 0 & 1 & 0 & 0 & 0 & 0 & 0 \\ 0 & 0 & 0 & 0 & 0 & 0 & 0 & -1 & 0 & 0 & 0 & 0 \\ 0 & 0 & 0 & 0 & 0 & 0 & 0 & 0 & 1 & 0 & 0 & 0 \end{bmatrix}, \tag{6.11}$$

and

$$\Gamma(\sigma_{v2}) = \begin{bmatrix} 0 & 0 & 0 & 0 & 0 & 0 & 0 & 0 & 0 & 1 & 0 & 0 \\ 0 & 0 & 0 & 0 & 0 & 0 & 0 & 0 & 0 & 0 & 1 & 0 \\ 0 & 0 & 0 & 0 & 0 & 0 & 0 & 0 & 0 & 0 & 0 & -1 \\ 0 & 0 & 0 & 0 & 0 & 0 & 1 & 0 & 0 & 0 & 0 & 0 \\ 0 & 0 & 0 & 0 & 0 & 0 & 0 & 1 & 0 & 0 & 0 & 0 \\ 0 & 0 & 0 & 0 & 0 & 0 & 0 & 0 & -1 & 0 & 0 & 0 \\ 0 & 0 & 0 & 1 & 0 & 0 & 0 & 0 & 0 & 0 & 0 & 0 \\ 0 & 0 & 0 & 0 & 1 & 0 & 0 & 0 & 0 & 0 & 0 & 0 \\ 0 & 0 & 0 & 0 & 0 & -1 & 0 & 0 & 0 & 0 & 0 & 0 \\ 1 & 0 & 0 & 0 & 0 & 0 & 0 & 0 & 0 & 0 & 0 & 0 \\ 0 & 1 & 0 & 0 & 0 & 0 & 0 & 0 & 0 & 0 & 0 & 0 \\ 0 & 0 & -1 & 0 & 0 & 0 & 0 & 0 & 0 & 0 & 0 & 0 \end{bmatrix}. \tag{6.12}$$

6.2.5 Step 5: Determine the number and type of irreducible representations

The classes of C_{4v} are determined prior to the irreducible representations (IRs). The inverses of the operators in this group are examined to determine the classes. The inverses are

$$\begin{aligned} &E^{-1} = E,\ C_4^{-1} = C_4^3,\ C_2^{-1} = C_2,\ (C_4^3)^{-1} = C_4, \\ &\sigma_{v1}^{-1} = \sigma_{v1},\ \sigma_{v2}^{-1} = \sigma_{v2},\ \sigma_{d1}^{-1} = \sigma_{d1},\ \sigma_{d2}^{-1} = \sigma_{d2}. \end{aligned} \tag{6.13}$$

As mentioned in chapter 4 (step 5) the classes are determined by applying the products $O_i A O_i^{-1}$, where A is the operator to determine the class of, and O_i is all of the other operators in this group (i.e., $O_i \in C_{4v}$). For the C_4 operator this is explicitly expressed as

$$\begin{aligned} &EC_4E^{-1} = C_4,\ C_4C_4C_4^{-1} = C_4,\ C_2C_4C_2^{-1} = C_4,\ C_4^3C_4(C_4^3)^{-1} = C_4, \\ &\sigma_{v1}C_4\sigma_{v1}^{-1} = C_4^3,\ \sigma_{v2}C_4\sigma_{v2}^{-1} = C_4^3,\ \sigma_{d1}C_4\sigma_{d1}^{-1} = C_4^3,\ \sigma_{d2}C_4\sigma_{d2}^{-1} = C_4^3. \end{aligned} \tag{6.14}$$

Eqn. 6.14 indicates that the operators C_4 and C_4^3 form a class. Recall that the notation used to define a class of operators is $\{C_4, C_4^3\}$. Repeating this process for the other operators leads to the following classes: $\{E\}$, $\{C_4, C_4^3\}$, $\{C_2\}$, $\{\sigma_{v1}, \sigma_{v2}\}$, and $\{\sigma_{d1}, \sigma_{d2}\}$. These form the character table 6.2 [140].

It is interesting to note from the action table (Table 6.1) that the y and z components either transform into themselves (i.e., $z \to \pm z$, $y \to \pm y$) or each other (i.e., $z \to \pm y$, $y \to \pm z$), but the x component only transforms into itself (i.e., $x \to \pm x$). This indicates that the symmetry functions are independent, and that the operations are carried out separately for x and y-z.

The dimensionality of each IR is determined from the dimensionality of class $\{E\}$ in the character table (Table 6.2). Thus, IRs A_1, A_2, B_1, and B_2 are all 1-D and ε is 2-D (see second column of Table 6.2). From theorem 4.2.3 the sum of the

Table 6.2
Character table for the C_{4v} point group.

$\mathbf{C_{4v}}$	$\mathbf{E}$	$\mathbf{2C_4}$	$\mathbf{C_2}$	$\mathbf{2\sigma_{d1}}$	$\mathbf{2\sigma_{v1}}$
A_1	1	1	1	1	1
A_2	1	1	1	-1	-1
B_1	1	-1	1	1	-1
B_2	1	-1	1	-1	1
ε	2	0	-2	0	0
Γ^x	4	0	0	2	0
Γ^{yz}	8	0	0	0	0

squares of these dimensions is equal to the number of elements in the group, 8 (i.e., $1^2 + 1^2 + 1^2 + 1^2 + 2^2 = 8$).

For an intersection, with equal stiffness on both fractures, the number of times the IR occurs along the diagonal blocks of $\Gamma'(O_i)$ (Eqn. 4.8), is expressed as

$$n^\alpha = \frac{1}{h}\left[1(\chi^*_E\chi^\alpha_E) + 2\left(\chi^*_{C_4}\chi^\alpha_{C_4}\right) + 1(\chi^*_{C_2}\chi^\alpha_{C_2}) + 2\left(\chi^*_{\sigma_{d1}}\chi^\alpha_{\sigma_{d1}}\right) + 2\left(\chi^*_{\sigma_{v1}}\chi^\alpha_{\sigma_{v1}}\right)\right], \quad (6.15)$$

where the coefficients, 1 and 2, represent how many operators are in each class. The results for the intersection in the y - z directions are

$$n^{A_1}_{yz} = \frac{1}{8}\left[8(1) + 2(0)(1) + (0)(1) + 2(0)(1) + 2(0)(1)\right] = 1, \quad (6.16a)$$

$$n^{A_2}_{yz} = \frac{1}{8}\left[8(1) + 2(0)(1) + (0)(1) + 2(0)(-1) + 2(0)(-1)\right] = 1, \quad (6.16b)$$

$$n^{B_1}_{yz} = \frac{1}{8}\left[8(1) + 2(0)(-1) + (0)(1) + 2(0)(1) + 2(0)(-1)\right] = 1, \quad (6.16c)$$

$$n^{B_2}_{yz} = \frac{1}{8}\left[8(1) + 2(0)(-1) + (0)(1) + 2(0)(-1) + 2(0)(1)\right] = 1, \quad (6.16d)$$

$$n^{\varepsilon}_{yz} = \frac{1}{8}\left[8(2) + 2(0)(0) + (0)(-2) + 2(0)(-1) + 2(0)(0)\right] = 2, \quad (6.16e)$$

and in the x direction

$$n_x^{A_1} = \frac{1}{8}\left[4(1) + 2(0)(1) + (0)(1) + 2(2)(1) + 2(0)(1)\right] = 1, \tag{6.17a}$$

$$n_x^{A_2} = \frac{1}{8}\left[4(1) + 2(0)(1) + (0)(1) + 2(2)(-1) + 2(0)(-1)\right] = 0, \tag{6.17b}$$

$$n_x^{B_1} = \frac{1}{8}\left[4(1) + 2(0)(-1) + (0)(1) + 2(2)(1) + 2(0)(-1)\right] = 1, \tag{6.17c}$$

$$n_x^{B_2} = \frac{1}{8}\left[4(1) + 2(0)(-1) + (0)(1) + 2(2)(-1) + 2(0)(1)\right] = 0, \tag{6.17d}$$

$$n_x^{\varepsilon} = \frac{1}{8}\left[4(2) + 2(0)(0) + (0)(-2) + 2(2)(0) + 2(0)(0)\right] = 1. \tag{6.17e}$$

6.2.6 Step 6: Analyze the information in the decomposition

Using the n^{α} terms (Eqns. 6.16 and 6.17), the decomposition of Γ into IRs for the y-z direction is represented as

$$\Gamma^{yz} = \Gamma^{A_1} + \Gamma^{A_2} + \Gamma^{B_1} + \Gamma^{B_2} + 2\Gamma^{\varepsilon}, \tag{6.18}$$

and in the x direction

$$\Gamma^{x} = \Gamma^{A_1} + \Gamma^{B_1} + \Gamma^{\varepsilon}. \tag{6.19}$$

From Eqn. 6.18 there are 8 degrees of freedom (dof) in the y-z direction (4(1-D)+2(2-D)=8) and 4 dof in the x direction (2(1-D)+1(2-D)=4).

6.2.7 Step 7: Generate the symmetry functions

It should be noted that up to this point the entire analysis could have been carried out using 2-D coordinates (i.e., only the y-z plane) without any loss of generality because the third dimension, x, does not mix with the other two, $y - z$. To see this, examine the matrix elements of Eqns. 6.5-6.12, noting that the x coordinate does not have any y or z terms, but that the y and z terms have components of each other.

However, the use of the x coordinate does provide some insight into the motion at the tips using a full 3-D coordinate analysis. Since the x dimension does not mix with the other two (i.e., y and z), to get a full 3-D analysis of how the symmetry coordinates transform, two arbitrary vectors ($\bar{\mathbf{V}}$ in theorem 4.2.5) must be used. These vectors must contain at least one component in the x direction and one component in the y or z direction. The two $\bar{\mathbf{V}}$ vectors are chosen as

$$\bar{\mathbf{V}}_x = [1\ 0\ 0\ 0\ 0\ 0\ 0\ 0\ 0\ 0\ 0\ 0]^T, \tag{6.20}$$

and

$$\bar{\mathbf{V}}_y = [0\ 1\ 0\ 0\ 0\ 0\ 0\ 0\ 0\ 0\ 0\ 0]^T, \tag{6.21}$$

and used in theorem 4.2.5.

The symmetry coordinates that transforms the 1-D IRs are expressed, using theorem 4.2.5, as

$$\bar{\mathbf{V}}^{\mathbf{A_1}} \propto \left[\Gamma(E) + \Gamma(C_4) + \Gamma(C_4^3) + \Gamma(C_2) + \Gamma(\sigma_{v1}) + \Gamma(\sigma_{v2}) + \Gamma(\sigma_{d1}) + \Gamma(\sigma_{d2})\right] \bar{\mathbf{V}}, \tag{6.22a}$$

$$\bar{\mathbf{V}}^{\mathbf{A_2}} \propto \left[\Gamma(E) + \Gamma(C_4) + \Gamma(C_4^3) + \Gamma(C_2) - \Gamma(\sigma_{v1}) - \Gamma(\sigma_{v2}) - \Gamma(\sigma_{d1}) - \Gamma(\sigma_{d2})\right] \bar{\mathbf{V}}, \tag{6.22b}$$

$$\bar{\mathbf{V}}^{\mathbf{B_1}} \propto \left[\Gamma(E) - \Gamma(C_4) - \Gamma(C_4^3) + \Gamma(C_2) - \Gamma(\sigma_{v1}) - \Gamma(\sigma_{v2}) + \Gamma(\sigma_{d1}) + \Gamma(\sigma_{d2})\right] \bar{\mathbf{V}}, \tag{6.22c}$$

$$\bar{\mathbf{V}}^{\mathbf{B_2}} \propto \left[\Gamma(E) - \Gamma(C_4) - \Gamma(C_4^3) + \Gamma(C_2) + \Gamma(\sigma_{v1}) + \Gamma(\sigma_{v2}) - \Gamma(\sigma_{d1}) - \Gamma(\sigma_{d2})\right] \bar{\mathbf{V}}. \tag{6.22d}$$

Using Eqns. 6.20- 6.22, together with the results from Eqns. 6.5-6.12, the normalized displacements for each IR are

$$\bar{\mathbf{V}}_x^{A_1} = \frac{1}{2}\left[\begin{array}{cccccccccccc} 1 & 0 & 0 & 1 & 0 & 0 & 1 & 0 & 0 & 1 & 0 & 0 \end{array}\right]^T, \tag{6.23a}$$

$$\bar{\mathbf{V}}_y^{A_1} = \frac{1}{\sqrt{8}} \begin{bmatrix} 0 & 1 & 1 & 0 & -1 & 1 & 0 & -1 & -1 & 0 & 1 & -1 \end{bmatrix}^T, \tag{6.23b}$$

$$\bar{\mathbf{V}}_x^{A_2} = \begin{bmatrix} 0 & 0 & 0 & 0 & 0 & 0 & 0 & 0 & 0 & 0 & 0 & 0 \end{bmatrix}^T, \tag{6.24a}$$

$$\bar{\mathbf{V}}_y^{A_2} = \frac{1}{\sqrt{8}} \begin{bmatrix} 0 & 1 & -1 & 0 & 1 & 1 & 0 & -1 & 1 & 0 & -1 & -1 \end{bmatrix}^T, \tag{6.24b}$$

$$\bar{\mathbf{V}}_x^{B_1} = \frac{1}{2} \begin{bmatrix} 1 & 0 & 0 & -1 & 0 & 0 & 1 & 0 & 0 & -1 & 0 & 0 \end{bmatrix}^T, \tag{6.25a}$$

$$\bar{\mathbf{V}}_y^{B_1} = \frac{1}{\sqrt{8}} \begin{bmatrix} 0 & 1 & 1 & 0 & 1 & -1 & 0 & -1 & -1 & 0 & -1 & 1 \end{bmatrix}^T, \tag{6.25b}$$

and

$$\bar{\mathbf{V}}_x^{B_2} = \begin{bmatrix} 0 & 0 & 0 & 0 & 0 & 0 & 0 & 0 & 0 & 0 & 0 & 0 \end{bmatrix}^T, \tag{6.26a}$$

$$\bar{\mathbf{V}}_y^{B_2} = \frac{1}{\sqrt{8}} \begin{bmatrix} 0 & 1 & -1 & 0 & -1 & -1 & 0 & -1 & 1 & 0 & 1 & 1 \end{bmatrix}^T, \tag{6.26b}$$

where ^{T} represents the transpose of the matrix.

The symmetry functions in Eqns. 6.23-6.26 are used to visualize the normalized vectors of motion at the tips of the four media, shown in Fig. 6.2. The top and bottom rows of Fig. 6.2 are views of the x-y plane and are used to show the x-component of the motion, which is independent from the y and z components. It is interesting that the A_2 and B_1 modes exhibit no x component of motion in any of the media.

The central images in Fig. 6.2 view the y-z plane, which are used for the remainder of this work. The A_1 and B_2 modes indicate the presence of breathing modes isolated near the tips of the media. These breathing modes (see section 4.3.2) only exist for negative Poisson's ratio materials in a single wedge but are now predicted to exist in the same media as the wagging modes. The wagging modes (A_2 and B_1) are also predicted to be localized to the tips of the media, but available for the same material parameters as the breathing modes.

The 2 dimensional representation (ε) is slightly more complicated to analyze. The results of the action table (Table 6.1) are expressed as matrices for the basis functions ($r_y,\ r_z$) as

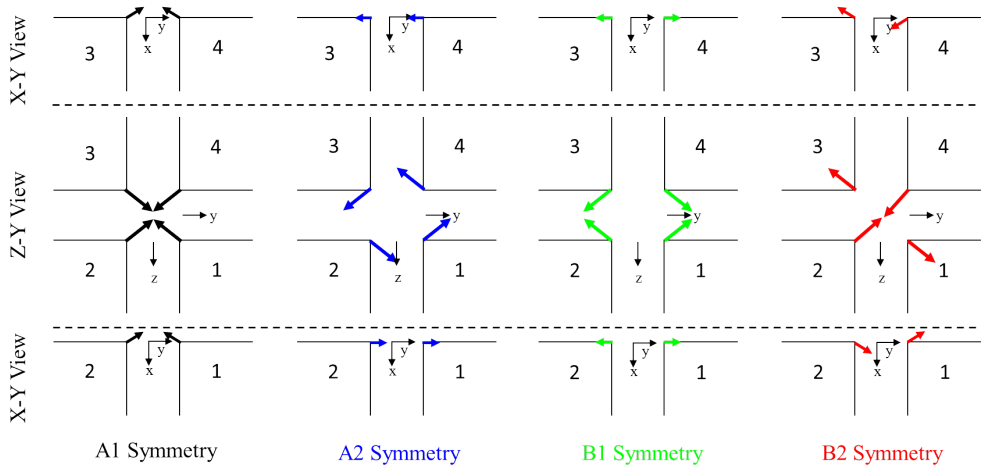

Figure 6.2. Predicted vibrational modes of the four 1D modes of the intersection with equal stiffness (Fig. 6.1). Motion at the tips is based on Eqns. 6.23-6.26. The top and bottom rows view the x-y plane, the middle row views the y-z plane.

$$\Gamma^{\varepsilon}(E) = \begin{bmatrix} 1 & 0 \\ 0 & 1 \end{bmatrix}, \tag{6.27}$$

$$\Gamma^{\varepsilon}(C_2) = \begin{bmatrix} -1 & 0 \\ 0 & -1 \end{bmatrix}, \tag{6.28}$$

$$\Gamma^{\varepsilon}(C_4) = \begin{bmatrix} 0 & -1 \\ 1 & 0 \end{bmatrix}, \tag{6.29}$$

$$\Gamma^{\varepsilon}(C_4^3) = \begin{bmatrix} 0 & 1 \\ -1 & 0 \end{bmatrix}, \tag{6.30}$$

$$\Gamma^{\varepsilon}(\sigma_{v1}) = \begin{bmatrix} -1 & 0 \\ 0 & 1 \end{bmatrix}, \tag{6.31}$$

$$\Gamma^{\varepsilon}(\sigma_{v2}) = \begin{bmatrix} 1 & 0 \\ 0 & -1 \end{bmatrix}, \tag{6.32}$$

$$\Gamma^{\varepsilon}(\sigma_{d1}) = \begin{bmatrix} 0 & 1 \\ 1 & 0 \end{bmatrix}, \tag{6.33}$$

and

$$\Gamma^{\varepsilon}(\sigma_{d2}) = \begin{bmatrix} 0 & -1 \\ -1 & 0 \end{bmatrix}. \tag{6.34}$$

The above notation represents the effect of these operators on the basis functions for the ε IR. As an example $\Gamma^{\varepsilon}(C_4)r_y \to r_z$, and $\Gamma^{\varepsilon}(C_4)r_z \to -r_y$, which is the matrix form of the results in the action table (Table 6.1).

There are two symmetry functions for this IR, differentiated by the labels row-1 and row-2 symmetry functions. Using the diagonal elements of the above matrices (Eqns. 6.27 -6.34) to indicate the $\Gamma^{\alpha}_{mm}(O_k)$ terms in theorem 4.2.5, the results for row-1 are

$$V_1^{\varepsilon} \propto \left[\Gamma(E) - \Gamma(C_2) - \Gamma(\sigma_{v1}) + \Gamma(\sigma_{v2})\right] \bar{\mathbf{V}}, \tag{6.35}$$

and for row-2

$$V_2^{\varepsilon} \propto \left[\Gamma(E) - \Gamma(C_2) + \Gamma(\sigma_{v1}) - \Gamma(\sigma_{v2})\right] \bar{\mathbf{V}}. \tag{6.36}$$

Note that $C_4,\ C_4^3,\ \sigma_{d1}$, and σ_{d2} have zeros on the diagonal in Eqns. 6.27-6.34 so no terms appear in Eqns. 6.35-6.36.

For the row-1 symmetry functions (Eqn. 6.35) and the above results (Eqns. 6.5-6.12) the x, y, and z components are all unique, and necessary to fulfill the required dof (step 6 above) resulting in

$$\bar{\mathbf{V}}^{\varepsilon}_{1x} = \frac{1}{2}\begin{bmatrix} 1 & 0 & 0 & -1 & 0 & 0 & -1 & 0 & 0 & 1 & 0 & 0 \end{bmatrix}^T, \tag{6.37a}$$

$$\bar{\mathbf{V}}^{\varepsilon}_{1y} = \frac{1}{2}\begin{bmatrix} 0 & 1 & 0 & 0 & 1 & 0 & 0 & 1 & 0 & 0 & 1 & 0 \end{bmatrix}^T, \tag{6.37b}$$

$$\bar{\mathbf{V}}^{\varepsilon}_{1z} = \frac{1}{2}\begin{bmatrix} 0 & 0 & 1 & 0 & 0 & -1 & 0 & 0 & 1 & 0 & 0 & -1 \end{bmatrix}^T. \tag{6.37c}$$

Similarly, the row-2 symmetry function (Eqn. 6.35) yields

$$\bar{\mathbf{V}}^{\varepsilon}_{2x} = \frac{1}{2}\begin{bmatrix} 1 & 0 & 0 & 1 & 0 & 0 & -1 & 0 & 0 & -1 & 0 & 0 \end{bmatrix}^T, \tag{6.38a}$$

$$\bar{\mathbf{V}}^{\varepsilon}_{2y} = \frac{1}{2}\begin{bmatrix} 0 & 1 & 0 & 0 & -1 & 0 & 0 & 1 & 0 & 0 & -1 & 0 \end{bmatrix}^T, \tag{6.38b}$$

$$\bar{\mathbf{V}}^{\varepsilon}_{2z} = \frac{1}{2}\begin{bmatrix} 0 & 0 & 1 & 0 & 0 & 1 & 0 & 0 & 1 & 0 & 0 & 1 \end{bmatrix}^T. \tag{6.38c}$$

Visualizations of these symmetry functions are given in Figs. 6.3 and 6.4. The y-components of the row-1 symmetry functions (Fig. 6.3b) and z components of the row-2 symmetry functions (Fig. 6.4c) are translation. For all other modes, the media maintains a constant center of motion. Note that the symbols for the x-components in these figures represent into (X) and out of (o) the page .

It should be mentioned that there is a degeneracy between the two x components (Figs. 6.3a and 6.4a) because one is obtained from the other by means of the operators in the group (theorem 6.2.1). For example, the row-2 x component is obtained from the row-1 x component with the application of the C_4 operator, or the opposite using the C_4^3 operator. The same is true between the row-1 z (Fig. 6.3c) and row-2 y components (Fig. 6.4b).

Theorem 6.2.1 *Let $\mathcal{H}$ be a Hermitian matrix that commutes with the elements of the group. If $\bar{\mathbf{V}}^{\lambda}$ is an eigenvector of $\mathcal{H}$ with eigenvalue λ, then $O_i\bar{\mathbf{V}}^{\lambda}$ is also an*

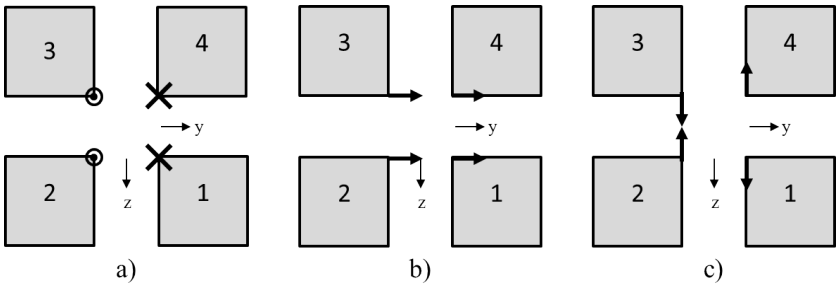

Figure 6.3. Visualization of the row-1 symmetry functions for the ε IR used in the intersection wave geometry with equal stiffness on each fracture plane (Fig. 6.1). The a) x-components, b) y-components, and c) z-components.

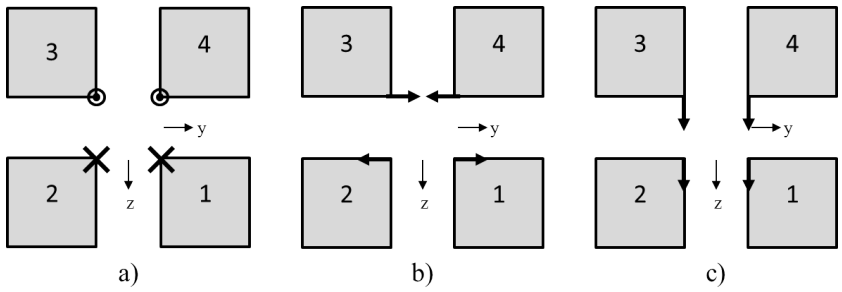

Figure 6.4. Visualization of the row-2 symmetry functions for the ε IR used in the intersection wave geometry with equal stiffness on each fracture plane (Fig. 6.1). The a) x-components, b) y-components, and c) z-components.

eigenvector with eigenvalue λ, where O_i is any element of the group (i.e., $O_i \in G$) [140].

6.3 Group Theory Analysis-Unequal Stiffness

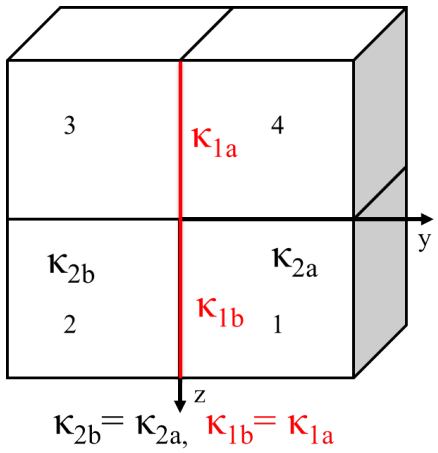

Figure 6.5. Geometry used for the intersection group theory analysis for fracture planes having unequal stiffness.

Similar to the derivation for the equal stiffness case above, an analysis of the case when the two fracture planes have different stiffnesses (Fig. 6.5) is given here. The

vertical fracture, which has specific stiffnesses κ_{1a} and κ_{1b} (Fig. 6.5), is held at a constant value such that $\kappa_{1a} = \kappa_{1b} =$ constant, while the horizontal fracture, which has specific stiffness κ_{2a} and κ_{2b} (Fig. 6.5), is varied, but uniform along the fracture plane such that $\kappa_{2a} = \kappa_{2b} =$ variable. The $\kappa_x,\ \kappa_y,\ \kappa_z$ components are set equal, and the media are assumed to be identical.

6.3.1 Step 1: Identify the point group and its symmetry operations

The geometry of the unequal stiffness case examined here is identical to that of the equal stiffness case described in the previous section. The symmetry operators change because the stiffnesses are no longer the same on the vertical and horizontal fracture planes. The point $x = y = z = 0$ is unchanged after the operations E, C_2, σ_{v1}, and σ_{v2} are applied. These operators belong to the group C_{2v}, which is an Abelian, finite group, of order 4. This is different than the WW, CWW, and the equal case discussed in the previous section.

6.3.2 Step 2: Specify the coordinate system and basis functions

The same coordinate system used in the equal stiffness derivation is used here, i.e., displacement vectors at each tip labeled $r_\alpha,\ \alpha = x, y, z$ (see Fig. 6.5).

6.3.3 Step 3: Determine the effects of the symmetry operations on the basis functions

The effect of each operator on the displacement vector is expressed as

$$\Gamma(E) r_\alpha(i) \rightarrow r_\beta(f),\ \alpha = x, y, z \tag{6.39a}$$

$$\Gamma(C_2) r_\alpha(i) \rightarrow r_\beta(f),\ \alpha = x, y, z \tag{6.39b}$$

$$\Gamma(\sigma_{v1}) r_\alpha(i) \rightarrow r_\beta(f),\ \alpha = x, y, z \tag{6.39c}$$

$$\Gamma(\sigma_{v2})r_\alpha(i) \rightarrow r_\beta(f),\ \alpha = x, y, z. \tag{6.39d}$$

The expressions in Eqns. 6.39 are summarized in the action table (Table 6.3).

Table 6.3
Action table for the C_{2v} point group.

	E	C_2	σ_{v1}	σ_{v2}
$r_x(i)$	$r_x(f)$	$r_x(f)$	$r_x(f)$	$r_x(f)$
$r_y(i)$	$r_y(f)$	$-r_y(f)$	$-r_y(f)$	$r_y(f)$
$r_z(i)$	$r_z(f)$	$-r_z(f)$	$r_z(f)$	$-r_z(f)$
1	1	3	2	4
2	2	4	1	3
3	3	1	4	2
4	4	2	3	1

6.3.4 Step 4: Construct a matrix representation for each element using the basis functions

The same vector (Eqn. 6.3) used in the equal stiffness case is used here to construct the matrix representations of the operators. Since all the operators in C_{2v} also exist in C_{4v}, this analysis is the same as step 4 for the equal stiffness case. The matrix representations of the operators are given in Eqns. 6.6, 6.8, 6.11, and 6.12 and are not repeated here.

6.3.5 Step 5: Determine the number and type of irreducible representations

This step is similar to the results of step 5 for the equal stiffness case but with minor variations. Although it would appear that the classes for C_{2v} are the same

as those contained within C_{4v}, this is not the case. Here the σ_{v1} and σ_{v2} operators form their own classes, which is shown by applying the inverses (Eqn. 6.13) to each operator as

$$E\sigma_{v1}E^{-1} = \sigma_{v1}, \tag{6.40a}$$

$$C_2\sigma_{v1}C_2^{-1} = \sigma_{v1}, \tag{6.40b}$$

$$\sigma_{v1}\sigma_{v1}\sigma_{v1}^{-1} = \sigma_{v1}, \tag{6.40c}$$

$$\sigma_{v2}\sigma_{v1}\sigma_{v2}^{-1} = \sigma_{v1}, \tag{6.40d}$$

and

$$E\sigma_{v2}E^{-1} = \sigma_{v2}, \tag{6.41a}$$

$$C_2\sigma_{v2}C_2^{-1} = \sigma_{v2}, \tag{6.41b}$$

$$\sigma_{v1}\sigma_{v2}\sigma_{v1}^{-1} = \sigma_{v2}, \tag{6.41c}$$

$$\sigma_{v2}\sigma_{v2}\sigma_{v2}^{-1} = \sigma_{v2}. \tag{6.41d}$$

In a similar fashion, the other classes are found for the group C_{2v}. In summary, they are $\{E\}$, $\{C_2\}$, $\{\sigma_{v1}\}$, and $\{\sigma_{v2}\}$. The corresponding character table is shown in Table 6.4.

The final three rows in the character table (Table 6.4) were obtained by examining the action table (Table 6.3) [140]. Only the E operator leaves any of the vector components unchanged or negated (i.e., $r_\alpha(a) \rightarrow \pm r_\alpha(a)$). Thus, the character for the operator E is 4 and all the other operators have characters of 0.

With the use of the character table (Table 6.4), the number of times each IR occurs along the diagonal blocks of $\Gamma'(O_i)$ is determined using Eqn. 4.8. The general result is

$$n^\beta = \frac{1}{h}\left[\chi_E^*\chi_E^\beta + \chi_{C_2}^*\chi_{C_2}^\beta + \chi_{\sigma_{v1}}^*\chi_{\sigma_{v1}}^\beta + \chi_{\sigma_{v2}}^*\chi_{\sigma_{v2}}^\beta\right]. \tag{6.42}$$

The unequal stiffness intersection is characterized by

Table 6.4
Character table for the C_{2v} point group.

$\mathbf{C_{2v}}$	$\mathbf{E}$	$\mathbf{C_2}$	$\sigma_{\mathbf{v1}}$	$\sigma_{\mathbf{v2}}$
A_1	1	1	1	1
A_2	1	1	-1	-1
B_1	1	-1	1	-1
B_2	1	-1	-1	1
Γ^x	4	0	0	0
Γ^y	4	0	0	0
Γ^z	4	0	0	0

$$n_\alpha^{A_1} = \frac{1}{4}\left[(4)(1)+(0)(1)+(0)(1)+(0)(1)\right] = 1,\ \alpha = x, y, z, \tag{6.43a}$$

$$n_\alpha^{A_2} = \frac{1}{4}\left[(4)(1)+(0)(1)+(0)(-1)+(0)(-1)\right] = 1,\ \alpha = x, y, z, \tag{6.43b}$$

$$n_\alpha^{B_1} = \frac{1}{4}\left[(4)(1)+(0)(-1)+(0)(1)+(0)(-1)\right] = 1,\ \alpha = x, y, z, \tag{6.43c}$$

$$n_\alpha^{B_2} = \frac{1}{4}\left[(4)(1)+(0)(-1)+(0)(-1)+(0)(1)\right] = 1,\ \alpha = x, y, z. \tag{6.43d}$$

Equation 6.43 has the same n values for the x, y, and z directions.

6.3.6 Step 6: Analyze the information in the decomposition

Using Eqn. 6.43, the decomposition of Γ into IRs for the unequal stiffness case, in any direction, is

$$\Gamma^\alpha = \Gamma^{A_1} + \Gamma^{A_2} + \Gamma^{B_1} + \Gamma^{B_2},\ \alpha = x, y, z. \tag{6.44}$$

The number of dof for this decomposition is 4 in each direction (4(1-D)=4).

6.3.7 Step 7: Determine the symmetry functions

Using the projection operator, defined in theorem 4.2.5 (section 4.2.7), the symmetry coordinates that transform into 1-D IRs for the group C_{2v} are expressed as

$$\bar{\mathbf{V}}^{A_1} \propto [\Gamma(E) + \Gamma(C_2) + \Gamma(\sigma_{v1}) + \Gamma(\sigma_{v2})]\,\bar{\mathbf{V}}, \tag{6.45a}$$

$$\bar{\mathbf{V}}^{A_2} \propto [\Gamma(E) + \Gamma(C_2) - \Gamma(\sigma_{v1}) - \Gamma(\sigma_{v2})]\,\bar{\mathbf{V}}, \tag{6.45b}$$

$$\bar{\mathbf{V}}^{B_1} \propto [\Gamma(E) - \Gamma(C_2) + \Gamma(\sigma_{v1}) - \Gamma(\sigma_{v2})]\,\bar{\mathbf{V}}, \tag{6.45c}$$

$$\bar{\mathbf{V}}^{B_2} \propto [\Gamma(E) - \Gamma(C_2) - \Gamma(\sigma_{v1}) + \Gamma(\sigma_{v2})]\,\bar{\mathbf{V}}. \tag{6.45d}$$

Unlike the equal stiffness case examined above, the coordinates have no mixing for the unequal stiffness analysis presented here (i.e., x, y, and z do not mix). The symmetry functions must be determined for each coordinate separately to fully characterize the vibrational modes of the intersection with unequal stiffnesses (Fig. 6.5). Three $\bar{\mathbf{V}}$ vectors are needed to do this. They are

$$\bar{\mathbf{V}}_x = [1\ 0\ 0\ 0\ 0\ 0\ 0\ 0\ 0\ 0\ 0\ 0]^T, \tag{6.46a}$$

$$\bar{\mathbf{V}}_y = [0\ 1\ 0\ 0\ 0\ 0\ 0\ 0\ 0\ 0\ 0\ 0]^T, \tag{6.46b}$$

$$\bar{\mathbf{V}}_z = [0\ 0\ 1\ 0\ 0\ 0\ 0\ 0\ 0\ 0\ 0\ 0]^T. \tag{6.46c}$$

Using these vectors, the displacements for each IR after normalization are

$$\bar{\mathbf{V}}_x^{A_1} = \frac{1}{2}[1\ 0\ 0\ 1\ 0\ 0\ 1\ 0\ 0\ 1\ 0\ 0]^T, \tag{6.47a}$$

$$\bar{\mathbf{V}}_y^{A_1} = \frac{1}{2}[0\ 1\ 0\ 0 - 1\ 0\ 0 - 1\ 0\ 0\ 1\ 0]^T, \tag{6.47b}$$

$$\bar{\mathbf{V}}_z^{A_1} = \frac{1}{2}[0\ 0\ 1\ 0\ 0\ 1\ 0\ 0 - 1\ 0\ 0 - 1]^T, \tag{6.47c}$$

$$\bar{\mathbf{V}}_x^{A_2} = \frac{1}{2}[1\ 0\ 0\ \ -1\ 0\ 0\ 1\ 0\ 0\ \ -1\ 0\ 0]^T, \tag{6.48a}$$

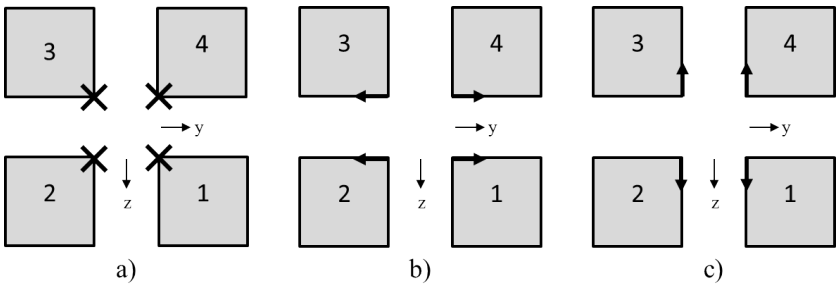

Figure 6.6. Visualization of the symmetry functions for the A_1 IR used in the intersection wave geometry with unequal stiffness on each fracture plane (Fig. 6.5). The a) x-components, b) y-components, and c) z-components.

$$\bar{\mathbf{V}}_y^{A_2} = \frac{1}{2}\left[0\ 1\ 0\ 0\ 1\ 0\ 0\ -1\ 0\ 0\ -1\ 0\right]^T, \tag{6.48b}$$

$$\bar{\mathbf{V}}_z^{A_2} = \frac{1}{2}\left[0\ 0\ 1\ 0\ 0\ -1\ 0\ 0\ -1\ 0\ 0\ 1\right]^T, \tag{6.48c}$$

$$\bar{\mathbf{V}}_x^{B_1} = \frac{1}{2}\left[1\ 0\ 0\ 1\ 0\ 0\ -1\ 0\ 0\ -1\ 0\ 0\right]^T, \tag{6.49a}$$

$$\bar{\mathbf{V}}_y^{B_1} = \frac{1}{2}\left[0\ 1\ 0\ 0\ -1\ 0\ 0\ 1\ 0\ 0\ -1\ 0\right]^T, \tag{6.49b}$$

$$\bar{\mathbf{V}}_z^{B_1} = \frac{1}{2}\left[0\ 0\ 1\ 0\ 0\ 1\ 0\ 0\ 1\ 0\ 0\ 1\right]^T, \tag{6.49c}$$

and

$$\bar{\mathbf{V}}_x^{B_2} = \frac{1}{2}\left[1\ 0\ 0\ -1\ 0\ 0\ -1\ 0\ 0\ 1\ 0\ 0\right]^T, \tag{6.50a}$$

$$\bar{\mathbf{V}}_y^{B_2} = \frac{1}{2}\left[0\ 1\ 0\ 0\ 1\ 0\ 0\ 1\ 0\ 0\ 1\ 0\right]^T, \tag{6.50b}$$

$$\bar{\mathbf{V}}_z^{B_2} = \frac{1}{2}\left[0\ 0\ 1\ 0\ 0\ -1\ 0\ 0\ 1\ 0\ 0\ -1\right]^T. \tag{6.50c}$$

These symmetry functions are visualized in Figs. 6.6-6.9. The A_1 x-component (Fig. 6.6a), B_1 z-component (Fig. 6.8c), and B_2 y-component (Fig. 6.9b) are all translation modes, while the remainder of the oscillations keep the center of mass stationary, as required. Here again the 'X' and 'o' symbols are used to represent into and out of the page, respectively. Figures 6.6-6.9 show the individual components of

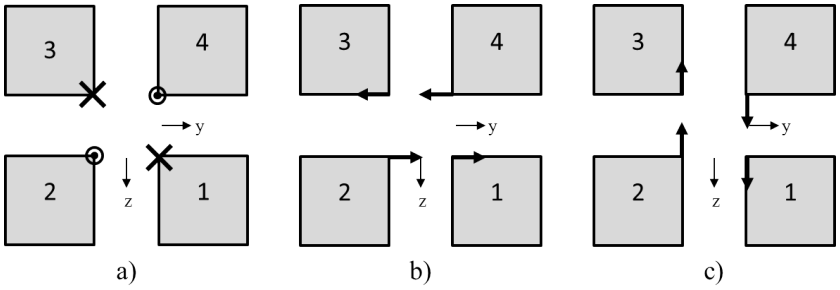

Figure 6.7. Visualization of the symmetry functions for the A_2 IR used in the intersection wave geometry with unequal stiffness on each fracture plane (Fig. 6.5). The a) x-components, b) y-components, and c) z-components.

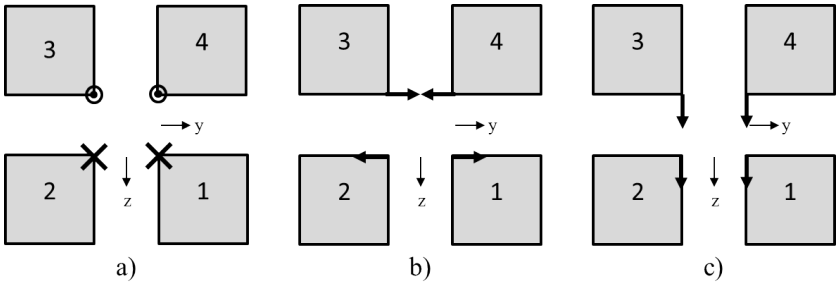

Figure 6.8. Visualization of the symmetry functions for the B_1 IR used in the intersection wave geometry with unequal stiffness on each fracture plane (Fig. 6.5). The a) x-components, b) y-components, and c) z-components.

the vibrational modes for the unequal stiffness case that form only four modes, as expected for the 4 dof represented here.

The four modes combined are shown in Fig. 6.10. Similar to the results of the equal stiffness vibrational modes, the top and bottom rows show views of the x-y plane, where all four modes have x components. The central row of Fig. 6.10 are views of the y-z plane that view the direction of propagation for the intersection wave (i.e., into the page). The four predicted modes are all wagging type modes (section 4.3.2), unlike the equal stiffness case that had a mixture of wagging and breathing modes (Fig. 6.2).

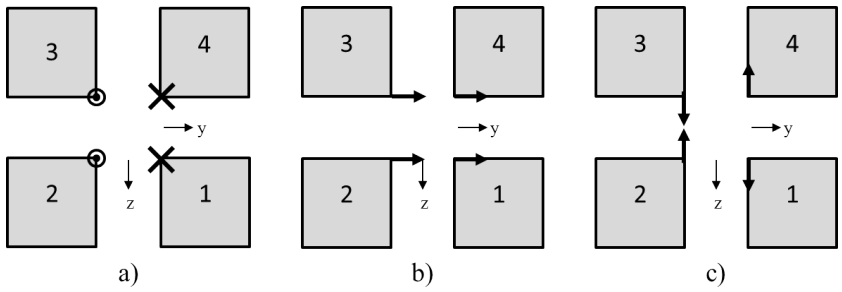

Figure 6.9. Visualization of the symmetry functions for the B_2 IR used in the intersection wave geometry with unequal stiffness on each fracture plane (Fig. 6.5). The a) x-components, b) y-components, and c) z-components.

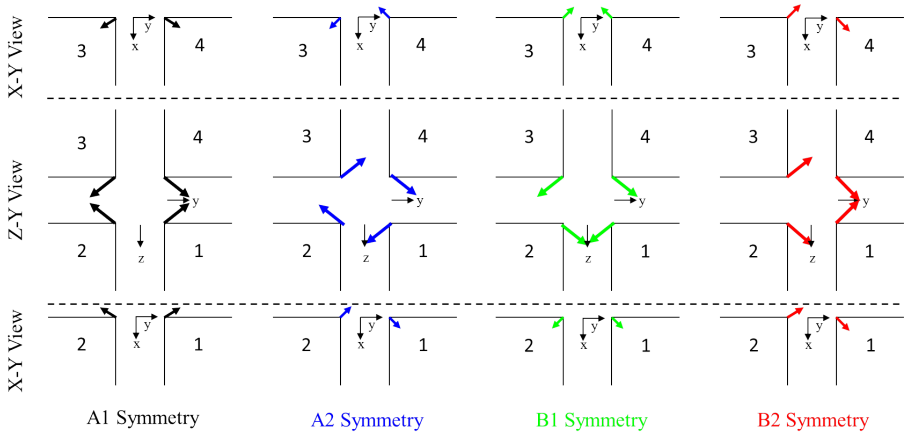

Figure 6.10. Visualization of the symmetry functions for the IR used in the intersection wave geometry with unequal stiffness on each fracture plane (Fig. 6.5). The components from Figs. 6.6-6.9 are combined to visualize the overall motion of the intersection.

There are a set of analogous breathing modes that can be observed if the material properties are allowed to support such modes (Fig. 6.11). However, since only negative Poisson's ratio materials support breathing type modes, they will be ignored here.

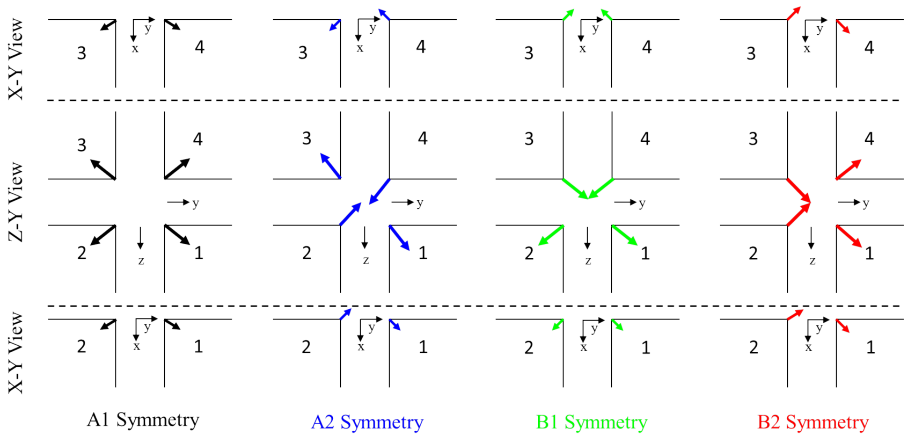

Figure 6.11. Breathing modes of Fig. 6.10.

6.3.8 Summary

The results of two different stiffness cases were analyzed and discussed here. The results indicated that the state of contact along the fracture plane plays a significant role in the vibrational modes observed along the fracture intersection. The next sections will derive an intersection wave, followed by the numerical analysis, experimental verification, and results.

6.4 Intersection Wave Theoretical Derivation

This section gives a derivation of a new type of wave that propagates along a fracture intersection. The derivation uses a similar approach to that for the CWW given in chapter 5. The full derivation is described here in great detail as this is the first appearance of the information in the literature. Those places that match the CWW methodology exactly are referenced and not repeated.

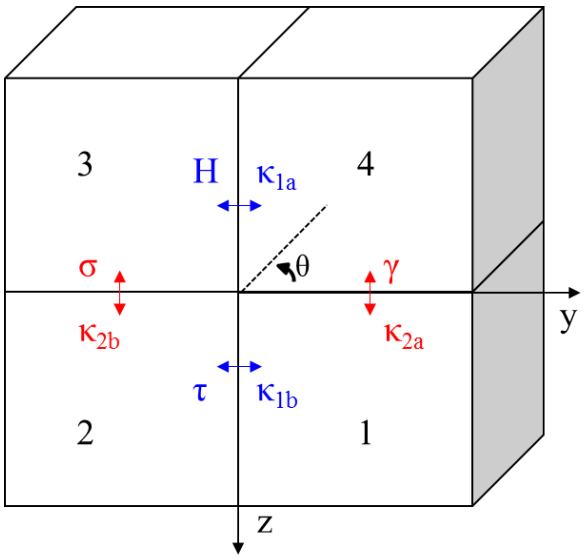

Figure 6.12. Geometry of four blocks with orthogonal fractures and stresses (Greek symbols) for characterizing the intersection waves. θ represents the transducer polarization reference angle.

6.4.1 Problem Geometry

In this derivation, the media are defined such that the fracture exists on the $x-z$ and $x-y$ planes between the four media (Fig. 6.12). Medium 1 exists in the region $x>0, y>0, z>0$, medium 2 exists in the region $x>0, y<0, z>0$, medium 3 exists in the region $x>0, y<0, z<0$ and medium 4 exists in the region $x>0, y>0, z<0$ (Fig. 6.12). Medium η has mass density $\rho^{(\eta)}$, and elastic moduli $C^{(\eta)}_{\alpha,\beta,\mu,\nu},$. The lower-case Greek letters indicates the Cartesian indices (i.e., $\alpha=1,2,3$ is x,y,z direction).

The initial portion of the derivation for the intersection wave is the same as the CWW derivation (section 5.3). From Eqns. 5.12 -5.19 the same variables and equations apply to the intersection and are not repeated here. A different set of displacement amplitudes is used to expand the media in a linear series of Laguerre functions as

$$\tilde{U}_{\alpha}^{(1/2)}(y,z) = \sum_{m,n=0}^{\infty} a_{mn}^{(\alpha,1/2)} \phi_m(\pm ky)\phi_n(kz), \tag{6.51}$$

$$\tilde{U}_{\alpha}^{(3/4)}(y,z) = \sum_{m,n=0}^{\infty} a_{mn}^{(\alpha,3/4)} \phi_m(\mp ky)\phi_n(-kz), \tag{6.52}$$

where the ϕ functions are the same as Eqns. 5.21-5.22.

The goal of the section is to solve for the a_{mn} terms. To do this, the expansions in Eqns. 6.51 and 6.52 are substituted into the equations of motion (Eqn. 5.19) leaving

$$\begin{aligned} -\rho^{(1/2)}\omega^2 \sum_{m,n=0}^{\infty} a_{m,n}^{(\alpha,1/2)} \phi_m(\pm ky)\phi_n(kz) = \\ \sum_{\beta,\mu,\nu=1}^{3} D_\beta C_{\alpha,\beta,\mu,\nu}^{(1/2)} D_\nu \sum_{m,n=0}^{\infty} a_{m,n}^{(\mu,1/2)} \phi_m(\pm ky)\phi_n(kz), \end{aligned} \tag{6.53}$$

$$\begin{aligned} -\rho^{(3/4)}\omega^2 \sum_{m,n=0}^{\infty} a_{m,n}^{(\alpha,3/4)} \phi_m(\mp ky)\phi_n(-kz) = \\ \sum_{\beta,\mu,\nu=1}^{3} D_\beta C_{\alpha,\beta,\mu,\nu}^{(3/4)} D_\nu \sum_{m,n=0}^{\infty} a_{m,n}^{(\mu,3/4)} \phi_m(\mp ky)\phi_n(-kz). \end{aligned} \tag{6.54}$$

Both sides of Eqn 6.53 are multiplied by $\sum_{pq} \phi_p(\pm ky)\phi_q(kz)$ while both sides of Eqn. 6.54 are multiplied by $\sum_{pq} \phi_p(\mp ky)\phi_q(-kz)$. Then, integration over the quarter space for each medium is performed. This leads to the following for the left hand side (lhs) of Eqns. 6.53-6.54, respectively

$$\begin{aligned} lhs^{(1/2)} = \mp \int_0^{\infty} \int_0^{\pm\infty} \int_0^{\infty} \rho^{(1/2)}\omega^2 \\ \sum_{m,n=0}^{\infty} a_{m,n}^{(\alpha,1/2)} \phi_m(\pm ky)\phi_n(kz)\phi_p(\pm ky)\phi_q(kz)\mathrm{d}x\mathrm{d}y\mathrm{d}z, \end{aligned} \tag{6.55}$$

$$\begin{aligned} lhs^{(3/4)} = \mp \int_0^{\infty} \int_0^{\mp\infty} \int_0^{-\infty} \rho^{(3/4)}\omega^2 \\ \sum_{m,n=0}^{\infty} a_{m,n}^{(\alpha,3/4)} \phi_m(\mp ky)\phi_n(-kz)\phi_p(\mp ky)\phi_q(-kz)\mathrm{d}x\mathrm{d}y\mathrm{d}z. \end{aligned} \tag{6.56}$$

The $\mp$ sign came from a change in the limits of the integration over y. The two integrals over x cancel out with the right hand side (rhs), which leaves for the lhs, using Eqn. 5.25,

$$lhs^{(1/2)} = -\rho^{(1/2)}\omega^2 \sum_{m,n=0}^{\infty} a_{m,n}^{(\alpha,1/2)} \frac{\delta_{pm}}{k} \frac{\delta_{qn}}{k}, \tag{6.57}$$

$$lhs^{(3/4)} = -\rho^{(3/4)}\omega^2 \sum_{m,n=0}^{\infty} a_{m,n}^{(\alpha,3/4)} \frac{\delta_{pm}}{k} \frac{\delta_{qn}}{k}, \tag{6.58}$$

which is simplified to

$$lhs^{(1/2)} = -\rho^{(1/2)}v^2 \sum_{m,n=0}^{\infty} a_{m,n}^{(\alpha,1/2)} \delta_{pm}\delta_{qn}, \tag{6.59}$$

$$lhs^{(3/4)} = -\rho^{(3/4)}v^2 \sum_{m,n=0}^{\infty} a_{m,n}^{(\alpha,3/4)} \delta_{pm}\delta_{qn}. \tag{6.60}$$

For the rhs of Eqns. 6.53-6.54

$$\begin{aligned} rhs^{(1/2)} = \pm \int_0^{\infty} \int_0^{\pm\infty} \sum_{\beta,\mu,\nu=1}^{3} D_\beta C_{\alpha,\beta,\mu,\nu}^{(1/2)} D_\nu \\ \sum_{m,n=0}^{\infty} a_{m,n}^{(\mu,1/2)} \phi_m(\pm ky)\phi_n(kz)\phi_p(\pm ky)\phi_q(kz)\mathrm{d}y\mathrm{d}z, \end{aligned} \tag{6.61}$$

$$\begin{aligned} rhs^{(3/4)} = \pm \int_0^{-\infty} \int_0^{\mp\infty} \sum_{\beta,\mu,\nu=1}^{3} D_\beta C_{\alpha,\beta,\mu,\nu}^{(3/4)} D_\nu \\ \sum_{m,n=0}^{\infty} a_{m,n}^{(\mu,3/4)} \phi_m(\mp ky)\phi_n(-kz)\phi_p(\mp ky)\phi_q(-kz)\mathrm{d}y\mathrm{d}z. \end{aligned} \tag{6.62}$$

Substituting equation 5.17 into Eqns. 6.61-6.62 leaves

$$rhs^{(1/2)} = \pm \sum_{\beta=1}^{3} D_\beta \int_0^{\infty} \int_0^{\pm\infty} \tilde{T}_{\alpha,\beta}^{(1/2)}(y,z)\phi_p(\pm ky)\phi_q(kz)\mathrm{d}y\mathrm{d}z, \tag{6.63}$$

$$rhs^{(3/4)} = \pm \sum_{\beta=1}^{3} D_\beta \int_0^{-\infty} \int_0^{\mp\infty} \tilde{T}_{\alpha,\beta}^{(3/4)}(y,z)\phi_p(\mp ky)\phi_q(-kz)\mathrm{d}y\mathrm{d}z. \tag{6.64}$$

Expanding the sum over β yields

$$\begin{aligned} rhs^{(1/2)} = &\pm ik \int_0^{\infty} \int_0^{\pm\infty} \tilde{T}_{\alpha,1}(y,z)\phi_p(\pm ky)\phi_q(kz)\mathrm{d}y\mathrm{d}z \\ &\pm \frac{\partial}{\partial \mathrm{y}} \int_0^{\infty} \int_0^{\pm\infty} \tilde{T}_{\alpha,2}(y,z)\phi_p(\pm ky)\phi_q(kz)\mathrm{d}y\mathrm{d}z \\ &\pm \frac{\partial}{\partial \mathrm{z}} \int_0^{\infty} \int_0^{\pm\infty} \tilde{T}_{\alpha,3}(y,z)\phi_p(\pm ky)\phi_q(kz)\mathrm{d}y\mathrm{d}z, \end{aligned} \tag{6.65}$$

$$\begin{aligned} rhs^{(3/4)} = &\pm ik \int_0^{-\infty} \int_0^{\mp\infty} \tilde{T}_{\alpha,1}(y,z)\phi_p(\mp ky)\phi_q(-kz)\mathrm{d}y\mathrm{d}z \\ &\pm \frac{\partial}{\partial \mathrm{y}} \int_0^{-\infty} \int_0^{\mp\infty} \tilde{T}_{\alpha,2}(y,z)\phi_p(\mp ky)\phi_q(-kz)\mathrm{d}y\mathrm{d}z \\ &\pm \frac{\partial}{\partial \mathrm{z}} \int_0^{-\infty} \int_0^{\mp\infty} \tilde{T}_{\alpha,3}(y,z)\phi_p(\mp ky)\phi_q(-kz)\mathrm{d}y\mathrm{d}z. \end{aligned} \tag{6.66}$$

The second term in Eqns. 6.65 and 6.66 is integrated by parts $\int uv'\mathrm{d}y = uv - \int vu'\mathrm{d}y$. The parts are (being careful of the sign of each integral)

$$\begin{aligned} &u = \phi_p(\pm ky), \quad v = \frac{\partial}{\partial y} \int_0^{\pm\infty} \int_0^{\pm\infty} \tilde{T}_{\alpha,2}(y,z)\phi_q(\mp kz)\mathrm{d}z\mathrm{d}y = \\ &\int_0^{\pm\infty} \tilde{T}_{\alpha,2}(y,z)\phi_q(\mp kz)\mathrm{d}z \\ &u' = \frac{d\phi_p(\pm ky)}{dy}, \quad v' = \frac{\partial}{\partial y} \int_0^{\pm\infty} \tilde{T}_{\alpha,2}(y,z)\phi_q(\mp kz)\mathrm{d}z. \end{aligned} \tag{6.67}$$

The second term is called $N^{(\eta)}$, $\eta = 1,2,3,4$ where

$$\begin{aligned} N^{(1)} = &[\phi_p(ky) \int_0^{\infty} \tilde{T}_{\alpha,2}(y,z)\phi_q(kz)\mathrm{d}z]_0^{y=\infty} - \\ &\int_0^{\infty} \int_0^{\infty} \tilde{T}_{\alpha,2}(y,z)\phi_q(kz)\frac{\mathrm{d}\phi_p(ky)}{\mathrm{d}y}\mathrm{d}z\mathrm{d}y, \end{aligned} \tag{6.68}$$

$$\begin{aligned} N^{(1)} = &-\phi_p(0) \int_0^{\infty} \tilde{T}_{\alpha,2}(0,z)\phi_q(kz)\mathrm{d}z - \\ &\int_0^{\infty} \int_0^{\infty} \tilde{T}_{\alpha,2}(y,z)\phi_q(kz)\frac{\mathrm{d}\phi_p(ky)}{\mathrm{d}y}\mathrm{d}z\mathrm{d}y, \end{aligned} \tag{6.69}$$

$$N^{(2)} = [\phi_p(-ky)\int_0^\infty \tilde{T}_{\alpha,2}(y,z)\phi_q(kz)\mathrm{d}z]_{-\infty}^{y=0} - \int_{-\infty}^0\int_0^\infty \tilde{T}_{\alpha,2}(y,z)\phi_q(kz)\frac{\mathrm{d}\phi_p(-ky)}{\mathrm{d}y}\mathrm{d}z\mathrm{d}y, \tag{6.70}$$

$$N^{(2)} = \phi_p(0)\int_0^\infty \tilde{T}_{\alpha,2}(0,z)\phi_q(kz)\mathrm{d}z - \int_{-\infty}^0\int_0^\infty \tilde{T}_{\alpha,2}(y,z)\phi_q(kz)\frac{\mathrm{d}\phi_p(-ky)}{\mathrm{d}y}\mathrm{d}z\mathrm{d}y, \tag{6.71}$$

$$N^{(3)} = [\phi_p(-ky)\int_{-\infty}^0 \tilde{T}_{\alpha,2}(y,z)\phi_q(-kz)\mathrm{d}z]_{-\infty}^{y=0} - \int_{-\infty}^0\int_{-\infty}^0 \tilde{T}_{\alpha,2}(y,z)\phi_q(-kz)\frac{\mathrm{d}\phi_p(-ky)}{\mathrm{d}y}\mathrm{d}z\mathrm{d}y, \tag{6.72}$$

$$N^{(3)} = \phi_p(0)\int_{-\infty}^0 \tilde{T}_{\alpha,2}(0,z)\phi_q(-kz)\mathrm{d}z - \int_{-\infty}^0\int_{-\infty}^0 \tilde{T}_{\alpha,2}(y,z)\phi_q(-kz)\frac{\mathrm{d}\phi_p(-ky)}{\mathrm{d}y}\mathrm{d}z\mathrm{d}y, \tag{6.73}$$

$$N^{(4)} = [\phi_p(ky)\int_{-\infty}^0 \tilde{T}_{\alpha,2}(y,z)\phi_q(-kz)\mathrm{d}z]_0^{y=\infty} - \int_0^\infty\int_{-\infty}^0 \tilde{T}_{\alpha,2}(y,z)\phi_q(-kz)\frac{\mathrm{d}\phi_p(ky)}{\mathrm{d}y}\mathrm{d}z\mathrm{d}y, \tag{6.74}$$

$$N^{(4)} = -\phi_p(0)\int_{-\infty}^0 \tilde{T}_{\alpha,2}(0,z)\phi_q(-kz)\mathrm{d}z - \int_0^\infty\int_{-\infty}^0 \tilde{T}_{\alpha,2}(y,z)\phi_q(-kz)\frac{\mathrm{d}\phi_p(ky)}{\mathrm{d}y}\mathrm{d}z\mathrm{d}y, \tag{6.75}$$

where the relation $\phi(\pm\infty) = 0$ is utilized. The stress at the interface between media 1 and 2 (Fig. 6.12) is defined as

$$\tau_n^{(\alpha,\eta)} \equiv \int_0^\infty \tilde{T}_{\alpha,2}(0,z)\phi_n(kz)\mathrm{d}z, \tag{6.76}$$

and between media 3 and 4 (Fig. 6.12) as

$$H_n^{(\alpha,\eta)} \equiv \int_{-\infty}^{0} \tilde{T}_{\alpha,2}(0,z)\phi_n(-kz)\mathrm{d}z. \tag{6.77}$$

Substituting Eqns. 6.76 and 6.77 into Eqns. 6.68 - 6.75 yields

$$N^{(1)} = -\phi_p(0)\tau_q^{(\alpha,1)} - \int_0^{\infty}\int_0^{\infty} \tilde{T}_{\alpha,2}(y,z)\phi_q(kz)\frac{\mathrm{d}\phi_p(ky)}{\mathrm{d}y}\mathrm{d}z\mathrm{d}y, \tag{6.78}$$

$$N^{(2)} = \phi_p(0)\tau_q^{(\alpha,2)} - \int_{-\infty}^{0}\int_0^{\infty} \tilde{T}_{\alpha,2}(y,z)\phi_q(kz)\frac{\mathrm{d}\phi_p(-ky)}{\mathrm{d}y}\mathrm{d}z\mathrm{d}y, \tag{6.79}$$

$$N^{(3)} = \phi_p(0)H_q^{(\alpha,3)} - \int_{-\infty}^{0}\int_{-\infty}^{0} \tilde{T}_{\alpha,2}(y,z)\phi_q(-kz)\frac{\mathrm{d}\phi_p(-ky)}{\mathrm{d}y}\mathrm{d}z\mathrm{d}y, \tag{6.80}$$

$$N^{(4)} = -\phi_p(0)H_q^{(\alpha,4)} - \int_0^{\infty}\int_{-\infty}^{0} \tilde{T}_{\alpha,2}(y,z)\phi_q(-kz)\frac{\mathrm{d}\phi_p(ky)}{\mathrm{d}y}\mathrm{d}z\mathrm{d}y. \tag{6.81}$$

The third term in Eqns. 6.65 and 6.66 is integrated by parts (watch the sign),

$$\begin{aligned} &u = \phi_q(\pm kz), \quad v = \frac{\partial}{\partial z}\int_0^{\pm\infty}\int_0^{\pm\infty} \tilde{T}_{\alpha,3}(y,z)\phi_p(\pm ky)\mathrm{d}y\mathrm{d}z = \\ &\int_0^{\pm\infty} \tilde{T}_{\alpha,3}(y,z)\phi_p(\pm ky)\mathrm{d}y, \\ &u' = \frac{d\phi_q(\pm kz)}{dz}, \quad v' = \frac{\partial}{\partial z}\int_0^{\pm\infty} \tilde{T}_{\alpha,3}(y,z)\phi_p(\pm ky)\mathrm{d}y. \end{aligned} \tag{6.82}$$

This term is called $R^{(\eta)}$ and is expressed as

$$\begin{aligned} R^{(1)} = [\phi_q(kz)\int_0^{\infty} \tilde{T}_{\alpha,3}(y,z)\phi_p(ky)\mathrm{d}y]_0^{z=\infty} - \\ \int_0^{\infty}\int_0^{\infty} \tilde{T}_{\alpha,3}(y,z)\phi_p(ky)\frac{\mathrm{d}\phi_q(kz)}{\mathrm{d}z}\mathrm{d}y\mathrm{d}z, \end{aligned} \tag{6.83}$$

$$\begin{aligned} R^{(1)} = -\phi_q(0)\int_0^{\infty} \tilde{T}_{\alpha,3}(y,0)\phi_p(ky)\mathrm{d}y - \\ \int_0^{\infty}\int_0^{\infty} \tilde{T}_{\alpha,3}(y,z)\phi_p(ky)\frac{\mathrm{d}\phi_q(kz)}{\mathrm{d}z}\mathrm{d}y\mathrm{d}z, \end{aligned} \tag{6.84}$$

$$R^{(1)} = -\phi_q(0)\gamma_p^{(\alpha,1)} - \int_0^\infty \int_0^\infty \tilde{T}_{\alpha,3}(y,z)\phi_p(ky)\frac{\mathrm{d}\phi_q(kz)}{\mathrm{d}z}\mathrm{d}y\mathrm{d}z, \tag{6.85}$$

$$R^{(2)} = [\phi_q(kz)\int_{-\infty}^0 \tilde{T}_{\alpha,3}(y,z)\phi_p(-ky)\mathrm{d}y]_0^{z=\infty} - \int_0^\infty \int_{-\infty}^0 \tilde{T}_{\alpha,3}(y,z)\phi_p(-ky)\frac{\mathrm{d}\phi_q(kz)}{\mathrm{d}z}\mathrm{d}y\mathrm{d}z, \tag{6.86}$$

$$R^{(2)} = -\phi_q(0)\int_{-\infty}^0 \tilde{T}_{\alpha,3}(y,0)\phi_p(-ky)\mathrm{d}y - \int_0^\infty \int_{-\infty}^0 \tilde{T}_{\alpha,3}(y,z)\phi_p(-ky)\frac{\mathrm{d}\phi_q(kz)}{\mathrm{d}z}\mathrm{d}y\mathrm{d}z, \tag{6.87}$$

$$R^{(2)} = -\phi_q(0)\sigma_p^{(\alpha,2)} - \int_0^\infty \int_{-\infty}^0 \tilde{T}_{\alpha,3}(y,z)\phi_p(-ky)\frac{\mathrm{d}\phi_q(kz)}{\mathrm{d}z}\mathrm{d}y\mathrm{d}z, \tag{6.88}$$

$$R^{(3)} = [\phi_q(-kz)\int_{-\infty}^0 \tilde{T}_{\alpha,3}(y,z)\phi_p(-ky)\mathrm{d}y]_{-\infty}^{z=0} - \int_{-\infty}^0 \int_{-\infty}^0 \tilde{T}_{\alpha,3}(y,z)\phi_p(-ky)\frac{\mathrm{d}\phi_q(-kz)}{\mathrm{d}z}\mathrm{d}y\mathrm{d}z, \tag{6.89}$$

$$R^{(3)} = \phi_q(0)\int_{-\infty}^0 \tilde{T}_{\alpha,3}(y,0)\phi_p(-ky)\mathrm{d}y - \int_{-\infty}^0 \int_{-\infty}^0 \tilde{T}_{\alpha,3}(y,z)\phi_p(-ky)\frac{\mathrm{d}\phi_q(-kz)}{\mathrm{d}z}\mathrm{d}y\mathrm{d}z, \tag{6.90}$$

$$R^{(3)} = \phi_q(0)\sigma_p^{(\alpha,3)} - \int_{-\infty}^0 \int_{-\infty}^0 \tilde{T}_{\alpha,3}(y,z)\phi_p(-ky)\frac{\mathrm{d}\phi_q(-kz)}{\mathrm{d}z}\mathrm{d}y\mathrm{d}z, \tag{6.91}$$

$$R^{(4)} = [\phi_q(-kz)\int_0^\infty \tilde{T}_{\alpha,3}(y,z)\phi_p(ky)\mathrm{d}y]_{-\infty}^{z=0} - \int_{-\infty}^0 \int_0^\infty \tilde{T}_{\alpha,3}(y,z)\phi_p(ky)\frac{\mathrm{d}\phi_q(-kz)}{\mathrm{d}z}\mathrm{d}y\mathrm{d}z, \tag{6.92}$$

$$R^{(4)} = \phi_q(0)\int_0^\infty \tilde{T}_{\alpha,3}(y,0)\phi_p(ky)\mathrm{d}y - \int_{-\infty}^0\int_0^\infty \tilde{T}_{\alpha,3}(y,z)\phi_p(ky)\frac{\mathrm{d}\phi_q(-kz)}{\mathrm{d}z}\mathrm{d}y\mathrm{d}z, \tag{6.93}$$

$$R^{(4)} = \phi_q(0)\gamma_p^{(\alpha,4)} - \int_{-\infty}^0\int_0^\infty \tilde{T}_{\alpha,3}(y,z)\phi_p(ky)\frac{\mathrm{d}\phi_q(-kz)}{\mathrm{d}z}\mathrm{d}y\mathrm{d}z, \tag{6.94}$$

where the stress between media 2 and 3 (Fig. 6.12) is defined as

$$\sigma_n^{(\alpha,\eta)} \equiv \int_{-\infty}^0 \tilde{T}_{\alpha,3}(y,0)\phi_n(-ky)\mathrm{d}y, \tag{6.95}$$

and between media 1 and 4 (Fig. 6.12) as

$$\gamma_n^{(\alpha,\eta)} \equiv \int_0^\infty \tilde{T}_{\alpha,3}(y,0)\phi_n(ky)\mathrm{d}y. \tag{6.96}$$

Equations 6.78, 6.79, 6.85 and 6.88 are substituted into Eqn. 6.65, while Eqns. 6.80, 6.81, 6.91 and 6.94 are substituted into Eqn. 6.66. The results for the rhs are

$$\begin{aligned} rhs^{(1)} = {} & ik\int_0^\infty\int_0^\infty \tilde{T}_{\alpha,1}(y,z)\phi_p(ky)\phi_q(kz)\mathrm{d}y\mathrm{d}z - \phi_p(0)\tau_q^{(\alpha,1)} \\ & - \int_0^\infty\int_0^\infty \tilde{T}_{\alpha,2}(y,z)\phi_q(kz)\frac{\mathrm{d}\phi_p(ky)}{\mathrm{d}y}\mathrm{d}y\mathrm{d}z \\ & - \phi_q(0)\gamma_p^{(\alpha,1)} - \int_0^\infty\int_0^\infty \tilde{T}_{\alpha,3}(y,z)\phi_p(ky)\frac{\mathrm{d}\phi_q(kz)}{\mathrm{d}z}\mathrm{d}y\mathrm{d}z, \end{aligned} \tag{6.97}$$

$$\begin{aligned} rhs^{(2)} = {} & ik\int_0^\infty\int_{-\infty}^0 \tilde{T}_{\alpha,1}(y,z)\phi_p(-ky)\phi_q(kz)\mathrm{d}y\mathrm{d}z + \phi_p(0)\tau_q^{(\alpha,2)} \\ & - \int_0^\infty\int_{-\infty}^0 \tilde{T}_{\alpha,2}(y,z)\phi_q(kz)\frac{\mathrm{d}\phi_p(-ky)}{\mathrm{d}y}\mathrm{d}y\mathrm{d}z \\ & - \phi_q(0)\sigma_p^{(\alpha,2)} - \int_0^\infty\int_{-\infty}^0 \tilde{T}_{\alpha,3}(y,z)\phi_p(-ky)\frac{\mathrm{d}\phi_q(kz)}{\mathrm{d}z}\mathrm{d}y\mathrm{d}z, \end{aligned} \tag{6.98}$$

$$
\begin{aligned}
rhs^{(3)} = ik \int_{-\infty}^{0}\int_{-\infty}^{0} \tilde{T}_{\alpha,1}(y,z)\phi_p(-ky)\phi_q(-kz)\mathrm{d}y\mathrm{d}z + \phi_p(0)H_q^{(\alpha,3)} \\
- \int_{-\infty}^{0}\int_{-\infty}^{0} \tilde{T}_{\alpha,2}(y,z)\phi_q(-kz)\frac{\mathrm{d}\phi_p(-ky)}{\mathrm{d}y}\mathrm{d}y\mathrm{d}z \\
+ \phi_q(0)\sigma_p^{(\alpha,3)} - \int_{-\infty}^{0}\int_{-\infty}^{0} \tilde{T}_{\alpha,3}(y,z)\phi_p(-ky)\frac{\mathrm{d}\phi_q(-kz)}{\mathrm{d}z}\mathrm{d}y\mathrm{d}z,
\end{aligned}
\tag{6.99}
$$

$$
\begin{aligned}
rhs^{(4)} = ik \int_{-\infty}^{0}\int_{0}^{\infty} \tilde{T}_{\alpha,1}(y,z)\phi_p(ky)\phi_q(-kz)\mathrm{d}y\mathrm{d}z - \phi_p(0)H_q^{(\alpha,4)} \\
- \int_{-\infty}^{0}\int_{0}^{\infty} \tilde{T}_{\alpha,2}(y,z)\phi_q(-kz)\frac{\mathrm{d}\phi_p(ky)}{\mathrm{d}y}\mathrm{d}y\mathrm{d}z \\
+ \phi_q(0)\gamma_p^{(\alpha,4)} - \int_{-\infty}^{0}\int_{0}^{\infty} \tilde{T}_{\alpha,3}(y,z)\phi_p(ky)\frac{\mathrm{d}\phi_q(-kz)}{\mathrm{d}z}\mathrm{d}y\mathrm{d}z.
\end{aligned}
\tag{6.100}
$$

The three remaining integrals in Eqns. 6.97- 6.100 are combined to form

$$
rhs^{(\eta)} = \sum_{\mu=1}^{3}\sum_{m,n=0}^{\infty} -a_{m,n}^{(\mu,\eta)} M_{p,q,m,n}^{(\alpha,\mu,\eta)},
\tag{6.101}
$$

where $a_{m,n}$ was defined in Eqns. 6.51 and 6.52, and $\bar{\mathbf{M}}$ is defined as

$$
\begin{aligned}
M_{pq,mn}^{(\alpha,\mu,1/2)} = \pm \sum_{\beta,\nu=1}^{3} \int_0^{\infty}\int_0^{\pm\infty} \Big[D_\beta(k)\phi_p(\pm ky)\phi_q(kz)\Big]^* C_{\alpha\beta\mu\nu}^{(1/2)} \\
\Big[D_\nu(k)\phi_m(\pm ky)\phi_n(kz)\Big]\mathrm{d}y\mathrm{d}z,
\end{aligned}
\tag{6.102}
$$

$$
\begin{aligned}
M_{pq,mn}^{(\alpha,\mu,3/4)} = \pm \sum_{\beta,\nu=1}^{3} \int_0^{-\infty}\int_0^{\mp\infty} \Big[D_\beta(k)\phi_p(\mp ky)\phi_q(-kz)\Big]^* C_{\alpha\beta\mu\nu}^{(3/4)} \\
\Big[D_\nu(k)\phi_m(\mp ky)\phi_n(-kz)\Big]\mathrm{d}y\mathrm{d}z.
\end{aligned}
\tag{6.103}
$$

$[D_\beta\phi_p\phi_q]^*$ in the first term of Eqns. 6.102 and 6.103 arose from the sign difference between the real and imaginary parts of Eqns. 6.97 - 6.100. Applying the above notation, Eqns. 6.97 - 6.100 become

$$rhs^{(1)} = -\phi_p(0)\tau_q^{(\alpha,1)} - \phi_q(0)\gamma_p^{(\alpha,1)} - \sum_{\mu=1}^{3}\sum_{m,n=0}^{\infty} a_{mn}^{(\mu,1)} M_{p,q,m,n}^{(\alpha,\mu,1)}, \tag{6.104}$$

$$rhs^{(2)} = \phi_p(0)\tau_q^{(\alpha,2)} - \phi_q(0)\sigma_p^{(\alpha,2)} - \sum_{\mu=1}^{3}\sum_{m,n=0}^{\infty} a_{mn}^{(\mu,2)} M_{p,q,m,n}^{(\alpha,\mu,2)}, \tag{6.105}$$

$$rhs^{(3)} = \phi_p(0)H_q^{(\alpha,3)} + \phi_q(0)\sigma_p^{(\alpha,3)} - \sum_{\mu=1}^{3}\sum_{m,n=0}^{\infty} a_{mn}^{(\mu,3)} M_{p,q,m,n}^{(\alpha,\mu,3)}, \tag{6.106}$$

and

$$rhs^{(4)} = -\phi_p(0)H_q^{(\alpha,4)} + \phi_q(0)\gamma_p^{(\alpha,4)} - \sum_{\mu=1}^{3}\sum_{m,n=0}^{\infty} a_{mn}^{(\mu,4)} M_{p,q,m,n}^{(\alpha,\mu,4)}. \tag{6.107}$$

Substituting Eqns. 6.59 and 6.60 into the rhs above yields for medium 1

$$\sum_{\mu=1}^{3}\sum_{m,n=0}^{\infty} \left(M_{p,q,m,n}^{(\alpha,\mu,1)} - \rho^{(1)}v^2\delta_{\alpha\mu}\delta_{pm}\delta_{qn}\right) a_{mn}^{(\mu,1)} = -\phi_p(0)\tau_q^{(\alpha,1)} - \phi_q(0)\gamma_p^{(\alpha,1)}, \tag{6.108}$$

for medium 2

$$\sum_{\mu=1}^{3}\sum_{m,n=0}^{\infty} \left(M_{p,q,m,n}^{(\alpha,\mu,2)} - \rho^{(2)}v^2\delta_{\alpha\mu}\delta_{pm}\delta_{qn}\right) a_{mn}^{(\mu,2)} = \phi_p(0)\tau_q^{(\alpha,2)} - \phi_q(0)\sigma_p^{(\alpha,2)}, \tag{6.109}$$

for medium 3

$$\sum_{\mu=1}^{3}\sum_{m,n=0}^{\infty} \left(M_{p,q,m,n}^{(\alpha,\mu,3)} - \rho^{(3)}v^2\delta_{\alpha\mu}\delta_{pm}\delta_{qn}\right) a_{mn}^{(\mu,3)} = \phi_p(0)H_q^{(\alpha,3)} + \phi_q(0)\sigma_p^{(\alpha,3)}, \tag{6.110}$$

and for medium 4

$$\sum_{\mu=1}^{3}\sum_{m,n=0}^{\infty} \left(M_{p,q,m,n}^{(\alpha,\mu,4)} - \rho^{(4)}v^2\delta_{\alpha\mu}\delta_{pm}\delta_{qn}\right) a_{mn}^{(\mu,4)} = -\phi_p(0)H_q^{(\alpha,4)} + \phi_q(0)\gamma_p^{(\alpha,4)}. \tag{6.111}$$

Using Eqns. 6.108 - 6.111 above, the similarity transformation (Appendix D) is applied to obtain

$$\bar{\mathbf{a}}^{(1)} = \bar{\mathbf{G}}^{(1)}(-\bar{\boldsymbol{\tau}}^{(1)} - \bar{\boldsymbol{\gamma}}^{(1)}), \tag{6.112}$$

$$\bar{\mathbf{a}}^{(2)} = \bar{\mathbf{G}}^{(2)}(\bar{\boldsymbol{\tau}}^{(2)} - \bar{\boldsymbol{\sigma}}^{(2)}), \tag{6.113}$$

$$\bar{\mathbf{a}}^{(3)} = \bar{\mathbf{G}}^{(3)}(\bar{\mathbf{H}}^{(3)} + \bar{\boldsymbol{\sigma}}^{(3)}), \tag{6.114}$$

$$\bar{\mathbf{a}}^{(4)} = \bar{\mathbf{G}}^{(4)}(-\bar{\mathbf{H}}^{(4)} + \bar{\boldsymbol{\gamma}}^{(4)}), \tag{6.115}$$

where $\bar{\mathbf{G}}$ is from the similarity transformation (Appendix D). In index notation, this becomes

$$a_{mn}^{(\alpha,1)} = G_{mnpq}^{(\alpha,\beta,1)} \left(-\tau_q^{(\beta)} - \gamma_p^{(\beta)}\right), \tag{6.116}$$

$$a_{mn}^{(\alpha,2)} = G_{mnpq}^{(\alpha,\beta,2)} \left(\tau_q^{(\beta)} - \sigma_p^{(\beta)}\right), \tag{6.117}$$

$$a_{mn}^{(\alpha,3)} = G_{mnpq}^{(\alpha,\beta,3)} \left(H_q^{(\beta)} + \sigma_p^{(\beta)}\right), \tag{6.118}$$

$$a_{mn}^{(\alpha,4)} = G_{mnpq}^{(\alpha,\beta,4)} \left(-H_q^{(\beta)} + \gamma_p^{(\beta)}\right), \tag{6.119}$$

where

$$G_{mnpq}^{(\alpha,\beta,\eta)} = \sum_{j=1}^{j_{max}} \frac{V_{mn}^{(\alpha,\eta)}(j) V_{pq}^{(\beta,\eta)*}(j)}{\lambda(j) - \rho^{(\eta)} v^2}, \ \eta = 1,2,3,4, \tag{6.120}$$

λ is the eigenvalue of $\bar{\mathbf{M}}$, V_{mn} are the m, n components of the eigenvectors of $\bar{\mathbf{M}}$ and

$$j_{max} = 3(m_{max} + 1)(n_{max} + 1). \tag{6.121}$$

See Appendix D for a full derivation of $\bar{\mathbf{G}}$.

It should be noted that this definition is different than that used on the RS or the CWW (Eqn. 5.90 in chapter 5) [103, 138]. Because the stress terms on the rhs of

Eqns. 6.108 - 6.111 have different indices, they must be carefully multiplied together, with no compression on the matrix index terms. For the CWW and RS waves, the p and m terms were compressed because of the symmetries of the matrices that existed.

The above relationships (Eqns. 6.116 - 6.119) can be written out as matrices. Eqn. 6.116 is written as

$$\begin{pmatrix} G_{0000}^{(1,1,1)} & G_{0010}^{(1,1,1)} & G_{0001}^{(1,1,1)} & G_{0011}^{(1,1,1)} & G_{0000}^{(1,2,1)} & \dots & G_{0011}^{(1,3,1)} \\ G_{1000}^{(1,1,1)} & G_{1010}^{(1,1,1)} & \dots & & & & \vdots \\ \vdots & & & & \ddots & & \vdots \\ G_{1100}^{(3,1,1)} & \dots & & \dots & & \dots & G_{1111}^{(3,3,1)} \end{pmatrix} \begin{pmatrix} -\phi_0(0)\tau_0^{(1)} - \phi_0(0)\gamma_0^{(1)} \\ -\phi_1(0)\tau_0^{(1)} - \phi_0(0)\gamma_1^{(1)} \\ -\phi_0(0)\tau_1^{(1)} - \phi_1(0)\gamma_0^{(1)} \\ -\phi_1(0)\tau_1^{(1)} - \phi_1(0)\gamma_1^{(1)} \\ -\phi_0(0)\tau_0^{(2)} - \phi_0(0)\gamma_0^{(2)} \\ \vdots \\ -\phi_1(0)\tau_1^{(3)} - \phi_1(0)\gamma_1^{(3)} \end{pmatrix} = \begin{pmatrix} a_{00}^{(1)} \\ a_{10}^{(1)} \\ a_{01}^{(1)} \\ a_{11}^{(1)} \\ a_{00}^{(2)} \\ \vdots \\ a_{11}^{(3)} \end{pmatrix}. \tag{6.122}$$

Note the different subscripts on the τ and γ terms. The size of the $\bar{\mathbf{G}}$ matrix is j_{max} x j_{max}, the size of the second matrix is j_{max} x 1, and the $\bar{\mathbf{a}}$ matrix is size j_{max} x 1.

The displacement at the interface is defined as

$$U_n^{(\alpha,1/2)} \equiv k \int_0^\infty \phi_n(kz) \tilde{U}_\alpha^{(1/2)}(0,z) \mathrm{d}z, \tag{6.123}$$

$$U_n^{(\alpha,3/4)} \equiv k \int_{-\infty}^0 \phi_n(-kz) \tilde{U}_\alpha^{(3/4)}(0,z) \mathrm{d}z. \tag{6.124}$$

Applying the expansion in Eqns. 6.51 and 6.52 yields

$$U_n^{(\alpha,1/2)} = k\int_0^\infty \phi_n(kz)\sum_{m,n=0}^{\infty} a_{m,n}^{(\alpha,1/2)}\phi_m(0)\phi_n(kz)\mathrm{d}z, \tag{6.125}$$

$$U_n^{(\alpha,3/4)} = k\int_{-\infty}^0 \phi_n(-kz)\sum_{m,n=0}^{\infty} a_{m,n}^{(\alpha,3/4)}\phi_m(0)\phi_n(-kz)\mathrm{d}z. \tag{6.126}$$

Using Eqn. 5.25, this simplifies to

$$U_n^{(\alpha,\eta)} = \sum_{m=0}^{\infty} a_{mn}^{(\alpha,\eta)},\ \eta = 1,2,3,4. \tag{6.127}$$

Similarly, integrating in the y direction, leaves

$$U_m^{(\alpha,\eta)} = \sum_{n=0}^{\infty} a_{mn}^{(\alpha,\eta)},\ \eta = 1,2,3,4. \tag{6.128}$$

Applying Eqns. 6.127-6.128 to Eqn. 6.122 yields

$$\begin{pmatrix} G_{0000}^{(1,1,1)} + G_{1000}^{(1,1,1)} & G_{0010}^{(1,1,1)} + G_{1010}^{(1,1,1)} & \dots & G_{0011}^{(1,3,1)} + G_{0011}^{(1,3,1)} \\ G_{0100}^{(1,1,1)} + G_{1100}^{(1,1,1)} & \dots & & \vdots \\ \vdots & \ddots & & \vdots \\ G_{0100}^{(3,1,1)} + G_{1100}^{(3,1,1)} & \dots & & G_{0111}^{(3,3,1)} + G_{1111}^{(3,3,1)} \end{pmatrix} \begin{pmatrix} -\phi_0(0)\tau_0^{(1)} - \phi_0(0)\gamma_0^{(1)} \\ -\phi_1(0)\tau_0^{(1)} - \phi_0(0)\gamma_1^{(1)} \\ -\phi_0(0)\tau_1^{(1)} - \phi_1(0)\gamma_0^{(1)} \\ -\phi_1(0)\tau_1^{(1)} - \phi_1(0)\gamma_1^{(1)} \\ -\phi_0(0)\tau_0^{(2)} - \phi_0(0)\gamma_0^{(2)} \\ \vdots \\ -\phi_1(0)\tau_1^{(3)} - \phi_1(0)\gamma_1^{(3)} \end{pmatrix} = \begin{pmatrix} U_0^{(1)} \\ U_1^{(1)} \\ U_0^{(2)} \\ \vdots \\ U_1^{(3)} \end{pmatrix}. \tag{6.129}$$

The size of $\bar{\mathbf{G}}$ is now $3(n_{max}+1)$ x j_{max}, the size of the second matrix is j_{max} x 1, and $\bar{\mathbf{U}}$ is size $3(n_{max}+1)$ x 1. This idea was applied to the remainder of the equations (Eqns. 6.112-6.115) yielding

$$\bar{\mathbf{U}}^{(1)} = \bar{\mathbf{G}}^{(1)}(-\bar{\boldsymbol{\tau}}^{(1)} - \bar{\boldsymbol{\gamma}}^{(1)}), \tag{6.130}$$

$$\bar{\mathbf{U}}^{(2)} = \bar{\mathbf{G}}^{(2)}(\bar{\boldsymbol{\tau}}^{(2)} - \bar{\boldsymbol{\sigma}}^{(2)}), \tag{6.131}$$

$$\bar{\mathbf{U}}^{(3)} = \bar{\mathbf{G}}^{(3)}(\bar{\mathbf{H}}^{(3)} + \bar{\boldsymbol{\sigma}}^{(3)}), \tag{6.132}$$

$$\bar{\mathbf{U}}^{(4)} = \bar{\mathbf{G}}^{(4)}(-\bar{\mathbf{H}}^{(4)} + \bar{\boldsymbol{\gamma}}^{(4)}), \tag{6.133}$$

or in terms of the individual components

$$U_n^{(\alpha,1)} = G_{npq}^{(\alpha,\beta,1)}(-\phi_p(0)\tau_q^{(\beta,1)} - \phi_q(0)\gamma_p^{(\beta,1)}), \tag{6.134}$$

$$U_n^{(\alpha,2)} = G_{npq}^{(\alpha,\beta,2)}(\phi_p(0)\tau_q^{(\beta,2)} - \phi_q(0)\sigma_p^{(\beta,2)}), \tag{6.135}$$

$$U_n^{(\alpha,3)} = G_{npq}^{(\alpha,\beta,3)}(\phi_p(0)H_q^{(\beta,3)} + \phi_q(0)\sigma_p^{(\beta,3)}), \tag{6.136}$$

$$U_n^{(\alpha,4)} = G_{npq}^{(\alpha,\beta,4)}(-\phi_p(0)H_q^{(\beta,4)} + \phi_q(0)\gamma_p^{(\beta,4)}), \tag{6.137}$$

where

$$G_{npq}^{(\alpha,\beta,\eta)} = \sum_{j=1}^{j_{max}} \sum_{m=0}^{m_{max}} \frac{V_{mn}^{(\alpha,\eta)}(j) V_{pq}^{(\beta,\eta)*}(j)}{\lambda(j) - \rho^{(\eta)} v^2}, \ \eta = 1,2,3,4. \tag{6.138}$$

Equation 6.129 becomes

$$\begin{pmatrix} G_{000}^{(1,1,1)} & G_{010}^{(1,1,1)} & G_{001}^{(1,1,1)} & G_{011}^{(1,1,1)} & \dots & G_{011}^{(1,3,1)} \\ G_{100}^{(1,1,1)} & G_{110}^{(1,1,1)} & \dots & & & \vdots \\ \vdots & & & \ddots & & \vdots \\ G_{100}^{(3,1,1)} & \dots & & & \dots & G_{111}^{(3,3,1)} \end{pmatrix} \begin{pmatrix} -\phi_0(0)\tau_0^{(1)} - \phi_0(0)\gamma_0^{(1)} \\ -\phi_1(0)\tau_0^{(1)} - \phi_0(0)\gamma_1^{(1)} \\ -\phi_0(0)\tau_1^{(1)} - \phi_1(0)\gamma_0^{(1)} \\ -\phi_1(0)\tau_1^{(1)} - \phi_1(0)\gamma_1^{(1)} \\ -\phi_0(0)\tau_0^{(2)} - \phi_0(0)\gamma_0^{(2)} \\ \vdots \\ -\phi_1(0)\tau_1^{(3)} - \phi_1(0)\gamma_1^{(3)} \end{pmatrix} = \begin{pmatrix} U_0^{(1)} \\ U_1^{(1)} \\ U_0^{(2)} \\ \vdots \\ U_1^{(3)} \end{pmatrix}. \tag{6.139}$$

The size of the $\bar{\mathbf{G}}$ matrix is the same as before ($3(n_{max}+1)$ x j_{max}).

Now that the m, n terms are suppressed, the p, q terms are suppressed in a similar fashion by distributing the $\bar{\mathbf{G}}$ terms in Eqns. 6.134-6.137, leaving

$$U_n^{(\alpha,1)} = -G_{npq}^{(\alpha,\beta,1)}\phi_p(0)\tau_q^{(\beta,1)} - G_{npq}^{(\alpha,\beta,1)}\phi_q(0)\gamma_p^{(\beta,1)}, \tag{6.140}$$

$$U_n^{(\alpha,2)} = G_{npq}^{(\alpha,\beta,2)}\phi_p(0)\tau_q^{(\beta,2)} - G_{npq}^{(\alpha,\beta,2)}\phi_q(0)\sigma_p^{(\beta,2)}, \tag{6.141}$$

$$U_n^{(\alpha,3)} = G_{npq}^{(\alpha,\beta,3)}\phi_p(0)H_q^{(\beta,3)} + G_{npq}^{(\alpha,\beta,3)}\phi_q(0)\sigma_p^{(\beta,3)}, \tag{6.142}$$

$$U_n^{(\alpha,4)} = -G_{npq}^{(\alpha,\beta,4)}\phi_p(0)H_q^{(\beta,4)} + G_{npq}^{(\alpha,\beta,4)}\phi_q(0)\gamma_p^{(\beta,4)}, \tag{6.143}$$

which changes Eqn. 6.139 to

$$\begin{pmatrix} G_{000}^{(1,1,1)} & G_{010}^{(1,1,1)} & G_{001}^{(1,1,1)} & G_{011}^{(1,1,1)} & \dots & G_{011}^{(1,3,1)} \\ G_{100}^{(1,1,1)} & G_{110}^{(1,1,1)} & \dots & & & \vdots \\ \vdots & & & \ddots & & \vdots \\ G_{100}^{(3,1,1)} & \dots & & & \dots & G_{111}^{(3,3,1)} \end{pmatrix} \left\{ \begin{pmatrix} -\phi_0(0)\tau_0^{(1)} \\ -\phi_1(0)\tau_0^{(1)} \\ -\phi_0(0)\tau_1^{(1)} \\ -\phi_1(0)\tau_1^{(1)} \\ -\phi_0(0)\tau_0^{(2)} \\ \vdots \\ -\phi_1(0)\tau_1^{(3)} \end{pmatrix} - \begin{pmatrix} \phi_0(0)\gamma_0^{(1)} \\ \phi_0(0)\gamma_1^{(1)} \\ \phi_1(0)\gamma_0^{(1)} \\ \phi_1(0)\gamma_1^{(1)} \\ \phi_0(0)\gamma_0^{(2)} \\ \vdots \\ \phi_1(0)\gamma_1^{(3)} \end{pmatrix} \right\} = \begin{pmatrix} U_0^{(1)} \\ U_1^{(1)} \\ U_0^{(2)} \\ \vdots \\ U_1^{(3)} \end{pmatrix}. \tag{6.144}$$

The ϕ terms in Eqns. 6.140-6.143 are all 1, so as long as they are counted correctly, you can reduce another index by combining the p and q terms to leave

$$U_n^{(\alpha,1)} = -G_{nq}^{(\alpha,\beta,1)}\tau_q^{(\beta,1)} - G_{np}^{(\alpha,\beta,1)}\gamma_p^{(\beta,1)}, \tag{6.145}$$

$$U_n^{(\alpha,2)} = G_{nq}^{(\alpha,\beta,2)}\tau_q^{(\beta,2)} - G_{np}^{(\alpha,\beta,2)}\sigma_p^{(\beta,2)}, \tag{6.146}$$

$$U_n^{(\alpha,3)} = G_{nq}^{(\alpha,\beta,3)}H_q^{(\beta,3)} + G_{np}^{(\alpha,\beta,3)}\sigma_p^{(\beta,3)}, \tag{6.147}$$

$$U_n^{(\alpha,4)} = -G_{nq}^{(\alpha,\beta,4)}H_q^{(\beta,4)} + G_{np}^{(\alpha,\beta,4)}\gamma_p^{(\beta,4)}, \tag{6.148}$$

where

$$G_{nq}^{(\alpha,\beta,\eta)} = \sum_{j=1}^{j_{max}}\sum_{m=0}^{m_{max}}\sum_{p=0}^{p_{max}}\frac{V_{mn}^{(\alpha,\eta)}(j)V_{pq}^{(\beta,\eta)*}(j)}{\lambda(j)-\rho^{(\eta)}v^2},\ \eta = 1,2,3,4, \tag{6.149}$$

and

$$G_{np}^{(\alpha,\beta,\eta)} = \sum_{j=1}^{j_{max}}\sum_{m=0}^{m_{max}}\sum_{q=0}^{q_{max}}\frac{V_{mn}^{(\alpha,\eta)}(j)V_{pq}^{(\beta,\eta)*}(j)}{\lambda(j)-\rho^{(\eta)}v^2},\ \eta = 1,2,3,4, \tag{6.150}$$

which can be rewritten using the notation of the CWW as

$$G_{nq}^{(\alpha,\beta,\eta)} = \sum_{j=1}^{j_{max}}\frac{Q_n^{(\alpha,\eta)}(j)Q_q^{(\beta,\eta)*}(j)}{\lambda(j)-\rho^{(\eta)}v^2},\ \eta = 1,2,3,4, \tag{6.151}$$

and

$$G_{np}^{(\alpha,\beta,\eta)} = \sum_{j=1}^{j_{max}}\frac{Q_n^{(\alpha,\eta)}(j)Q_p^{(\beta,\eta)*}(j)}{\lambda(j)-\rho^{(\eta)}v^2},\ \eta = 1,2,3,4, \tag{6.152}$$

where

$$Q_n^{(\alpha,\eta)}(j) = \sum_{m=0}^{m_{max}}V_{mn}^{(\alpha,\eta)}(j), \tag{6.153}$$

$$Q_p^{(\alpha,\eta)}(j) = \sum_{q=0}^{q_{max}}V_{pq}^{(\alpha,\eta)}(j), \tag{6.154}$$

$$Q_q^{(\alpha,\eta)}(j) = \sum_{p=0}^{p_{max}} V_{pq}^{(\alpha,\eta)}(j). \tag{6.155}$$

The final equations of motion (Eqns. 6.145-6.148) must be solved to find the velocity of the intersection wave. These are written in matrix form (Eqn. 6.144) as

$$\begin{pmatrix} G_{000}^{(1,1,1)} + G_{010}^{(1,1,1)} & G_{001}^{(1,1,1)} + G_{011}^{(1,1,1)} & \dots & G_{001}^{(1,3,1)} + G_{011}^{(1,3,1)} \\ G_{100}^{(1,1,1)} + G_{110}^{(1,1,1)} & \dots & & \vdots \\ \vdots & \ddots & & \vdots \\ G_{100}^{(3,1,1)} + G_{110}^{(3,1,1)} & \dots & \dots & G_{101}^{(3,3,1)} + G_{111}^{(3,3,1)} \end{pmatrix} \begin{pmatrix} -\tau_0^{(1)} \\ -\tau_1^{(1)} \\ -\tau_0^{(2)} \\ -\tau_1^{(2)} \\ -\tau_0^{(3)} \\ -\tau_1^{(3)} \end{pmatrix}$$

$$+ \begin{pmatrix} G_{000}^{(1,1,1)} + G_{001}^{(1,1,1)} & G_{010}^{(1,1,1)} + G_{011}^{(1,1,1)} & \dots & G_{010}^{(1,3,1)} + G_{011}^{(1,3,1)} \\ G_{100}^{(1,1,1)} + G_{101}^{(1,1,1)} & G_{110}^{(1,1,1)} + G_{111}^{(1,1,1)} & \dots & \vdots \\ \vdots & & \ddots & \vdots \\ G_{100}^{(3,1,1)} + G_{101}^{(3,1,1)} & \dots & \dots & G_{110}^{(3,3,1)} + G_{111}^{(3,3,1)} \end{pmatrix} \begin{pmatrix} -\gamma_0^{(1)} \\ -\gamma_1^{(1)} \\ -\gamma_0^{(2)} \\ -\gamma_1^{(2)} \\ -\gamma_0^{(3)} \\ -\gamma_1^{(3)} \end{pmatrix} \tag{6.156}$$

$$= \begin{pmatrix} U_0^{(1)} \\ U_1^{(1)} \\ U_0^{(2)} \\ \vdots \\ U_1^{(3)} \end{pmatrix}.$$

where the size of the $\bar{\mathbf{G}}$ matrix is now $3(n_{max}+1)$ x $3(p_{max}+1)$, the size of $\bar{\boldsymbol{\tau}}$, $\bar{\boldsymbol{\gamma}}$, and $\bar{\mathbf{U}}$ is $3(n_{max}+1)$ x 1 (note this is for $p_{max} = n_{max} = m_{max} = q_{max}$).

In the format of G_{np} or G_{nq} Eqn. 6.156 becomes

$$\begin{pmatrix} G_{00}^{(1,1,1)} & G_{01}^{(1,1,1)} & \dots & G_{01}^{(1,3,1)} \\ G_{10}^{(1,1,1)} & \dots & & \vdots \\ \vdots & \ddots & & \vdots \\ G_{10}^{(3,1,1)} & \dots & \dots & G_{11}^{(3,3,1)} \end{pmatrix} \begin{pmatrix} -\tau_0^{(1)} \\ -\tau_1^{(1)} \\ -\tau_0^{(2)} \\ -\tau_1^{(2)} \\ -\tau_0^{(3)} \\ -\tau_1^{(3)} \end{pmatrix} + \begin{pmatrix} G_{00}^{(1,1,1)} & G_{01}^{(1,1,1)} & \dots & G_{01}^{(1,3,1)} \\ G_{10}^{(1,1,1)} & \dots & & \vdots \\ \vdots & \ddots & & \vdots \\ G_{10}^{(3,1,1)} & \dots & \dots & G_{11}^{(3,3,1)} \end{pmatrix} \begin{pmatrix} -\gamma_0^{(1)} \\ -\gamma_1^{(1)} \\ -\gamma_0^{(2)} \\ -\gamma_1^{(2)} \\ -\gamma_0^{(3)} \\ -\gamma_1^{(3)} \end{pmatrix} = \begin{pmatrix} U_0^{(1)} \\ U_1^{(1)} \\ U_0^{(2)} \\ \vdots \\ U_1^{(3)} \end{pmatrix}, \tag{6.157}$$

where the first $\bar{\mathbf{G}}$ matrix is G_{nq} and the second is G_{np}.

Using the same arguments and derivation that were used to derive Eqn. 6.157 (except summing over m for the a_{mn} terms in Eqn. 6.122) yields

$$U_m^{(\alpha,1)} = -G_{mq}^{(\alpha,\beta,1)}\tau_q^{(\beta,1)} - G_{mp}^{(\alpha,\beta,1)}\gamma_p^{(\beta,1)}, \tag{6.158}$$

$$U_m^{(\alpha,2)} = G_{mq}^{(\alpha,\beta,2)}\tau_q^{(\beta,2)} - G_{mp}^{(\alpha,\beta,2)}\sigma_p^{(\beta,2)}, \tag{6.159}$$

$$U_m^{(\alpha,3)} = G_{mq}^{(\alpha,\beta,3)}H_q^{(\beta,3)} + G_{mp}^{(\alpha,\beta,3)}\sigma_p^{(\beta,3)}, \tag{6.160}$$

$$U_m^{(\alpha,4)} = -G_{mq}^{(\alpha,\beta,4)}H_q^{(\beta,4)} + G_{mp}^{(\alpha,\beta,4)}\gamma_p^{(\beta,4)}, \tag{6.161}$$

where

$$G_{mq}^{(\alpha,\beta,\eta)} = \sum_{j=1}^{j_{max}} \sum_{n=0}^{n_{max}} \sum_{p=0}^{p_{max}} \frac{V_{mn}^{(\alpha,\eta)}(j)V_{pq}^{(\beta,\eta)*}(j)}{\lambda(j) - \rho^{(\eta)}v^2} = \sum_{j=1}^{j_{max}} \frac{Q_m^{(\alpha,\eta)}(j)Q_q^{(\beta,\eta)*}(j)}{\lambda(j) - \rho^{(\eta)}v^2}, \ \eta = 1,2,3,4, \tag{6.162}$$

$$G_{mp}^{(\alpha,\beta,\eta)} = \sum_{j=1}^{j_{max}} \sum_{n=0}^{n_{max}} \sum_{q=0}^{q_{max}} \frac{V_{mn}^{(\alpha,\eta)}(j) V_{pq}^{(\beta,\eta)*}(j)}{\lambda(j) - \rho^{(\eta)} v^2} = \sum_{j=1}^{j_{max}} \frac{Q_m^{(\alpha,\eta)}(j) Q_p^{(\beta,\eta)*}(j)}{\lambda(j) - \rho^{(\eta)} v^2}, \ \eta = 1,2,3,4, \tag{6.163}$$

and

$$Q_m^{(\alpha,\eta)}(j) = \sum_{n}^{n_{max}} V_{mn}^{(\alpha,\eta)}(j). \tag{6.164}$$

Eqns. 6.158-6.161 are independent of Eqns. 6.145 - 6.148 because $\sum_m a_{mn}$ is independent of $\sum_n a_{mn}$.

6.4.2 Boundary Conditions

Using an approach analogous to the boundary conditions applied to the CWW (section 5.3.6), the intersection is characterized as a DD boundary condition or non-welded interface (see Appendix A.2) along each fracture. This is expressed as

$$\tilde{U}_\beta^{(1)} - \tilde{U}_\beta^{(2)} = \frac{\tilde{T}_{\beta,y}^{(1)}}{\kappa_{\beta 1b}}, \ \beta = x,y,z, \tag{6.165}$$

$$\tilde{U}_\beta^{(4)} - \tilde{U}_\beta^{(3)} = \frac{\tilde{T}_{\beta,y}^{(4)}}{\kappa_{\beta 1a}}, \ \beta = x,y,z, \tag{6.166}$$

$$\tilde{U}_\beta^{(1)} - \tilde{U}_\beta^{(4)} = \frac{\tilde{T}_{\beta,z}^{(1)}}{\kappa_{\beta 2a}}, \ \beta = x,y,z, \tag{6.167}$$

and

$$\tilde{U}_\beta^{(2)} - \tilde{U}_\beta^{(3)} = \frac{\tilde{T}_{\beta,z}^{(2)}}{\kappa_{\beta 2b}}, \ \beta = x,y,z. \tag{6.168}$$

Multiplying Eqn. 6.165 by $\sum_l \phi_l(kz)$, expanding using Eqn. 6.51, and integrating over the quarter space (carefully tracking the dummy variables and keeping the n term) leaves

$$\sum_{m=0}^{\infty} \left[\frac{a_{m,n}^{(\beta,1)}}{k} - \frac{a_{m,n}^{(\beta,2)}}{k} \right] = \frac{\tau_n^{(\beta,1)}}{\kappa_{\beta 1b}}. \tag{6.169}$$

This process is repeated for Eqn. 6.166 by multiplying by $\sum_l \phi_l(-kz)$, expanding using Eqn. 6.52, and integrating over the quarter space, which leaves

$$\sum_{m=0}^{\infty} \left[\frac{a_{m,n}^{(\beta,4)}}{k} - \frac{a_{m,n}^{(\beta,3)}}{k} \right] = \frac{H_n^{(\beta,4)}}{\kappa_{\beta 1a}}. \tag{6.170}$$

Again, Eqn. 6.167 is multiplied by $\sum_l \phi_l(ky)$, expanded using Eqns. 6.51 and 6.52, and integrated over the quarter space, which leaves

$$\sum_{n=0}^{\infty} \left[\frac{a_{m,n}^{(\beta,1)}}{k} - \frac{a_{m,n}^{(\beta,4)}}{k} \right] = \frac{\gamma_m^{(\beta,1)}}{\kappa_{\beta 2a}}. \tag{6.171}$$

Finally, Eqn. 6.168 is multiplied by $\sum_l \phi_l(-ky)$, expanded using Eqns. 6.51 and 6.52 and integrated over the quarter space leaving

$$\sum_{n=0}^{\infty} \left[\frac{a_{m,n}^{(\beta,2)}}{k} - \frac{a_{m,n}^{(\beta,3)}}{k} \right] = \frac{\sigma_m^{(\beta,2)}}{\kappa_{\beta 2b}}. \tag{6.172}$$

Equations 6.169 - 6.172 are simplified, using Eqns. 6.127 and 6.128, to the form

$$[U_n^{(\beta,1)} - U_n^{(\beta,2)}] = \frac{k}{\kappa_{\beta 1b}} \tau_n^{(\beta,1)}, \tag{6.173}$$

$$[U_n^{(\beta,4)} - U_n^{(\beta,3)}] = \frac{k}{\kappa_{\beta 1a}} H_n^{(\beta,4)}, \tag{6.174}$$

$$[U_m^{(\beta,1)} - U_m^{(\beta,4)}] = \frac{k}{\kappa_{\beta 2a}} \gamma_m^{(\beta,1)}, \tag{6.175}$$

and

$$[U_m^{(\beta,2)} - U_m^{(\beta,3)}] = \frac{k}{\kappa_{\beta 2b}} \sigma_m^{(\beta,2)}. \tag{6.176}$$

The stress boundary conditions assume continuity of stress across each interface and are expressed as

$$\tau_n^{(\beta,1)} = \tau_n^{(\beta,2)}, \tag{6.177}$$

$$H_n^{(\beta,4)} = H_n^{(\beta,3)}, \tag{6.178}$$

$$\gamma_n^{(\beta,1)} = \gamma_n^{(\beta,4)}, \tag{6.179}$$

and

$$\sigma_n^{(\beta,2)} = \sigma_n^{(\beta,3)}. \tag{6.180}$$

Applying the continuous stress boundary conditions (Eqns. 6.177 - 6.180) to the relationships between the displacement and stress at the interface (Eqns. 6.134 - 6.137), along with the DD boundary conditions (Eqns. 6.173 - 6.176), yields

$$[U_n^{(\beta,1)} - U_n^{(\beta,2)}] = \frac{k}{\kappa_{\beta 1b}} \tau_n^{(\beta)}, \tag{6.181}$$

$$[U_n^{(\beta,4)} - U_n^{(\beta,3)}] = \frac{k}{\kappa_{\beta 1a}} H_n^{(\beta)}, \tag{6.182}$$

$$[U_m^{(\beta,1)} - U_m^{(\beta,4)}] = \frac{k}{\kappa_{\beta 2a}} \gamma_m^{(\beta)}, \tag{6.183}$$

$$[U_m^{(\beta,2)} - U_m^{(\beta,3)}] = \frac{k}{\kappa_{\beta 2b}} \sigma_m^{(\beta)}, \tag{6.184}$$

$$U_n^{(\alpha,1)} = -G_{nq}^{(\alpha,\beta,1)} \tau_q^{(\beta)} - G_{np}^{(\alpha,\beta,1)} \gamma_p^{(\beta)}, \tag{6.185}$$

$$U_n^{(\alpha,2)} = G_{nq}^{(\alpha,\beta,2)} \tau_q^{(\beta)} - G_{np}^{(\alpha,\beta,2)} \sigma_p^{(\beta)}, \tag{6.186}$$

$$U_n^{(\alpha,3)} = G_{nq}^{(\alpha,\beta,3)} H_q^{(\beta)} + G_{np}^{(\alpha,\beta,3)} \sigma_p^{(\beta)}, \tag{6.187}$$

$$U_n^{(\alpha,4)} = -G_{nq}^{(\alpha,\beta,4)} H_q^{(\beta)} + G_{np}^{(\alpha,\beta,4)} \gamma_p^{(\beta)}, \tag{6.188}$$

$$U_m^{(\alpha,1)} = -G_{mq}^{(\alpha,\beta,1)} \tau_q^{(\beta)} - G_{mp}^{(\alpha,\beta,1)} \gamma_p^{(\beta)}, \tag{6.189}$$

$$U_m^{(\alpha,2)} = G_{mq}^{(\alpha,\beta,2)} \tau_q^{(\beta)} - G_{mp}^{(\alpha,\beta,2)} \sigma_p^{(\beta)}, \tag{6.190}$$

$$U_m^{(\alpha,3)} = G_{mq}^{(\alpha,\beta,3)} H_q^{(\beta)} + G_{mp}^{(\alpha,\beta,3)} \sigma_p^{(\beta)}, \tag{6.191}$$

and

$$U_m^{(\alpha,4)} = -G_{mq}^{(\alpha,\beta,4)} H_q^{(\beta)} + G_{mp}^{(\alpha,\beta,4)} \gamma_p^{(\beta)}, \tag{6.192}$$

where the media label on the stresses is not shown due to the continuous stress boundary conditions.

6.4.3 Secular Equations

An eigenvalue problem is setup for the 12 equations to describe the intersection. Using the above relations (Eqns. 6.181 - 6.192) the problem becomes

$$\Big(A\Big)\Big(B\Big) = \Big(0\Big) \tag{6.193}$$

where

$$\Big(A\Big) = \begin{pmatrix}
I & 0 & 0 & 0 & 0 & 0 & 0 & 0 & G_{nq}^{(\alpha,\beta,1)} & G_{np}^{(\alpha,\beta,1)} & 0 & 0 \\
0 & I & 0 & 0 & 0 & 0 & 0 & 0 & -G_{nq}^{(\alpha,\beta,2)} & 0 & G_{np}^{(\alpha,\beta,2)} & 0 \\
0 & 0 & I & 0 & 0 & 0 & 0 & 0 & 0 & 0 & -G_{np}^{(\alpha,\beta,3)} & -G_{nq}^{(\alpha,\beta,3)} \\
0 & 0 & 0 & I & 0 & 0 & 0 & 0 & 0 & -G_{np}^{(\alpha,\beta,4)} & 0 & G_{nq}^{(\alpha,\beta,4)} \\
0 & 0 & 0 & 0 & I & 0 & 0 & 0 & G_{mq}^{(\alpha,\beta,1)} & G_{mp}^{(\alpha,\beta,1)} & 0 & 0 \\
0 & 0 & 0 & 0 & 0 & I & 0 & 0 & -G_{mq}^{(\alpha,\beta,2)} & 0 & G_{mp}^{(\alpha,\beta,2)} & 0 \\
0 & 0 & 0 & 0 & 0 & 0 & I & 0 & 0 & 0 & -G_{mp}^{(\alpha,\beta,3)} & -G_{mq}^{(\alpha,\beta,3)} \\
0 & 0 & 0 & 0 & 0 & 0 & 0 & I & 0 & -G_{mp}^{(\alpha,\beta,4)} & 0 & G_{mq}^{(\alpha,\beta,4)} \\
I & -I & 0 & 0 & 0 & 0 & 0 & 0 & -\frac{k}{\kappa_{1b}} & 0 & 0 & 0 \\
0 & 0 & -I & I & 0 & 0 & 0 & 0 & 0 & 0 & 0 & -\frac{k}{\kappa_{1a}} \\
0 & 0 & 0 & 0 & I & 0 & 0 & -I & 0 & -\frac{k}{\kappa_{2a}} & 0 & 0 \\
0 & 0 & 0 & 0 & 0 & I & -I & 0 & 0 & 0 & -\frac{k}{\kappa_{2b}} & 0
\end{pmatrix}, \tag{6.194}$$

$$\Big(B\Big) = \begin{pmatrix}
U_n^{(\alpha,1)} \\
U_n^{(\alpha,2)} \\
U_n^{(\alpha,3)} \\
U_n^{(\alpha,4)} \\
U_m^{(\alpha,1)} \\
U_m^{(\alpha,2)} \\
U_m^{(\alpha,3)} \\
U_m^{(\alpha,4)} \\
\tau^{(\beta)} \\
\gamma^{(\beta)} \\
\sigma^{(\beta)} \\
H^{(\beta)}
\end{pmatrix}, \tag{6.195}$$

I is the identity matrix, and 0 is the null matrix.

Solving for the value of velocity when the determinant of the coefficient matrix is equal to zero (i.e., $|A| = 0$) in Eqn. 6.193 yields the velocity of the intersection wave. When the boundaries are changed (e.g., $\kappa \to 0$) the secular equation for the intersection reverts to the CWW secular equation (Eqn. 5.98) in the presence of any two blocks and one fracture remaining. If three of the four media are removed, or all $\kappa \to 0$, the WW solution in the remaining media ($|\bar{\mathbf{G}}| = 0$) is left, as expected.

6.4.4 Solving Matrix $\bar{\mathbf{M}}$

The same relationships used in the CWW derivation (section 5.3.4) are applied to solve the $\bar{\mathbf{M}}$ matrices for the intersection (Eqns. 6.108-6.111). The $C^{(1/2)}_{\alpha\beta\mu\nu}$ for the media creating the intersection discussed here is the general orthorhombic anisotropy case which is written as

$$C_{\alpha\beta\mu\nu} = \begin{pmatrix} C_{11} & C_{12} & C_{13} & 0 & 0 & 0 \\ C_{12} & C_{22} & C_{23} & 0 & 0 & 0 \\ C_{13} & C_{23} & C_{33} & 0 & 0 & 0 \\ 0 & 0 & 0 & C_{44} & 0 & 0 \\ 0 & 0 & 0 & 0 & C_{55} & 0 \\ 0 & 0 & 0 & 0 & 0 & C_{66} \end{pmatrix}. \tag{6.196}$$

Applying this to the definitions of $\bar{\mathbf{M}}$ (Eqns. 6.102 and 6.103) the components of $\bar{\mathbf{M}}$ are expressed as

$$M^{(1,1,1/2)}_{pq,mn} = \Big[C^{(1/2)}_{11}\delta_{pm}\delta_{qn} + C^{(1/2)}_{66}\delta_{qn}\Gamma_{p,m} + C^{(1/2)}_{55}\delta_{pm}\Gamma_{q,n} \Big], \tag{6.197}$$

$$M^{(1,1,3/4)}_{pq,mn} = \Big[C^{(3/4)}_{11}\delta_{pm}\delta_{qn} + C^{(3/4)}_{66}\delta_{qn}\Gamma_{p,m} + C^{(3/4)}_{55}\delta_{pm}\Gamma_{q,n} \Big], \tag{6.198}$$

$$M^{(1,2,1/2)}_{pq,mn} = \pm \Big[-i\delta_{qn}C^{(1/2)}_{12}\Psi_{p,m} + i\delta_{qn}C^{(1/2)}_{66}\Psi_{m,p} \Big], \tag{6.199}$$

$$M^{(1,2,3/4)}_{pq,mn} = \mp\Big[- i\delta_{qn}C^{(3/4)}_{12}\Psi_{p,m} + i\delta_{qn}C^{(3/4)}_{66}\Psi_{m,p}\Big], \tag{6.200}$$

$$M^{(1,3,1/2)}_{pq,mn} = \Big[- iC^{(1/2)}_{13}\delta_{pm}\Psi_{q,n} + iC^{(1/2)}_{55}\delta_{pm}\Psi_{n,q}\Big], \tag{6.201}$$

$$M^{(1,3,3/4)}_{pq,mn} = \Big[iC^{(3/4)}_{13}\delta_{pm}\Psi_{q,n} - iC^{(3/4)}_{55}\delta_{pm}\Psi_{n,q}\Big], \tag{6.202}$$

$$M^{(2,1,1/2)}_{pq,mn} = \pm\Big[- iC^{(1/2)}_{66}\delta_{qn}\Psi_{p,m} + iC^{(1/2)}_{12}\delta_{qn}\Psi_{m,p}\Big], \tag{6.203}$$

$$M^{(2,1,3/4)}_{pq,mn} = \mp\Big[- iC^{(3/4)}_{66}\delta_{qn}\Psi_{p,m} + iC^{(3/4)}_{12}\delta_{qn}\Psi_{m,p}\Big], \tag{6.204}$$

$$M^{(2,2,1/2)}_{pq,mn} = \delta_{pm}\delta_{qn}C^{(1/2)}_{66} + \delta_{qn}C^{(1/2)}_{22}\Gamma_{p,m} + \delta_{pm}C^{(1/2)}_{44}\Gamma_{q,n}, \tag{6.205}$$

$$M^{(2,2,3/4)}_{pq,mn} = \delta_{pm}\delta_{qn}C^{(3/4)}_{66} + \delta_{qn}C^{(3/4)}_{22}\Gamma_{p,m} + \delta_{pm}C^{(3/4)}_{44}\Gamma_{q,n}, \tag{6.206}$$

$$M^{(2,3,1/2)}_{pq,mn} = \pm\left[C^{(1/2)}_{23}\Psi_{m,p}\Psi_{q,n} + C^{(1/2)}_{44}\Psi_{p,m}\Psi_{n,q}\right], \tag{6.207}$$

$$M^{(2,3,3/4)}_{pq,mn} = \pm\left[C^{(3/4)}_{23}\Psi_{m,p}\Psi_{q,n} + C^{(3/4)}_{44}\Psi_{p,m}\Psi_{n,q}\right], \tag{6.208}$$

$$M^{(3,1,1/2)}_{pq,mn} = -i\delta_{pm}C^{(1/2)}_{55}\Psi_{q,n} + i\delta_{pm}C^{(1/2)}_{13}\Psi_{n,q}, \tag{6.209}$$

$$M^{(3,1,3/4)}_{pq,mn} = i\delta_{pm}C^{(3/4)}_{55}\Psi_{q,n} - i\delta_{pm}C^{(3/4)}_{13}\Psi_{n,q}, \tag{6.210}$$

$$M^{(3,2,1/2)}_{pq,mn} = \pm\left[C^{(1/2)}_{44}\Psi_{m,p}\Psi_{q,n} + C^{(1/2)}_{23}\Psi_{n,q}\Psi_{p,m}\right], \tag{6.211}$$

$$M^{(3,2,3/4)}_{pq,mn} = \pm\left[C^{(3/4)}_{44}\Psi_{m,p}\Psi_{q,n} + C^{(3/4)}_{23}\Psi_{n,q}\Psi_{p,m}\right], \tag{6.212}$$

$$M_{pq,mn}^{(3,3,1/2)} = \delta_{pm}\delta_{qn}C_{55}^{(1/2)} + \delta_{qn}C_{44}^{(1/2)}\Gamma_{m,p} + \delta_{pm}C_{33}^{(1/2)}\Gamma_{n,q}, \tag{6.213}$$

and

$$M_{pq,mn}^{(3,3,3/4)} = \delta_{pm}\delta_{qn}C_{55}^{(3/4)} + \delta_{qn}C_{44}^{(1/2)}\Gamma_{m,p} + \delta_{pm}C_{33}^{(3/4)}\Gamma_{n,q}. \tag{6.214}$$

When Eqns. 6.197 - 6.214 are assembled to form matrix $\bar{\mathbf{M}}$, the result is a Hermitian ($\bar{\mathbf{M}} = \bar{\mathbf{M}}^{\dagger}$) matrix, independent of k. The transformation used on the CWW (section 5.3.5) is also applied to the intersection result (Eqns. 6.108-6.111). An example calculation is shown in Appendix G.

6.5 Numerical Analysis of Intersection Waves

6.5.1 Introduction

The theoretical model for intersection waves, provided in section 6.4, is used to analyze the displacements of the intersection and determine the velocity of intersection waves. A custom Matlab code was developed (Appendix F) to calculate the velocity of intersection waves along with the displacements and decay properties of the intersection. Results are presented for an intersection between two orthogonal fractures in both isotropic and anisotropic media.

6.5.2 Equal Stiffness-Isotropic

The case for a fracture system with uniform stiffness is analyzed first, i.e., the most symmetric geometry. The stiffness along both the vertical and horizontal fracture is set equal, along with the x, y, and z components. The four media were assumed identical and isotropic for this portion of the analysis, and the material parameters used were $\rho = 2500\ \frac{kg}{m^3}$ and $\mu_L = 10\ GPa$. These two parameters, along with Poisson's ratio, determine the properties of the media under investigation. Similar to the CWW analysis (chapter 5), 15 expansion terms were used to analyze the intersection wave.

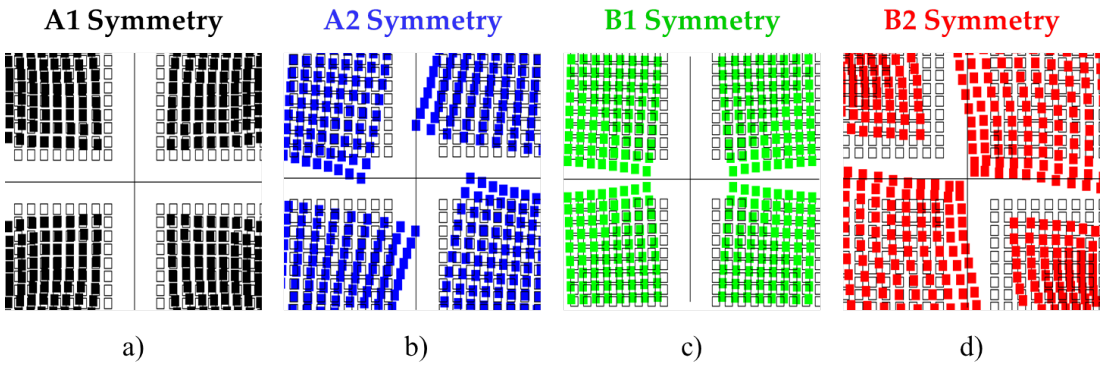

Figure 6.13. Calculated particle motion from the equal stiffness intersection. Note that the four modes match those predicted by group theory in Fig. 6.2.

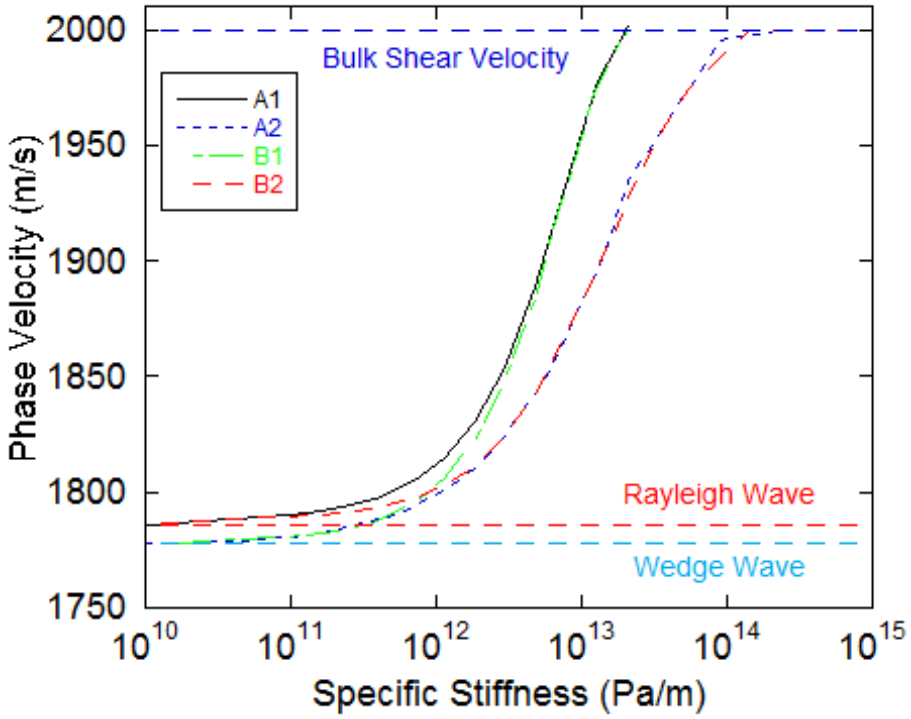

Figure 6.14. Intersection wave with equal stiffness fractures for isotropic media with a Poisson's ratio of +0.1.

The secular equation for the intersection (Eqn. 6.193) was solved using the parameters listed above, and several solutions were found within the expected velocity

range (i.e., WW to bulk S-wave velocity). The displacements at the intersection were calculated and four unique modes were found and are shown in Fig. 6.13. The four 1D modes, two wagging and two breathing, match those predicted by group theory for the equal stiffness intersection (Fig. 6.2). The fifth mode, ε, shown in Fig. 6.4b was not found in this analysis. This is not unexpected as this theoretical method assumes each wedge vibrates in either a breathing or wagging type motion, and the ε mode has neither type of motion. Further theoretical work is needed to determine the existence of this mode.

Using these particle motions as a guide to separate the different solutions, an analysis was performed to determine the effects of material properties on intersection waves. The results of isotropic media, with Poisson's ratio of +0.1, +0.2, and +0.3 are shown in Figs. 6.14- 6.16, respectively. For all three Poisson's ratio values, the A_2 and B_1 modes propagate with speeds that start at the WW velocity and increase up to the bulk S-wave velocity, with increasing specific stiffness. This trend is expected because the A_2 and B_1 modes both have wagging type motion, which is only supported in positive Poisson's ratio media [153].

The velocity for the other two modes (i.e., A_1 and B_2), which have breathing type motion, begin at the Rayleigh wave velocity and increase up to the bulk S-wave velocity as a function of specific stiffness (Fig. 6.14 - 6.16). A wedge cannot support these breathing modes for the positive Poisson's ratio used so the A_1 and B_2 modes are excited at the Rayleigh wave velocity, which is the speed of a delocalized WW. Note that all of these modes have overlap in the dispersion curves (Figs. 6.14-6.16). Without the use of group theory to determine which modes are expected, it would have been difficult to isolate the unique vibrational modes for these parameters.

It was shown in section 4.3.3 that the breathing type WW should exist for negative Poisson's ratio materials. The natural question then arises, do the breathing intersection modes also exist for these parameters? To answer this question, the same material parameters used above are analyzed for a Poisson's ratio of -0.3 to compare with the results of Fig. 6.16, which has a Poisson's ratio of +0.3.

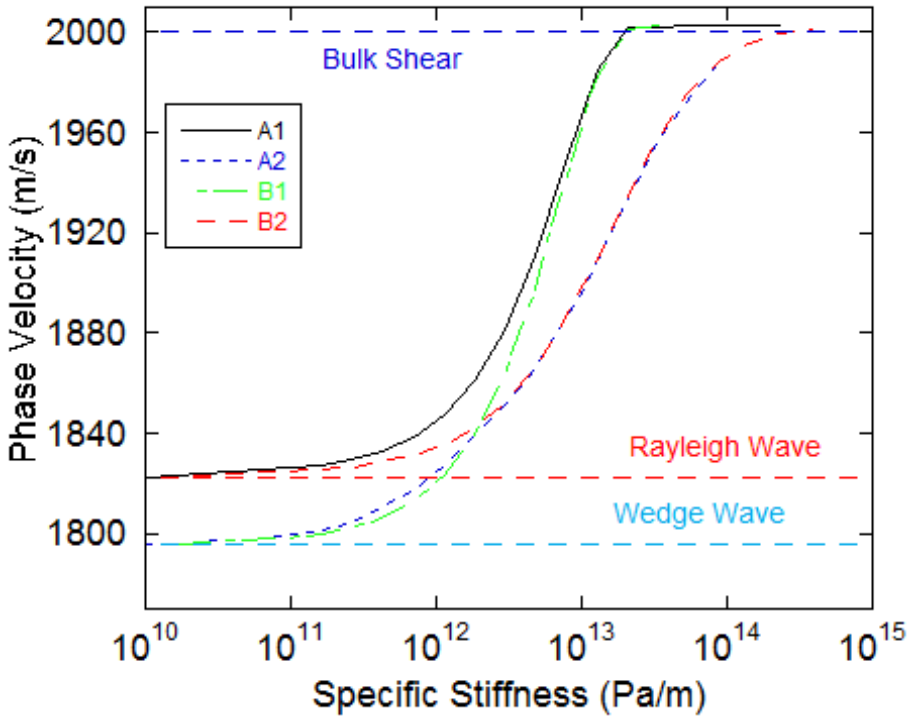

Figure 6.15. Intersection wave with equal stiffness fractures for isotropic media with a Poisson's ratio of +0.2.

The results, shown in Fig. 6.17, indicate a switch in properties among the modes in comparison to Fig. 6.16. For the Poisson's ratio of -0.3 the speeds of the A_1 and B_2 modes, which have breathing type motion, begin at the WW velocity and increase up to the bulk S-wave velocity as a function of specific stiffness. This is not surprising because the material parameters are now able to support the breathing type WWs. For the other two modes, A_2 and B_1, which have wagging type motion (Fig. 6.13), the velocity begins at the Rayleigh wave velocity and increases up to the bulk S-wave velocity. These results indicate that whichever media is used to create the intersection, i.e., positive or negative Poisson's ratio media, determines which of the four 1D modes for the equal stiffness case are supported at the WW and Rayleigh wave velocity.

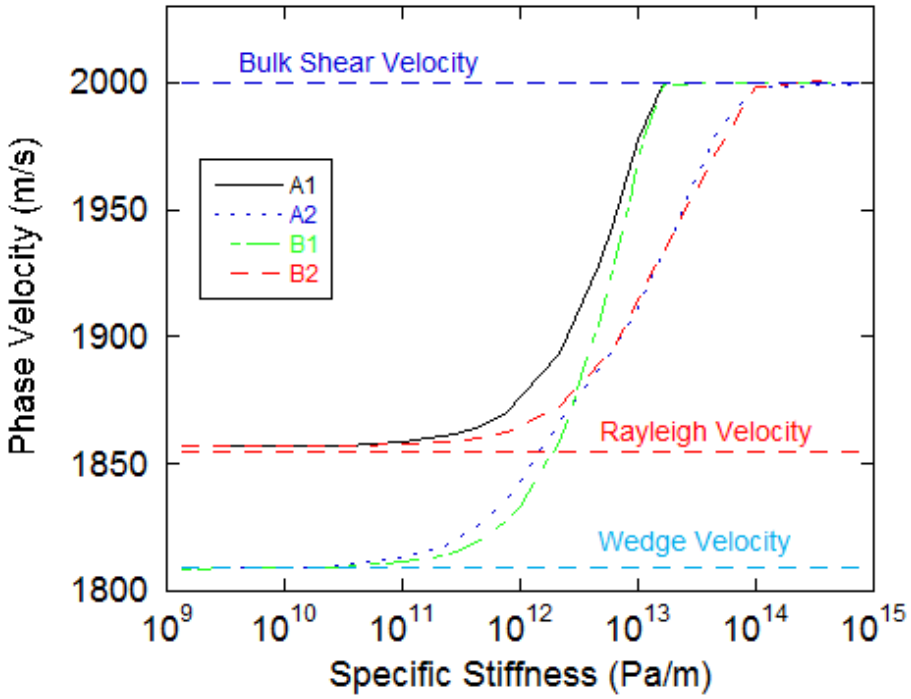

Figure 6.16. Intersection wave with equal stiffness fractures from isotropic media with a Poisson's ratio of +0.3. Note that the wagging type modes (A_2 and B_1) start at the WW velocity at low stiffness and the breathing type (A_1 and B_2) modes start at the Rayleigh wave velocity.

6.5.3 Equal Stiffness-Anisotropic

A similar analysis was performed using anisotropic material parameters. The material properties used are those of the anisotropic aluminum bars listed in Table H.3. The velocity of the intersection wave, when the stiffnesses among the fractures are not equal, is shown in Fig. 6.18. In agreement with the isotropic results, the velocity of the A_2 and B_1 modes begin at the WW for low specific stiffness. The velocity of the A_1 and B_2 modes, which have breathing type motion, begin at the Rayleigh wave velocity for low specific stiffness. All four modes increase in velocity as a function of specific stiffness, in agreement with the isotropic analysis presented above. The particle motion is identical to Fig. 6.13.

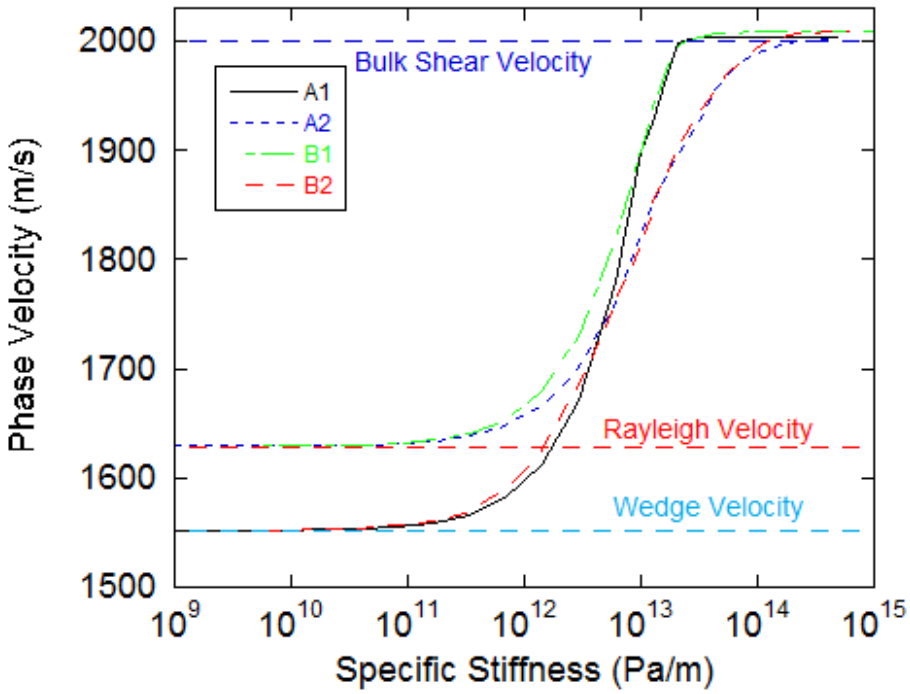

Figure 6.17. Intersection wave with equal stiffness fractures from isotropic media with a Poisson ratio of -0.3. Note that the wagging type modes (A_2 and B_1) start at the Rayleigh wave velocity at low stiffness and the breathing type (A_1 and B_2) modes start at the WW velocity.

6.5.4 Unequal Stiffness-anisotropic

Although the equal stiffness and material parameters case discussed above is important, a more realistic case is when the two fracture planes have unequal stiffness. Stress distributions in the Earth and in laboratory experiments often are non-uniform on purpose (e.g., biaxial loading, local stress gradients). Here, the anisotropic aluminum bar parameters of Table H.3 were used to analyze the effect of various fracture conditions on the intersection waves under unequal stiffness settings.

As expected, several solutions to the secular equation for the intersection waves (Eqn. 6.193) were found. These solutions were analyzed, and found to yield the four unique vibrational modes, shown in Fig. 6.19. All four modes are wagging

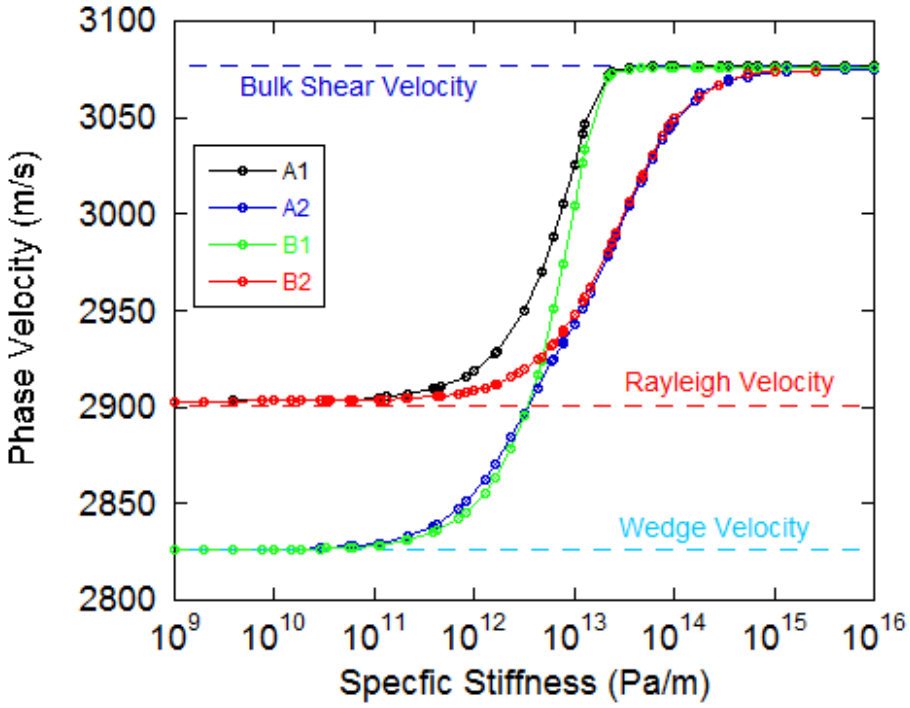

Figure 6.18. Numerical intersection wave results for anisotropic material parameters (Table H.3) with equal stiffness along all fractures.

type wedge vibrations, as expected for these material parameters, and agree with the results predicted by group theory from section 6.3. Analyzing the particle motion of each solution found from the Matlab code, the four modes were isolated from each other.

In the first case, the stiffness of the vertical fracture was maintained with a constant specific stiffness of 0.1 $\frac{TPa}{m}$ while the stiffness of the horizontal fracture was varied from 10 $\frac{GPa}{m}$ to 1 $\frac{PPa}{m}$ (Fig. 6.20a). For a specific stiffness of 0.1 $\frac{TPa}{m}$ on the vertical fracture, the fractures are essentially uncoupled. Blocks 1-4 and 2-3 are only coupled along the horizontal fracture (Fig. 6.12), which results in a geometry and loading condition that supports a CWW type wave. As shown in Fig. 6.20a, at low specific stiffness on the horizontal fracture, all 4 blocks are uncoupled, leading to WW type velocities. As the horizontal fracture plane is closed (i.e., specific stiffness

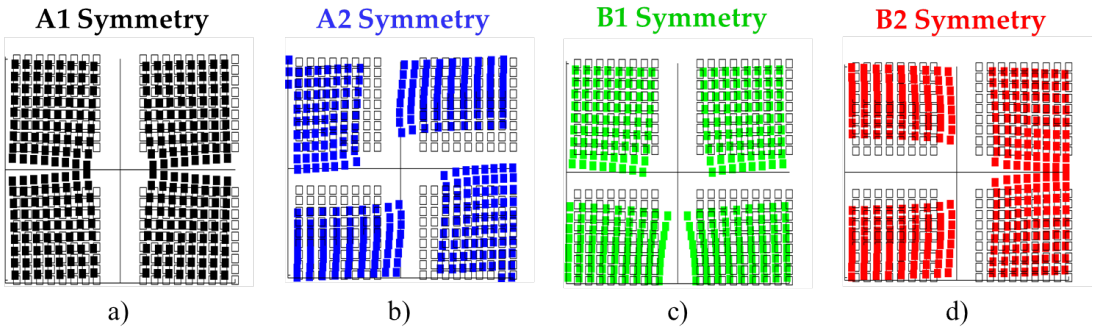

Figure 6.19. Calculated particle motion from the unequal stiffness intersection. Note that the four modes match those predicted by group theory in Fig. 6.10.

increases), the presence of a free surface on the vertical fracture plane leads to, at most, a Rayleigh wave velocity.

When the specific stiffness on the vertical fracture is increased to 1 $\frac{TPa}{m}$ or 10 $\frac{TPa}{m}$, the observed intersection velocity varies as shown in Figs. 6.20b-c. The increase in coupling across the vertical fracture leads to an increase in the observed velocity of these modes. For these specific stiffnesses on the vertical fracture, blocks 3-4 and 1-2 (Fig. 6.12) are partially coupled, leading to a velocity above the WW velocity, even at low specific stiffness on the horizontal fracture plane. Once the horizontal fracture plane is essentially welded (high stiffness) the partial closing of the vertical fracture prevents the velocity of the intersection wave from completely reaching the bulk S-wave velocity, because the intersection is not fully welded.

Finally, when a high specific stiffness is applied to the vertical fracture plane (1 $\frac{PPa}{m}$) the plane is welded. The resulting velocity of the intersection wave, shown in Fig. 6.20d, verifies this. At low specific stiffness on the horizontal plane (i.e., x-axis in Fig. 6.20) the horizontal plane is acting as a free surface, supporting Rayleigh wave type modes. As the horizontal plane couples together, the velocity of the modes increases and eventually reaches a state where all four blocks are welded and a bulk S-wave is supported.

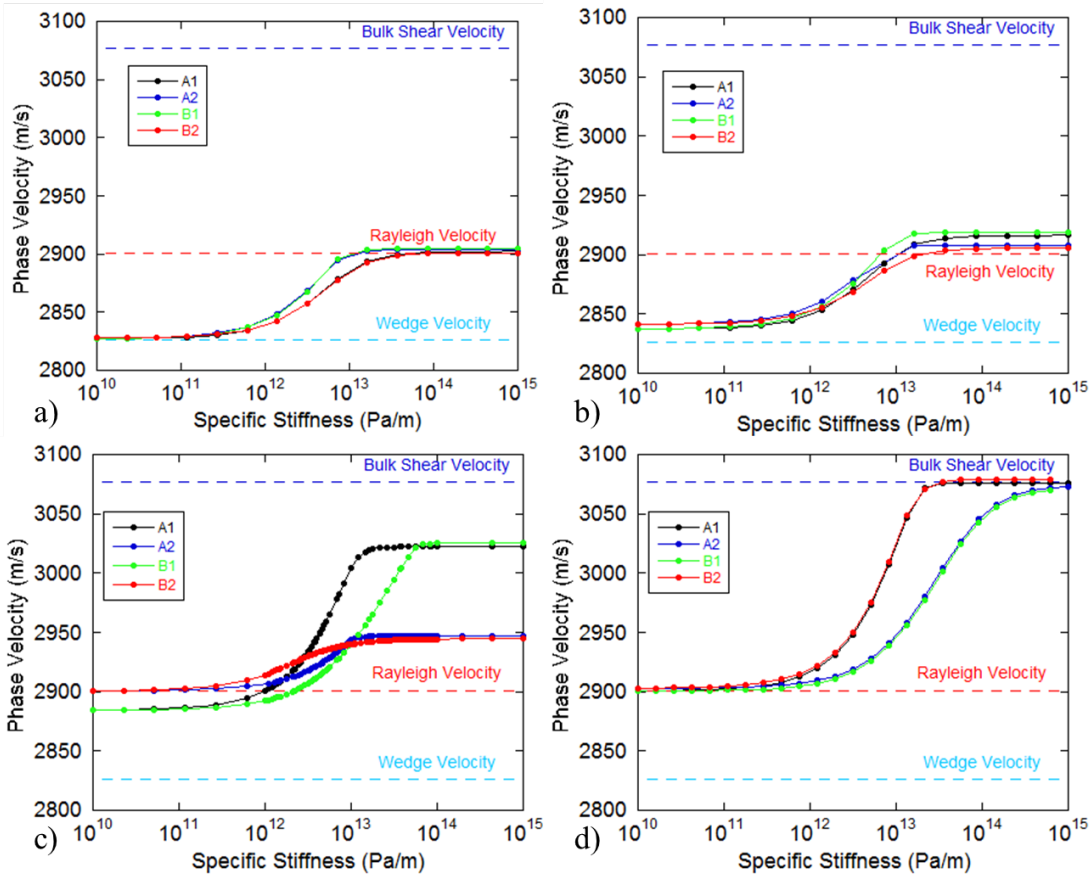

Figure 6.20. Numerical results for the anisotropic intersection wave using unequal stiffness settings (parameters in Table H.3). The stiffness along the vertical fracture (κ_1 Fig. 6.12) was held constant at a) $0.1\frac{TPA}{m}$, b) $1\frac{TPa}{m}$, c) $10\frac{TPA}{m}$, and d) $1\frac{PPa}{m}$. The horizontal fracture (κ_2 was altered as shown on the x-axis.

An alternative method to analyze the data from Fig. 6.20 is to make these into a surface. The surfaces are shown in Fig. 6.21 for all four modes. When both fractures have low stiffness, all of the modes have velocities at the WW velocity (wedge valley Fig. 6.21). When one of the stiffnesses is increased, the velocity also increases up to the Rayleigh wave velocity (Rayleigh plateau Fig. 6.21). This range matches the results observed for the CWW and indicates what happens at a single fracture when one of the fractures is held open.

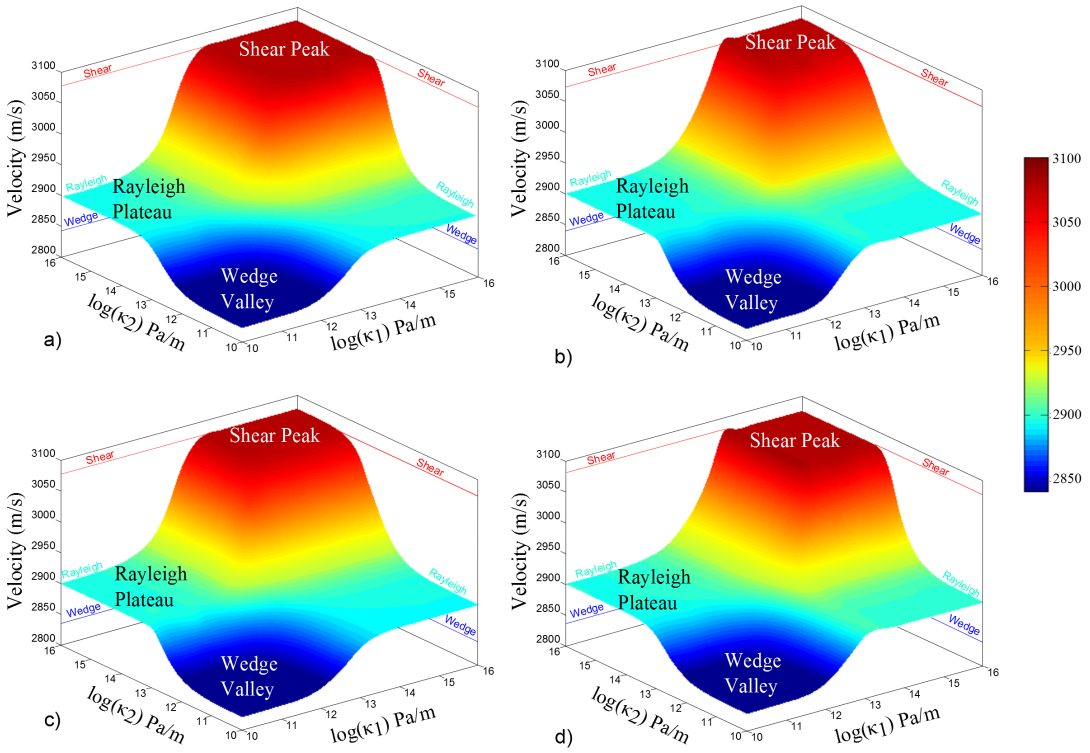

Figure 6.21. Surfaces showing the velocity of the intersection wave for modes a) A_1, b) A_2, c) B_1, and d) B_2 as a function of the two stiffnesses (κ_1 and κ_2) in unequal stiffness cases.

If one fracture is closed (i.e., $log(\kappa) > 14\ \frac{Pa}{m}$) the behavior is different. When the vertical fracture (κ_1) is at high stiffness and the horizontal fracture (κ_2) is at low stiffness the intersection behaves as a free surface and supports Rayleigh type waves (Rayleigh plateau Fig. 6.21). When the horizontal fracture stiffness (κ_2) increases, the intersection wave velocity also increases until both fractures are welded and support bulk S waves (shear peak Fig. 6.21). The same behavior is seen when the two stiffnesses are changed, i.e. when the horizontal stiffness is held at a high value and the vertical stiffness is varied. These regions of the intersection wave correspond to interface wave type behavior, as expected. These surfaces indicate the possible regions of existence for the intersection wave when the fracture intersection is under unequal stiffness conditions.

6.5.5 Effect of Shear and Normal Stiffness Components

A parameter study was performed for the unequal stiffness case to determine the effects the components of the stiffness terms have, i.e., the x, y, and z components. A stiffness of 10 $\frac{TPa}{m}$ on the vertical fracture and a varying stiffness for the horizontal fracture was used. This case was selected because all four modes were between the WW and S-wave velocity, with neither high nor low stiffness reaching these velocity limits (Fig. 6.20c). Any effects from unequal x, y, or z components should be apparent. The case with all the x, y, z components equal for this stiffness condition is shown in Fig. 6.20c. Only the components that had an effect on the velocity dispersion curve are shown here, those components that had no effect, are not presented.

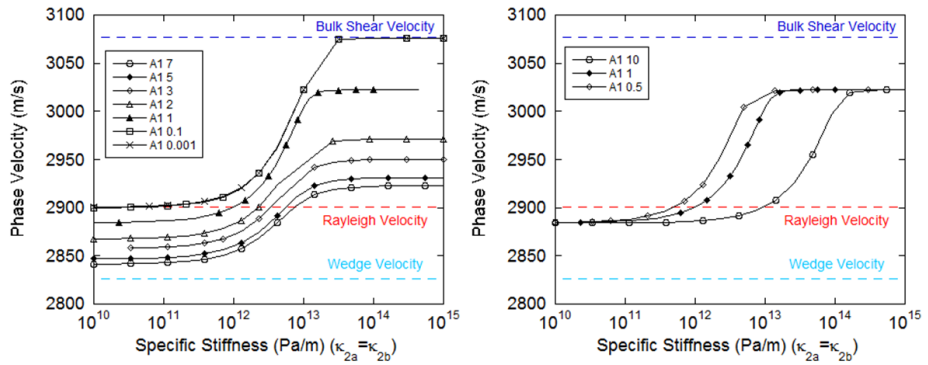

Figure 6.22. Effect of changing the components of stiffness on both the vertical and horizontal fracture for the A_1 mode. Changing a) the y component on the vertical fracture and b) the z component on the horizontal fracture. All other components had no effect on the A_1 mode.

The analysis yields different results for all four modes with unequal stiffness components. The results of the A_1 mode are shown in Fig. 6.22. When the y component on the vertical fracture is varied, the A_1 velocity changes in magnitude but is unaffected by the varying horizontal fracture. When the z component of the horizontal fracture stiffness (κ_2) is changed, the velocity of the A_1 mode is a function of specific

stiffness, as shown in Fig. 6.22b. All other components (i.e., x, z on vertical fracture and x, y on the horizontal fracture) have no effect on the A_1 mode, and are not shown.

The A_2 mode is more strongly affected by the components of the specific stiffness. When the x or z component of the specific stiffness on the vertical fracture are altered, the velocity of the A_2 mode changes. The x component effects the velocity at low and high stiffness (Fig. 6.23a) while the z component effects only the velocity at low stiffness (Fig. 6.23b). When the x and y parameters on the horizontal fracture are varied, the result is less dramatic, but still affect the velocity of the A_2 mode. The x component on the horizontal fracture, shown in Fig. 6.23c, shifts the velocity along the specific stiffness axis, but has no effect on the limits or slope of the dispersion curve. The y component on the horizontal fracture has a very small effect, but does change the slope of the dispersion curve as shown in Fig. 6.23d.

Only the y component on the vertical fracture affected the B_1 mode (Fig. 6.24a). The functional dependence of this mode changes speed as well as range of the velocity predicted for these modes. Along the horizontal fracture, both the x and y components of the specific stiffness affect the variation with horizontal stiffness for the B_1 mode. The x component shifts the velocity in stiffness, but maintains the same limits, while the y component has a very small effect on the slope of the curve (Figs. 6.24b, c).

Finally, the B_2 mode is affected by the x and z components of specific stiffness along the vertical fracture plane. These changes show a variation in velocity and a small shift in curvature (Figs. 6.25a,b). Along the horizontal fracture plane, only the z component of the specific stiffness affects the B_2 mode. Variations in the z component shift the velocity as a function of specific stiffness (Fig. 6.25c).

These results indicate a strong sensitivity of the state of an intersection to variations in the specific stiffness components and suggest that intersection waves can be manipulated and controlled by variations in the components of the specific stiffness. Although the above discussion only changed one component of the specific stiffness at a time, when more than one component is changed, the effect of each individual component is applied to the intersection wave results. In other words, the effect of

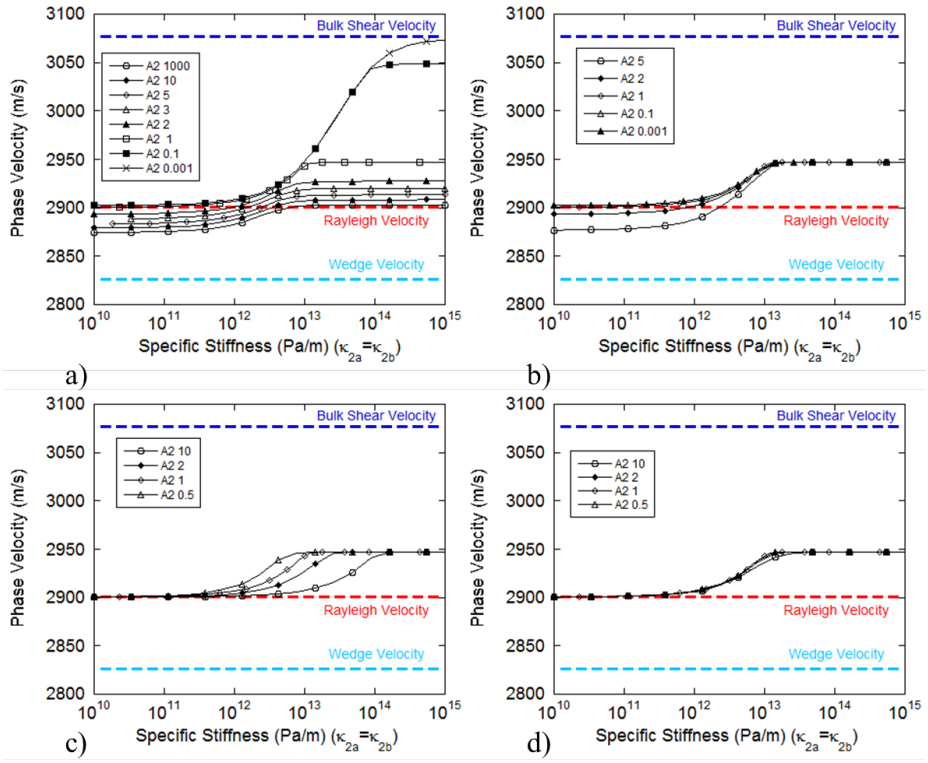

Figure 6.23. Effect of changing the components of stiffness on both the vertical and horizontal fracture on the A_2 mode. Changing a) the x component on the vertical fracture, b) the z component on the vertical fracture, c) the x component on the horizontal fracture, and d) the y component on the horizontal fracture. All other components had no effect on the A_2 mode.

the components are independent and are superposed when more than one component varies.

6.5.6 Summary

The results of the numerical study presented here indicate the expected results for the experimental study, which is described next. The equal stiffness case is very unlikely to be reached in an experiment, due to minor variations in contact area, loading configurations, and material properties. For this reason, the unequal stiffness

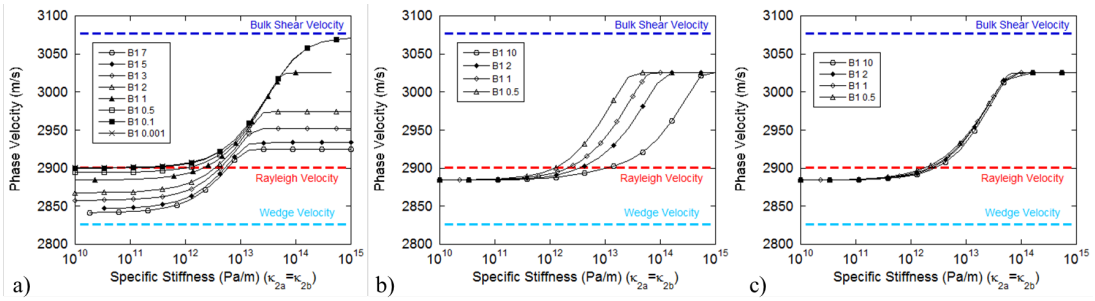

Figure 6.24. Effect of changing the components of stiffness on both the vertical and horizontal fracture on the B_1 mode. Changing a) the y component on the vertical fracture, b) the x component on the horizontal fracture, and c) the y component on the horizontal fracture. All other components had no effect on the B_1 mode.

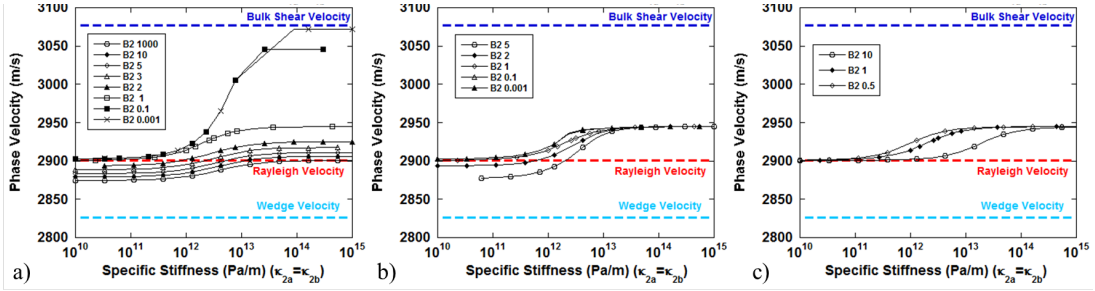

Figure 6.25. Effect of changing the components of stiffness on both the vertical and horizontal fracture on the B_2 mode. Changing a) the x component on the vertical fracture, b) the z component on the vertical fracture, and c) the z component on the horizontal fracture. All other components had no effect on the B_2 mode.

case, which is more reasonable, is used to examine the experimental results in the remainder of this work.

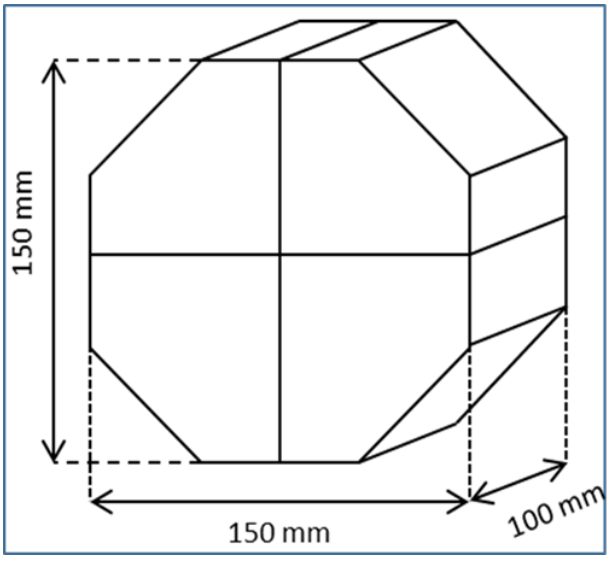

Figure 6.26. Sample dimensions of the hexagonal aluminum used in the intersection experimental analysis.

6.6 Experimental Setup

6.6.1 Introduction

Experiments to measure intersection waves are described in this chapter along with a discussion of the results. The experiments are similar to those used for the CWW in section 5.5, except that biaxial loading conditions and fracture intersections, instead of surface fractures, are also studied.

6.6.2 Samples

Two types of aluminum samples were used for the intersection wave experiments. The first was a hexagonal cut sample of aluminum with dimensions shown in Fig. 6.26. The second aluminum samples were the same long bars that were used in section 5.5 (Fig. 5.19). The material properties and sizes of these samples are listed in Tables H.2 - H.3.

6.6.3 Biaxial Load Frame Setup

Two different biaxial load frame systems were used for the intersection wave analysis. For both systems the same horizontal load frame was utilized. The horizontal load frame was an in house built 222 kN load frame with a Parker actuator and an Interface, model 1220AF-50K-B, 222 kN load cell. For the hexagonal samples, this load frame was used in conjunction with a Soil Test 445 kN vertical load frame controlled by Tiab v2.06.17 software and monitored with an Interface, model 1232ACK-100K-B, 445 kN load cell. The horizontal frame was supported with a set of chains supported by a mechanical lift system. The system is shown in Fig. 6.27.

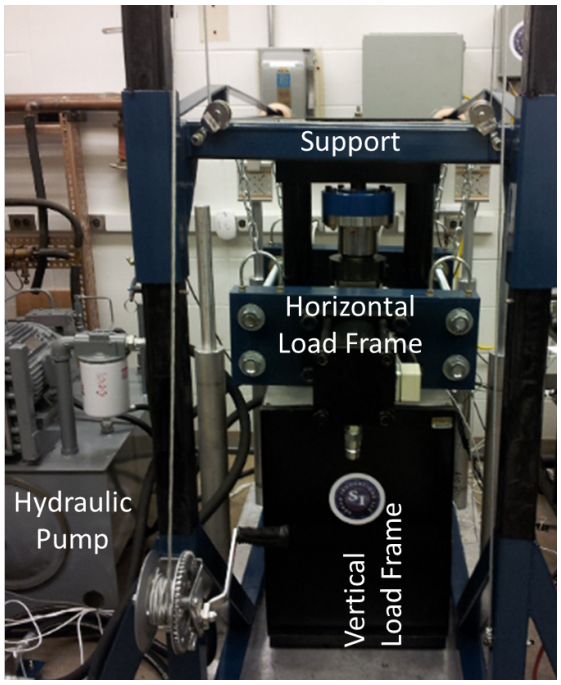

Figure 6.27. The biaxial load frame system used to study intersection waves on the hexagonal samples. The vertical and horizontal load frames are labeled, as well as the hydraulic pump and support for the horizontal frame.

For the long aluminum bar samples, a larger vertical load frame was required due to the limited size of the Soil Test frame. The vertical frame used was the same Instron load frame described in section 5.5. For this system, the horizontal load was

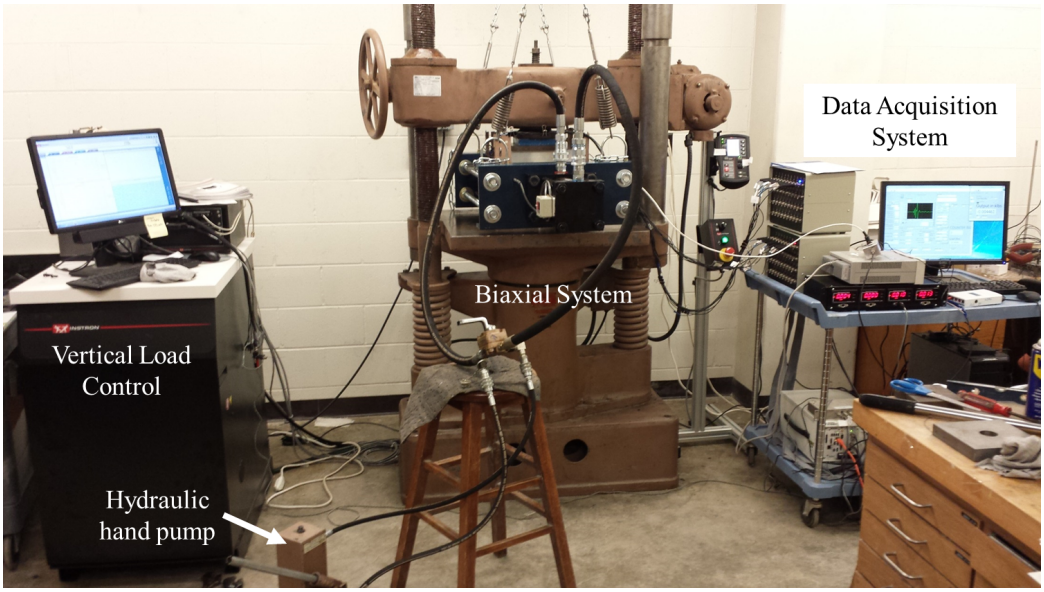

Figure 6.28. The biaxial load frame system with vertical load control, horizontal hand pump control, and the data acquisition system used to study the aluminum bars.

adjusted using a hand hydraulic pump while the load was measured by a load cell and stored using a Labview controlled program on the same computer as the transducer arrays (Fig. 6.28). A detailed description of the support built for the horizontal load frame is described below.

To suspend the 222 kN load frame, a support system was built onto the structure of the Instron load frame. A 1.91 cm ($\frac{3}{4}$ in.) thick, low-carbon steel bar measuring 20.32 cm x 60.96 cm (8 in. x 24 in.), was attached to a low-carbon steel square tube measuring 6.35 cm x 6.35 cm x 91.44 cm (2.5 in. x 2.5 in. x 36 in.) with long, 1.27 cm wide ($\frac{1}{2}$ in.) bolts supporting and stabilizing the structure. A 0.64 cm x 10.16 cm ($\frac{1}{4}$ in. x 4 in.) galvanized steel eyelet was screwed into each end of the square tube and fastened with nylon nuts to attach the chain quick connects from the supporting chains on the load frame. This setup is shown in Fig. 6.29a.

Due to the nature of the load frame operation, the two frames were required to be independently supported and have swivel heads on each frame [222, 223]. In addition, hanging the 222 kN frame allowed it to rotate, if needed, to reduce any stress buildup

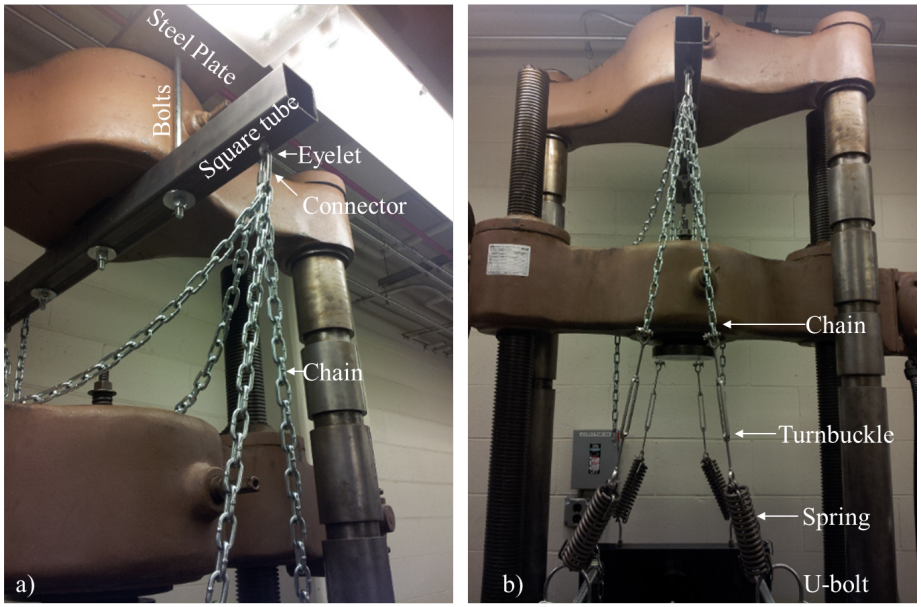

Figure 6.29. a) Top support on the Instron load frame to support the 222 kN load frame. b) Connection from the support to the load frame using chains, turnbuckles, and springs.

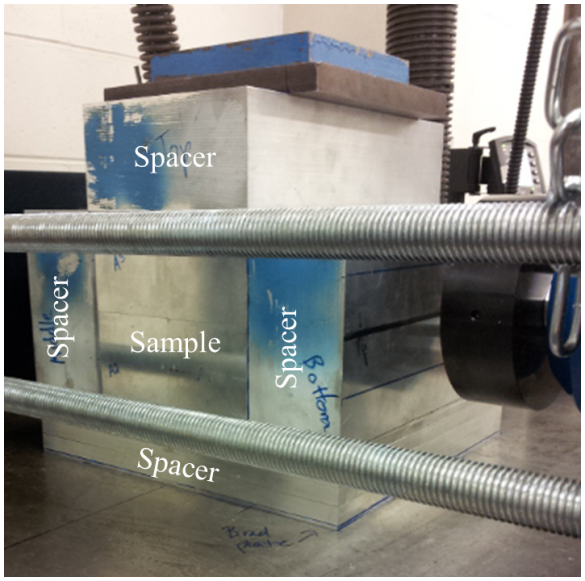

Figure 6.30. The spacers above, below, and on either side of the sample within the biaxial load frames.

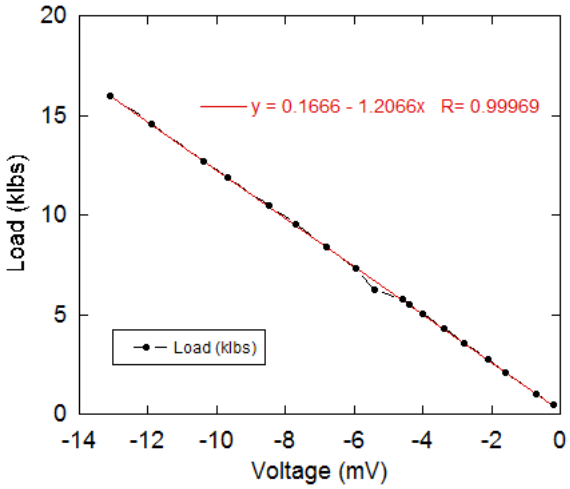

Figure 6.31. Calibration and fit of the load cell for the horizontal frame.

on the surfaces of the samples. To achieve this, the 222 kN load frame was supported with a series of type 302 stainless steel safety extension springs 20.32 cm, 163.3 kg limit (8 in. long, 360 lbs. limit) connected to type 316 stainless steel turnbuckles 226.8 kg limit (jaw and jaw, 500 lbs. limit), and metal chains connected to u-bolt supports on the load frame, all of which are shown in Fig. 6.29b. The turnbuckles allow minor changes to be made in the position of the load frame, making leveling easier. The springs allow the support to hang freely and remove excess build up of stress.

The samples were placed within the load frames, with spacers above, below, and on either side to help evenly distribute the load (Fig. 6.30) [99]. Once the samples and spacers were centered, the transducer array platens (see section 5.5) were placed onto the samples and experiments are performed. The calibration of the load 50klbs load cell used on the horizontal load frame is shown in Fig. 6.31.

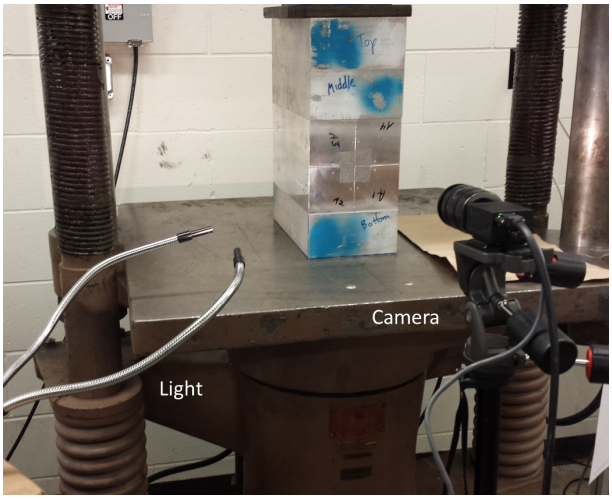

Figure 6.32. Setup of four aluminum bars used in uniaxial DIC experiments. The light source is shown on the left and the camera is shown on the right.

6.6.4 Digital Image Correlation Setup

Uniaxial

A similar digital image correlation (DIC) experiment to that described in section 5.5.4 was performed on the intersection. The setup for the four block case is shown in Fig. 6.32, with the speckle paint on each corner shown in Fig. 6.33. Note that the speckle pattern was only applied to 2.54 cm squares on the corner of each sample because the viewing window of the CCD camera was limited. This was larger than the transducer size (0.5 in.) so the intersection wave was well within this scanned area.

Biaxial

In addition to the uniaxial DIC experiments, biaxial DIC experiments were also performed. Using the biaxial system described in the previous section, the bar samples were placed inside of the setup and analyzed to verify the loading conditions under

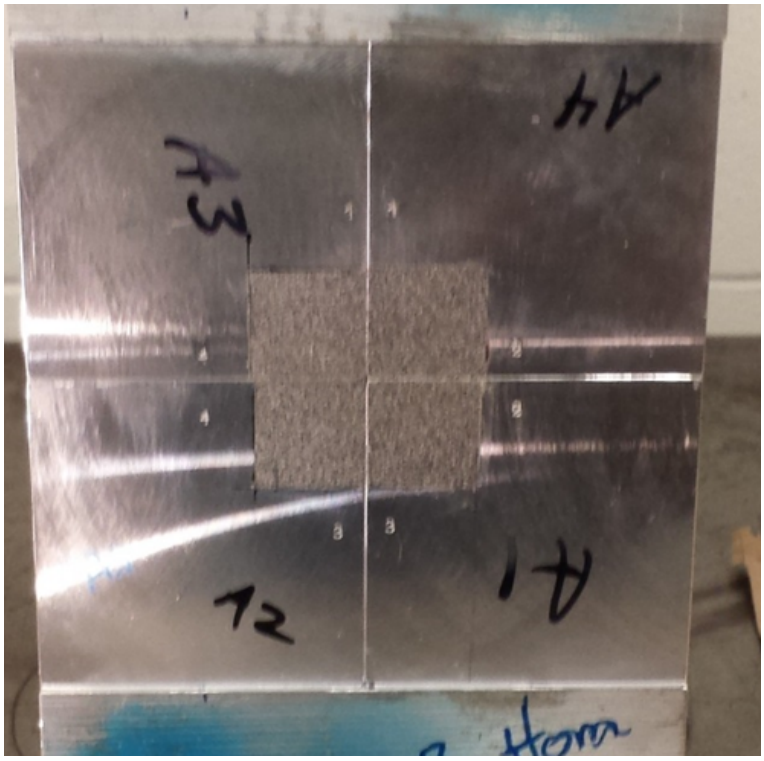

Figure 6.33. Speckle paint for the four aluminum bars used in DIC experiments. The speckle paint is shown on each sample near the intersection.

biaxial load. Due to the geometry of the load frames, the setup was rotated to that shown in Fig. 6.34. The same camera, light source, speckle paint, and process were used in this experimental analysis.

6.7 Experimental Results

6.7.1 Introduction

The results of the intersection wave, under various loading conditions, are presented here along with an analysis of the results. First, the loading conditions in the experiments are examined based on the DIC results. Then, the ultrasonic signals and wave analysis are presented.

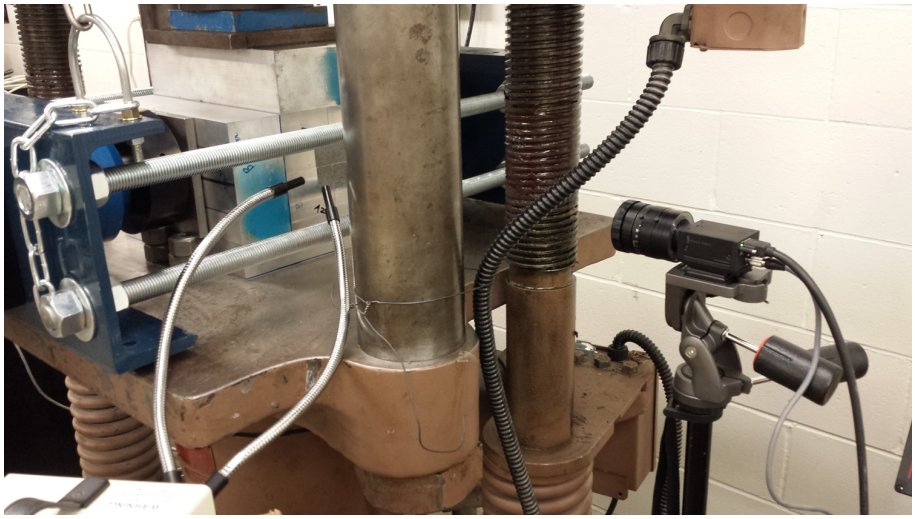

Figure 6.34. DIC setup for biaxial loading investigation of the long aluminum samples. The camera and light source are visible in the image. Setup is rotated 90° from that in Fig. 6.32.

6.7.2 Digital Image Correlation- Uniaxial Loading

The horizontal and vertical displacements of the samples during uniaxial load, Figs. 6.35 and 6.36, respectively, were determined from DIC analysis of the surface. The images were analyzed as described in section 6.6.4. Horizontal displacements (Fig. 6.35) from the DIC measurements indicate that the intersection under uniaxial loading has small displacements relative to the vertical displacement discussed below. The measured displacements are on the order of a few microns (see scale bars) and are uniform within the samples and across the horizontal fracture plane. There is a slight discontinuity across the vertical fracture plane, which most likely arises from the lack of horizontal confinement. The vertical fracture is not coupled as it would be for biaxial loading conditions.

The vertical displacements (Fig. 6.36) are on the order of mm and are more uniform than the horizontal displacements, across all fracture planes. As the load is increased from 100 kN to 400 kN (Figs. 6.36a-d) the amplitude of the displacement also increases. There are small variations within the viewing window, but across both

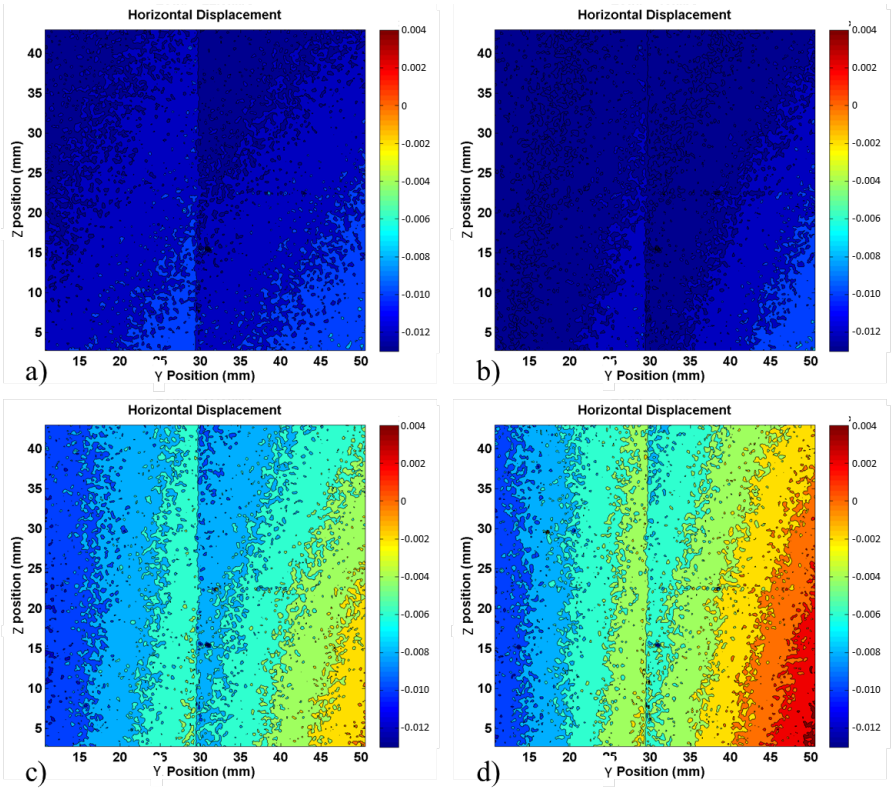

Figure 6.35. DIC results for the horizontal displacement of four aluminum bars under uniaxial load. The image is viewing the y-z plane (Fig. 6.12) with the vertical load at a) 100 kN, b) 200 kN, c) 300 kN, and d) 400 kN. The fractures are located along the lines Y= 22.5 mm and Z = 30 mm.

the vertical and horizontal fractures the displacements are uniform and roughly continuous. These results indicate that under uniaxial loading, the maximum displacements are in the direction of the applied load and are roughly uniform throughout the samples. This also verifies that the applied load is being distributed by the spacers.

6.7.3 Digital Image Correlation - Biaxial Loading

The uniformity of applied loads was also examined for biaxial loading conditions using DIC. For this test, a horizontal load of 45 kN was applied to the sample while the vertical load varied between 0-400 kN. The horizontal displacement of the sample

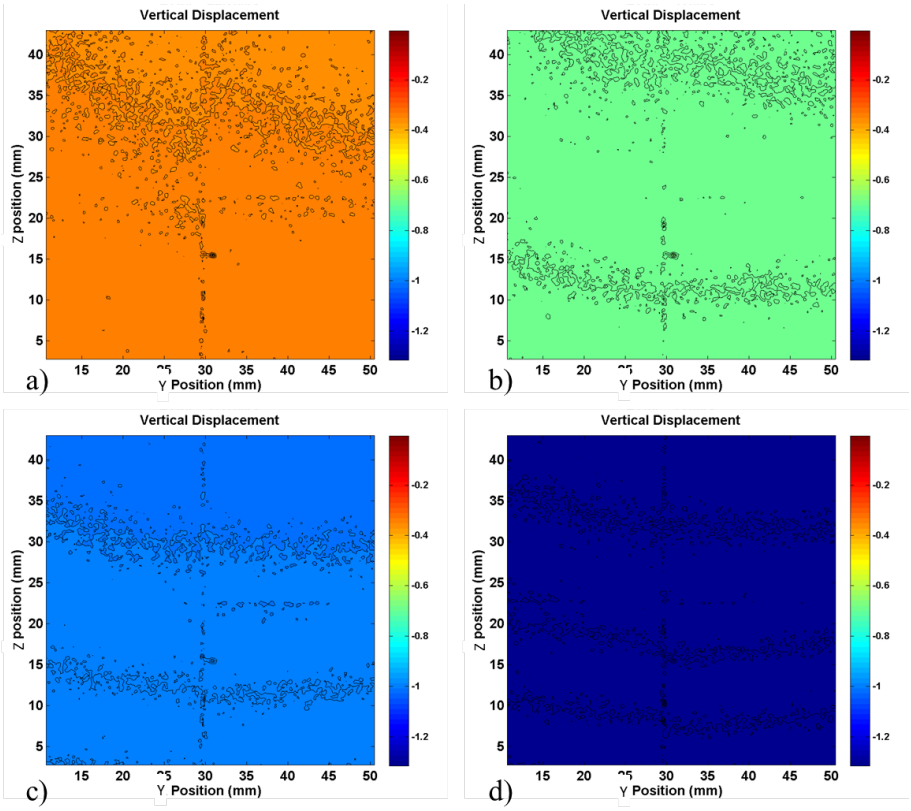

Figure 6.36. DIC results for the vertical displacement of four aluminum bars under uniaxial load. The image is viewing the y-z plane (Fig. 6.12) with the vertical load at a) 100 kN, b) 200 kN, c) 300 kN, and d) 400 kN. The fractures are located along the lines Y= 22.5 mm and Z = 30 mm.

is shown, for several different loads, in Fig. 6.37. For the first 300 kN, the horizontal displacement changes very little. However, at a load of 400 kN (Fig. 6.37d), the displacement increases and indicates that the increasing vertical load causes horizontal expansion (i.e., Poisson effect). During each loading step, the displacement was roughly uniform throughout the measured region, indicating that the load was evenly distributed at the surface along each fracture.

The vertical displacements also showed very uniform behavior as a function of load (Fig. 6.38). The vertical displacements were much larger than the horizontal displacements, because of the loading conditions. Figure 6.38 illustrates that even

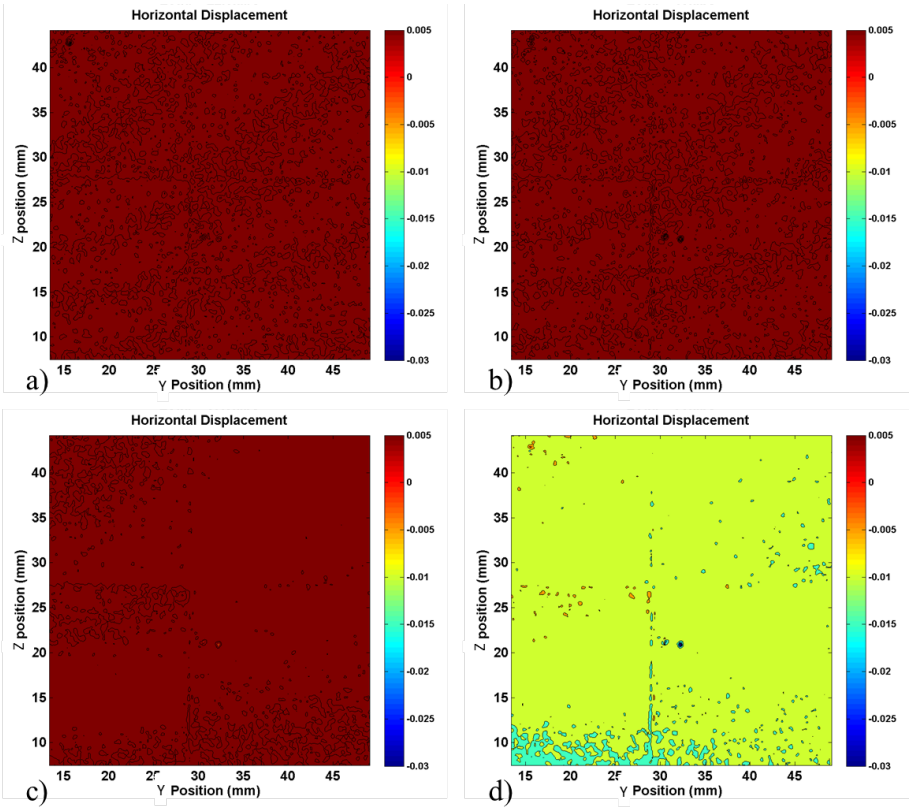

Figure 6.37. DIC results for the horizontal displacement of four aluminum bars under biaxial load. Image is viewing the y-z plane (Fig. 6.12) with the horizontal load held at 45 kN and the vertical load at a) 100 kN, b) 200 kN, c) 300 kN, and d) 400 kN. The fractures are located along the lines Y = 27 mm and Z = 27 mm.

under biaxial loading conditions, the surface deformation was uniform among the four blocks, with only slight variations along the fracture plane.

6.8 Acoustic Wave Propagation Results

6.8.1 Uniaxial Loading Results

The existence of intersection waves was explored for the long aluminum bars as a function of uniaxial loading. The Instron load frame was used to apply a normal load to the intersection from 0-400 kN, in 2.22 kN steps. The received waveforms, for four

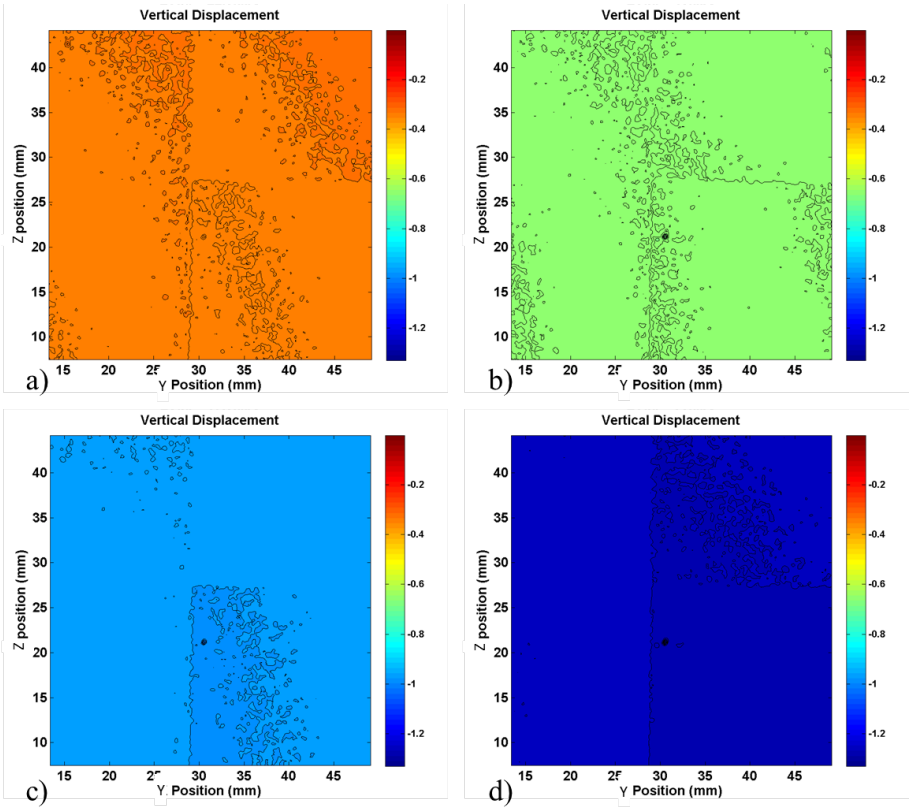

Figure 6.38. DIC results for the vertical displacement of four aluminum bars under biaxial load. Image is viewing the y-z plane (Fig. 6.12) with the horizontal load held at 45 kN and the vertical load at a) 100 kN, b) 200 kN, c) 300 kN, and d) 400 kN. The fractures are located along the lines Y = 27 mm and Z = 27 mm.

different polarization angles, are shown in Fig. 6.39. The sample was free to expand horizontally because of the uniaxial loading conditions used in this experiment.

When the S-wave source was polarized at $\theta = 0°$ (Fig. 6.39a), the observed signals arrived between the WW and Rayleigh waves, similar in behavior to a CWW. The intersection wave in the $\theta = 0°$ polarization was not sensing a fully coupled signal due to the uniaxial load conditions. For uniaxial loading in the vertical direction, the vertical fracture had no confinement and very little coupling along it. The $\theta = 0°$ polarization was highly sensitive to the coupling on the vertical fracture, and so does not pass the Rayleigh wave arrival time because the vertical fracture does not close

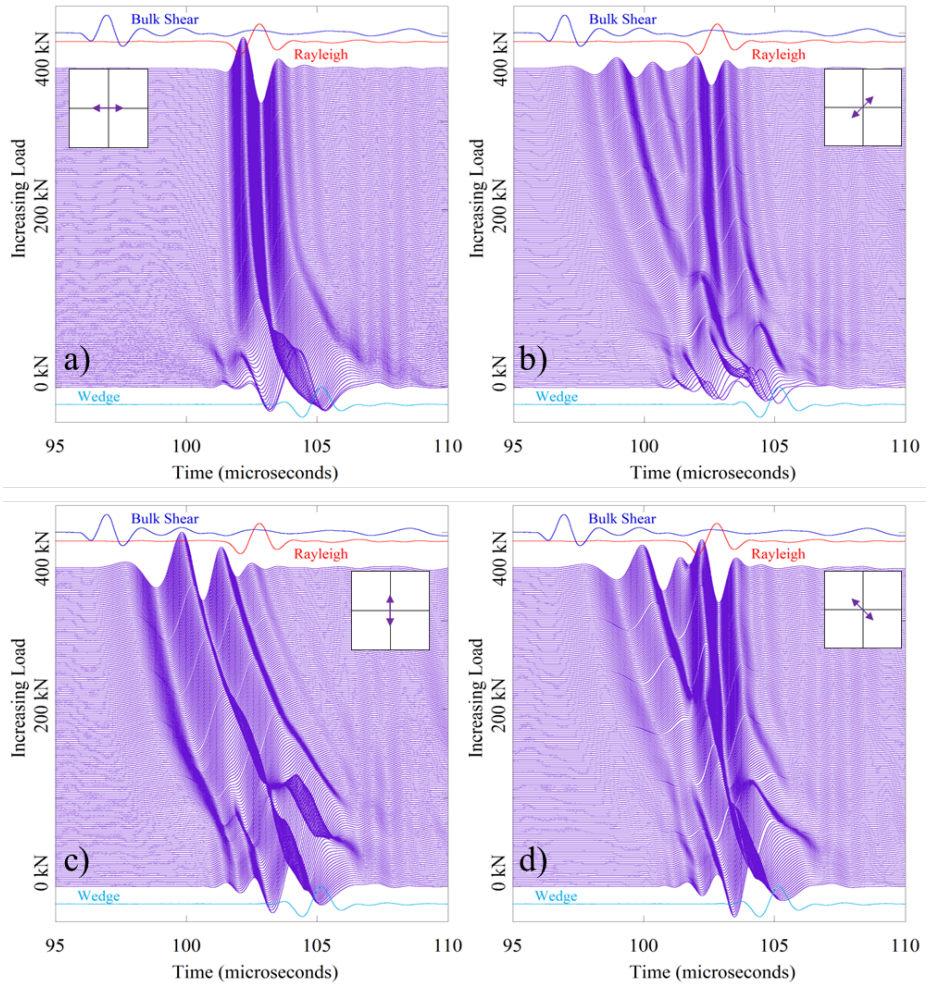

Figure 6.39. Waveforms from the long aluminum bars under uniaxial load. The transducer at the intersection was polarized according to θ in Fig. 6.12 at a) 0°, b) 45°, c) 90°, and d) 135°.

significantly. Another way to view this result is to think of the vertical fracture in a non-contact condition. Under this concept, the blocks are separated, leaving two CWW geometries (i.e., blocks 1-4 and 2-3). This polarization senses the change in contact as a CWW would, yielding the results in Fig. 6.39a. This is verified later in this section.

At a polarization angle of $\theta = 90°$ the observed signals are very different (Fig. 6.39c). When the applied load was low (< 100 kN) the intersection wave showed lots of interference, and several modes were apparent. As the load increased (> 200

kN) two main peaks, with no obvious interference, emerged and propagated with faster arrival times as the load was increased. In juxtaposition to the $\theta = 0°$ results discussed above (Fig. 6.39a), this polarization was highly sensitive to the load applied to the horizontal fracture.

When the transducer polarization was rotated to $\theta = 45°$ or $\theta = 135°$ (Fig. 6.12), the observed signals, shown in Figs. 6.39b, d, indicated an amalgamation of the signals from the 0° and 90° components. One wave appeared to remains near the Rayleigh wave arrival, similar to the $\theta = 0°$ result, while another wave decreased in arrival time, similar to the $\theta = 90°$ result, passing through the first wave and approached the bulk S-wave arrival time. It is not surprising that these two waves are observed from these transducer polarizations, which are between the two polarizations discussed above. These trends in polarization dependence indicate the sensitivity of the intersection to polarization under uniaxial loading.

To verify the explanation for the observed polarization effects above, the same experiment was performed with a 5 mm gap along the vertical fracture to completely decouple the fracture. 5 mm was chosen to completely separate the media while

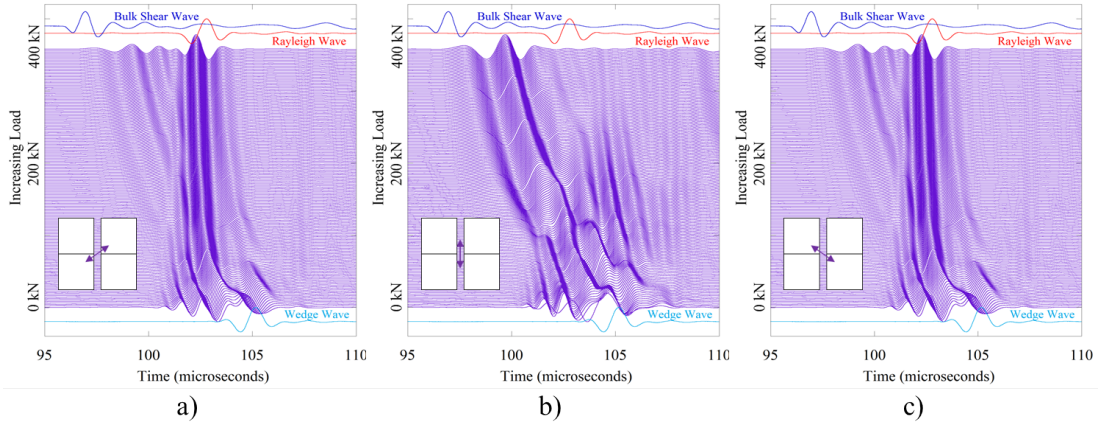

Figure 6.40. Waveforms from the long aluminum bars under uniaxial load with a 5 mm gap along the vertical fracture. The transducer at the intersection was polarized according to θ in Fig. 6.12 at a) 45°, b) 90°, and c) 135°.

simultaneously allowing the transducer to be in contact with all four blocks of the intersection. The results of these experiments are shown in Fig. 6.40.

The $\theta = 90°$ polarization, under uniaxial load with the 5 mm gap, is shown in Fig. 6.40b. Comparing these signals to the signals with the same polarization for the blocks with no gap (Fg. 6.39c), similarities are observed. For the first $\sim$ 100 kN, large interference is detected (Fig. 6.40b) followed by the emergence of two main peaks. Unlike the no gap experiments, the 5 mm gap results also excited signals near the WW arrival time at high load ($\sim$ 200 kN). These were most likely due to the free surface of the vertical fracture in the gap that allowed WW type modes to be excited.

When the transducer polarization was set to $\theta = 45°$ or $\theta = 135°$ with the 5 mm gap, the signal between the WW and Rayleigh wave dominated (Fig. 6.40a, c). However, there was still an observed signal propagating through the dominant peak heading towards the bulk S-wave in both cases. Comparisons of the 45° and 135° results with (Fig. 6.39b, d) and without (Fig. 6.40a, c) the gap indicated the mode between the WW and Rayleigh wave was dominated by the horizontal fracture properties, while the mode between the WW and bulk S-wave was strongly dependent upon the vertical fracture coupling. This verifies the hypothesized analysis of the no gap experiments.

To help determine the dominant trends in the observed signals of the no gap experiments, the peaks in the signals of Fig. 6.39, within 3 standard deviations from the absolute maximum, were tracked as the load was increased. The velocity of these peaks, for each polarization mentioned above, is shown in Fig. 6.41. For the 0° polarization the velocity (Fig. 6.41a), indicated the intersection was guiding CWW type signals. The velocity of this mode's main peak only ranged between the WW and Rayleigh wave velocity; further demonstrating that under uniaxial loading conditions, the horizontal fracture was closing while the vertical fracture was held open.

When the transducer polarization was rotated to $\theta = 90°$, the observed velocity of the signal peaks was between the WW and Rayleigh wave velocity at low loads and traveled between the Rayleigh wave and bulk S-wave velocity at high loads (Fig.

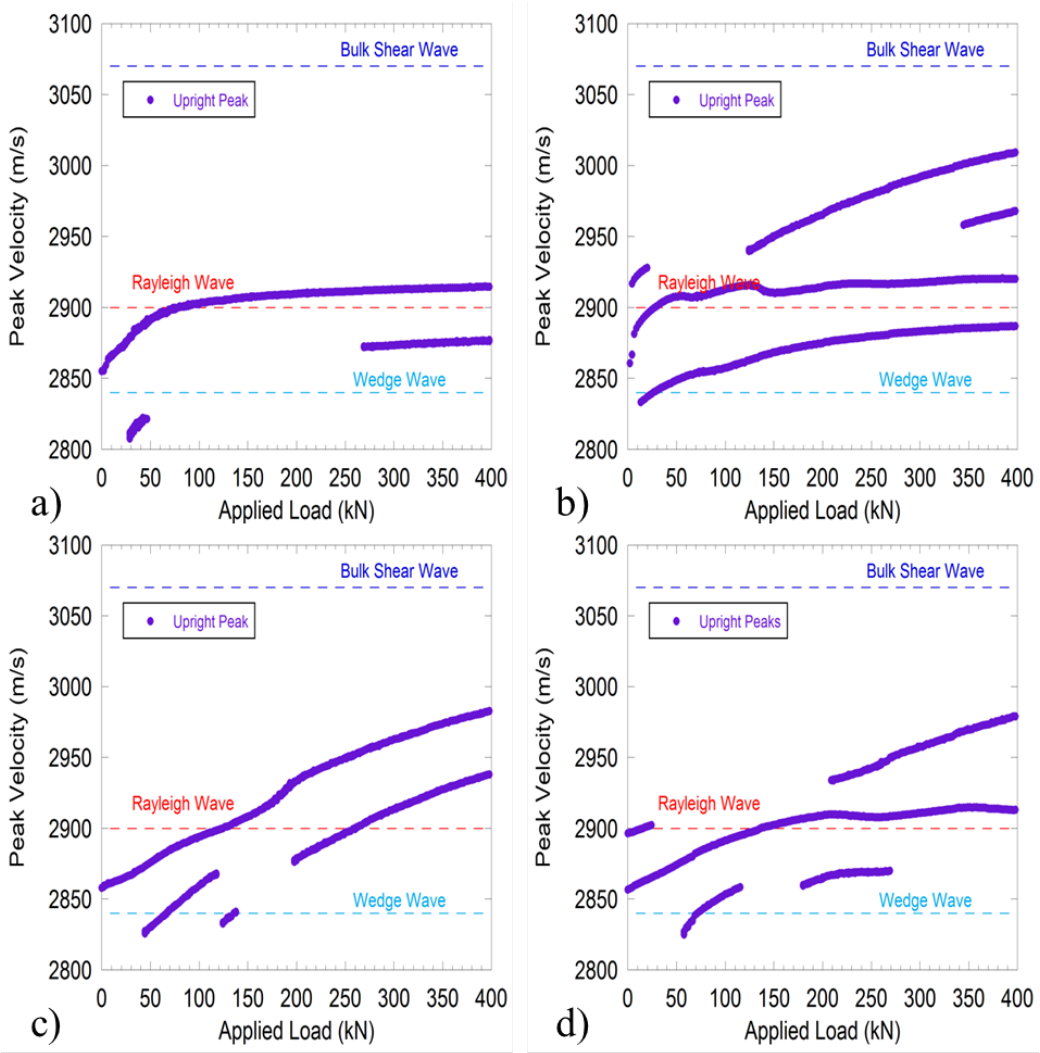

Figure 6.41. Velocity of the peaks within 3 standard deviations of the absolute maximum in Fig. 6.39. The transducer at the intersection was polarized according to θ in Fig. 6.12 at a) 0°, b) 45°, c) 90°, and d) 135°.

6.41c). Note that all of the peaks exceeded the Rayleigh wave velocity with increasing load and none remained constant in time.

For polarizations $\theta = 45°$ or $\theta = 135°$ the signal peaks (Figs. 6.41b, d) exhibited influences from the two polarizations described above (0° and 90°). At least two dominant modes exist within these observed signals and possibly more. One of

these modes (lowest two curves in Figs. 6.41b, d) propagated between the WW and Rayleigh wave velocity and remained at the Rayleigh wave velocity even for high external loads. However, there was a second mode that exceeded the Rayleigh wave velocity, similar to the trend for 90°, and approached the bulk S-wave velocity as a function of increasing external load (top curves in Figs. 6.41b, d). All of these results verify the expected trends discussed above.

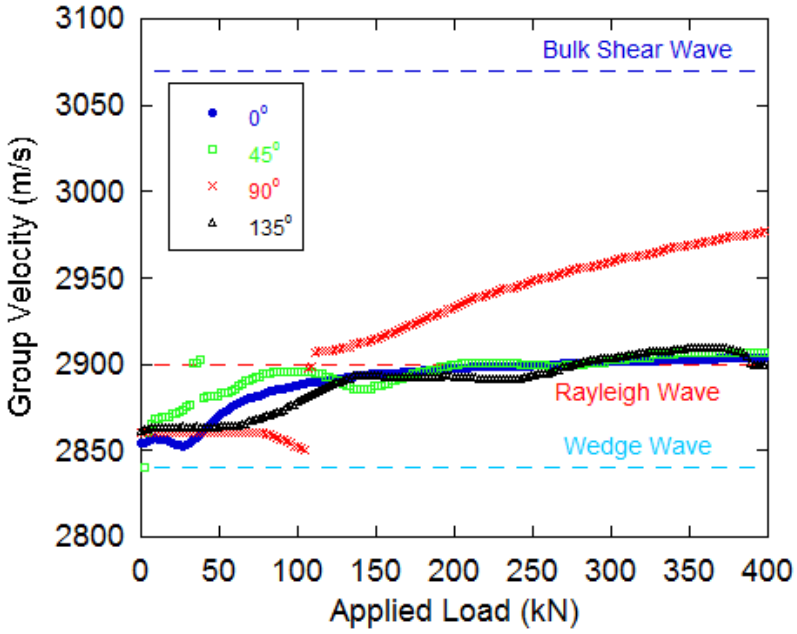

Figure 6.42. Group velocity calculated from Nolte-Hilbert wavelets for the uniaxially loaded signals in Fig. 6.39. The transducer at the intersection was polarized according to θ in Fig. 6.12 at 0°, 45°, 90°, and 135°.

An alternative analysis method is to examine the energy components of the signal using wavelets (Appendix E), as was done for the CWW in section 5.6. The wavelet used in this analysis was the Nolte-Hilbert wavelet, which rigidly adheres to the admissibility condition, allowing the original signal to be obtained from the analyzed wavelet without any loss of information [221].

The peak in the energy of the wavelet, for the signals in Fig. 6.39, was used to calculate the group velocity for the four polarizations studied. Results are shown in

Fig. 6.42 as a function of load. For the $\theta = 0°$, $45°$, and $135°$ polarizations (blue circle, green square, and black triangle symbols in Fig. 6.42) the peak energy of the intersection signal was more strongly confined to the mode that traveled with speeds between the WW and Rayleigh wave velocity. To see this compare Fig. 6.41 to Fig. 6.42. Note that the frequency varies slightly with load.

The group velocity for the $\theta = 90°$ polarization (red x symbols in Fig. 6.42) differs from the others. At low uniaxial load the received signal energy traveled slightly above the WW velocity; and around 100 kN the velocity increased, exceeding the Rayleigh wave velocity, and approached the bulk S-wave velocity. This indicated that the $90°$ polarization measured a strong guided-mode that exhibited the fully predicted wave velocities for the intersection under uniaxial loading. The wavelet analysis demonstrated that the energy was confined to the CWW type mode, except for $\theta = 90°$, even when more modes were present in the observed signals (Fig. 6.39). This indicates that uniaxial loading only excited the Rayleigh to bulk S-wave mode under polarizations parallel to the direction of applied load.

6.8.2 Biaxial Loading Results- Hexagonal Samples

Before showing the biaxial loading intersection results, the bulk and surface waves propagating through and along the hexagonal aluminum samples are discussed (Fig. 6.43). As expected, the P-wave arrives first, followed by the S-wave, Rayleigh wave, and WW. Note that the WW arrival time is very close to the Rayleigh wave arrival time because of the small size of the sample (Fig. 6.26).

Similar to the uniaxial analysis, the intersection wave behavior was investigated as a function of polarization. However, due to the addition of biaxial loading capabilities, the excitation polarization was again studied. Because the results from the uniaxial study indicated that the $45°$ and $135°$ polarizations were a superposition of the modes at $0°$ and $90°$, only the $0°$ and $90°$ polarizations are discussed here.

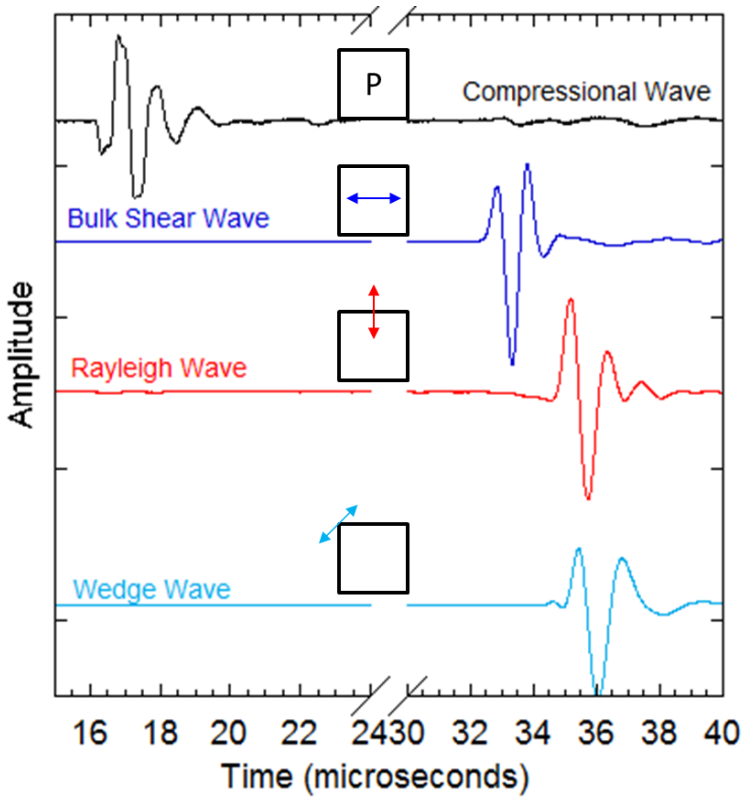

Figure 6.43. Bulk and surface waves from the hexagonal aluminum samples. The insets show the polarization of the transducer required to excite these signals.

The $\theta = 0°$ and $\theta = 90°$ intersection waves were propagated along the hexagonal intersection, with a vertical load of 6.7 kN and a variable horizontal load from 0-178 kN, (Fig. 6.44b). For the $\theta = 90°$ polarization, the transducer was oriented perpendicular to the direction of variable load (purple in Fig. 6.44b). The received signals indicated that at low applied loads the intersection was highly mobile, yielding noisy signals with various arrival times (lower purple signals in Fig. 6.44a). Once the intersection came into better contact, the observed signals pin at the Rayleigh wave velocity and did not appear to be influenced by the loading conditions.

When the transducer was polarized at $\theta = 0°$, i.e., parallel to the variable loading direction, the observed signals were affected by the external loading conditions (Fig. 6.44c). Under low external load the observed signals arrived near the WW and

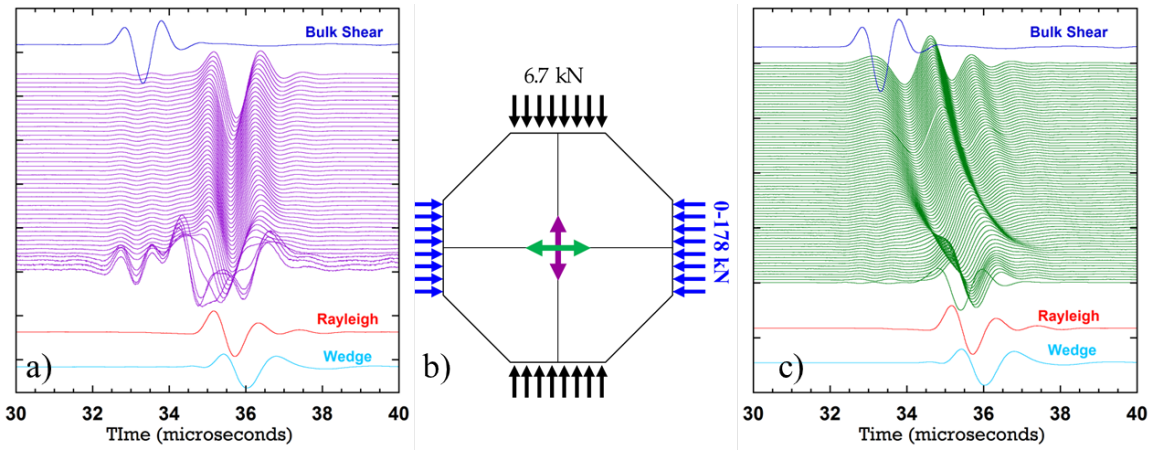

Figure 6.44. Signals propagating along the intersection of the hexagonal aluminum samples. b) The loading configuration and transducer polarizations. a) Signals when the transducer is polarized perpendicular to variable loading direction ($\theta = 90°$). c) Signals when the transducer is polarized parallel to the variable loading condition ($0°$).

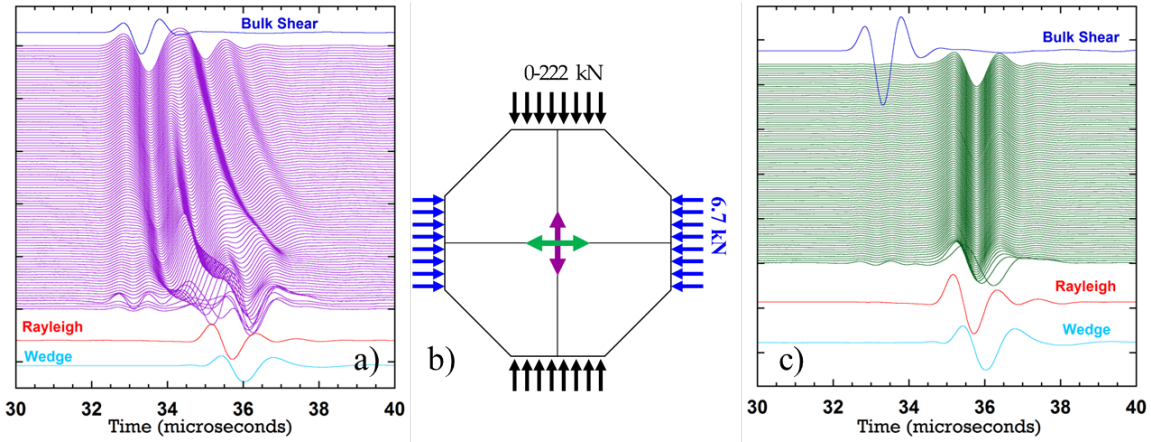

Figure 6.45. The same as Fig. 6.44 but with the loading directions switched as shown in b). a) Signals when the transducer polarization is parallel ($\theta = 90°$) to the variable loading direction. c) Signals when the transducer polarization is perpendicular ($\theta = 0°$) to the variable loading direction.

Rayleigh wave. As the load was increased (higher signals in Fig. 6.44c) the arrival time decreased and the received signals approached the bulk S-wave arrival time. This result was opposite that observed in the $\theta = 90^\circ$ case of Fig. 6.44a, because like the uniaxial experiments above in these tests only a small load confined the horizontal frame.

To verify that this trend was not a result of the material nor loading frame, an analogous experiment was performed but for the opposite loading condition. In this experiment, shown in Fig. 6.45b, the vertical load frame was varied from 0 - 222 kN and the horizontal load frame was held constant at 6.7 kN. The same two polarizations were used at the intersection (i.e., $\theta = 0^\circ$ and 90°) to determine the effect of loading and polarization on the observed intersection waves.

As expected, the transducer parallel to the variable loading direction (90° in Fig. 6.45b) observed an intersection wave that depended on the external load. Similar to Fig. 6.44c, the signals for this loading case had an arrival time near the WW or Rayleigh wave and decreased in arrival time as the external load was increased (Fig. 6.45a). The perpendicular polarization (0° in Fig. 6.45b) observed a Rayleigh wave arrival time, with little to no dependence on the external load applied at the intersection, shown in Fig. 6.45c. This was also in agreement with the previous experimental results of Fig. 6.44a.

The group velocity for these experiments was analyzed using the same Nolte-Hilbert wavelet as the previously discussed. The velocity of the results in Fig. 6.44 are shown in Fig. 6.46. As expected, the $\theta = 90^\circ$ polarization demonstrated large variations in velocity for the first ~ 40 kN and then the velocity asymptoted to the Rayleigh wave velocity (purple symbols in Fig. 6.46). The $\theta = 0^\circ$ polarization had a velocity that started near the Rayleigh wave velocity at low loads and increased in velocity towards the bulk S-wave velocity as a function of load (green symbols in Fig. 6.46). These results agree with the analysis from the corresponding signals (Fig. 6.44a, c).

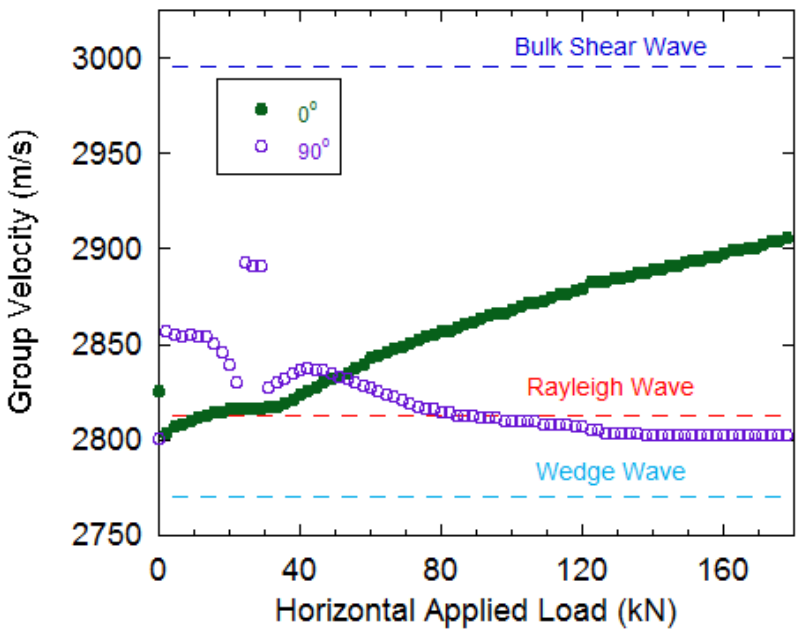

Figure 6.46. Group velocity, from the peak in the wavelet energy, for the intersection waves in Fig. 6.44.

The group velocity analysis of Fig. 6.45 is more complicated. For the $\theta = 0°$ results (green symbols in Fig. 6.47) the wavelet analysis verified that the signal started at the WW velocity and quickly increased to the Rayleigh wave velocity ($\sim$ 10 kN in Fig. 6.47). After $\sim$ 10 kN the velocity remains near the Rayleigh wave throughout the loading sequence. The observed effect from the $\theta = 90°$ polarization was somewhat strange (purple symbols in Fig. 6.47). For the first $\sim$ 40 kN, the signal increased from the WW to above the Rayleigh wave velocity. Between 40 and 70 kN, very little change was observed in velocity. After 70 kN, the velocity decreased until a load of $\sim$ 100 kN, at which point the velocity remained roughly constant (2825 $\frac{m}{s}$) until an abrupt jump in the velocity was observed at 160 kN and increased towards the bulk S-wave for the remainder of the load.

These strange effects are from the energy localization changing modes. To demonstrate this, wavelets are shown at various loads in Fig. 6.48. At low loads (Fig. 6.48a) the energy of the wavelet was localized in one lobe. As the load increased to 45 kN,

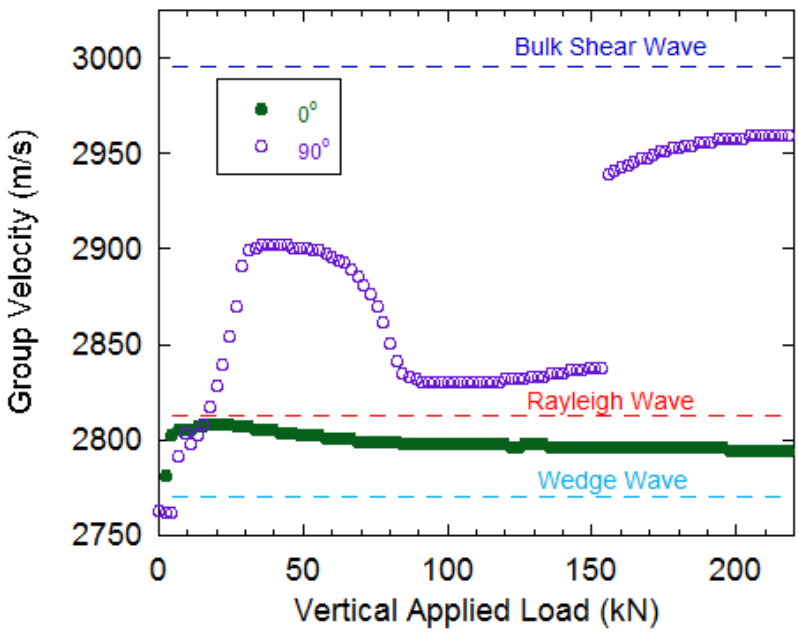

Figure 6.47. Group velocity, from the peak in the wavelet energy, for the intersection waves in Fig. 6.45.

two lobes appeared in the wavelet but the energy was confined to the bottom lobe (Fig. 6.48b). Once the load reached 111 kN, the energy switched to the upper lobe (Fig. 6.48c) causing the decrease in velocity observed in Fig. 6.47. As the load increased to 185 kN, the energy switched back to the bottom lobe and the velocity was again increased (Fig. 6.48d). This is observed in the sharp jump in velocity around 160 kN. It appears that these results demonstrate the intersection wave can excite multiple modes.

These results indicate that the polarization of the transducer relative to the direction of loading is sampling the load similar to the uniaxial results in section 6.8.1. To fully exploit the usefulness of this dependence, an experiment was conducted with changing loading directions. The 90° transducer polarization was used (inset of Fig. 6.49a) and the biaxial loading system was applied in two ways. First, the vertical load was held constant at 6.67 kN while the horizontal load was increased from 0 - 44.5 kN; this is graphically represented in the bottom purple region of Fig. 6.49a.

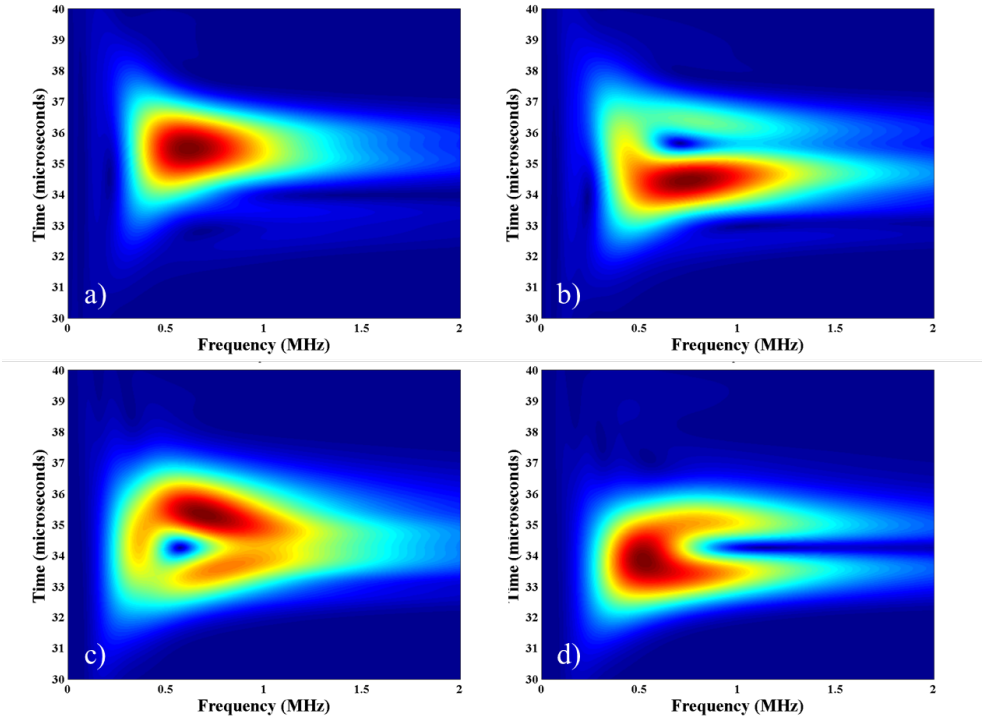

Figure 6.48. Wavelets from the hexagonal aluminum signals in Fig. 6.45a used to explain the results in Fig. 6.47. Wavelets are at a vertical load of a) 22.25 kN, b) 44.5 kN, c) 111.2 kN, and d) 185 kN.

Next, the horizontal load frame was kept at 44.5 kN and the vertical load frame was increased from 6.67 kN up to 300 kN, indicated by the upper orange region of Fig. 6.49a.

Observed signals at the intersection for these loading conditions are shown in Fig. 6.49b. The first set of loading conditions (lower purple region) excited Rayleigh wave modes (shown in the purple signals of Fig. 6.49b). Similar to the previous results (Figs. 6.44a, 6.45c, and 6.39a) this indicated a low amount of coupling on the horizontal fracture due to the loading conditions. When the loading condition switched, entering the upper orange region of Fig. 6.49a, intersection signals exhibited a much stronger dependence on load (upper orange of Fig. 6.49b). This switch in sensitivity was caused by the change in loading direction that had both fractures coupling together and was sensing the changes similar to the results of Figs. 6.44c,

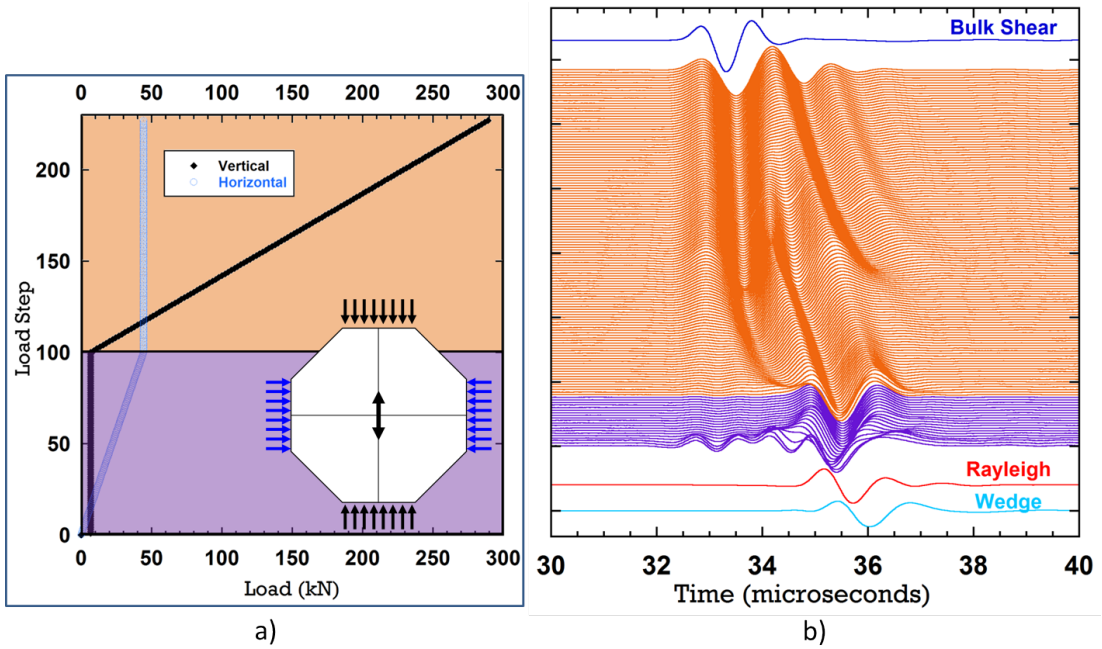

Figure 6.49. Steering the intersection wave by varying the direction of loading. a) The horizontal direction is loaded first (purple region), then held constant while the vertical direction is loaded (orange region). Inset shows polarization relative to load frames. Signals from the intersection are shown in b) with the same color labels.

6.45a, and 6.39c. The arrival time of the signal changed, and at least two modes merged into one at high loads (top orange signals at $\sim$ 34 μs in Fig. 6.49b). This steering of the intersection wave fully demonstrated the sensitivity of the intersection to the loading conditions experienced.

Results from Fig. 6.49 demonstrate that the intersection is highly sensitive to the loading conditions and that the stiffness of each fracture plane can be changed independently. A qualitative description of the velocity results for this experiment is shown in Fig. 6.50. The surface is from the long aluminum bar parameters, but the general trend of the surface should be identical for the hexagonal aluminum sample. During the first portion of the loading cycle (purple in Fig. 6.49a) only the stiffness on the vertical fracture (κ_1) is changing. This change corresponds to the region on the intersection wave surface shown in the purple arrow of Fig. 6.50. The velocity

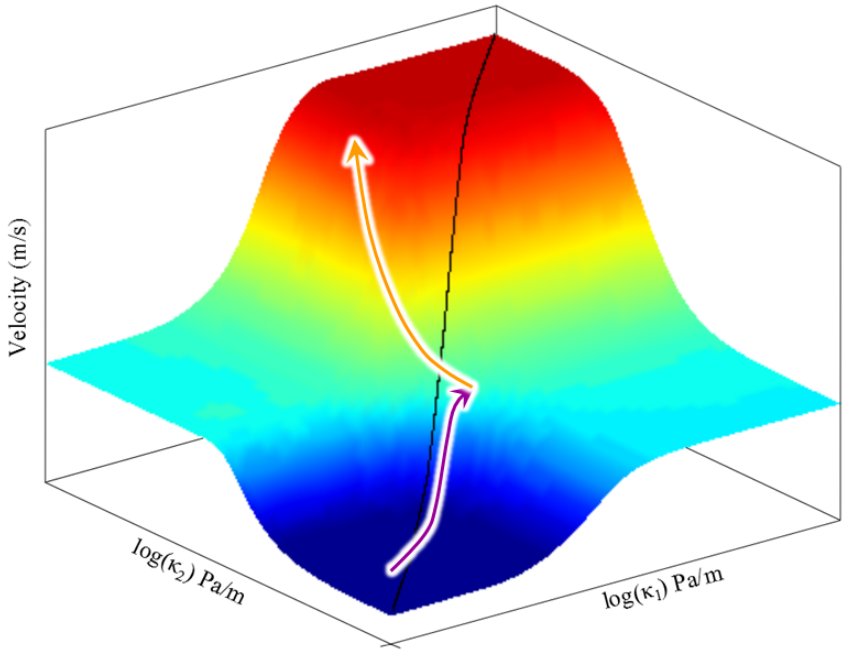

Figure 6.50. Qualitative description of the results of Fig. 6.49 on the theoretical surfaces for the unequal stiffness condition. The black line indicates the equal stiffness curve.

starts at or near the WW velocity and as the load is increased the velocity increases up to the Rayleigh plateau, but does not exceed the Rayleigh velocity. When the loading direction is changed (orange of Fig. 6.49) the horizontal fracture stiffness is increased (κ_2). This corresponds to the orange arrow on the surface of Fig. 6.50. The vertical fracture is now essentially closed and the increase in load on the horizontal fracture further increases the velocity of the intersection wave up the side of the surface heading towards the shear peak (Fig. 6.50). This demonstrates the usefulness of the surfaces in comprehending the observed data at the intersection.

6.8.3 Biaxial Loading Results- Bar Samples

Measurements of intersection waves were also made on anisotropic aluminum bars (Fig. 5.19) under biaxial loading. Bulk and surface waves for these bars are shown

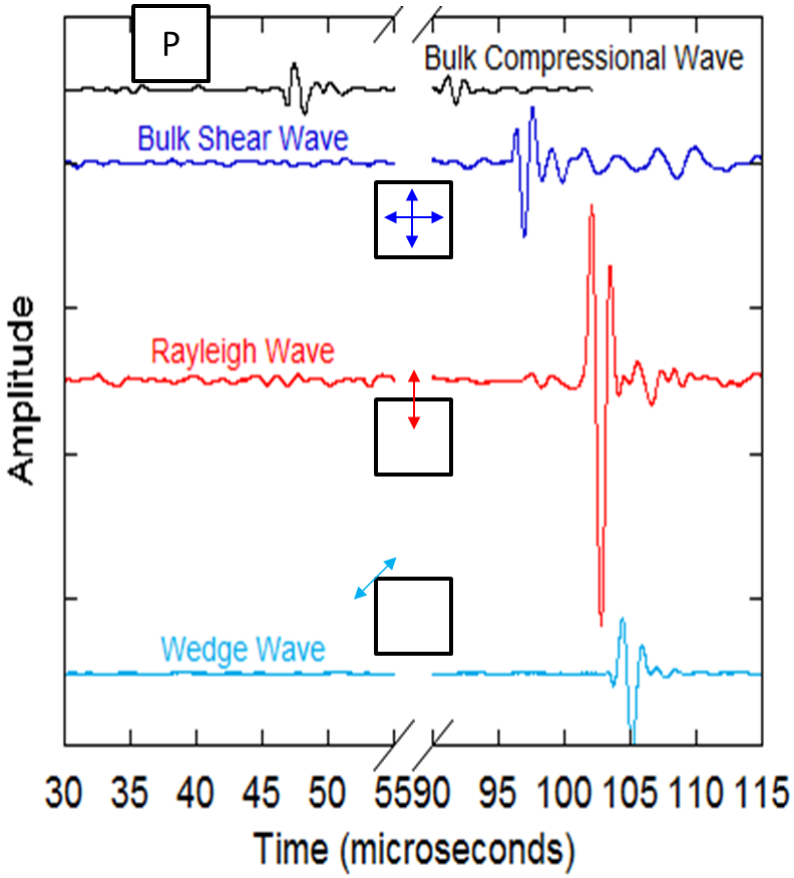

Figure 6.51. Bulk and surface waves propagating through and along the long direction of the aluminum bars (Fig. 5.19). Note that compared with the smaller hexagonal signals (Fig. 6.43) the Rayleigh and WWs are more separated, due to the increased length of the sample.

in Fig. 6.51. As expected, the order of the signals is P, S, Rayleigh, and WW, respectively. It should be mentioned that this sample is anisotropic, with transversely isotropic symmetry (section 2.3.2). The symmetry planes are in the direction of propagation (i.e., the long direction (x)) and so both the $\theta = 0°$ and $\theta = 90°$ polarization yield the same P- and S- waves. However, signals propagating through the short sides of the sample (Fig. 5.19) have different velocities. Since the sample is not a cube, a direct comparison of these signals is not given. The velocities of each wave, and its polarization, are listed in Table H.3.

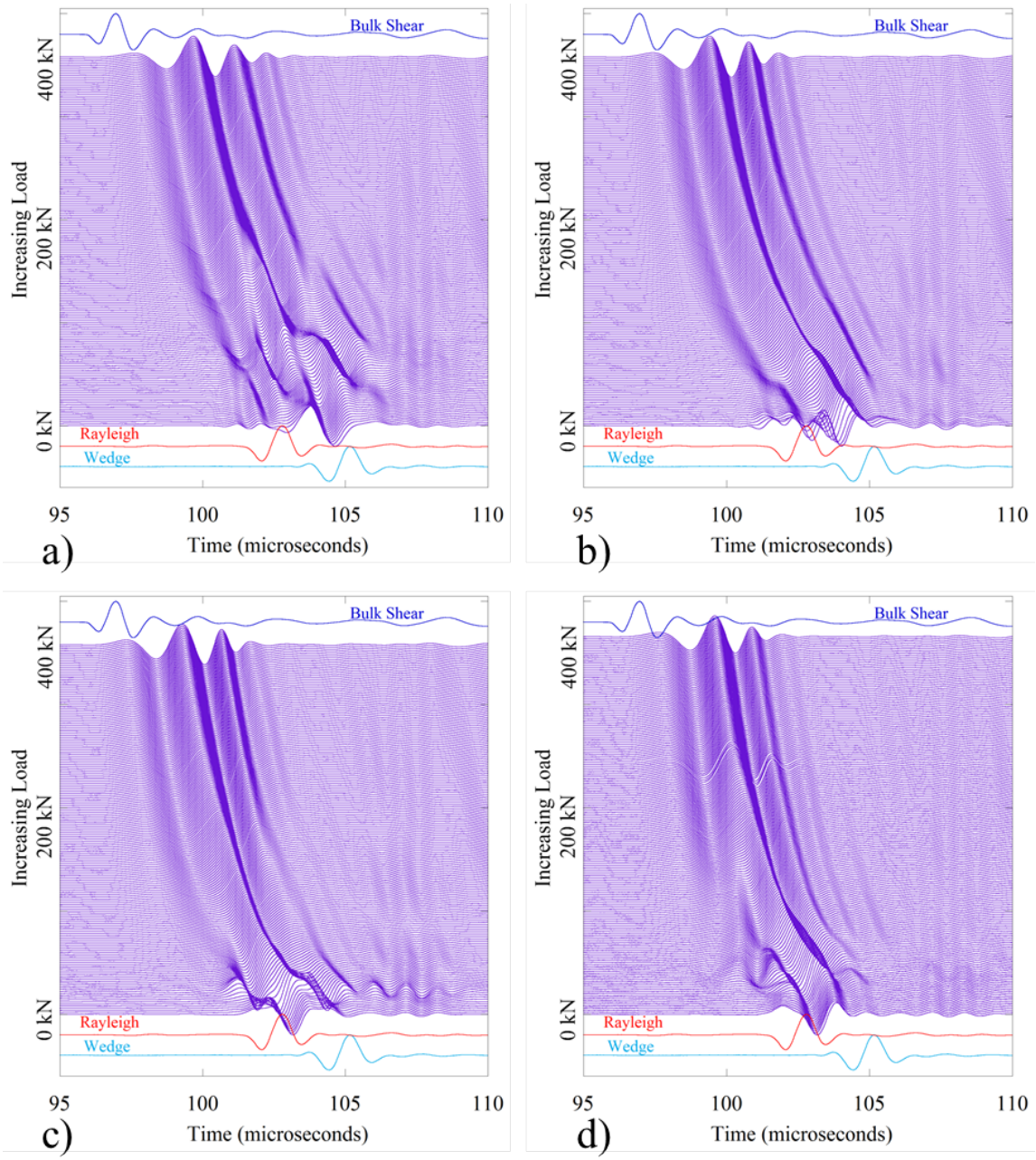

Figure 6.52. Signals along the intersection in the long aluminum samples for various biaxial loads. For all cases the vertical load ranged from 0 to 400 kN as listed on the y-axis. The horizontal load was a) 2.22 kN, b) 8.88 kN, c) 22.2 kN, and d) 66.6 kN. S-wave, Rayleigh, and WW signals are shown for reference.

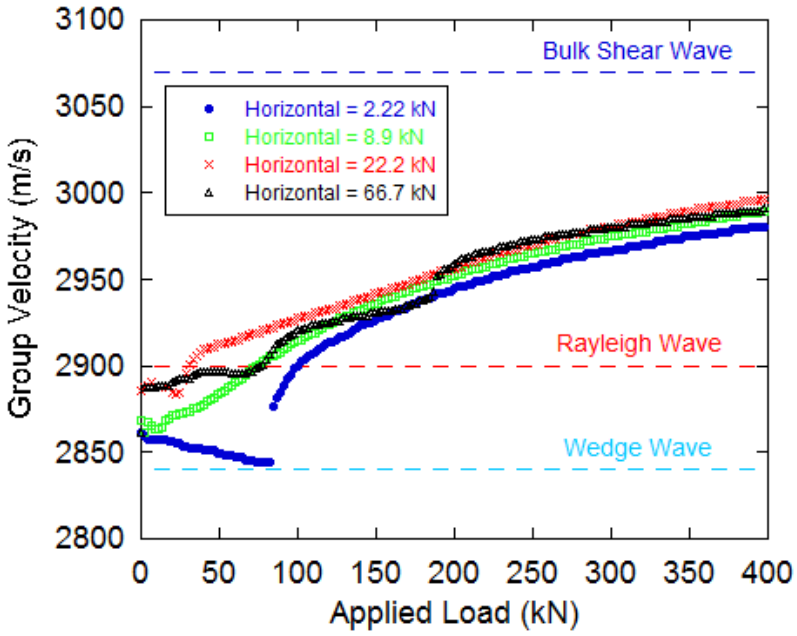

Figure 6.53. Group velocity, from peak in wavelet energy, for the signals from Fig. 6.52. The vertical load is shown on the x-axis.

The biaxial loading investigation using the hexagonal samples showed a strong dependence of the intersection wave on polarization and applied load. Here, the effects of various horizontal loads, with the same vertical load, are explored. The four loading conditions examined are vertical loads ranging from 0 - 400 kN and horizontal load held constant at 2.22 kN, 8.88 kN, 22.2 kN, and 66.6 kN with a transducer polarization of $\theta = 90°$ (Fig. 6.52).

For the 2.22 kN horizontal load shown in Fig. 6.52a the stacked signals started near the WW velocity and as the vertical load was increased, several modes were observed to merge and interfere between $\sim$ 102 and 105 μs. Near a vertical load of 200 kN only two dominant peaks existed, and for the remainder of this experiment the signal decreased in arrival time and approached the bulk S-wave signal.

When the horizontal load was increased to 8.88 kN (Fig. 6.52b) and 22.2 kN (Fig. 6.52c), the observed signals exhibited less interference and at low vertical load arrived near the Rayleigh wave time (bottom signals in Fig. 6.52b, c). This indicated

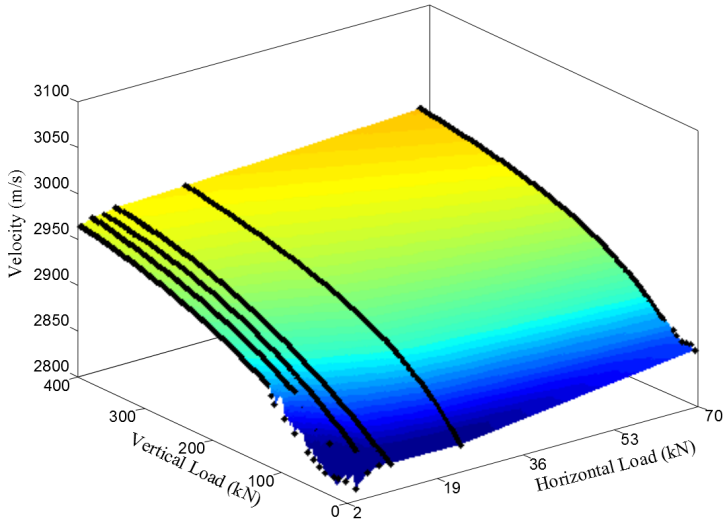

Figure 6.54. Surface from experimental measurements of the intersection wave under various biaxial loading conditions with a shear source polarized at 90°.

that the horizontal load had sufficiently closed the vertical fracture plane, causing the observed effects. As the vertical load was increased, the arrival time decreased, heading towards the bulk S-wave arrival time.

The highest horizontal load of 66.6 kN (Fig. 6.52d) had a similar effect but with one dominant peak in the signal that began between the WW and Rayleigh wave arrival time and decreased with little interference from the other modes. These results demonstrate the sensitivity of the intersection to the loading condition of the intersection in biaxial load.

The group velocity of these results was calculated in the same way as before. The results (Fig. 6.53) demonstrate that the change in horizontal load (Fig. 6.53) affects the velocity of the intersection wave. The velocity at low vertical load (x-axis in Fig. 6.53) has the most dramatic effects. Once the vertical load was significant enough to close the intersection ($>$ 150 kN in Fig. 6.53), the signals all exhibited similar

velocity trends with slight variations due to the different loading configurations on the horizontal axis.

The results of the experimental study on the $\theta = 90^\circ$ polarization are summarized by a surface of velocities in Fig. 6.54. If both loads are low the velocity of the intersection propagates near the WW velocity, as expected. When the vertical load is increased but the horizontal load is low (i.e., $< 10kN$) the intersection wave heads up to the Rayleigh plateau (see Fig. 6.21). When both loading directions are high the velocity increases and heads towards the bulk S wave velocity (orange peak Fig. 6.54). This is expected when comparing with the theoretical results of Fig. 6.21. The velocity did not reach the bulk S wave velocity because the loading conditions were not high enough to sufficiently close the intersection. A larger load frame is required to demonstrate the full range of existence or a smaller sample (shown for the hexagonal samples above) . This demonstrates the agreement between the theoretical predictions and experimentally observed signals.

6.8.4 Biaxial Loading Polarization Effects - Bars

The polarization of the intersection wave was also examined in the long aluminum bar samples in the same way it was examined under uniaxial loading conditions in section 6.8.1. Using the same angle (θ) definition, shown in Fig. 6.12, transducer polarizations of 0°, 45°, 90°, and 135° were examined under biaxial loading conditions. For all cases the vertical load was varied from 0 - 400 kN, while the horizontal load was held constant at 8.88 kN for the 0° polarization and 22.2 kN for the other polarizations.

0° polarization results, for the above loading conditions, are shown in Fig. 6.55a. As a function of load, this polarization indicates that the intersection supports WW type modes at low external loads. As the load is increased in the vertical direction, the intersection waves pin at the Rayleigh wave arrival time. This was similar to the CWW results from chapter 5, which indicated that the small horizontal load applied

in this experiment (2.22 kN) was not sufficient to close the vertical fracture plane. Essentially, this is the same effect discussed in section 6.8.1.

When the polarization was rotated to $\theta = 90°$, the signal exhibited the full arrival time regime, i.e., WW to the bulk S-wave, as shown in Fig. 6.55c. There was very little interference observed in the received signals compared to the uniaxial loading condition in section 6.8.3.

When the polarization of the intersection transducer was $\theta = 45°$ or 135°, observed signals exhibited significant interference and mode crossing (Figs. 6.55b, d). Analogous to the uniaxial polarization effects (Fig. 6.39b, d) these polarizations exhibited trends from both the 0° and 90° modes. At low applied loads the signals arrive near the WW, and as the load was increased, multiple modes and interference effects were observed (near 100 - 200 kN in Figs. 6.55b, d). This indicated these polarizations were probably sampling some of behavior from both fractures.

The group velocity analysis was also carried out for this experiment (Fig. 6.56) and indicated differences from the uniaxial analysis in Fig. 6.42. For the $\theta = 0°$ polarization (circles in Fig. 6.56) under biaxial loading conditions the signal began near the WW velocity and increased just past the Rayleigh wave velocity and asymptoted for the entire range of applied vertical load. The $\theta = 90°$ polarization results (x symbols Fig. 6.56) also began near the WW velocity for low load, but increased past the Rayleigh wave velocity, towards the bulk S-wave velocity, as the vertical load was increased. These two results are similar to the uniaxial trend observed in Fig. 6.42.

For the two polarizations between these extremes, i.e., $\theta = 45°$ or 135°, the group velocity (square and triangle in Fig. 6.56) increased in a similar fashion to the 90° polarization, passing the Rayleigh wave velocity and heading towards the bulk S-wave velocity. This result is opposite what happened under uniaxial loading (Fig. 6.42) where these polarizations were more strongly confined to the 0° polarization velocity trend, now they are more strongly confined to the 90° behavior. The abrupt variation in velocity for these two modes near 170 kN in Fig. 6.56 was due to a the energy switching lobes in the wavelet, similar to the observed effect in Fig. 6.48.

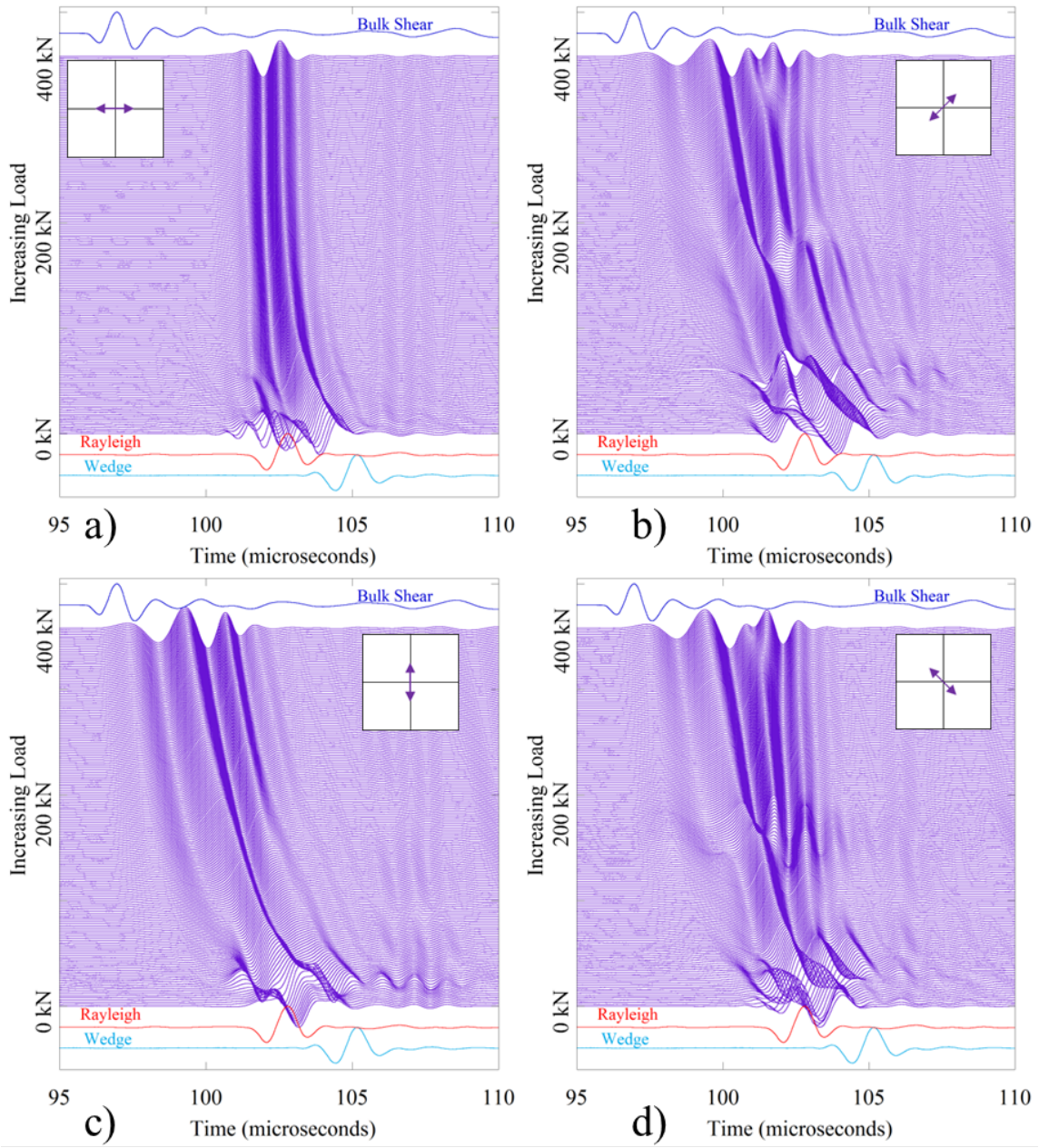

Figure 6.55. Polarization dependence of the intersection wave in the aluminum bar samples under biaxial loads. For all figures, the vertical load was increased from 0 to 400 kN, as labeled on the y axis. The horizontal load was held at a) 8.88 kN and b-d) 22.2 kN. The polarization was θ = a) 0°, b) 45°, c) 90°, and d) 135° from Fig. 6.12.

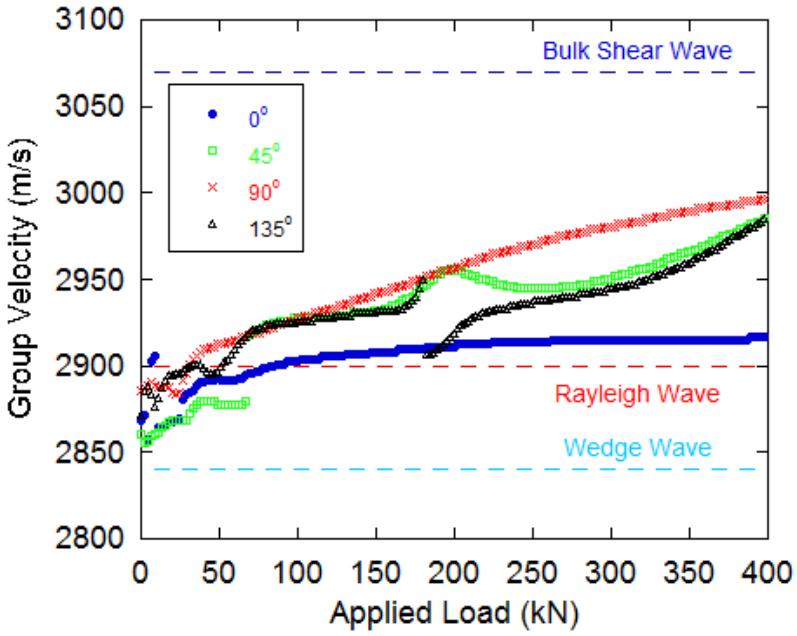

Figure 6.56. Group velocity from peak in wavelet energy for the polarization study in Fig. 6.55. The bulk S, Rayleigh, and WW are all shown for reference.

6.8.5 Summary

The results of this chapter indicate that the intersection does support localized vibrational modes, which are a function of the specific stiffness and frequency. Group theory was analyzed for two different symmetries and predicted the existence of at least four unique vibrational modes when the fractures had uniform conditions. It was interesting to observe that the intersection under completely symmetric conditions supported both wagging and breathing type modes, while the intersection under different vertical and horizontal fracture conditions only supported one or the other.

A theoretical derivation was carried out using a similar formulation to the CWW analyzed in chapter 5 and a secular equation was derived for localized modes at an orthogonal intersection. Numerical analysis was performed on these localized modes and all four predicted vibrational modes were found to exist, with the exception of the doublet ε mode. The predicted velocity regime ranged between the WW and

bulk S-wave velocity, or Rayleigh wave and bulk S-wave velocity, depending on the parameters used.

Uniaxial and biaxial load experimental investigations were performed to verify the existence of the intersection waves. Strong dependence was found between the polarization and direction of loading. The observed signals were analyzed and found to exhibit characteristics consistent with the predicted modes from group theory and the theoretical analysis.

7. Conclusions

This dissertation presented the theoretical and experimental framework for understanding elastic wave propagation along an intersection between orthogonal fractures. This was achieved by conceptually viewing an intersection as composed of four wedges, each of which supports a wedge wave (WW) that is localized at the corner of two free surfaces (chapter 4). Group theory was used to predict the possible vibrational modes of the WW. For WWs, two types of motion exist, wagging or breathing, where the wagging motion is the most common, and exists in isotropic media for positive Poisson's ratio media. The breathing mode mostly exists in negative Poisson's ratio media but is supported by a wedge of nearly any apex angle. Extensive work has been performed in the literature, both theoretically and experimentally, to verify the existence of the WW and several results from these studies were presented.

With the WW formulation as a building block, two wedges were coupled to form coupled wedge waves (CWW) that are highly localized to the coupled corners and propagate along a surface fracture, i.e., fracture intersecting a free surface (chapter 5). This wave exists because the coupling of two wedges is sensitive to the contact area between the corners. Displacement discontinuity (DD) boundary conditions, which successfully characterize single fractures, were used to describe the coupling between the corners. Group theory was also applied to the CWW geometry for two identical media and predicted that two modes of the CWW exist for any given set of material properties. Numerical results for CWWs were dispersive in frequency and specific stiffness, which results from a non-welded contact described by DD boundary conditions.

Experiments were performed on isotropic and anisotropic aluminum samples, with machined surfaces, to verify the existence of CWW using piezoelectric contact transducers. Observed waveforms were localized at the surface fracture and traveled with

speeds between the WW and Rayleigh wave velocity, as predicted by the numerical results. The behavior of CWW was extremely sensitive to the material properties (i.e., anisotropy) of the samples. Theoretical predictions for the CWW did not match the experimental results when isotropic parameters were assumed; however, once the correct anisotropic parameters were used the numerical results agreed with the experimental observations.

Using the CWW as a guide, an orthogonal intersection was investigated. Group theory was fundamental to the analysis of the intersection because of the high degree of symmetry and presence of degeneracy. Two different cases were analyzed, an intersection with equal material properties and fracture stiffnesses, and the same material properties with unequal fracture stiffnesses. For the case with equal properties, five unique normal vibrational modes were predicted, one of which was a degenerate 2D mode. For the unequal case, four 1D normal vibrational modes were predicted to exist.

A theoretical model that extended the approach used to model the CWW was applied to the two cases described above. A secular equation, which depended upon the material properties and geometry, was derived in chapter 6. Numerical results for the intersection indicated mode crossings in the predicted solutions, and vibrational modes predicted by group theory were used as a guide to separate these modes and determine the properties of each.

The theoretical approach for the case with equal fracture properties matched the four 1D vibrational modes but was unable to characterize the 2D mode. The 2D mode was not observed in the theoretical results because only breathing or wagging type WW motion was assumed, which is not present for the 2D mode. The unequal case was also analyzed, and the four theoretically determined 1D modes were found to match the group theory results.

Intersection waves were investigated experimentally and found to depend on the relationship between the polarization of the shear source transducer and the direction of applied load. Several experiments were described to analyze the effects of these

properties using both uniaxial and biaxial loading conditions. Results indicated that intersection waves do exist and several modes are excited depending on the loading conditions (biaxial vs. uniaxial).

7.1 Polarization

The existence and measurement of modes guided by fractures depend on the polarization of the shear components of the source and receiver. This is also true for the waves presented in this dissertation.

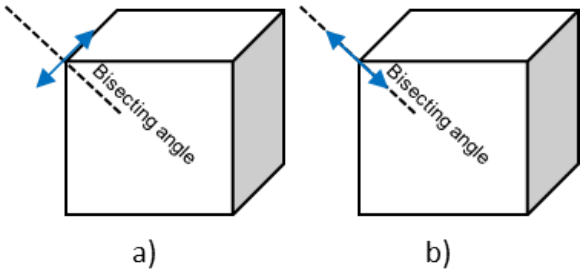

Figure 7.1. a) Source polarization required to excite a WW. b) Polarization which delocalizes into Rayleigh waves.

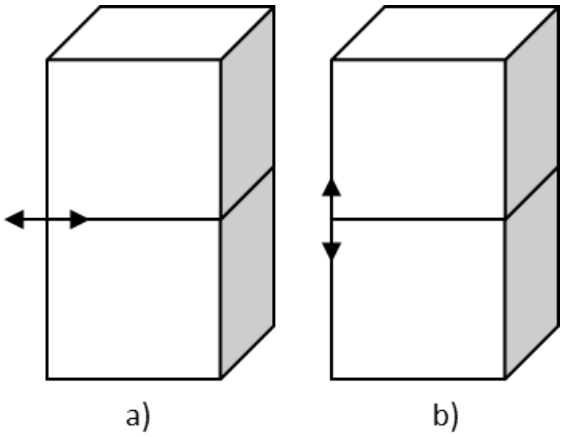

Figure 7.2. a) Source polarization required to excite a CWW. b) Polarization which delocalizes into interface waves.

For example, the WW, which is localized near a corner, is excited when the shear transducer polarization is perpendicular to the bisecting angle of the wedge (Fig. 7.1a). When the polarization is aligned parallel to this bisecting angle the WW energy delocalizes into Rayleigh waves on both free surfaces, resulting in a change in arrival time as well as amplitude of the received signal (Fig. 7.1b). The same polarization is used to excite both the wagging and breathing types of motion, although the breathing mode is mainly excited in materials with negative Poisson's ratio.

Generation of CWWs is also a function of shear source polarization for both isotropic and anisotropic media. The CWW is excited when the source excitation polarization is parallel to the fracture, i.e., normal to the free surface (Fig. 7.2a). When the polarization is rotated perpendicular to the fracture and parallel to the free surface, the received signal behaves like an interface wave, which is localized to the fracture plane, not the corners of the surface fracture (Fig. 7.2b).

The polarization needed to generate intersection waves is more complicated than for the other types of waves, which is not surprising considering the increased complexity of the problem. Under uniaxial load the excitation polarization at the intersection indicated sensitivity to loading when the polarization was parallel to the direction of loading (Fig. 7.3b). When the polarization was perpendicular to the direction of loading, the received signals exhibited signatures characteristic of the CWW. Further experimental investigation indicated that the uniaxial load did not close the fracture parallel to the loading direction (vertical fracture in Fig. 7.3). Thus, the perpendicular polarization was not significantly affected by the uniaxial loading direction (Fig. 7.3a). When the polarization was between these two extremes, i.e., 45° polarizations, observed signals were observed to be a superposition of the signals from parallel and perpendicular polarizations, as expected.

Under biaxial load, the relationship between the polarization and loading direction was again found to be important. At low horizontal load, the vertical fracture was not sufficiently coupled, and a result similar to the uniaxial case was observed. As the horizontal load was increased, the coupling along the vertical fracture also increased,

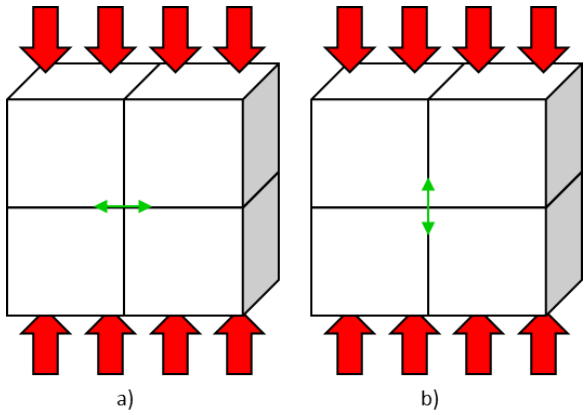

Figure 7.3. a) Intersection with load perpendicular to the uniaxial load. b) Intersection with load parallel to the uniaxial load.

and the observed intersection wave was found to behave as predicted by the numerical analysis. One interesting result of the polarization study on the intersection was that the loading direction can be determined from the observed velocity trends at the intersection. This result has implications for the remote characterization of stress fields in the laboratory and field.

7.2 Velocity

A significant amount of discussion focused on the velocity of various elastic waves. Velocity is often used to identify the type of wave that is observed. The best physical explanation for the variation in velocity as a function of wave type is given by Ash et al., (1969) [145] who discussed the elastic restraining forces on a given volume element within some geometry. The magnitude of these forces is proportional to the observed velocity and is used to make conceptual arguments for the velocity of each type of wave.

The bulk P- and S- wave velocities, which were discussed in chapter 2, are proportional to the square root of the elastic constants. In this work, the bulk S-wave was used to compare the velocities of surface and coupled waves. The Rayleigh wave

velocity, which has been studied for over 100 years, is typically within 10 % of the bulk S-wave, and highly localized to the surface. Recent theoretical advances analyzing Rayleigh waves have determined simple, analytic solutions for the Rayleigh wave velocity as a function of the material parameters (chapter 3).

For the WW, its slow velocity was the dominant characteristic that drove the interest in studying it for use as a delay line. The WW was predicted to propagate slower than the Rayleigh wave, from a few percent in an $\psi = 90°$ wedge to less than half the Rayleigh wave velocity in small angle wedges (chapter 4). Significant work to theoretically model the variations in velocity with geometry and material properties were verified by experimental studies.

The CWW that was introduced in this work exhibited dispersive velocity trends because of the DD boundary conditions, and was found to exist between the WW and Rayleigh wave velocity. The dispersion for the CWW, shown in Fig. 7.4, indicates that when the blocks are separated (i.e., low coupling or uncoupled) WWs are excited. As the media are coupled, the WWs couple together, increasing in velocity until a welded condition is reached, yielding the Rayleigh wave velocity. It is useful to compare this result to the interface wave. Interface waves are coupled Rayleigh waves that propagate along a fracture plane. Interface waves also exhibit dispersive behavior and exist between the Rayleigh wave velocity at low applied loads and the bulk S-wave velocity at high applied loads (i.e., high coupling). The comparison of CWW and interface wave modes (Fig. 7.4), provides a complete picture of the velocity trends exhibited on a single fracture, both in the plane and at the free surface.

Intersection waves exhibited behavior common to Rayleigh, WW, CWW, interface waves, and bulk S-waves. The equal stiffness case predicted velocity regimes between the WW and bulk S-wave velocity for two of the four modes and between the Rayleigh wave and bulk S-wave velocity for the other two modes (Fig. 7.5). Analysis of the WWs supported for a given set of material properties determined which intersection wave modes existed in each velocity regime. If the intersection materials supported wagging modes for each wedge, then the two wagging mode waves (A_2 and

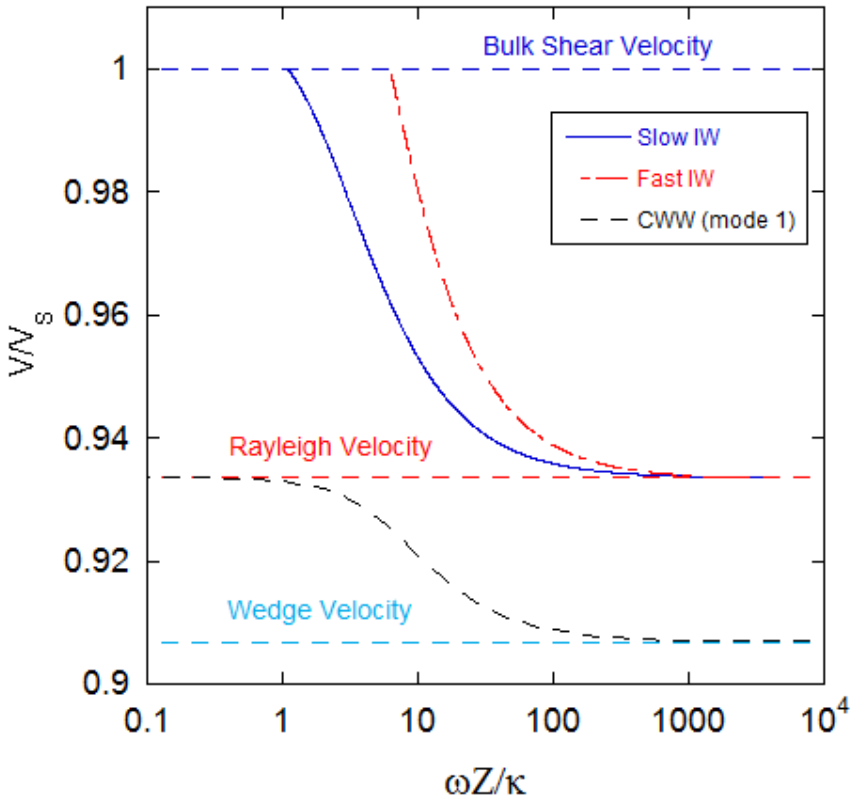

Figure 7.4. Dispersion characteristics of the interface wave (IW) and CWW related to the bulk and surface waves as a function of normalized frequency. ω is the frequency, Z is the impedance, and κ is the specific stiffness.

B_1) traveled between the WW and bulk S-wave while the two breathing modes (A_1 and B_2), which are not supported by a single wedge, existed between the Rayleigh and bulk S-wave velocity (Fig. 7.5). The opposite behavior is observed when the media support only breathing modes.

When the fractures defining the intersection have unequal stiffnesses, intersection waves depend on the coupling (or stiffness) of each fracture. If the vertical fracture is weakly coupled, the intersection wave velocity ranges between the WW and Rayleigh wave velocity, similar to the CWW result (Fig. 7.4). For strong coupling (i.e., high specific stiffness) on the vertical fracture the intersection acted like a single fracture with wave velocities between the Rayleigh and bulk S-wave velocity, similar to the

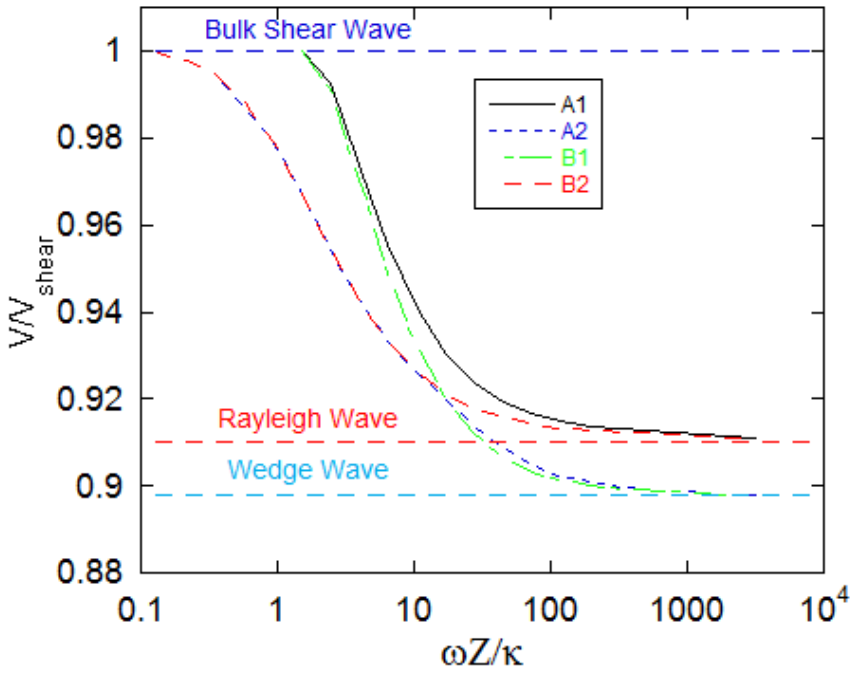

Figure 7.5. Dispersion characteristics of the intersection wave velocity, normalized by the bulk S-wave velocity, as a function of normalized frequency. ω is the frequency, Z is the impedance, and κ is the specific stiffness.

interface wave results (Fig. 7.4). Between these two extremes, the unequal intersection velocities varied, always within the WW and bulk S-wave extremes. These results indicated the sensitivity of the intersection wave under unequal stiffness to the intersection properties. It is important to note that while intersection waves may travel at speeds similar to the interface wave, the particle motion of these waves is different.

7.3 Future Work

Although the work presented here verified theoretically and experimentally the existence of CWW and intersection waves, many questions still remain regarding intersections. The main question is, can these waves can be observed in rock with

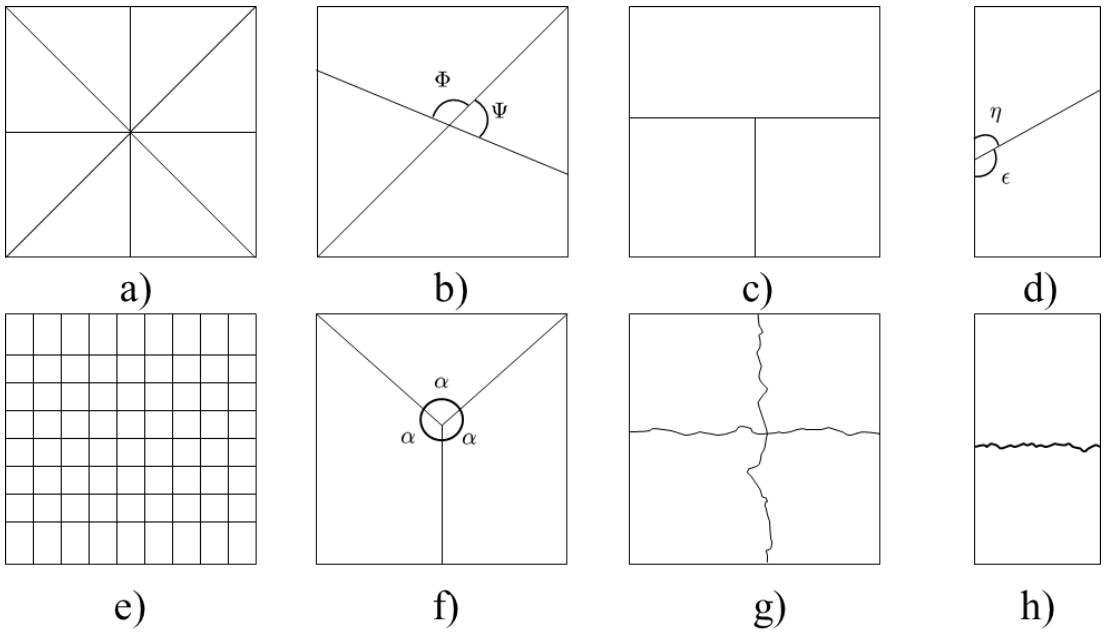

Figure 7.6. Other types of fracture intersections to be studied. a) star like intersections, b) non-orthogonal fracture intersections, c) $\top$ type intersections, d) non-orthogonal single fractures, e) orthogonal fracture networks, f) Y type intersections, g) rock fracture intersections, and h) rock single fractures. The Greek letters represent the angles between the fractures that are non-orthogonal.

natural fractures (Fig. 7.6g, h)? This author plans to investigate this in the future, but to date has not answered this question. Other theoretical and experimental investigations on the intersection need to be explored such as: non-orthogonal intersection waves (Fig. 7.6b), more than two fracture intersections (star like pattern Fig. 7.6a), fracture networks (i.e., more than one intersection, Fig. 7.6e), T- shaped (Fig. 7.6c), and the effect of intersections on waves propagated across an intersection instead of along it. These open questions are all interesting in respect to the analysis of the intersection wave and remain to be investigated. Examples of some of the types of intersections that still need analysis are shown in Fig. 7.6.

Finally, the main interest in studying elastic waves at intersections is to determine the hydraulic connectivity of networks. Although the mechanical properties are

interesting, the real goal is to determine if remote investigation of intersection waves can be used to extract hydraulic properties of intersections, and someday, fracture networks.

LIST OF REFERENCES

LIST OF REFERENCES

[1] P. LaPointe. It's the cracks that matter: Dfn modeling of everything rock. In *American Rock Mech. Assoc.*, 2012.

[2] L. J. Pyrak-Nolte. The seismic response of fractures and the interrelations among fracture properties. *Rock Mech., Mining Sci. and Geomech.*, 33(8):787–802, 1996.

[3] L. J. Pyrak-Nolte, L Myer, and N. G. W. Cook. Anisotropy in seismic velocities and amplitudes from multiple parallel fractures. *J. Geophys. Res.*, 95:11345–11358, 1990.

[4] L. J. Pyrak-Nolte, J. Xu, and G. Haley. Elastic interface waves propagating in a fracture. *Phys. Rev. Lett.*, 68(24):3650–3653, 1992.

[5] K. Nihei, B. Gu, L. Myer, L. J. Pyrak-Nolte, and N. G. W. Cook. Elastic interface wave propagation along a fracture. In *Int. Congress Rock Mech.*, volume 3, pages 1151–1157. Int. Soc. Rock Mech., 1995.

[6] S. Nakagawa, K. Nihei, and L. Myer. Elastic wave propagation along a set of parallel fractures. *Geophys. Res. Lett.*, 29(16), 2002.

[7] B. Gu, K. Nihei, L. Myer, and L. J. Pyrak-Nolte. Fracture interface waves. *J. Geophys. Res.*, 101(B1):827–835, 1996.

[8] B. Gu, R. Suarez-Rivera, K. Nihei, and L. Meyer. Incidence of plane waves upon a fracture. *Geophys. Res.*, 101(B11):25337–25346, 1996.

[9] L. J. Pyrak-Nolte, S. Roy, and B. Mullenbach. Interface waves propagated along a fracture. *Appl. Geophys.*, 35:79–87, 1996.

[10] C. Petrovitch, D. Nolte, and L. Pyrak-Nolte. Scaling of fluid flow versus fracture stiffness. *Geophys. Res. Lett.*, 40:2076–2080, 2013.

[11] C. Xian, D. Nolte, and L. Pyrak-Nolte. Compressional waves guided between parallel fractures. *Int. J. Rock Mech. Min. Sci.*, 38:765–776, 2001.

[12] L. J. Pyrak-Nolte and N. G. W. Cook. Elastic interface waves along a fracture. *Geophys. Res. Lett.*, 14(11):1107–1110, 1987.

[13] K. Nihei, L. Myer, N. G. W. Cook, and Y. Weidong. Effects of non-welded interfaces on guided sh-waves. *Geophys. Res. Lett.*, 21(9):745–748, 1994.

[14] B. Gu, K. Nihei, and L. Myer. Numerical simulation of elastic wave propagation in fractured rock with the boundary integral equation method. *Geophys. Res.*, 101(B7):15933–15943, 1996.

[15] B. Gu, K. Nihei, and L. Myer. Numerical investigation of fracture interface waves. *J. Acoust. Am.*, 102(1):120–127, 1997.

[16] S. Shao and L. J. Pyrak-Nolte. Interface waves along fractures in anisotropic media. *Geophys.*, 78(4):T99–T112, 2013.

[17] Y. Zhang, S. Chi, M. Willis, M. Toksoz, and D. Burns. Orientation estimation for multiple large fractures by scattering energy, 2006.

[18] E. Hakami and E. Larsson. Aperture measurements and flow experiments on a single natural fracture. *Int. J. Rock Mech. Min. Sci. and Geomech. Abstr.*, 33(4):395–404, 1996.

[19] R. A. Nelson. *Geologic analysis of naturally fractured reservoirs.* Gulf professional publishing, USA, 2nd edition, 2001.

[20] J. G. Rubino, L. Guarracino, T. M. Muller, and K. Holliger. Do seismic waves sense fracture connectivity? *Geophys. Res. Lett.*, 40(4):692–696, 2013.

[21] N. G. W. Cook. Natural joints in rock: mechanical, hydraulic and seismic behaviour and properties under normal stress. *Int. J. Rock Mech. Min. Sci. & Geomech. Abstr.*, 29(3):198–223, 1992.

[22] R. Caputo. Evolution of orthogonal sets of coeval extension joints. *Terra Nova*, 7(5):479–490, 1995.

[23] D. L. Hopkins. The implications of joint deformation in analyzing the properties and behavior of fractured rock masses, underground excavations and faults. *Int. J. Rock Mech. Min. Sci.*, 37:175–202, 2000.

[24] D. L. Hopkins. *The effect of surface roughness on joint stiffness, aperture, and acoustic wave propagation.* Ph.d. dissertation, 1991.

[25] R. Hodgson. Review of significant early studies in lineament tectonics. In R. A. Hodgson, S. P. Gay, and J. Y. Benjamins, editors, *1st Int. Conf. on the New Basement Tectonics*, pages 1–10, USA, 1974. The Utah Geological Association.

[26] T. X. Bai and D. D. Pollard. Getting more for less: The unusual efficiency of fluid flow in fractures. *Geophys. Res. Lett.*, 28(1):65–68, 2001.

[27] P. Davy, R. Le Goc, and C. Darcel. A model of fracture nucleation, growth and arrest, and consequences for fracture density and scaling. *J. Geophys. Res. Sol. Earth*, 118(4):1393–1407, 2013.

[28] J. E. Olson. Fracture aperture, length and pattern geometry development under biaxial loading: a numerical study with applications to natural, cross-jointed systems. *Geol. Soc. Spec. Publ., London*, 289:123–142, 2007.

[29] S. I. Ozkaya and J. Mattner. Fracture connectivity from fracture intersections in borehole image logs. *Computers and Geosci.*, 29:143–153, 2003.

[30] B. Larsen, I. Grunnaleite, and A. Gudmundsson. How fracture systems affect permeability development in shallow-water carbonate rocks an example from the Gargano Peninsula, Italy. *J. Struct.Geol.*, 32(9):1212–1230, 2010.

[31] F. Agosta, M. Alessandroni, M. Antonellini, E. Tondi, and M. Giorgioni. From fractures to flow: A field-based quantitative analysis of an outcropping carbonate reservoir. *Tectonophysics*, 490(3-4):197–213, 2010.

[32] L. N. Germanovich and R. P. Lowell. Percolation theory, thermoelasticity, and discrete hydrothermal venting in the Earth's crust. *Science*, 255(5051):1564–1566, 1992.

[33] V. Grechka and M. Kachanov. Effective elasticity of fractured rocks: a snapshot of the work in progress. *Geophys.*, 71(6):W45–W58, 2006.

[34] V. Grechka and M. Kachanov. Effective elasticity of rocks with closely spaced and intersecting cracks. *Geophys.*, 71(3):D85–D91, 2006.

[35] M. Kachanov and E. Montagut. A simple analysis of intersecting cracks and cracks intersecting a hole. *International Journal of Fracture*, 40:R61–R65, 1989.

[36] W. Fauriat and M. Kachanov. Compliance of star-like cracks: non-equivalence to holes, and the effect of random shape irregularities. *Lett. Frac. and Micromech.*, 170:207–210, 2011. Computer modeling of cracks as a superposition of cracks forming star like patterns, intersections, etc.

[37] L. Maerten, E. Willemse, D. Pollard, and K. Rawnsley. Slip distributions on intersecting normal faults. *J. Struc. Geol.*, 21:259–271, 1999.

[38] T. Bai, L. Maerten, M. Gross, and A. Aydin. Orthogonal cross joints: do they imply a regional stress rotation? *J. Struct. Geol.*, 24:77–88, 2002.

[39] K. Kalenchuck, M. Diederichs, and S. McKinnon. Characterizing block geometry in jointed rockmasses. *Rock Mech. and Mining Sci.*, 43:1212–1225, 2006.

[40] L. J. Pyrak-Nolte, L. Myer, N. G. W. Cook, and P. Witherspoon. Hydraulic and mechanical properties of natural fractures in low permeability rock. In G. Herget and S. Vongpaisal, editors, *6th International congress on rock mechanics*, pages 224–231, 1987.

[41] J. Zhao, Y. X. Zhou, A. M. Hefny, J. G. Cai, S. G. Chen, H. B. Li, J. F. Liu, M. Jain, S. T. Foo, and C. C. Seah. Rock dynamics research related to cavern development for ammunition storage. *Tunneling and underground space technology*, 14(4):513–526, 1999.

[42] D. Pollard and A. Aydin. Progress in understanding jointing over the past century. *Geological Society of America Bulletin*, 100(8):1181–1204, 1988.

[43] A. Aydin and J. M. Degraff. Evolution of polygonal fracture patterns in lava flows. *Science*, 239(4839):471–476, 1988.

[44] N. Hast. The existence of horizontal stress fields and orthogonal fracture systems in the Moon's crust. *Mod. Geol.*, 4:73–84, 1973.

[45] C. H. Okubo and A. S. McEwen. Fracture-controlled paleo-fluid flow in Candor Chasma, Mars. *Science*, 315(983):983–985, 2007.

[46] C. Birnie, F. Fuenten, R. Stesky, and E. Hauber. Underlying structural control of small-scale faults and fractures in West Candor Chasma, Mars. *J. Geophys. Res.*, 117(E11001), 2012.

[47] E. L. Harp. Fracture systems of Mars. In R. A. Hodgson, S. P. Gay, and J. Y. Benjamins, editors, *1st Int. Conf. on the New Basement Tectonics*, pages 389–408. The Utah Geological Association.

[48] G. Fielder, R. J. Fryer, P. J. S. Gash, J. L. Whitfor-Stark, and L. Wilson. Lineament patterns on the Moon, Mars, and Mercury. In R. A. Hodgson, S. P. Gay, and J. Y. Benjamins, editors, *1st Int. Conf. on the New Basement Tectonics*, pages 379–388, USA. The Utah Geological Association.

[49] A. Aydin. Fractures, faults, and hydrocarbon entrapment, migration and flow. *Marine and Petrol. Geol.*, 17(7):797–814, 2000.

[50] J. Johnson and S. Brown. Experimental mixing variability in intersecting natural fractures. *Geophys. Res. Lett.*, 28(22):4303–4306, 2001.

[51] J. Johnson, S. Brown, and H. Stockman. Fluid flow and mixing in rough-walled fracture intersections. *Geophys. Res.*, 111(B12206):1–16, 2006.

[52] R. Glass, M. Nicholl, S.E. Pringle, and T. Wood. Unsaturated flow through a fracture-matrix network: Dynamic preferential pathways in mesoscale laboratory experiments. *Water Resorce Res.*, 38(12), 2002.

[53] R. Glass, M. Nicholl, H. Rajaram, and T. Wood. Unsaturated flow through fracture networks: Evolution of liquid phase structure, dynamics, and the critical importance of fracture intersections. *Water Resource Res.*, 39(12), 2003.

[54] T. Wood, M. Nicholl, and R. Glass. Fracture intersections as integrators for unsaturated flow. *Geophys. Res. Lett.*, 29(24), 2002.

[55] T. Wood, M. Nicholl, and R. Glass. Influence of fracture intersections under unsaturated, low-flow conditions. *Water Resources Res.*, 41(W04017):1–17, 2005.

[56] Y. Park, K. Lee, G. Kosakowski, and B. Berkowitz. Transport behavior in three-dimensional fracture intersections. *Water Resources Res.*, 39(8):1–9, 2003.

[57] M. Bagheri and A. Settari. Effects of fractures on reservoir deformation and flow modeling. *Can. Geotech. J.*, 43:574–586, 2006.

[58] V. Michalis, A. Kalarakis, E. Skouras, and V. Burganos. Mixing within fracture intersections during colloidal suspension flow. *Water Resource Res.*, 45(W08429):1–10, 2009.

[59] Y. Zhang, C. Sayers, and J. Adachi. The use of effective medium theories for seismic wave propagation and fluid flow in fractured reservoirs under applied stress. *J. Geophys. Res.*, 177:205–221, 2009.

[60] K. D. Rawnsley, T. Rives, J. P. Petit, S. R. Hencher, and A. C. Lumsden. Joint development in perturbed stress-fields near faults. *J. Struc. Geol.*, 14(8-9):939–951, 1992.

[61] T. Rives, K. Rawnsley, and J. Petit. Analogue simulation of natural orthogonal joint set formation in brittle varnish. *Struct. Geol.*, 16(3):419–429, 1994.

[62] K. Storetvedt and A. Scheidegger. Orthogonal joint systems in the Bergen Area, Southwest Norway, and their regional significance. *Phys. Earth and Plan. Inter.*, 73:255–263, 1992.

[63] W. Dunne and C. North. Orthogonal fracture systems at the limits of thrusting: an example from Southwestern Wales. *J. Struc. Geol.*, 12(2):207–215, 1990.

[64] M. Gross. The origin and spacing of cross joints: examples from the Monterey formation, Santa Barbara coastline, California. *J. Struc. Geol.*, 15(6):737–751, 1993.

[65] H. Memarian and C. L. Fergusson. Multiple fracture sets in the Southeastern Permian-triassic Sydney Basin, New South Wales. *Aust. J. Earth Sci.*, 50(1):49–61, 2003.

[66] M. K. Corbett. Origin of pervasive orthogonal fracturing of the Earth's crust. In R. A. Hodgson, S. P. Gay, and J. Y. Benjamins, editors, *Proc. 2nd Int. Conf. on Basement Tectonics*, pages 319–325, USA, 1976. Basement Tectonics Comittee, Inc.

[67] G. E. Thomas. The crustal fracture system of North America and its possible origin. In R. A. Hodgson, S. P. Gay, and J. Y. Benjamins, editors, *1st Int. Conf. on the New Basement Tectonics*, pages 537–548, USA. The Utah Geological Society.

[68] S. W. Squyres, A. H. Knoll, R. E. Arvidson, B. C. Clark, J. P. Grotzinger, B. L. Jolliff, S. M. McLennan, N. Tosca, J. F. Bell III, W. M. Calvin, W. H. Fearrand, T. D. Golotch, M. P. Golombek, K. E. Herkenhoff, J. R. Johnson, G. Klingelhofer, H. Y. McSween, and A. S. Yen. Two years at Meridiani Planum: results from the Opportunity Rover. *Science*, 313:1403–1407, 2006.

[69] L. Goehring and S. W. Morris. Cracking mud, freezing dirt, and breaking rocks. *Physics Today*, 67(11):39–44, 2014.

[70] W. Dunne, D. Ferrill, J. G. Crider, Hill B., D. Waiting, P. C. La Femina, A. P. Morris, and R. W. Fedors. Orthogonal jointing during coeval igneous degassing and normal faulting, Yucca Mountain, Nevada. *GSA Bulletin*, 115(12):1492–1509, 2003.

[71] L. Plug and B. Werner. Fracture networks in frozen ground. *Geophys. Res.*, 106(B5):8599–8613, 2001.

[72] K. Helbig and L. Thomsen. 75-plus years of anisotropy in exploration and reservoir seismics: A historical review of concepts and methods. *Geophys.*, 70(6):9ND–23ND, 2005.

[73] K. Helbig. *Foundations of anisotropy for exploration seismics*, volume 22 of *Handbook of Geophysical exploration.* Elsevier Science, Inc., Great Britain, 1994.

[74] M. Schoenberg and C.M. Sayers. Seismic anisotropy of fractured rock. *Geophys.*, 60(1):204–211, 1995.

[75] J. Wolfe. *Imaging phonons: Acoustic wave propagation in solids*, volume 1. Cambridge University Press, Cambridge, UK, 1998.

[76] C. Kohlhauser and C. Hellmich. Determination of Poisson's ratios in isotropic, transversely isotropic, and orthotropic materials by means of combined ultrasonic-mechanical testing of normal stiffnesses: Applications to metals and wood. *European J. Mech. A Solids*, 33:82–98, 2012.

[77] V. Bucur and R. Archer. Elastic constants for wood by an ultrasonic method. *Wood Sci. Technol.*, 18:255–265, 1984.

[78] S. Najafi, V. Bucur, and G. Ebrahimi. Elastic constants of particleboard with ultrasonic technique. *Materials Letters*, 59:2039–2042, 2005.

[79] P. Sanders and D. Yuhas. Frictional material elastic property round robin study. In *25th annual brake colloquium*, volume 01, pages 1–12, 2007.

[80] V. Bucur. *Acoustics of Wood*. CRC Press Inc., Boca Raton, 2 edition, 2006.

[81] A. Every. Determination of the elastic constants of anisotropic solids. *NDT and E int.*, 27(1):3–10, 1994.

[82] R. Vestrum. *Group and phase velocity inversions for the general anisotropic stiffness tensor*. Masters thesis, 1994.

[83] B. C. Abell, S. Shao, and L. J. Pyrak-Nolte. Measurements of elastic constants in anisotropic media. *Geophys.*, 79(5):349–362, 2014.

[84] G. Mavko, T. Mukerji, and J. Dvorkin. *The rock physics handbook: Tools for seismic analysis in porous media*, volume 1. Cambridge University Press, Cambridge, UK, 1 edition, 1998.

[85] R. Mirman. *Point groups, space groups, crystals, molecules*. World Scientific Publishing Co. Pt. Ltd., 1999.

[86] J. Aussel and J. P. Monchalin. Precision laser-ultrasonic velocity measurement and elastic constant determination. *Ultrason.*, 27:165–177, 1989.

[87] B. Castagnede, J. Jenkins, and W. Sachse. Optimal determination of the elastic constants of composite materials from ultrasonic wave-speed measurements. *J. Appl. Phys.*, 67(6):2753–2761, 1990.

[88] J. Chai and T. Wu. Determinations of anisotropic elastic constants using laser-generated surface waves. *J. Acoust. Soc. Am.*, 95(6):3232–3241, 1994.

[89] S. Dahmen, H. Ketata, M. Ghozlen, and B. Hosten. Elastic constants measurement of anisotropic Olivier wood plates using air-coupled transducers generated Lamb wave and ultrasonic bulk wave. *Ultrason.*, 50:502–507, 2010.

[90] A. Every and W. Sachse. Determination of the elastic constants of anisotropic solids from acoustic-wave group-velocity measurements. *Phys. Rev. B*, 42(13):8196–8207, 1990.

[91] I. Ihara, H. Koguchi, N. Uchida, T. Aizawa, and J. Kihara. Inversion of dual mode surface waves to determine elastic constants of anisotropic solid. In *IEEE Ultrasonics Symposium*, pages 545–549, 1997.

[92] K. Jakata and A. Every. Determination of the dispersive elastic constants of the cubic crystals Ge, Si, GaAs, and InSb. *Phys. Rev. B*, 77:174301–1 – 174301–10, 2008.

[93] M. Lei, H. Ledbetter, and Y. Xie. Elastic constants of a material with orthorhombic symmetry: An alternative measurement approach. *J. Appl. Phys.*, 76(5):2738–2741, 1994.

[94] L. Pagnotta. Determining elastic constants of materials with interferometric techniques. *Inv. prob. Sci. and Eng.*, 14(8):801–818, 2006.

[95] L. Wang. Determination of the ray surface and recovery of elastic constants of anisotropic elastic media: a direct and inverse approach. *Phys. Condens. Matter*, 7:3863–3880, 1995.

[96] D. E. Yuhas and M. P. Yuhas. *Friction materials elastic constant measurements*, volume 1, chapter 12, page 391. SAE International (R-353), USA, 2006.

[97] I. Tsvankin. Anisotropic parameters and p-wave velocity for orthorhombic media. *Geophys.*, 62(4):1292–1309, 1997.

[98] L. Thomsen. Weak elastic anisotropy. *Geophys.*, 51(10):1954–1966, 1986.

[99] J. C. Jaeger, N. G. W. Cook, and R. W. Zimmerman. *Fundamentals of Rock Mechanics*. Blackwell Publishing, Singapore, 4 edition, 2007.

[100] K. Aki and P. Richards. *Quantitative Seismology*, volume 1. W. H. Freeman and Company, 1980.

[101] J. M. Carcione. *Wave fields in real media: wave propagation in anisotropic, anelastic and porous media*, volume 31, page 380. Elsevier Science Ltd., Oxford, UK, 1 edition, 2001.

[102] I. Tsvankin. P-wave signatures and notation for transversely isotropic media: An overview. *Geophys.*, 61(2):467–483, 1996.

[103] B. C. Abell and L. J. Pyrak-Nolte. Coupled wedge waves. *J. Acoust. Soc. Am.*, 134(5):3551–3560, 2013.

[104] Lord Rayleigh. On waves propagated along the plane surface of an elastic solid. *Proc. R. Soc. Lond. A*, 17:4–11, 1885.

[105] M. Rahman and J. Barber. Exact expressions for the roots of the secular equation for Rayleigh waves. *Transactions of the ASME*, 62:250–252, 1995.

[106] M. Rahman and T. Michelitsch. A note on the formula for the Rayleigh wave speed. *Wave Motion*, 43:272–276, 2006.

[107] P. Vinh and R. W. Ogden. On formulas for the Rayleigh wave speed. *Wave Motion*, 39:191–197, 2004.

[108] P. Vinh and R. W. Ogden. Formulas for the Rayleigh wave speed in orthotropic elastic solids. *Arch. Mech.*, 56(3):247–265, 2004.

[109] X. Li. On approximate analytic expressions for the velocity of Rayleigh waves. *Wave Motion*, 44:120–127, 2006.

[110] D. Nkemzi. A simple and explicit algebraic expression for the Rayleigh wave velocity. *Mech. Res. Comm.*, 35:201–205, 2008.

[111] H. Mechkour. The exact expressions for the roots of Rayleigh wave equation. In *Int. Colloquium of Math. in Eng. and Numerical Phys. MENP2*, pages 96–104. Geometry Balkan Press, 2002.

[112] J. G. Scholte. The range of existence of Rayleigh and Stoneley waves. *Mon. Not. Roy. Astro. Soc., Geophys. Suppl.*, 5(5):120, 1947.

[113] P. Chadwick. The existence of pure surface modes in elastic materials with orthorhombic symmetry. *J. Sound Vib.*, 47(1):39–52, 1976.

[114] J. Grima. Auxetic metamaterials. 2010.

[115] R. Stoneley. Elastic waves at the surface of separation of two solids. *Proc. Roy. Soc. (London)*, 106:416–428, 1924.

[116] K. Sezawa and K. Kanai. The range of possible existence of Stoneley-waves, and some related problems. *Bull. Earthquake Res. Inst. (Tokyo)*, 17(1):1–8, 1939.

[117] T. C. Lim and M. J. P. Musgrave. Stoneley waves in anisotropic media. *Nature*, 225:372, 1970.

[118] W. Johnson. The propagation of Stoneley and Rayleigh waves in anisotropic elastic media. *Bull. Seis. Soc. Am.*, 60(4):1105–1122, 1970.

[119] P. Vinh, P. Malischewsky, and P. Giang. Formulas for the speed and slowness of Stoneley waves in bonded isotropic elastic half-spaces with the same bulk wave velocities. *Int. J. Eng. Sci.*, 60:53–58, 2012.

[120] P. Vinh and P. Giang. On formulas for the velocity of Stoneley waves propagating along the loosely bonded interface of two elastic half-spaces. *Wave Motion*, 48:647–667, 2011.

[121] K. Sezawa and G. Nishimura. Rayleigh-type waves propagated along an inner stratum of a body. *Bull. Earthquake Res. Inst. (Tokyo)*, 5:85–91, 1928.

[122] M. Schoenberg. Elastic wave behavior across linear slip interfaces. *J. Acoust. Soc. Am.*, 68:1516–1521, 1980.

[123] G. S. Murty. Theoretical model for attenuation and dispersion of Stoneley waves at loosely bonded interface of elastic half spaces. *Phys. Earth Planet. Inter.*, 11:65–79, 1975.

[124] J. P. Jones and J. S. Whittier. Waves at a flexibly bonded interface. *J. Appl. Mech.*, 34(4):905–909, 1967.

[125] G. S. Murty. Wave propagation at an unbonded interface between two elastic half-spaces. *J. Acoust. Soc. Am.*, 58(5):1094–1095, 1975.

[126] S. I. Rokhlin and Y. J. Wang. Analysis of boundary conditions for elastic wave interaction with an interface between two solids. *J. Acoust. Soc. Am.*, 89(2):503–515, 1991.

[127] G. S. Murty and V. Kumar. Elastic wave propagation with kinematic discontinuity along a non-ideal interface between two isotropic elastic half-spaces. *J. Nondestr. Evaluation*, 10(2):39–53, 1991.

[128] A. R. Banghar, G. S. Murty, and I. V. V. Raghavacharyulu. On the parametric model of loose bonding of elastic half spaces. *J. Acoust. Soc. Am.*, 60(5):1071–1078, 1976.

[129] S. Roy and L. J. Pyrak-Nolte. Observation of a distinct compressional-mode interface wave on a single fracture. *Geophys. Res. Lett.*, 24(2):173–176, 1997.

[130] S. Nakagawa. *Acoustic resonance characteristics of rock and concrete containing fractures*. Ph.d. dissertation, 1998.

[131] A. Ekern, R. Suarez-Rivera, and A. Hansen. Investigation of interface wave propagation along planar fractures in sedimentary rocks. In J. J. K Daemen and R. Schulz, editors, *35th US Symposium on Rock Mechanics*, pages 161–167. Balkema, Rotterdam, 1995.

[132] S. Biwa, A. Suzuki, and N. Ohno. Evaluation of interface wave velocity, reflection coefficients and interfacial stiffnesses of contacting surfaces. *Ultrason.*, 43:495–502, 2005.

[133] V. Kumar and G. S. Murty. Influence of external pressure on interfacial wave propagation at a loosely bonded solid-solid interface. *IEEE Trans. Sonics and Ultrason.*, SU-29(3):138–142, 1982.

[134] T. Valier-Brasier, T. Dehoux, and B. Audoin. Scaled behavior of interface waves at an imperfect solid-solid interface. *J. Appl. Phys.*, 112:024904–1–024904–12, 2012.

[135] S. Nakagawa, K. Nihei, and L. Myer. Shear-induced conversion of seismic waves across single fractures. *Int. J. Rock Mech. Min. Sci.*, 37:203–218, 2000.

[136] D. Bogy. Edge-bonded dissimilar orthogonal elastic wedges under normal and shear loading. *J. of Appl. Mech.*, pages 460–466, 1968.

[137] B. V. Budaev and D. B. Bogy. Scattering of Rayleigh and Stoneley waves by two adhering elastic wedges. *Wave Motion*, 33:321–337, 2001.

[138] E. Sokolova, A. Kovalev, A. Maznev, and A. Mayer. Acoustic waves guided by the intersection of a surface and an interface of two elastic media. *Wave Motion*, 49:388–393, 2012.

[139] A. W. Joshi. *Group theory for physicists*. Halsted Press, New Jersey, USA, 1973.

[140] T. Wolfram and S. Ellialtioglu. *Applications of group theory to atoms, molecules, and solids*, volume 1. Cambridge University Press, NY, 2014.

[141] S. L. Moss, A. A. Maradudin, and S. L. Cunningham. Vibrational edge modes for wedges with arbitrary interior angles. *Phys. Rev. B*, 8:2999–3008, 1973.

[142] A. A. Maradudin, R. F. Wallis, D. L. Mills, and R. L. Ballard. Vibrational edge modes in finite crystals. *Phys. Rev. B*, 6(4):1106–1111, 1973.

[143] W. A. Wooster. *Tensors and group theory for the physical properties of crystals*. Clarendon Press, Oxford, 1973.

[144] J. Chen, J. Ping, and F. Wang. *Group representation theory for physicists*. World Scientific Publishing Co., 2 edition, 2002.

[145] E. Ash, R. M. De La Rue, and R.F. Humphyryes. Microsound surface waveguides. *IEEE Trans. Microwave theory Tech.*, MTT-17(11):882–892, 1969.

[146] P. E. Lagasse. Analysis of a dispersion free guide for elastic waves. *Electron. Lett.*, 8:372–373, 1972.

[147] P. Lagasse, I. Mason, and E. Ash. Acoustic surface waveguides - analysis and assessment. *IEEE Trans. Microwave theory Tech.*, 21:225–236, 1973.

[148] P. Lagasse and I. Mason. Analysis of propagation in ridge guides for acoustic surface waves. *Electron. Lett.*, 8(4):82–84, 1971.

[149] P. Lagasse. Finite element analysis of dispersion-free guides for elastic surface waves. In *Ultrasonics symposium*, pages 436–439. IEEE, 1972.

[150] A. A. Maradudin. Surface waves. *Feskorperprobleme*, 12:1–116, 1981.

[151] W. Ludwig and B. Lengeler. Surface waves and rotational invariance in lattice theory. *Solid State Commun.*, 2:83–86, 1964.

[152] I. V. Kamotskii. Surface wave running along the edge of an elastic wedge. *St. Petersburg Math J.*, 20(1):59–63, 2009.

[153] G. L. Zavorokhin and A. I. Nazarov. On elastic waves in a wedge. *J. Math. Sciences*, 176(6):646–650, 2011.

[154] M. Debilly. Acoustic technique applied to the measurement of the free edge wave velocity. *Ultrason.*, 34:611–619, 1996.

[155] V. V. Bozhenko, K. M. Ivanov-Shits, M. I. Sluch, and I. Y. Solodov. Experimental study of wedge acoustic waves. *Sov. Phys. Acoust.*, 31(2):151–152, 1985.

[156] P. Lagasse. Acoustic surface waveguides. In *Ultrasonics symposium*, pages 115–120. IEEE, 1972.

[157] S. Datta, M. J. Hoskins, and B. J. Hunsinger. Line acoustic waves on cleaved edges. *Appl. Phys. Lett.*, 32(1):3–5, 1978.

[158] I. M. Mason, M. D. Motz, and J. Chambers. Parametric interaction of acoustic surface wedge waves. *Electron. Lett.*, 8(17):429–430, 1972.

[159] M. DeBilly, A. C. Hladky-Hennion, and R. Bossut. On the localization of the antisymmetric flexural edge waves for obtuse angles. *Ultrason.*, 36:995–1001, 1998.

[160] T. Wu, Y. Chen, and C. Yang. Anti-symmetric flexural modes propagating along a wedge tip with a defect. *Proc. of SPIE*, 8347:834719, 2012.

[161] M. DeBilly, A. C. Hladky-Hennion, and R. Bossut. The effect of imperfections on acoustic wave propagation along a wedge waveguide. *Ultrason.*, 37:413–416, 1999.

[162] E. Sokolova, A. Kovalev, R. Timler, and A. Mayer. On the dispersion of wedge acoustic waves. *Wave Motion*, 50:233–245, 2013.

[163] X. Jia and M. DeBilly. Observation of the dispersion behavior of surface acoustic waves in a wedge waveguide by laser ultrasonics. *Appl. Phys. Lett.*, 61:2970–2972, 1992.

[164] C. Yang and I. Liu. Optical visualization of acoustic wave propagating along the wedge tip. *Proc. of SPIE*, 8321:83211W, 2011.

[165] P. Tung and C Yang. Anti-symmetric flexural modes for the detection of humidity variation. *IEEE Trans. Ultrason., Ferro. and Freq. control.*, 60(4):771–776, 2013.

[166] A. P. Mayer, A. Lomonosov, and P. Hess. Nonlinear acoustic waves localized at crystal edges. In *IEEE International Ultrasonics Symposium*, pages 1088–1091, 2009.

[167] E. Liu, J. A. Hudson, and T. Pointer. Equivalent medium representation of fractured rock. *J. Geophys. Res.*, 105(B2):2981–3000, 2000.

[168] A. M. Lomonosov, P. Hess, and A. P. Mayer. Silicon edges as one-dimensional waveguides for dispersion-free and supersonic leaky wedge waves. *Appl. Phys. Lett.*, 101:031904–1 – 031904–4, 2012.

[169] W. C. Wang and C. H. Yang. Antisymmetric flexural modes propagating along apex of piezoelectric wedges. *Japan J. Appl. Phys.*, 46(9A):5939–5943, 2007.

[170] I. H. Liu and C. Yang. An investigation on wedge waves and the interaction with a defect using a quantitative laser ultrasound visualization system. In *IEEE International Ultrasonics Symposium*, pages 817–820, 2010.

[171] P. D. Pupyrev, A. M. Lomonosov, P. Hess, and A. P. Mayer. Symmetry effects on elastic wedge waves at anisotropic edges. *J. Appl. Phys.*, 115(243504):1–11, 2014.

[172] M. Debilly. On the influence of loading on the velocity of guided acoustic waves propagating in linear elastic wedges. *J. Acoust. Soc. Am.*, 100:659–662, 1996.

[173] V. V. Krylov. On the velocities of localized vibration modes in immersed solid wedges. *J. Acoust. Soc. Am.*, 103:767–770, 1998.

[174] J. Chamuel. Edge waves along immersed elastic elliptical wedges with range dependent apex angle. *Ultrasonic Symposium*, pages 313–318, 1993.

[175] J. McKenna, G. D. Boyd, and R. N. Thurston. Plate theory solutions for guided flexural acoustic waves along the tip of a wedge. *IEEE Trans. Sonics Ultrason.*, 3:178–186, 1974.

[176] A. A. Krushynska. Flexural edge waves in semi-infinite elastic plates. *J. Sound Vib.*, 330:1964–1976, 2011.

[177] D. Parker. Elastic wedge waves. *J. Mech. Phys. Solids*, 40(7):1583–1593, 1992.

[178] E. Sokolova, A. Kovalev, and A. Mayer. Second-order nonlinearity of wedge acoustic waves in anisotropic media. *Wave Motion*, 50:246–252, 2013.

[179] A. Krylov and Parker D. Harmonic generation and parametric mixing in wedge acoustic waves. *Wave Motion*, 15:185–200, 1992.

[180] V. T. Grinchenko and V. V. Meleshko. Properties of harmonic waves propagating along the edge of a right-angle elastic wedge. *Sov. Phys. Acoust.*, 27(2):112–116, 1981.

[181] R. S. Wagers. Phase velocity relation for an acoustic wedge guide mode. *J. Appl. Phys.*, 44(11):4813–4815, 1973.

[182] A. C. Hladky-Hennion. Finite element analysis of the propagation of acoustic waves in waveguides. *J. Sound Vib.*, 194(2):119–136, 1996.

[183] P. Lagasse. Finite element analysis of piezoelectric elastic waveguides. *IEEE Trans. Sonics and Ultrason.*, SU-20(4):354–359, 1973.

[184] I. Mason, R. De La Rue, R. Schmidt, E. Ash, and P. Lagasse. Ridge guides for acoustic surface waves. *Electron. Lett.*, 7(14):395–397, 1971.

[185] V. V. Krylov. Distinctive characteristics of guided surface-wave propagation in complex topographic structures. *Sov. Phys. Acoust.*, 33:407–411, 1987.

[186] V. V. Krylov. On the existence of a symmetric acoustic mode in a quadratic solid wedge. *Moscow Univ. Phys. Bull.*, 46:45–49, 1991.

[187] V. V. Krylov. Localized vibration modes propagating along edges of cylindrical and conical wedge-like structures. *J. Sound Vib.*, 227:215–221, 1999.

[188] T. M. Sharon, A. A. Maradudin, and S. L. Cunningham. Rectangular- ridge vibrational modes. *Electron. Lett.*, 10:229–230, 1975. erratum in Electron. Lett., 11, 356, 1975.

[189] A. A. Maradudin and K. R. Subbaswamy. Edge localized vibration modes on a rectangular ridge. *J. Appl. Phys.*, 48:3410–3414, 1977.

[190] C. Yang and J. Liaw. Observation of dispersion behavior of acoustic wedge waves propagating along the tip of a circular wedge with laser ultrasonics. *Jpn. J. Appl. Phys.*, 39:2741–2743, 2000.

[191] P. Lagasse, M. Cabus, and M. Verplanken. The influence of truncation on dispersion of wedge guides. In *Ultraonics Symposium*, pages 121–124. IEEE, 1974.

[192] Z. L. Li, I. Achenbach, J. D.and Komsky, and Y. C. Lee. Reflection and transmission of obliquely incident surface waves by an edge of a quarter space: Theory and experiment. *J. Appl. Mech.*, 59:349–355, 1992.

[193] M. Debilly. On the scattering of antisymmetric edge modes. *J. Acoust. Soc. Am.*, 101(6):3261–3269, 1997.

[194] V. V. Krylov and A. V. Shanin. Influence of elastic anisotropy on the velocities of acoustic wedge modes. *Sov. Phys. Acoust.*, 37:65–67, 1991.

[195] A. L. Shuvalov and V. V. Krylov. Localized vibration modes in free anisotropic wedges. *J. Acoust. Soc. Am.*, 107:657–600, 2000.

[196] A. D. Boardman, R. Garcia-Molina, A. Gras-Marti, and E. Louis. Electrostatic edge modes of a hyperbolic dielectric wedge: Analytical solution. *Phys. Rev. B*, 32:6045–6047, 1985.

[197] A. Eguiluz and A. A. Maradudin. Electrostatic edge modes along a parabolic wedge. *Phys. Rev. B*, 14:5526–5528, 1976.

[198] Y. Zhou, W. Chen, and C. Lu. Elastic waves in multiferroic cylinders of sectorial cross-section. *Composites: Part B*, 43:3001–3008, 2012.

[199] J. S. Yang. Shear horizontal vibrations of a piezoelectric/ferroelectric wedge. *Acta Mech.*, 173:13–17, 2004.

[200] S. Datta and B. Hunsinger. Analysis of surface waves using orthogonal functions. *J. Appl. Phys.*, 49(475):476–479, 1977.

[201] R. Adler, M. Hoskins, S. Datta, and B. Hunsinger. Unusual parametric effects on line acoustic waves. *IEEE Trans. Sonics and Ultrason.*, 26:345–347, 1979.

[202] T. Sharon, A. A. Maradudin, and S. L. Cunningham. Vibrational edge modes for small angle wedges. *Phys. Rev. B*, 8(12):6024–6026, 1973.

[203] T. Sharon. Edge modes for piezoelectric wedges of arbitrary interior angles. In *IEEE Ultrasonic Symposium*, pages 126–130.

[204] A. A. Maradudin. Edge modes. *Japan J. Appl. Phys. Suppl.*, 2:871–878, 1974.

[205] A. A. Oliner. Waveguides for acoustic surface waves: a review. *Proc. of the IEEE*, 64:615–627, 1976.

[206] S. Biryukov, Y. Gulyaev, V. Krylov, and V. Plessky. *Surface acoustic waves in inhomogeneous media*, volume 20. Springer-Verlag, Germany, 1995.

[207] P. Hess, A. Lomonosov, and A. P. Mayer. Laser based linear and nonlinear guided elastic waves at surfaces (2d) and wedges (1d). *Ultrason.*, 54:39–55, 2014.

[208] W. C. Wang, C. H. Yang, and A. S. Yang. Acoustic streaming induced by anti-symmetrical flexural modes near a wedge tip. In *IEEE International ultrasonics symposium*, pages 1047–1049, 2010.

[209] V. V. Krylov and E. Porteous. Wave like aquatic propulsion of mono hull marine vessels. *Ocean Eng.*, 37:378–386, 2010.

[210] C. Yin and T. H. Yu. An ultrasonic motor driven by traveling cylindrical wedge waves. pages 156–159.

[211] V. V. Krylov and G. V. Pritchard. Experimental investigation of the aquatic propulsion caused by localised flexural wave propagation in immersed wedges and plates. *Appl. Acoust.*, 68:97–113, 2007.

[212] D. Bogy. Two edge-bonded elastic wedges of different materials and wedge angles under surface tractions. *J. Appl. Mech.*, pages 377–386, 1971.

[213] C. J. Hsu and M. Schoenberg. Elastic waves through a simulated fractured medium. *Geophys.*, 58(7):964–977, 1993.

[214] L. J. Pyrak-Nolte, L. Myer, and N. G. W. Cook. Transmission of seismic waves across single natural fractures. *Geophys. Res.*, 95(B6):8617–8638, 1990.

[215] C. Hobday and M.H. Worthington. Field measurements of normal and shear fracture compliance. *Geophys. Prospect.*, 60:488–499, 2012.

[216] R. Lubbe, J. Sothcott, M. H. Worthington, and C. McCann. Laboratory estimates of normal and shear fracture compliance. *Geophys. Prospect.*, 56:239–247, 2008.

[217] M. K. Choi. *Characterization of fracture stiffness subjected to normal and shear stress.* Ph.d. dissertation, 2013.

[218] A. Hedayat, L. J. Pyrak-Nolte, and A. Bobet. Detection and quantification of slip along non-uniform frictional discontinuities using digital image correlation. *Geotech. Test. J.*, 37(5):1–14, 2014.

[219] A. Hedayat. *Mechanical and geophysical characterization of damage in rocks.* Ph.d. dissertation, 2013.

[220] L. J. Pyrak-Nolte and D. D. Nolte. Wavelet analysis of velocity dispersion of elastic interface waves propagating along a fracture. *Geophys. Res. Lett.*, 22(11):1329–1332, 1995.

[221] D. D. Nolte, L. J. Pyrak-Nolte, J. Beachy, and C. Ziegler. Transition from the displacement discontinuity limit to the resonant scattering regime for fracture interface waves. *Rock Mech. and Mining Sci.*, 37:219–230, 2000.

[222] A. Bobet. Influence of the loading apparatus on the stresses within biaxial specimens. *Geotech. Test. J.*, 24(3):256–272, 2001.

[223] A. Bobet and H. H. Einstein. Fracture coalescence in rock-type materials under uniaxial and biaxial compression. *In. J. Rock Mech. Min. Sci.*, 35(7):863–888, 1998.

[224] B. McGinty. Continuum mechanics, 2012.

[225] J. J. Sakurai. *Modern quantum mechanics revised edition.* Addison-Wesley Pubishing Company, Inc., USA, 1994.

[226] G. Arfken. *Mathematical methods of physicists*, volume 1. Academic Press Inc., London, 1968.

[227] B. Noble. *Applied Linear Algebra*, volume 1. Prentice-Hall, New Jersey, USA, 1969.

[228] J. Stensby. Hermitian matrices, 02/10/14 1998.

[229] R. Polikar. The wavelet tutorial, 1999.

[230] J. Ashmead. Morlet wavelets in quantum mechanics. *Quanta*, 1(1):58–70, 2012.

[231] J. Combes, A. Grossmann, and Ph. Tchamitchian. *Wavelets: time-frequency methods and phase space*. Springer-Verlag, Germany, 2 edition, 1989.

[232] Y. Sheng. *Wavelet Transform*, chapter 10. CRC and IEEE Press, Boca Raton, 1995.

[233] E. de K. Leffingwell. Ground ice wedges: The dominant form of ground ice on the North Coast of Alaska. *J. Geol.*, 23(7):635–654, 1915.

APPENDICES

Appendix A: Stress, Strain, and Displacement

A.1 Introduction

A brief derivation of relationships and definitions of stress, displacement discontinuity, and traction are presented here. For a more in depth discussion see the references [99, 100, 224]. Throughout this section, variables with hats (e.g., $\bar{\mathbf{t}}$) are vectors, bolded variables without hats (e.g., $\boldsymbol{\sigma}$) are tensors, and unbolded variables (e.g., x) are scalars.

Traction

Traction, $\bar{\mathbf{t}}$, is defined as the vector representation of the internal force vector acting on a cross section divided by the area of that cross section. In equation form this is

$$\bar{\mathbf{t}} = \frac{\bar{\mathbf{F}}_{internal}}{A}. \tag{A.1}$$

Equation A.1 is written in terms of the force as

$$\bar{\mathbf{F}} = \int \bar{\mathbf{t}} dA. \tag{A.2}$$

Stress

Stress is a tensor because it obeys standard coordinate transformation principles of tensors [99]. Stress represents the components of the traction vector (Fig. A.1). The components are usually termed the normal and shear stresses. Typically, the normal stress is defined as, σ, and the tangential stress as, τ; however, for this discussion ς is used for the normal stress and τ for the shear stress.

The definition of these components are

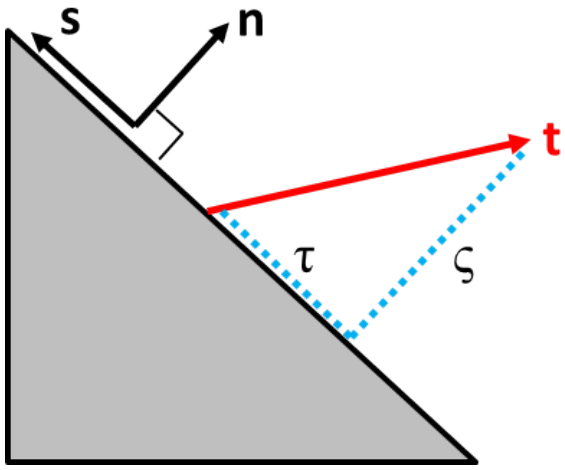

Figure A.1. Diagram indicating the meaning of the directions and stresses in this section. Note that the arrows represent vectors and the dashed lines represent scalars.

$$\varsigma = \bar{\mathbf{t}} \cdot \bar{\mathbf{n}}, \tag{A.3}$$

and

$$\tau = \bar{\mathbf{t}} \cdot \bar{\mathbf{s}}, \tag{A.4}$$

where ς and τ are scalars (i.e., dot products produce scalars), $\bar{\mathbf{n}}$ is the unit normal and $\bar{\mathbf{s}}$ is a unit vector perpendicular to $\bar{\mathbf{n}}$ and parallel to the surface. ς and τ only represent two components of the full stress tensor.

It should be mentioned that in 3-D there are an infinite number of $\bar{\mathbf{s}}$ vectors parallel to a surface. Typically, one vector is defined parallel to the page and another perpendicular to it.

Example calculating the stress components

Starting with a traction of $\bar{\mathbf{t}} = 9.39\mathbf{i}\ MPa$, and a unit normal to the 20° angled surface (Fig. A.1)

$$\bar{\mathbf{n}} = (cos(20^\circ), sin(20^\circ), 0)\,, \tag{A.5}$$

calculate the stress components.

The normal stress component on the surface is

$$\varsigma = \bar{\mathbf{t}} \cdot \bar{\mathbf{n}} = (9.39, 0, 0) \cdot (cos(20^\circ), sin(20^\circ), 0) = 9.39cos(20^\circ) = 8.82\ MPa. \tag{A.6}$$

Choosing a direction perpendicular to $\bar{\mathbf{n}}$ as

$$\bar{\mathbf{s}} = (-sin(20^\circ), cos(20^\circ), 0), \tag{A.7}$$

the shear stress component on the surface is calculated from the parallel vector as

$$\tau = \bar{\mathbf{t}} \cdot \bar{\mathbf{s}} = (9.39, 0, 0) \cdot (-sin(20^\circ), cos(20^\circ), 0) = -9.39sin(20^\circ) = -3.21\ MPa. \tag{A.8}$$

Stress Tensor and Traction Vector Relations

Next, the relationship between the traction vector, $\bar{\mathbf{t}}$, and the stress tensor, $\boldsymbol{\sigma}$, is determined. To do this, the sum of the forces on the object must be set to 0 (i.e., equilibrium). This derivation will use Fig. A.2 for reference.

Using Eqns. A.1, A.3, and A.4 the x and y components of the internal forces are

$$\begin{aligned} \varsigma_{xx} A cos(\theta) + \tau_{xy} A sin(\theta) &= t_x A, \\ \tau_{xy} A cos(\theta) + \varsigma_{yy} A sin(\theta) &= t_y A. \end{aligned} \tag{A.9}$$

The area cancels, leaving

$$\begin{aligned} \varsigma_{xx} cos(\theta) + \tau_{xy} sin(\theta) &= t_x, \\ \tau_{xy} cos(\theta) + \varsigma_{yy} sin(\theta) &= t_y. \end{aligned} \tag{A.10}$$

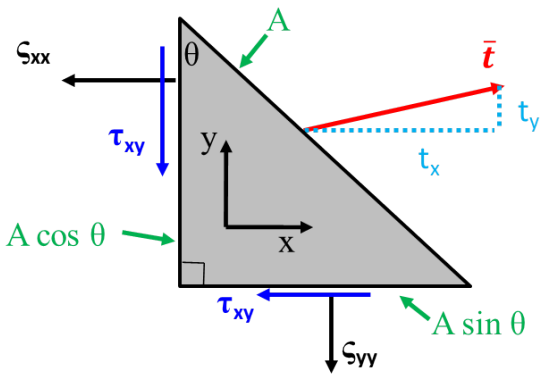

Figure A.2. Diagram indicating the meaning of the directions and stresses in this section. The arrows by A (green) are indicating the area of the face it points to. All other arrows are vectors.

Recall that the trigonometric functions indicate the components of the normal to the surface, i.e., $\bar{\mathbf{n}} = (cos\theta, sin\theta, 0)$ that the traction, $\bar{\mathbf{t}}$, is acting on (Fig. A.2). Replace the trigonometric functions with the components of the normal vector, n_x and n_y, yielding

$$\begin{aligned} \varsigma_{xx} n_x + \tau_{xy} n_y &= t_x, \\ \tau_{xy} n_x + \varsigma_{yy} n_y &= t_y. \end{aligned} \tag{A.11}$$

This result is summarized as

$$\bar{\mathbf{t}} = \boldsymbol{\sigma} \cdot \bar{\mathbf{n}}, \tag{A.12}$$

where $\boldsymbol{\sigma}$ is the tensor

$$\boldsymbol{\sigma} = \begin{bmatrix} \varsigma_{xx} & \tau_{xy} & \tau_{xz} \\ \tau_{yx} & \varsigma_{yy} & \tau_{yz} \\ \tau_{zx} & \tau_{zy} & \varsigma_{zz} \end{bmatrix}, \tag{A.13}$$

and

$$\tau_{ij} = \tau_{ji}, \;\; j, i = x, y, z. \tag{A.14}$$

Equation A.12 can be rewritten in tensor component notation as

$$t_i = \sigma_{ij} n_j, \;\; i, j = x, y, z, \tag{A.15}$$

where summations are implied, and the components represent the rows (or columns) of the vector and tensor. Equation A.15 in 3D is

$$\begin{aligned} \varsigma_{xx} n_x + \tau_{xy} n_y + \tau_{xz} n_z &= t_x, \\ \tau_{yx} n_x + \varsigma_{yy} n_y + \tau_{yz} n_z &= t_y, \\ \tau_{zx} n_x + \tau_{zy} n_y + \varsigma_{zz} n_z &= t_z. \end{aligned} \tag{A.16}$$

Example using the stress tensor

Given the stress tensor (in MPa)

$$\boldsymbol{\sigma} = \begin{bmatrix} 5 & 12 & 31 \\ 11 & 95 & 2 \\ 10 & 30 & 17 \end{bmatrix}, \tag{A.17}$$

calculate the traction vector on a surface with unit normal $\bar{\mathbf{n}} = (0.3, 0.65, 0.623)$.

From Eqn. A.12

$$\begin{Bmatrix} t_x \\ t_y \\ t_z \end{Bmatrix} = \begin{bmatrix} 5 & 12 & 31 \\ 11 & 95 & 2 \\ 10 & 30 & 17 \end{bmatrix} \begin{Bmatrix} 0.3 \\ 0.65 \\ 0.623 \end{Bmatrix} = \begin{Bmatrix} 28.61 \\ 66.30 \\ 33.09 \end{Bmatrix}. \tag{A.18}$$

In component notation $\bar{\mathbf{t}} = 28.61\mathbf{i} + 66.30\mathbf{j} + 33.09\mathbf{k}\ MPa$. The force can also be calculated, if the cross sectional area is known. For example, if the area is 200 mm^2, then the force would be $\bar{\mathbf{F}} = \bar{\mathbf{t}} A = 5722\mathbf{i} + 13260\mathbf{j} + 6618\mathbf{k}\ N$.

Stress Transformations

Recall that the normal, ς, and shear, τ, stress components (scalar) on a given surface are related to the traction vector, $\bar{\mathbf{t}}$, by Eqns. A.3 and A.4 and that the traction vector is related to the stress tensor by Eqn. A.12. Substituting the stress components into Eqn. A.12 gives

$$\varsigma = \bar{\mathbf{t}} \cdot \bar{\mathbf{n}} = (\boldsymbol{\sigma} \cdot \bar{\mathbf{n}}) \cdot \bar{\mathbf{n}} = \sigma_{ij} n_j n_i, \tag{A.19}$$

and

$$\tau = \bar{\mathbf{t}} \cdot \bar{\mathbf{s}} = (\boldsymbol{\sigma} \cdot \bar{\mathbf{s}}) \cdot \bar{\mathbf{n}} = \sigma_{ij} s_j n_i, \tag{A.20}$$

where summations are implied over the indices.

Example using the stress transformation

Using the stress tensor in equation A.17 calculate the normal and shear stresses on the surface with a normal vector of $\bar{\mathbf{n}} = 0.3i + 0.65j + 0.623k$.

The normal stress is

$$\varsigma = \sum_{i,j=1}^{3} \sigma_{ij} n_j n_i = \begin{Bmatrix} 0.300 & 0.650 & 0.623 \end{Bmatrix} \begin{bmatrix} 5 & 12 & 31 \\ 11 & 95 & 2 \\ 10 & 30 & 17 \end{bmatrix} \begin{Bmatrix} 0.300 \\ 0.650 \\ 0.623 \end{Bmatrix} = 72.292 \ MPa. \tag{A.21}$$

The shear stress is a bit more difficult because some specific unit vector parallel to the surface must be defined. Only one of the infinite possibilities is necessary. Using $\bar{\mathbf{s}} = (-0.32, 0.550, 0.000)$ (a dot product can verify the orthogonality of this vector to $\bar{\mathbf{n}}$). The shear stress is

$$\tau = \sum_{i,j=1}^{3} \sigma_{ij} s_j n_i = \begin{Bmatrix} -0.320 & 0.550 & 0.000 \end{Bmatrix} \begin{bmatrix} 5 & 12 & 31 \\ 11 & 95 & 2 \\ 10 & 30 & 17 \end{bmatrix} \begin{Bmatrix} 0.300 \\ 0.650 \\ 0.623 \end{Bmatrix} = 27.31 \ MPa. \tag{A.22}$$

Comparing the results of Eqn. A.22 to A.21 indicates that there is less than half of the shear stress in this direction ($\bar{\mathbf{s}} = (-0.32, 0.550, 0.000)$) compared to the normal direction. However, this is just one of the infinite possible shear directions possible. To see this, another direction, perpendicular to the shear vector used in Eqn. A.22 is chosen. This new shear direction is determined using the cross product

$$\bar{\mathbf{s}}_{\mathbf{2}} = \bar{\mathbf{n}} \times \bar{\mathbf{s}} = (0.300, 0.650, 0.623) \times (-0.320, 0.550, 0.000) = (-0.343, -0.199, 0.373). \tag{A.23}$$

So, the new shear stress (τ_2) that is perpendicular to the first shear stress (τ) is

$$\tau_2 = \begin{Bmatrix} -0.343 & -0.199 & 0.373 \end{Bmatrix} \begin{bmatrix} 5 & 12 & 31 \\ 11 & 95 & 2 \\ 10 & 30 & 17 \end{bmatrix} \begin{Bmatrix} 0.300 \\ 0.650 \\ 0.623 \end{Bmatrix} = -10.68\ MPa, \tag{A.24}$$

where the negative indicates that τ_2 is in the direction opposite $\bar{\mathbf{s}}_{\mathbf{2}}$.

A.2 Displacement Discontinuity

Now that the relationships between stress and traction have been derived, a derivation of the displacement discontinuity (DD) boundary conditions is presented. This derivation is based on several references [12, 122, 130]. Throughout this derivation the geometry is a fracture on the x-y plane with the z direction normal (Fig. A.3).

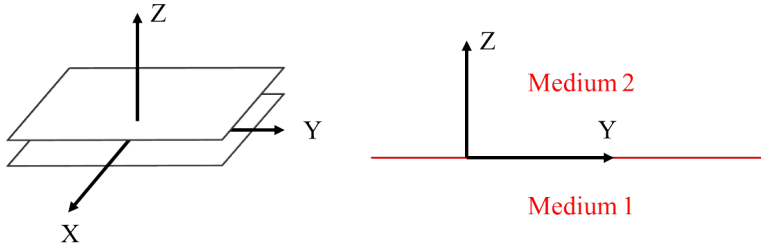

Figure A.3. Geometry used for the DD boundary condition derivation.

According to Schoenberg [122], "The stress traction which is continuous across the interface is assumed to be related to the discontinuity of displacement at each point." The DD vector is expressed as

$$\begin{aligned} \Delta\bar{\mathbf{u}} &= \bar{\mathbf{u}}^{(\mathbf{2})}(0,0,0^+) - \bar{\mathbf{u}}^{(\mathbf{1})}(0,0,0^-), \\ &OR \\ [u_j] &= u_j^{(2)} - u_j^{(1)},\ (j = x,y,z), \end{aligned} \tag{A.25}$$

where the superscripts denote the medium. With this definition, the boundary conditions are

$$\begin{aligned} t_i^{(1)} &= -t_i^{(2)} = \sigma_{zi}, \\ \sigma_{zi} &= \kappa_{ij}[u_j], \quad (i,j = x,y,z), \end{aligned} \tag{A.26}$$

where κ_{ij} are the specific stiffness components on the fracture plane. Recall that σ_{zx} and σ_{zy} are the tangential stresses and σ_{zz} is the normal stress on the fracture plane (Fig. A.3). Considering fractures without shear loading yields only the diagonal elements in the stiffness (i.e., $\kappa_{ij} = 0$ for $i \neq j$). The resulting DD boundary conditions are

$$\begin{aligned} \sigma_{zx} &= \kappa_{xx}[u_x], \\ \sigma_{zy} &= \kappa_{yy}[u_y], \\ \sigma_{zz} &= \kappa_{zz}[u_z], \\ t_x^{(1)} &= -t_x^{(2)} = \sigma_{zx}, \\ t_y^{(1)} &= -t_y^{(2)} = \sigma_{zy}, \\ t_z^{(1)} &= -t_z^{(2)} = \sigma_{zz}. \end{aligned} \tag{A.27}$$

The constitutive relations for the stresses are

$$\sigma_{ij}^{(\eta)} = \lambda_L^{(\eta)} \delta_{ij} \frac{\partial u_k}{\partial x_k} + \mu_L^{(\eta)} \left(\frac{\partial u_i}{\partial x_j} + \frac{\partial u_j}{\partial x_i} \right), \tag{A.28}$$

where λ_L and μ_L are the well known Lamé's parameters and δ_{ij} is the Kronecker delta function. For medium 1, the stresses become

$$\begin{aligned}
\sigma_{zx}^{(1)} &= \mu_L^{(1)} \left(\frac{\partial u_x}{\partial z} + \frac{\partial u_z}{\partial x} \right), \\
\sigma_{zy}^{(1)} &= \mu_L^{(1)} \left(\frac{\partial u_y}{\partial z} + \frac{\partial u_z}{\partial y} \right), \\
\sigma_{zz}^{(1)} &= \left(2\mu_L^{(1)} + \lambda_L^{(1)} \right) \frac{\partial u_z}{\partial z} + \lambda_L^{(1)} \left(\frac{\partial u_x}{\partial x} + \frac{\partial u_y}{\partial y} \right).
\end{aligned} \tag{A.29}$$

Note that typically one of the tangential stress components is suppressed in Eqn. A.29 since the waves are polarized and propagate in only two dimensions (or less).

The traction vector, $\bar{\mathbf{t}}$, is determined using equation A.12 and A.13 where the normal for the DD problem (Fig. A.3) is $\bar{\mathbf{n}} = (0, 0, 1)^T$. The result is

$$\bar{\mathbf{t}} = \begin{bmatrix} \sigma_{xx} & \sigma_{xy} & \sigma_{xz} \\ \sigma_{yx} & \sigma_{yy} & \sigma_{yz} \\ \sigma_{zx} & \sigma_{zy} & \sigma_{zz} \end{bmatrix} \begin{bmatrix} 0 \\ 0 \\ 1 \end{bmatrix} = \begin{bmatrix} \sigma_{xz} \\ \sigma_{yz} \\ \sigma_{zz} \end{bmatrix}. \tag{A.30}$$

Applied to the Eqn. A.27 (remembering Eqn. A.14) yields

$$\begin{bmatrix} u_x^{(2)} - u_x^{(1)} \\ u_y^{(2)} - u_y^{(1)} \\ u_z^{(2)} - u_z^{(1)} \end{bmatrix} = \begin{bmatrix} \frac{1}{\kappa_{xx}} & 0 & 0 \\ 0 & \frac{1}{\kappa_{yy}} & 0 \\ 0 & 0 & \frac{1}{\kappa_{zz}} \end{bmatrix} \begin{bmatrix} \sigma_{xz} \\ \sigma_{yz} \\ \sigma_{zz} \end{bmatrix} = \begin{bmatrix} \frac{1}{\kappa_{xx}} \sigma_{xz} \\ \frac{1}{\kappa_{yy}} \sigma_{yz} \\ \frac{1}{\kappa_{zz}} \sigma_{zz} \end{bmatrix}, \tag{A.31}$$

which is the DD theory used in this dissertation.

A.3 Free Surface

Between a solid and a vacuum there exists a boundary condition called a free surface boundary condition [100]. This free surface has a normal in the $\hat{n}$ direction (e.g., z for medium 1 in Fig. A.3). The free surface boundary condition is expressed as

$$t_i = \sigma_{ij} n_j = 0, \; n_j = \delta_{jz}, \tag{A.32}$$

which results in

$$\tau_{xz} = \tau_{yz} = \varsigma_{zz} = 0. \tag{A.33}$$

Note that there are no constraints on the stress components σ_{xx}, σ_{xy}, and σ_{yy}. This boundary condition was used to discover the famous Rayleigh wave [104].

Appendix B: Laguerre Functions

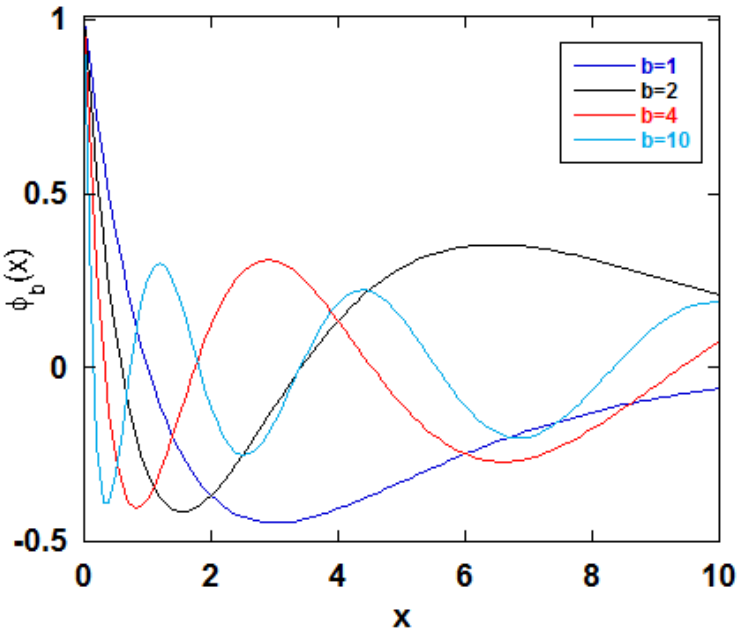

Figure B.1. Graphical representation of the $n = 1,\ n = 2,\ n = 4$, and $n = 10$ Laguerre functions.

Laguerre polynomials arise in several problems in mathematics and quantum mechanics. One example is the solution to the Schrödinger equation for the hydrogen atom [225]. The polynomials come from Laguerre's differential equation [226]

$$xy''(x) + (1 - x)y'(x) + ny(x) = 0. \tag{B.1}$$

where n is a real number. For positive values of n, Eqn. B.1 yields the Laguerre polynomials, $L_n(x)$ (Eqn. 5.21). The polynomials follow the recurrence relation

$$xL'_n(x) = nL_n(x) - nL_{n-1}(x) \tag{B.2}$$

where the $'$ is a derivative with respect to x. As shown by Arfken (1968) [226], the Laguerre polynomials do not form an orthogonal set by themselves, but through the use of a weighting function

$$\phi_n(x) = e^{-\frac{x}{2}} \frac{L_n(x)}{n!}. \tag{B.3}$$

This new form is orthonormal and complete on the interval $0 \leq x < \infty$ such that

$$\int_0^\infty e^{-x} L_m(x) L_n(x) dx = \int_0^\infty \phi_n(x) \phi_n(x) dx = \delta_{mn}, \tag{B.4}$$

where δ_{mn} is the Kronocker delta symbol [226]. Several Laguerre functions are shown in Fig. B.1.

Appendix C: Rayleigh Stoneley Wave Group Theory Analysis

C.1 Rayleigh-Stoneley Waves

The Rayleigh-Stoneley wave (RS) was predicted to exist by Sokolova et al., (2012) [138], but to this author's knowledge, no group theory analysis of this wave exists. The following will analyze the results of group theory applied to the RS wave.

Step 1: Identify the point group and its symmetry operations

The geometry for the RS wave is the same as that used in the CWW derivation (Fig. 5.1) except the material properties differ. The only operator that keeps the point symmetry unchanged is the identity operator, E. This leads to the point group C_1 which is order 1, Abelian, finite, and has no symmetry.

Step 2: Specify the coordinate system and basis functions

The same coordinate system used for the CWW is used here, i.e., a coordinate system at the tip of each wedge corner at the origin.

Step 3: Determine the effects of the symmetry operations on the basis functions

Because the identity is the only operator, all the basis functions transform into themselves. The (rather simple) action table is shown in Table C.1.

Step 4: Construct a matrix representation for each element using the basis functions

The matrix representation for the identity operator is the same as Eqn. 5.3 and is not repeated here.

Table C.1
Action table for the RS wave.

	E
r_x	r_x
r_y	r_y
r_z	r_z
1	1
2	2

Step 5: Determine the number and type of irreducible representations

The operator E is in a class of its own (i.e., $\{E\}$) with the character table given in Table C.2. From the character table, the number of times the IR is contained in the representation is

$$n^A = \frac{1}{1}\left[\chi_E^* \chi_E^A\right], \tag{C.1a}$$

$$n_x^A = n_y^A = n_z^A = \frac{1}{1}\left[(2)(1)\right] = 2. \tag{C.1b}$$

Table C.2
Character table for the RS wave.

C_1	E
A	1
Γ^x	2
Γ^y	2
Γ^z	2

Step 6: Analyze the information in the decomposition

The decomposition for the RS wave is

$$\Gamma^x = \Gamma^y = \Gamma^z = 2\Gamma^A. \tag{C.2}$$

Step 7: Determine the symmetry functions

The symmetry functions are determined from

$$\bar{\mathbf{V}}^A \propto [\Gamma(E)]\,\bar{\mathbf{V}}. \tag{C.3}$$

The resulting components of the symmetry functions are

$$\bar{\mathbf{V}}_x^A = \begin{pmatrix} 1 \\ 0 \\ 0 \\ 0 \\ 0 \\ 0 \end{pmatrix}, \qquad \bar{\mathbf{V}}_y^A = \begin{pmatrix} 0 \\ 1 \\ 0 \\ 0 \\ 0 \\ 0 \end{pmatrix}, \qquad \bar{\mathbf{V}}_z^A = \begin{pmatrix} 0 \\ 0 \\ 1 \\ 0 \\ 0 \\ 0 \end{pmatrix}. \tag{C.4}$$

Visualizations of Eqn. C.4 are shown in Fig. C.1. Equation C.4 may seem rather simple, but the results lead to predicted wagging and breathing modes for the RS wave (Fig. C.1 and C.2). Although only motion in medium 1 is predicted, the boundary conditions for the RS wave (continuous stress and displacement, i.e., welded), lead to medium 2 being excited (i.e., dragged along) to allow the boundary conditions to be met.

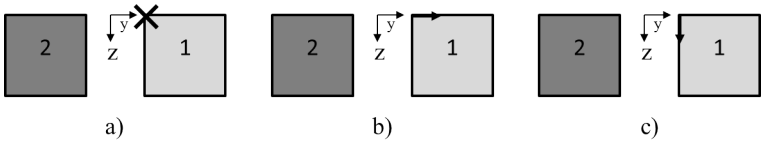

Figure C.1. Components of the A vibrational mode for the RS wave. a) X-components, b) y-components, and c) z-components.

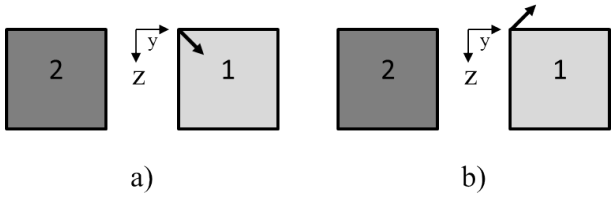

Figure C.2. The A vibrational mode for the RS wave. The a) breathing mode and b) wagging mode predicted by group theory.

Appendix D: Linear Algebra

This information is copied from the book, *Applied Linear Algebra* by Ben Noble (1969) [227].

Consider the equation

$$\bar{\mathbf{A}}\bar{\mathbf{x}} = \bar{\mathbf{b}}, \tag{D.1}$$

which is a notation for the system of equations

$$\begin{aligned} &x_1 + a_{1,2}x_2 + ... + a_{1,n}x_n = \beta_1, \\ &x_p + a_{1,p+1}x_{p+1} + ... + a_{2,n}x_n = \beta_2, \\ &\vdots \end{aligned} \tag{D.2}$$

where $a_{q,n}$ and β are constants.

Define s as the number of unknowns (x_n), m as the number of equations, and n as the total number of unknowns. The homogeneous form of Eqn. D.1 is

$$\bar{\mathbf{A}}\bar{\mathbf{x}} = \mathbf{0}. \tag{D.3}$$

For Eqn. D.3 to be true, Eqn. D.2 must have $\beta_i = 0$ for all i, so that the only two possible outcomes are:
i) If $s = n$ (thus $m \geq n$), then the only solution is $x = 0$. This is called the *Trivial Solution.* ii) If $s < n$, the equations possess an infinity of solutions given by assigning arbitrary values to x.

D.1 Eigenvalue Problems

Theorem D.1 *A system of homogeneous equations is represented by an eigenvalue problem as*

$$\left(\bar{\mathbf{A}} - \lambda\bar{\mathbf{I}}\right)\bar{\mathbf{x}} = 0, \tag{D.4}$$

where $\bar{\mathbf{I}}$ *is the identity matrix.*

Equation D.4 possesses only the trivial solution ($\bar{\mathbf{x}} = 0$*), unless the determinant of the coefficients is zero (i.e.,* $|\bar{\mathbf{A}} - \lambda\bar{\mathbf{I}}| = 0$*), which is defined as the secular or characteristic equation.*

Proof Take the determinant of Eqn. D.4 and use the identity $det(AB) = det(A)det(B)$ to yield

$$det\left((\bar{\mathbf{A}} - \lambda\bar{\mathbf{I}})\bar{\mathbf{x}}\right) = det\left((\bar{\mathbf{A}} - \lambda\bar{\mathbf{I}})\right) det\left(\bar{\mathbf{x}}\right) = 0. \tag{D.5}$$

Eqn. D.5 requires either the left or right determinant to equal zero. Since solutions, $\bar{\mathbf{x}}$, are sought that are non-zero, the first determinant in Eqn. D.5 must be 0 to have non-zero solutions. Thus,

$$det\left((\bar{\mathbf{A}} - \lambda\bar{\mathbf{I}})\right) = 0. \tag{D.6}$$

■

D.2 Similarity Transformation

Definition D.1 *If there exists a nonsingular matrix (i.e., a matrix that has an inverse),* $\bar{\mathbf{P}}$*, such that*

$$\bar{\mathbf{P}}^{-1}\bar{\mathbf{A}}\bar{\mathbf{P}} = \bar{\mathbf{B}}, \tag{D.7}$$

the matrix $\bar{\mathbf{B}}$ *is said to be similar to* $\bar{\mathbf{A}}$*, and it is said that* $\bar{\mathbf{B}}$ *is obtained from* $\bar{\mathbf{A}}$ *by means of a similarity transformation.*

Several theorems for similarity transformations are now presented.

Theorem D.2 *Similar matrices (*$\bar{\mathbf{A}}$*,* $\bar{\mathbf{B}}$*) have the same characteristic equations and the same eigenvalues.*

Proof For matrix $\bar{\mathbf{P}}$ it can be shown that if

$$det\left(\bar{\mathbf{P}}^{-1}\right) det\left(\bar{\mathbf{P}}\right) = det\left(\bar{\mathbf{P}}^{-1}\bar{\mathbf{P}}\right) = det\left(\bar{\mathbf{I}}\right) = 1, \tag{D.8}$$

then

$$det(\bar{\mathbf{B}} - \lambda\bar{\mathbf{I}}) = det(\bar{\mathbf{P}}^{-1}(\bar{\mathbf{A}} - \lambda\bar{\mathbf{I}})\bar{\mathbf{P}}) = det(\bar{\mathbf{P}}^{-1})det(\bar{\mathbf{A}} - \lambda\bar{\mathbf{I}})det(\bar{\mathbf{P}}), \tag{D.9}$$

where Eqns. D.4 and D.7 are used. Since the determinants in Eqn. D.9 are each constants, they commute and can be rearranged such that

$$det(\bar{\mathbf{P}}^{-1})det(\bar{\mathbf{P}})det(\bar{\mathbf{A}} - \lambda\bar{\mathbf{I}}) = det(\bar{\mathbf{A}} - \lambda\bar{\mathbf{I}}). \tag{D.10}$$

Thus,

$$det(\bar{\mathbf{B}} - \lambda\bar{\mathbf{I}}) = det(\bar{\mathbf{A}} - \lambda\bar{\mathbf{I}}). \tag{D.11}$$

■

Theorem D.3 *For a given matrix* $\bar{\mathbf{A}}$ *with n linearly independent eigenvectors, there exists a nonsingular matrix,* $\bar{\mathbf{P}}$*, such that*

$$\bar{\mathbf{P}}^{-1}\bar{\mathbf{A}}\bar{\mathbf{P}} = \bar{\mathbf{\Lambda}}, \tag{D.12}$$

where $\bar{\mathbf{\Lambda}}$ *is a diagonal matrix whose elements are the eigenvalues of* $\bar{\mathbf{A}}$*.*

Proof Suppose $\bar{\mathbf{A}}$ has n linearly independent eigenvectors $\bar{\mathbf{x}}_\mathbf{1}, \bar{\mathbf{x}}_\mathbf{2}, ...\bar{\mathbf{x}}_\mathbf{n}$. Then, we can define

$$\bar{\mathbf{P}} = \left[\bar{\mathbf{x}}_1, ..., \bar{\mathbf{x}}_n\right]. \tag{D.13}$$

Multiplying $\bar{\mathbf{A}}$ and $\bar{\mathbf{P}}$ leaves

$$\bar{\mathbf{A}}\bar{\mathbf{P}} = \left[\bar{\mathbf{A}}\bar{\mathbf{x}}_1, ..., \bar{\mathbf{A}}\bar{\mathbf{x}}_n\right] = \left[\lambda_1\bar{\mathbf{x}}_1, ..., \lambda_n\bar{\mathbf{x}}_n\right] = \bar{\mathbf{\Lambda}}\bar{\mathbf{P}}, \tag{D.14}$$

where $\bar{\mathbf{\Lambda}}$ is a diagonal matrix whose eigenvalues are $\lambda_1, ...\lambda_n$, i.e.

$$\bar{\mathbf{\Lambda}} = \begin{pmatrix} \lambda_1 & 0 & \cdots & 0 \\ 0 & \lambda_2 & \cdots & 0 \\ \vdots & \vdots & \ddots & \vdots \\ 0 & 0 & \cdots & \lambda_n \end{pmatrix}. \tag{D.15}$$

■

Theorem D.4 *A general square matrix* $\bar{\mathbf{A}}$ *can be reduced to diagonal form by a similarity transform if and only if* $\bar{\mathbf{A}}$ *possesses n linearly independent eigenvectors.*

Proof Same as the previous proof.

■

Theorem D.5 *(Spectral Theorem) This proof is from Stensby (1998) [228]. For a Hermitian matrix* $\bar{\mathbf{B}}$ *there exists a unitary matrix* $\bar{\mathbf{Q}}$ *(recall:* $\bar{\mathbf{Q}}^*\bar{\mathbf{Q}} = \bar{\mathbf{I}}$*), of the same size, such that* $\bar{\mathbf{Q}}^{-1}\bar{\mathbf{B}}\bar{\mathbf{Q}} = \bar{\mathbf{Q}}^*\bar{\mathbf{B}}\bar{\mathbf{Q}}$ *is a diagonal matrix with the eigenvalues of* $\bar{\mathbf{B}}$ *on*

its diagonal. It can also be shown that the eigenvectors of $\bar{\mathbf{B}}$ *are the columns of* $\bar{\mathbf{Q}}$.

Proof From the Schur formulation there exists an unitary matrix, $\bar{\mathbf{Q}}$, such that $\bar{\mathbf{Q}}^*\bar{\mathbf{B}}\bar{\mathbf{Q}}$ is of the Schur form. The Schur form says that this form is held when $\bar{\mathbf{U}}$ is an upper triangular matrix with the eigenvalues of $\bar{\mathbf{B}}$ on the diagonal. Since it can also be shown that

$$\left(\bar{\mathbf{Q}}^*\bar{\mathbf{B}}\bar{\mathbf{Q}}\right)^* = \bar{\mathbf{Q}}^*\bar{\mathbf{B}}^*\bar{\mathbf{Q}} = \bar{\mathbf{Q}}^*\bar{\mathbf{B}}\bar{\mathbf{Q}}, \tag{D.16}$$

which means that $\bar{\mathbf{Q}}^*\bar{\mathbf{B}}\bar{\mathbf{Q}}$ is also Hermitian. However, for upper triangular Hermitian matrices to exist, the off diagonal terms must be zero, leaving only the diagonal terms, which by the Shur formulation, are the eigenvalues. Thus,

$$\bar{\mathbf{D}} = \bar{\mathbf{Q}}^*\bar{\mathbf{B}}\bar{\mathbf{Q}}, \tag{D.17}$$

where $\bar{\mathbf{D}}$ is the diagonal of eigenvalues, which can be rearranged by multiplying and taking the conjugate transpose to give $\bar{\mathbf{D}}\bar{\mathbf{Q}} = \bar{\mathbf{B}}\bar{\mathbf{Q}}$. Thus, the only way for this to hold is if $\bar{\mathbf{Q}}$ is made of the eigenvectors of $\bar{\mathbf{B}}$.

■

EXAMPLE 1:

Take the matrix $\bar{\mathbf{A}}$ defined as

$$\bar{\mathbf{A}} = \begin{pmatrix} 1 & 1 & 0 \\ 0 & 2 & 1 \\ 0 & 0 & 3 \end{pmatrix}, \tag{D.18}$$

whose eigenvalues are $\lambda_1 = 1,\ \lambda_2 = 2,\ \lambda_3 = 3$ and eigenvectors are

$$\begin{pmatrix} 1 \\ 0 \\ 0 \end{pmatrix}, \quad \begin{pmatrix} 1 \\ 1 \\ 0 \end{pmatrix}, \quad \begin{pmatrix} 1 \\ 2 \\ 2 \end{pmatrix}. \tag{D.19}$$

We can then define a matrix $\bar{\mathbf{P}}$ from these eigenvectors as

$$\bar{\mathbf{P}} = \begin{pmatrix} 1 & 1 & 1 \\ 0 & 1 & 2 \\ 0 & 0 & 2 \end{pmatrix}, \tag{D.20}$$

with inverse

$$\bar{\mathbf{P}}^{-1} = \frac{1}{2} \begin{pmatrix} 2 & -2 & 1 \\ 0 & 2 & -2 \\ 0 & 0 & 1 \end{pmatrix}. \tag{D.21}$$

.

It can then be shown that

$$\bar{\mathbf{P}}^{-1} \bar{\mathbf{A}} \bar{\mathbf{P}} = \begin{pmatrix} 1 & 0 & 0 \\ 0 & 2 & 0 \\ 0 & 0 & 3 \end{pmatrix}, \tag{D.22}$$

which is the $\bar{\mathbf{\Lambda}}$ matrix as defined in equation D.15 above in which the diagonal elements are the eigenvalues.

Hermitian Matrices

A few relationships for Hermitian matrices will be derived here. Some are based on the work of John Stensby $EE448/528$ notes [228] others from Ben Noble's book [227].

Definition D.2 *A Hermitian matrix is one whose conjugate transpose is equal to itself (i.e.* $\bar{\mathbf{B}}^* = \bar{\mathbf{B}}$*). These must have real values along the diagonal and can have complex values on the off diagonal terms.*

Example

The following matrix is Hermitian

$$\bar{\mathbf{B}} = \begin{pmatrix} 2 & i & 4+i \\ -i & 7 & 0 \\ 4-i & 0 & 3 \end{pmatrix}. \tag{D.23}$$

To verify this, take the conjugate transpose, flip the columns for the rows, and take the complex conjugate of each term (e.g., term (2,3) becomes term $(3,2)^*$).

Theorem D.6 *A Hermitian matrix has real valued eigenvalues.*

Proof Let λ be the eigenvalue and $\bar{\mathbf{x}}$ be the eigenvector of matrix $\bar{\mathbf{B}}$. Then, multiply the characteristic equation by $\bar{\mathbf{x}}^*$ on the left to obtain

$$\begin{aligned} \bar{\mathbf{B}}\bar{\mathbf{x}} &= \lambda\bar{\mathbf{x}}, \\ \bar{\mathbf{x}}^*\bar{\mathbf{B}}\bar{\mathbf{x}} &= \bar{\mathbf{x}}^*\lambda\bar{\mathbf{x}}, \\ \bar{\mathbf{x}}^*\bar{\mathbf{B}}\bar{\mathbf{x}} &= \lambda\bar{\mathbf{x}}^*\bar{\mathbf{x}}. \end{aligned} \tag{D.24}$$

Since it is known that $\bar{\mathbf{x}}^*\bar{\mathbf{x}}$ is always real, look at the left hand side of Eqn. D.24

$$\left(\bar{\mathbf{x}}^*\bar{\mathbf{B}}\bar{\mathbf{x}}\right)^* = \bar{\mathbf{x}}^*\bar{\mathbf{B}}^*\bar{\mathbf{x}} = \bar{\mathbf{x}}^*\bar{\mathbf{B}}\bar{\mathbf{x}}. \tag{D.25}$$

This means that $\bar{\mathbf{x}}^*\bar{\mathbf{B}}\bar{\mathbf{x}}$ is Hermitian, and thus the diagonal terms must be real valued. So, the eigenvalues must also be real for this matrix. Thus, the eigenvalues of Hermitian matrices must be real.

■

D.3 Derivation of $\bar{\mathbf{G}}$

Starting with Eqns. 6.108- 6.111 rewritten as

$$\begin{aligned}
\bar{\mathbf{A}}_1\bar{\mathbf{a}}_1 &= (-\bar{\boldsymbol{\tau}}_1 - \bar{\boldsymbol{\gamma}}_1),\\
\bar{\mathbf{A}}_2\bar{\mathbf{a}}_2 &= (\bar{\boldsymbol{\tau}}_2 - \bar{\boldsymbol{\sigma}}_2),\\
\bar{\mathbf{A}}_3\bar{\mathbf{a}}_3 &= (\bar{\mathbf{H}}_3 + \bar{\boldsymbol{\sigma}}_3),\\
\bar{\mathbf{A}}_4\bar{\mathbf{a}}_4 &= (-\bar{\mathbf{H}}_4 + \bar{\boldsymbol{\gamma}}_4).
\end{aligned} \tag{D.26}$$

Multiply on the left by $\bar{\mathbf{V}}^*$ (where $\bar{\mathbf{V}}$ is unitary) and also insert an identity matrix $\bar{\mathbf{I}} = \bar{\mathbf{V}}\bar{\mathbf{V}}^*$ on the left side yielding

$$\begin{aligned}
\bar{\mathbf{V}}^*\bar{\mathbf{A}}_1\bar{\mathbf{V}}\bar{\mathbf{V}}^*\bar{\mathbf{a}}_1 &= \bar{\mathbf{V}}^*(-\bar{\boldsymbol{\tau}}_1 - \bar{\boldsymbol{\gamma}}_1),\\
\bar{\mathbf{V}}^*\bar{\mathbf{A}}_2\bar{\mathbf{V}}\bar{\mathbf{V}}^*\bar{\mathbf{a}}_2 &= \bar{\mathbf{V}}^*(\bar{\boldsymbol{\tau}}_2 - \bar{\boldsymbol{\sigma}}_2),\\
\bar{\mathbf{V}}^*\bar{\mathbf{A}}_3\bar{\mathbf{V}}\bar{\mathbf{V}}^*\bar{\mathbf{a}}_3 &= \bar{\mathbf{V}}^*(\bar{\mathbf{H}}_3 + \bar{\boldsymbol{\sigma}}_3),\\
\bar{\mathbf{V}}^*\bar{\mathbf{A}}_4\bar{\mathbf{V}}\bar{\mathbf{V}}^*\bar{\mathbf{a}}_4 &= \bar{\mathbf{V}}^*(-\bar{\mathbf{H}}_4 + \bar{\boldsymbol{\gamma}}_4).
\end{aligned} \tag{D.27}$$

Move the first four terms on the left side to the right side of the equations, using the correct matrix multiplication. This yields

$$\begin{aligned}
\bar{\mathbf{a}}_1 &= \bar{\mathbf{V}}\bar{\mathbf{V}}^*\bar{\mathbf{A}}_1^{-1}\bar{\mathbf{V}}\bar{\mathbf{V}}^*(-\bar{\boldsymbol{\tau}}_1 - \bar{\boldsymbol{\gamma}}_1),\\
\bar{\mathbf{a}}_2 &= \bar{\mathbf{V}}\bar{\mathbf{V}}^*\bar{\mathbf{A}}_2^{-1}\bar{\mathbf{V}}\bar{\mathbf{V}}^*(\bar{\boldsymbol{\tau}}_2 - \bar{\boldsymbol{\sigma}}_2),\\
\bar{\mathbf{a}}_3 &= \bar{\mathbf{V}}\bar{\mathbf{V}}^*\bar{\mathbf{A}}_3^{-1}\bar{\mathbf{V}}\bar{\mathbf{V}}^*(\bar{\mathbf{H}}_3 + \bar{\boldsymbol{\sigma}}_3),\\
\bar{\mathbf{a}}_4 &= \bar{\mathbf{V}}\bar{\mathbf{V}}^*\bar{\mathbf{A}}_4^{-1}\bar{\mathbf{V}}\bar{\mathbf{V}}^*(-\bar{\mathbf{H}}_4 + \bar{\boldsymbol{\gamma}}_4).
\end{aligned} \tag{D.28}$$

Apply the similarity transformation (Eqn. D.7). Recall, however, that

$$\bar{\mathbf{A}}_n = \bar{\mathbf{M}} - \rho^{(n)}v^2\bar{\mathbf{I}}, \tag{D.29}$$

so that the relationship $\bar{\mathbf{V}}^*\bar{\mathbf{A}}_n\bar{\mathbf{V}}$ becomes

$$
\begin{aligned}
&\bar{\mathbf{V}}^{*}\bar{\mathbf{A}}_{n}\bar{\mathbf{V}} = \\
&\bar{\mathbf{V}}^{*}(\bar{\mathbf{M}} - \rho^{(n)}v^{2}\bar{\mathbf{I}})\bar{\mathbf{V}} = \\
&\bar{\mathbf{V}}^{*}\bar{\mathbf{M}}\bar{\mathbf{V}} - \bar{\mathbf{V}}^{*}\rho^{(n)}v^{2}\bar{\mathbf{I}}\bar{\mathbf{V}} = \\
&\bar{\mathbf{V}}^{*}\bar{\mathbf{M}}\bar{\mathbf{V}} - \rho^{(n)}v^{2}\bar{\mathbf{I}}\bar{\mathbf{V}}^{*}\bar{\mathbf{V}} = \\
&\bar{\mathbf{V}}^{*}\bar{\mathbf{M}}\bar{\mathbf{V}} - \rho^{(n)}v^{2}\bar{\mathbf{I}}.
\end{aligned}
\tag{D.30}
$$

Equation D.30 used the fact that the identity matrix ($\bar{\mathbf{I}}$) commutes with all matrices. Recall that λ is the eigenvalue of $\bar{\mathbf{M}}$. Equation D.30 is expressed as

$$
\bar{\mathbf{V}}^{*}\bar{\mathbf{A}}_{n}\bar{\mathbf{V}} = (\lambda - \rho^{(n)}v^{2})\bar{\mathbf{I}},\ n = 1, 2, 3, 4. \tag{D.31}
$$

Applying equation D.31 to equation D.28 yields

$$
\begin{aligned}
\bar{\mathbf{a}}_{1} &= \frac{\bar{\mathbf{V}}\bar{\mathbf{V}}^{*}}{(\lambda - \rho^{(1)}v^{2})\bar{\mathbf{I}}}(-\bar{\boldsymbol{\tau}}_{1} - \bar{\boldsymbol{\gamma}}_{1}), \\
\bar{\mathbf{a}}_{2} &= \frac{\bar{\mathbf{V}}\bar{\mathbf{V}}^{*}}{(\lambda - \rho^{(2)}v^{2})\bar{\mathbf{I}}}(\bar{\boldsymbol{\tau}}_{2} - \bar{\boldsymbol{\sigma}}_{2}), \\
\bar{\mathbf{a}}_{3} &= \frac{\bar{\mathbf{V}}\bar{\mathbf{V}}^{*}}{(\lambda - \rho^{(3)}v^{2})\bar{\mathbf{I}}}(\bar{\mathbf{H}}_{3} + \bar{\boldsymbol{\sigma}}_{3}), \\
\bar{\mathbf{a}}_{4} &= \frac{\bar{\mathbf{V}}\bar{\mathbf{V}}^{*}}{(\lambda - \rho^{(4)}v^{2})\bar{\mathbf{I}}}(-\bar{\mathbf{H}}_{4} + \bar{\boldsymbol{\gamma}}_{4}),
\end{aligned}
\tag{D.32}
$$

which is used to define the matrix $\bar{\mathbf{G}}$ such that

$$
\begin{aligned}
\bar{\mathbf{a}}_{1} &= \bar{\mathbf{G}}^{(1)}(-\bar{\boldsymbol{\tau}}_{1} - \bar{\boldsymbol{\gamma}}_{1}), \\
\bar{\mathbf{a}}_{2} &= \bar{\mathbf{G}}^{(2)}(\bar{\boldsymbol{\tau}}_{2} - \bar{\boldsymbol{\sigma}}_{2}), \\
\bar{\mathbf{a}}_{3} &= \bar{\mathbf{G}}^{(3)}(\bar{\mathbf{H}}_{3} + \bar{\boldsymbol{\sigma}}_{3}), \\
\bar{\mathbf{a}}_{4} &= \bar{\mathbf{G}}^{(4)}(-\bar{\mathbf{H}}_{4} + \bar{\boldsymbol{\gamma}}_{4}),
\end{aligned}
\tag{D.33}
$$

where

$$
G^{(\alpha,\beta,\eta)}_{mnpq} = \sum_{j=1}^{j_{max}} \frac{V^{(\alpha,\eta)}_{mn}(j)V^{(\beta,\eta)*}_{pq}(j)}{\lambda(j) - \rho^{(\eta)}v^{2}},\ \eta = 1, 2, 3, 4, \tag{D.34}
$$

and j tells how many solutions there are with the maximum

$$j_{max} = 3(m_{max} + 1)(n_{max} + 1). \tag{D.35}$$

The index terms in the subscript of $\bar{\mathbf{G}}$ changed order due to the fact that this is similar to the inverse of M_{pqmn}.

Appendix E: Wavelets

E.1 Introduction to Wavelets

The material in this appendix is not meant to be a thorough review of wavelet analysis, but merely a reference and summary of some of the applications of wavelets used in this dissertation. For a further discussion of wavelets, please see the references [221, 229–232].

A *wavelet transformation* is a time and frequency transformation applied to a signal simultaneously. This transformation allows a wave to be decomposed into component *wavelets*. To see the usefulness of this type of transform, the time and frequency transformations must first be analyzed individually.

E.2 Transformations

The *time transformation* separates the time components of a frequency signal. Similarly, the *frequency transformation* separates the frequency components of a time signal. As an example, take a sinusoidal signal that has a frequency of 100 Hz and apply a frequency transform to the signal, the transform would give a spiked peak at 100 Hz.

The downfall of using these transformations individually is they only apply to *stationary signals*, i.e. a signal that has a constant frequency at all times. Since most signals are not of this type, the individual transformations alone lose their luster. Many signals used in the scientific community are of the *non-stationary signal* or chirp signal type. These signals have a variable frequency in time and can only be analyzed using frequency transformations when the time is unimportant.

Fourier Transformation

Before discussing wavelet transformations, it will be advantageous to briefly discuss the *Fourier transformation* (FT). The FT represents a set of periodic functions

by an infinite sum (i.e., integral) of exponential functions (i.e., plane waves). For example, the FT of some signal x(t) is represented as

$$X(f) = \int_{-\infty}^{\infty} x(t) e^{-2i\pi ft} dt, \tag{E.1}$$

where f is the frequency, i is the imaginary number and X(f) is the FT of x(t). The inverse of this function can also be expressed as

$$x(t) = \int_{-\infty}^{\infty} X(f) e^{2i\pi ft} df. \tag{E.2}$$

If the result of the FT integration is large, the signal (x(t)) has a dominant spectral component at frequency f. If the integral is 0, then no component of that specific frequency, f, exists within the signal, x(t). This procedure can be repeated at every frequency within some desired range.

Wavelet Transformation

To aid in analyzing non-stationary signals, the *wavelet transformation (WT)* was developed. The term *wavelet* means a small wave, and there are numerous types of wavelets. The WT applies a time and frequency transformation, simultaneously, to a signal. To do this it first decomposes the signal by filtering (high or low filter). This process is repeated down to small, filtered frequency windows. The transformation is then applied and analyzed.

Due to the Heisenberg uncertainty principle ($\Delta t \Delta \omega \geq \frac{1}{2}$), it is impossible to know the frequency and time simultaneously within some error. So, look at what spectral components exist at any time interval. Due to the uncertainty principle, higher frequencies are better resolved in time and lower frequencies are better resolved in frequency.

The continuous WT is defined as

$$\Psi(q, s) = \frac{1}{\sqrt{|s|}} \int x(t) \Psi^* \left(\frac{t - q}{s} \right) dt, \tag{E.3}$$

where q is the translation (related to the location of the window corresponding to time), s is the scale ($\frac{1}{f}$), $\Psi(t)$ is the transforming function (i.e., mother wavelet), and x(t) is the signal.

The *mother wavelet* refers to the function with different regions of support that are used in the transformation process and are derived from one function. It is a prototype for generating other window functions. Below are a few examples of different types of wavelets.

E.3 Wavelets

Mexican Hat Wavelet

One example of a wavelet is the mexican hat (i.e., Ricker wavelet) that comes from the second derivative of the Gaussian function (Fig. E.1)

$$\Psi(t) = \frac{2}{\sqrt{3\sigma}\pi^{\frac{1}{4}}}\left(1 - \frac{t^2}{\sigma^2}\right)e^{-\frac{t^2}{2\sigma^2}}. \tag{E.4}$$

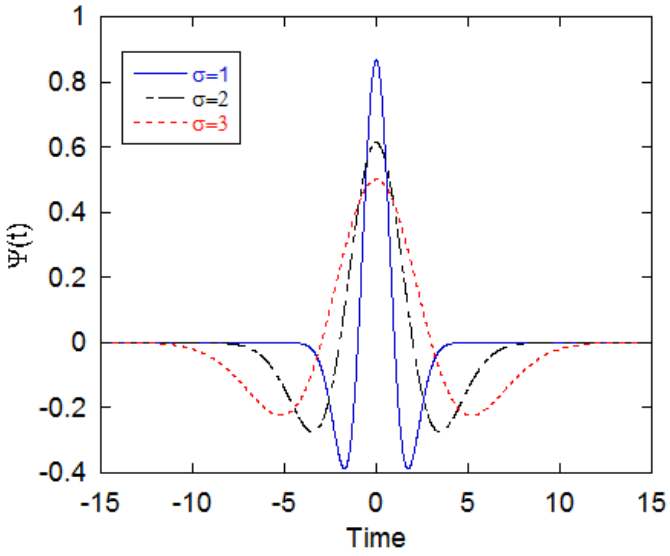

Figure E.1. Mexican hat wavelet for several values of σ.

Morlet Wavelet

Another famous wavelet, and perhaps the most widely used, is the Morlet wavelet [230]. The mother wavelet, $\Psi(t)$, of a Morlet wavelet is used to obtain a general wavelet, $\Psi_{s\tau}(t)$, by a scaling by factor, s, and displacing by q as

$$\Psi_{sq} \equiv |s|^{-\frac{1}{2}} \Psi\left(\frac{t-q}{s}\right), \tag{E.5}$$

where the mother wavelet is given by

$$\Psi(t) = \left(e^{-i\sigma t} - e^{-\frac{\sigma^2}{2}}\right) e^{-\frac{t^2}{2}}. \tag{E.6}$$

The second term in Eqn. E.6 is needed to ensure convergence of the inverse Morlet wavelet transform (see the admissibility condition below). Note that the value of the frequency, σ, does not matter as long as it is non-zero.

The general Morlet wavelet is created from the mother Morlet wavelet (Eqn. E.6) by scaling as

$$\Psi_{sq} \equiv |s|^{-\frac{1}{2}} \left(e^{-i\sigma\left(\frac{t-q}{s}\right)} - e^{-\frac{\sigma^2}{2}}\right) e^{-\frac{1}{2}\left(\frac{t-q}{s}\right)^2}. \tag{E.7}$$

Any square integrable function may be expressed as a sum over Morlet wavelets (even δ functions and plane waves).

Using these descriptions, along with the calculated admissibility constant, the normalized Morlet wavelet is expressed as [230],

$$\Psi_{sq}^{(norm)}(t) = \frac{e^{-\frac{t^2}{2}}(e^{i\sigma t} - e^{-\frac{\sigma^2}{2}})}{\sqrt{(1 + e^{-\sigma^2} - 2e^{-0.75\sigma^2})\sqrt{\pi}}}, \tag{E.8}$$

which is shown in Fig. E.2.

The inverse Morlet wavelet transform is expressed as

$$\Psi(t) = \frac{1}{C_\Psi} \int_s \int_q \frac{1}{s^2} \Psi(q,s) \hat{\Psi}\left(\frac{t-q}{s}\right) dqds, \tag{E.9}$$

where C_Ψ is the admissibility constant.

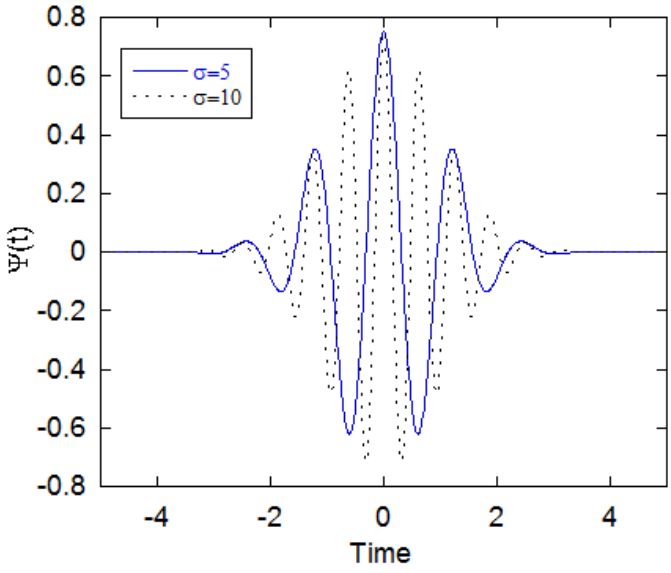

Figure E.2. Morlet wavelet for values of $\sigma = 5$ and 10.

Nolte-Hilbert Wavelet

The Morlet wavelet, although useful, is not rigorously admissible [221] (see next section). To completely satisfy the admissibility condition and balance the time-frequency localization for short pulses, only the imaginary part of the Morlet wavelet is used. A Hilbert transform is then applied to make an orthogonal, real valued wavelet given by

$$\Psi = \Psi_1 + i\Psi_2 \tag{E.10}$$

$$\Psi_1 = P\int_{-\infty}^{\infty} \frac{\Psi_2(u)}{x-u}du, \tag{E.11}$$

$$\Psi_2 = \frac{1}{\pi^{\frac{1}{4}}} e^{-\frac{x^2}{2}} sin(\sigma_o x), \tag{E.12}$$

where Ψ_1 is the Hilbert transformation, σ_o is the frequency (>5), and P is the Cauchy Principle Value. This new wavelet has been termed the Nolte-Hilbert wavelet.

To calculate Ψ_1 take a fast Fourier transformation of Ψ_2, switch the symmetric and antisymmetric parts by changing the sign of the values greater than $x = 0$, inverse

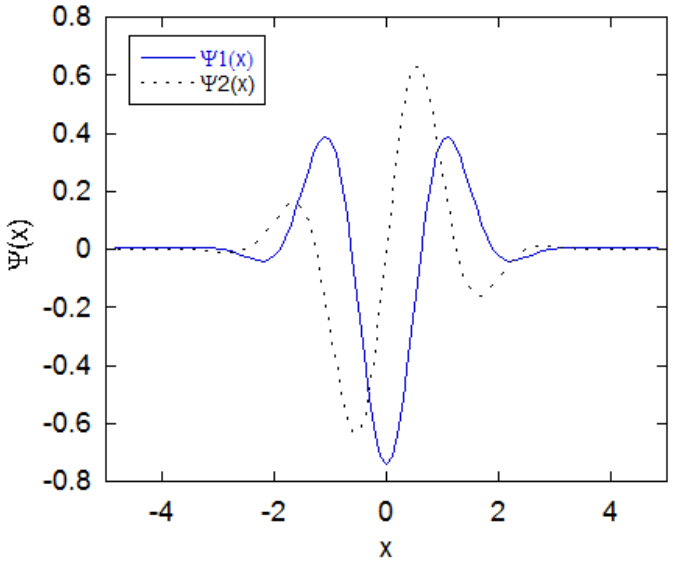

Figure E.3. Nolte Hilbert wavelet (Eqn. E.12) components, where $\sigma_o = \sqrt{2\pi}$.

fast FT, and then plot the negative imaginary parts. The results are shown in Fig. E.3. Further discussion of limits and applications of this wavelet are given by Nolte et al., (2000) [221].

When the frequency $\sigma_o = \sqrt{2\pi}$ is used, a balance of the time-frequency localization is obtained for short pulses and the admissibility condition is satisfied. This is the wavelet that is used within this dissertation, applied to the experimentally obtained waveforms.

E.4 Admissibility Condition

The admissibility condition demands the wavelet function be invertible, allowing the original signal to be recovered without losing any information [229–232]. A more formal definition can be stated as: the wavelet kernel must have a vanishing zeroth order moment for all choices of wavelet scales. When a square integrable function, with finite energy, satisfies this condition, it is a wavelet.

The admissibility condition is stated as [229]

$$C_\Psi = \left[2\pi \int_{-\infty}^{\infty} \frac{|\hat{\Psi}(\xi)|^2}{|\xi|} d\xi \right] < \infty, \tag{E.13}$$

where $\hat{\Psi}(\xi)$ is the FT of $\Psi(t)$ [1]. The wavelet decomposition fails when C_Ψ is not finite. When Ψ is differentiable, the admissibility condition is satisfied for

$$\hat{\Psi}(\sigma = 0) = 0, \implies \int \Psi(t) dt = 0, \tag{E.14}$$

which requires the wave to be oscillatory so that this integral can go to zero.

The admissibility condition is used to imply that the wavelet, Ψ, has weak convergence of the form

$$\int \int |\Psi^{(s,\tau)} >< \Psi^{(\tau,s)}| \frac{ds d\tau}{s^2}, \tag{E.15}$$

where the bra and ket notation has been utilized. It can be shown that this operator (in $L^2(R, dt)$ space) is the same as C_Ψ (Eqn. E.13) [232].

[1] Occasionally the 2π is dropped.

Appendix F: Code

F.1 Introduction

This appendix provides code which was implemented in Matlab 2013b to calculate the CWW and intersection waves in the numerical results sections in this work. Complete codes will be given with some description of what different sections of the code do.

F.2 Kronecker Delta and Heavyside Step Function

These define the Kronecker delta function and as delta(i,j) and the Heavyside step function as heav(f).

```
%Dirac Delta Function. Such that delta(i,j)=0 for i not equal j and
%delta(i,j)=1 for i=j;
function [delta]=delta(first,second);
if first == second
    %this is the =1 case.
    delta=1;
else
    %all other cases
    delta=0;
end

%heavyside step function Such that heav(n)= 0 for n<0 and heav(n)=1 for n>
%or = 0.
function [heav]=heav(n);
  if n<0
      %case where function is still 0
      heav=0;
  elseif n==0
      %function becomes 1 here.
      heav=1;
  else
```

```
    %all other cases
    heav=1;
end
```

F.3 Input Parameters

The material parameters, (e.g., density) are supplied here to calculate the $\bar{\mathbf{Q}}$ matrices.

```
%Input Material parameters for the 4 media making up the
%intersection here. Uses the eigM_int.m function
%--------------------------------------
%clear all values that will be used
clear eigvecs; clear eigvals; clear vecr; clear vecc; clear Snumsize;
clear Snum; clear count; clear ncnt; clear mcnt; clear mmax; clear nmax;
clear jmax; clear jcount; clear Qmat;
%--------------------------------------
%define the density (rho) and material parameters (Cij)
if medium==1
    rho=2717;%density
    C33=8.875e10;
    C11=1.0545e11;
    C13=3.70e10;
    C66=2.5607e10;
    C44=2.3645e10;
    C12=3.7e10;
    C22=8.875e10;
    C23=4.1460e10;
    C55=2.5607e10;
elseif medium==2
    rho=2717;%density
    C33=8.875e10;
    C11=1.0545e11;
    C13=3.70e10;
    C66=2.5607e10;
```

```
    C44=2.3645e10;
    C12=3.7e10;
    C22=8.875e10;
    C23=4.1460e10;
    C55=2.5607e10;
elseif medium==3
    rho=2717;%density
    C33=8.875e10;
    C11=1.0545e11;
    C13=3.70e10;
    C66=2.5607e10;
    C44=2.3645e10;
    C12=3.7e10;
    C22=8.875e10;
    C23=4.1460e10;
    C55=2.5607e10;
elseif medium==4
    rho=2717;%density
    C33=8.875e10;
    C11=1.0545e11;
    C13=3.70e10;
    C66=2.5607e10;
    C44=2.3645e10;
    C12=3.7e10;
    C22=8.875e10;
    C23=4.1460e10;
    C55=2.5607e10;
else
   disp('medium not defined');
end
%----------------------------------------
%Calculate the eigenvalues and eigenvectors using eigM_int.m
[eigvecsint,eigvalsint]=eigM_int;(C11,C12,C13,C22,C23,C33,C44,C55,C66,medium,p);

%----------------------------------------
```

```
%Make matrix for all the possible m and n values
Snumsize=0.5*(p+1)*(p+2);%calculate the number of terms
Snum=zeros(Snumsize,2);%Make Snum that size
count=1;%start counter
for ncnt=0:p
    for qcnt=0:p
        for pcnt=0:p
            Snum(count,1:3)=[ncnt pcnt qcnt];
            count=count+1;%Advance counter
        end
    end
end
mmax=max(Snum(:,1));%calculate the max m
nmax=max(Snum(:,1));%calculate the max n
pmax=max(Snum(:,2));%calculate the max p
qmax=max(Snum(:,3));%calculate the max q
jmax=3*(mmax+1)*(nmax+1);%calculate j max
%-----------------------------------------
%Make sure all elements less than 10^-15 are zero.
for ecol=1:3*(mmax+1)*(nmax+1)
    for erow=1:3*(mmax+1)*(nmax+1)
        if abs(eigvecsint(ecol,erow))<1e-15
            eigvecsint(ecol,erow)=0;
        end
    end
end
clear ecol;clear erow;
%-----------------------------------------
%Calculate Q_n=Q_q by summing terms in the eigenvectors.
%See equation 18 in paper.
%Q should be [3*(nmax+1) x jmax] in size as long as nmax=mmax.
for mcount=1:1:3*(mmax+1)%sum over m values.
    for jcount=1:1:jmax %sum over eigenvector number
        for sumterm=mcount+(mcount*mmax)-mmax:1:mcount*(mmax+1)%counter for each j
            value.
```

```
            if sumterm==mcount+(mcount*mmax)-mmax %check for starting value
              Qmat_int(mcount,jcount)=eigvecsint(sumterm,jcount);%Start the term
            else
              Qmat_int(mcount,jcount)=Qmat_int(mcount,jcount)+...
                  eigvecsint(sumterm,jcount);%add on the next term
            end
          end
      end
end


%Calculate Q_p by summing terms in the eigenvectors checked 10/13 working
for mcount=1:1:3*(mmax+1)%sum over m values.
      for jcount=1:1:jmax %sum over eigenvector number
          for sumterm=mcount+(p*(p+1)*(ceil(mcount/(p+1))-1)):(p+1):mcount+(p*(p+1)*(ceil(
               mcount/(p+1))))%counter for each j value.
            if sumterm==mcount+(p*(p+1)*(ceil(mcount/(p+1))-1)) %check for starting value
              Qmat_intp(mcount,jcount)=eigvecsint(sumterm,jcount);%Start the term
            else
              Qmat_intp(mcount,jcount)=Qmat_intp(mcount,jcount)+...
                  eigvecsint(sumterm,jcount);%add on the next term
            end
          end
      end
end
%-----------------------------------------
%Make all terms in Qmat_int and Qmat_intp less than 10^-15 =0

for qr=1:size(Qmat_int,1)
      for qc=1:size(Qmat_int,2)
          if abs(Qmat_int(qr,qc))<1e-15
              Qmat_int(qr,qc)=0;
          end
          if abs(Qmat_intp(qr,qc))<1e-15
              Qmat_intp(qr,qc)=0;
```

```
        end
    end
end
clear qr;clear qc;
%----------------------------------------
eigenmat=diag(eigvalsint);%put all the eigenvalues into a matrix.
%----------------------------------------
%Clear variables that are not needed
clear count; clear sumterm;clear mcount; clear jcount;
clear Snumsize; clear mcnt; clear ncnt;
```

F.4 $\bar{\mathbf{M}}$ Matrix

Definitions of the $\bar{\mathbf{M}}$ matrix terms for the intersection wave.

```
%M11 term from intersection waves
function [Mco11int]=Mco11int(d1,d2,d3,d4,C11,C12,C13,C22,C23,C33,C44,C55,C66,med);
if med==1
     Mco11int= delta(d1,d3)*delta(d2,d4)*C11+C66*delta(d2,d4)*(min(d1,d3)+0.5...
        -0.25*delta(d1,d3))+C55*delta(d1,d3)*(min(d2,d4)+0.5-0.25*delta(d2,d4));
elseif med==2
    Mco11int= delta(d1,d3)*delta(d2,d4)*C11+C66*delta(d2,d4)*(min(d1,d3)+0.5...
        -0.25*delta(d1,d3))+C55*delta(d1,d3)*(min(d2,d4)+0.5-0.25*delta(d2,d4));
elseif med==3
    Mco11int= delta(d1,d3)*delta(d2,d4)*C11+C66*delta(d2,d4)*(min(d1,d3)+0.5...
        -0.25*delta(d1,d3))+C55*delta(d1,d3)*(min(d2,d4)+0.5-0.25*delta(d2,d4));
elseif med==4
  Mco11int= delta(d1,d3)*delta(d2,d4)*C11+C66*delta(d2,d4)*(min(d1,d3)+0.5...
        -0.25*delta(d1,d3))+C55*delta(d1,d3)*(min(d2,d4)+0.5-0.25*delta(d2,d4));
else
    disp('medium not well defined');
end
end

%M12 from Intersection waves
function [Mco12int]=Mco12int(d1,d2,d3,d4,C11,C12,C13,C22,C23,C33,C44,C55,C66,med);
```

```
if med==1
    Mco12int= (−i∗(C12)∗delta(d2,d4)∗(−heav(d3−d1)+0.5∗delta(d1,d3))+...
        i∗C66∗delta(d2,d4)∗(−heav(d1−d3)+0.5∗delta(d1,d3)));
elseif med==2
    Mco12int= −(−i∗(C12)∗delta(d2,d4)∗(−heav(d3−d1)+0.5∗delta(d1,d3))+...
        i∗C66∗delta(d2,d4)∗(−heav(d1−d3)+0.5∗delta(d1,d3)));
elseif med==3
    Mco12int= −(−i∗(C12)∗delta(d2,d4)∗(−heav(d3−d1)+0.5∗delta(d1,d3))+...
        i∗C66∗delta(d2,d4)∗(−heav(d1−d3)+0.5∗delta(d1,d3)));
elseif med==4
   Mco12int= (−i∗(C12)∗delta(d2,d4)∗(−heav(d3−d1)+0.5∗delta(d1,d3))+...
        i∗C66∗delta(d2,d4)∗(−heav(d1−d3)+0.5∗delta(d1,d3)));
else
    disp('medium not well defined');
end
end

%M13 From Intersection Waves
function [Mco13int]=Mco13int(d1,d2,d3,d4,C11,C12,C13,C22,C23,C33,C44,C55,C66,med);
if med==1
    Mco13int=−i∗C13∗delta(d1,d3)∗(−heav(d4−d2)+0.5∗delta(d2,d4))+...
        i∗C55∗delta(d1,d3)∗(−heav(d2−d4)+0.5∗delta(d4,d2));
elseif med==2
    Mco13int=−i∗C13∗delta(d1,d3)∗(−heav(d4−d2)+0.5∗delta(d2,d4))+...
        i∗C55∗delta(d1,d3)∗(−heav(d2−d4)+0.5∗delta(d4,d2));
elseif med==3
    Mco13int=i∗C13∗delta(d1,d3)∗(−heav(d4−d2)+0.5∗delta(d2,d4))−...
        i∗C55∗delta(d1,d3)∗(−heav(d2−d4)+0.5∗delta(d4,d2));
elseif med==4
    Mco13int=i∗C13∗delta(d1,d3)∗(−heav(d4−d2)+0.5∗delta(d2,d4))−...
        i∗C55∗delta(d1,d3)∗(−heav(d2−d4)+0.5∗delta(d4,d2));
else
    disp('medium not well defined');
end
end
```

```
%M21 Intersection Wave
function [Mco21int]=Mco21int(d1,d2,d3,d4,C11,C12,C13,C22,C23,C33,C44,C55,C66,med);
if med==1
    Mco21int=−i∗C66∗(−heav(d3−d1)+0.5∗delta(d3,d1))∗delta(d4,d2)+...
    i∗(C12)∗(−heav(d1−d3)+0.5∗delta(d1,d3))∗delta(d4,d2);
elseif med==2
   Mco21int=−(−i∗C66∗(−heav(d3−d1)+0.5∗delta(d3,d1))∗delta(d4,d2)+...
    i∗(C12)∗(−heav(d1−d3)+0.5∗delta(d1,d3))∗delta(d4,d2));
elseif med==3
   Mco21int=−(−i∗C66∗(−heav(d3−d1)+0.5∗delta(d3,d1))∗delta(d4,d2)+...
    i∗(C12)∗(−heav(d1−d3)+0.5∗delta(d1,d3))∗delta(d4,d2));
elseif med==4
    Mco21int=−i∗C66∗(−heav(d3−d1)+0.5∗delta(d3,d1))∗delta(d4,d2)+...
    i∗(C12)∗(−heav(d1−d3)+0.5∗delta(d1,d3))∗delta(d4,d2);
else
    disp('medium not well defined');
end
end

%M22 Intersection Waves
function [Mco22int]=Mco22int(d1,d2,d3,d4,C11,C12,C13,C22,C23,C33,C44,C55,C66,med);
if med==1
    Mco22int=delta(d1,d3)∗delta(d2,d4)∗C66+C22∗delta(d2,d4)∗(min(d1,d3)+0.5−...
        0.25∗delta(d1,d3))+C44∗delta(d3,d1)∗(min(d2,d4)+0.5−0.25∗delta(d2,d4));
elseif med==2
    Mco22int=delta(d1,d3)∗delta(d2,d4)∗C66+C22∗delta(d2,d4)∗(min(d1,d3)+0.5−...
        0.25∗delta(d1,d3))+C44∗delta(d3,d1)∗(min(d2,d4)+0.5−0.25∗delta(d2,d4));
elseif med==3
    Mco22int=delta(d1,d3)∗delta(d2,d4)∗C66+C22∗delta(d2,d4)∗(min(d1,d3)+0.5−...
        0.25∗delta(d1,d3))+C44∗delta(d3,d1)∗(min(d2,d4)+0.5−0.25∗delta(d2,d4));
elseif med==4
    Mco22int=delta(d1,d3)∗delta(d2,d4)∗C66+C22∗delta(d2,d4)∗(min(d1,d3)+0.5−...
        0.25∗delta(d1,d3))+C44∗delta(d3,d1)∗(min(d2,d4)+0.5−0.25∗delta(d2,d4));
else
    disp('medium not well defined');
```

```
end
end

%M23 Intersection Waves
function [Mco23int]=Mco23int(d1,d2,d3,d4,C11,C12,C13,C22,C23,C33,C44,C55,C66,med);
if med==1
    Mco23int=(-heav(d1-d3)+0.5*delta(d1,d3))*(C23)*(-heav(d4-d2)+0.5*delta(d2,d4))+...
        (-heav(d3-d1)+0.5*delta(d1,d3))*C44*(-heav(d2-d4)+0.5*delta(d2,d4));
elseif med==2
    Mco23int=-((-heav(d1-d3)+0.5*delta(d1,d3))*(C23)*(-heav(d4-d2)+0.5*delta(d2,d4))+...
        (-heav(d3-d1)+0.5*delta(d1,d3))*C44*(-heav(d2-d4)+0.5*delta(d2,d4)));
elseif med==3
    Mco23int=(-heav(d1-d3)+0.5*delta(d1,d3))*(C23)*(-heav(d4-d2)+0.5*delta(d2,d4))+...
        (-heav(d3-d1)+0.5*delta(d1,d3))*C44*(-heav(d2-d4)+0.5*delta(d2,d4));
elseif med==4
    Mco23int=-((-heav(d1-d3)+0.5*delta(d1,d3))*(C23)*(-heav(d4-d2)+0.5*delta(d2,d4))+...
        (-heav(d3-d1)+0.5*delta(d1,d3))*C44*(-heav(d2-d4)+0.5*delta(d2,d4)));
else
    disp('medium not well defined');
end
end

%M31 Intersection Waves
function [Mco31int]=Mco31int(d1,d2,d3,d4,C11,C12,C13,C22,C23,C33,C44,C55,C66,med);
if med==1
    Mco31int=-i*delta(d1,d3)*C55*(-heav(d4-d2)+0.5*delta(d2,d4))+...
        i*delta(d1,d3)*C13*(-heav(d2-d4)+0.5*delta(d4,d2));
elseif med==2
    Mco31int=-i*delta(d1,d3)*C55*(-heav(d4-d2)+0.5*delta(d2,d4))+...
        i*delta(d1,d3)*C13*(-heav(d2-d4)+0.5*delta(d4,d2));
elseif med==3
   Mco31int=i*delta(d1,d3)*C55*(-heav(d4-d2)+0.5*delta(d2,d4))-...
        i*delta(d1,d3)*C13*(-heav(d2-d4)+0.5*delta(d4,d2));
elseif med==4
   Mco31int=i*delta(d1,d3)*C55*(-heav(d4-d2)+0.5*delta(d2,d4))-...
        i*delta(d1,d3)*C13*(-heav(d2-d4)+0.5*delta(d4,d2));
```

```
else
    disp('medium not well defined');
end
end

%M32 Intersection Waves
function [Mco32int]=Mco32int(d1,d2,d3,d4,C11,C12,C13,C22,C23,C33,C44,C55,C66,med);
if med==1
    Mco32int=(-heav(d1-d3)+0.5*delta(d1,d3))*(-heav(d4-d2)+0.5*delta(d2,d4))*C44+...
     C23*(-heav(d3-d1)+0.5*delta(d1,d3))*(-heav(d2-d4)+0.5*delta(d2,d4));
elseif med==2
    Mco32int=-((-heav(d1-d3)+0.5*delta(d1,d3))*(-heav(d4-d2)+0.5*delta(d2,d4))*C44+...
     C23*(-heav(d3-d1)+0.5*delta(d1,d3))*(-heav(d2-d4)+0.5*delta(d2,d4)));
elseif med==3
    Mco32int=(-heav(d1-d3)+0.5*delta(d1,d3))*(-heav(d4-d2)+0.5*delta(d2,d4))*C44+...
     C23*(-heav(d3-d1)+0.5*delta(d1,d3))*(-heav(d2-d4)+0.5*delta(d2,d4));
elseif med==4
    Mco32int=-((-heav(d1-d3)+0.5*delta(d1,d3))*(-heav(d4-d2)+0.5*delta(d2,d4))*C44+...
     C23*(-heav(d3-d1)+0.5*delta(d1,d3))*(-heav(d2-d4)+0.5*delta(d2,d4)));
else
    disp('medium not well defined');
end
end

%M33 Intersection Wave
function [Mco33int]=Mco33int(d1,d2,d3,d4,C11,C12,C13,C22,C23,C33,C44,C55,C66,med);
if med==1
    Mco33int=delta(d1,d3)*delta(d2,d4)*C55+C44*delta(d2,d4)*(min(d1,d3)+0.5-...
        0.25*delta(d1,d3))+C33*delta(d1,d3)*(min(d2,d4)+0.5-0.25*delta(d2,d4));
elseif med==2
    Mco33int=delta(d1,d3)*delta(d2,d4)*C55+C44*delta(d2,d4)*(min(d1,d3)+0.5-...
        0.25*delta(d1,d3))+C33*delta(d1,d3)*(min(d2,d4)+0.5-0.25*delta(d2,d4));
elseif med==3
    Mco33int=delta(d1,d3)*delta(d2,d4)*C55+C44*delta(d2,d4)*(min(d1,d3)+0.5-...
        0.25*delta(d1,d3))+C33*delta(d1,d3)*(min(d2,d4)+0.5-0.25*delta(d2,d4));
elseif med==4
```

```
    Mco33int=delta(d1,d3)*delta(d2,d4)*C55+C44*delta(d2,d4)*(min(d1,d3)+0.5-...
        0.25*delta(d1,d3))+C33*delta(d1,d3)*(min(d2,d4)+0.5-0.25*delta(d2,d4));
else
    disp('medium not well defined');
end
end
```

F.5 Eigenvalues and Eigenvectors of $\bar{\mathbf{M}}$

```
%For use on Intersection Waves to calculate eigenvalues and
%eigenvectors of the M Matrix.
%-----------------------------------------
%Mpqmn will be renamed
%as Mco with indices d1,d2,d3,d4 such that p=d1, q=d2, m=d3, n=d4.
%Use of the functions delta() and heav() will be used for delta function
%and heavyside step functions these are within the current folder.
%-----------------------------------------
function [eigvecMint,eigMint]=eigM_int(C11,C12,C13,C22,C23,C33,C44,C55,C66,medium,p);
%For medium 1-4. p is the mmax and nmax. i.e. number of expansion terms
%C11,C12,C13,C22,C23,C33,C44,C55,C66 are the elastic constants.
%-----------------------------------
%Clear variables that need to be used in this program.
clear ncnt; clear mcnt; clear count; clear Snum;
clear Msize; clear Mmat11; clear Mmat13; clear Mmat31; clear Mmat33;
%-------------------------------
%Make matrix for all the possible m and n values
count=1;%start counter
for ncnt=0:p
    for mcnt=0:p
            Snum(count,1)=mcnt;
            Snum(count,2)=ncnt;
            count=count+1;%Advance counter
    end
end
```

```
%--------------------------------
%Calculate the size of each Mmat matrix. m+n=p the number of terms used.
[Msize,Mcol]=size(Snum);
clear Mcol;
%Create matrices of zeros the same size to be filled.
Mmat11int=zeros(Msize,Msize);
Mmat12int=zeros(Msize,Msize);
Mmat13int=zeros(Msize,Msize);
Mmat21int=zeros(Msize,Msize);
Mmat22int=zeros(Msize,Msize);
Mmat23int=zeros(Msize,Msize);
Mmat31int=zeros(Msize,Msize);
Mmat32int=zeros(Msize,Msize);
Mmat33int=zeros(Msize,Msize);
%--------------------------------
%Calculate all the M matrices and then put them into matrix form. Here the transformation from
      Maradudin is used.
for mrow=1:Msize;%sum over the rows
    for mcol=1:Msize %sum over the columns
        Mmat11int(mrow,mcol)=Mco11int(Snum(mrow,1),Snum(mrow,2),Snum(mcol,1),...
            Snum(mcol,2),C11,C12,C13,C22,C23,C33,C44,C55,C66,medium);
        Mmat12int(mrow,mcol)=1i*Mco12int(Snum(mrow,1),Snum(mrow,2),...
            Snum(mcol,1),Snum(mcol,2),C11,C12,C13,C22,C23,C33,C44,C55,C66,medium);
        Mmat13int(mrow,mcol)=1i*Mco13int(Snum(mrow,1),Snum(mrow,2),...
            Snum(mcol,1),Snum(mcol,2),C11,C12,C13,C22,C23,C33,C44,C55,C66,medium);
        Mmat21int(mrow,mcol)=-1i*Mco21int(Snum(mrow,1),Snum(mrow,2),...
            Snum(mcol,1),Snum(mcol,2),C11,C12,C13,C22,C23,C33,C44,C55,C66,medium);
        Mmat22int(mrow,mcol)=Mco22int(Snum(mrow,1),Snum(mrow,2),Snum(mcol,1)...
            ,Snum(mcol,2),C11,C12,C13,C22,C23,C33,C44,C55,C66,medium);
        Mmat23int(mrow,mcol)=Mco23int(Snum(mrow,1),Snum(mrow,2),Snum(mcol,1)...
            ,Snum(mcol,2),C11,C12,C13,C22,C23,C33,C44,C55,C66,medium);
        Mmat31int(mrow,mcol)=-1i*Mco31int(Snum(mrow,1),Snum(mrow,2),...
            Snum(mcol,1),Snum(mcol,2),C11,C12,C13,C22,C23,C33,C44,C55,C66,medium);
        Mmat32int(mrow,mcol)=Mco32int(Snum(mrow,1),Snum(mrow,2),Snum(mcol,1)...
            ,Snum(mcol,2),C11,C12,C13,C22,C23,C33,C44,C55,C66,medium);
```

```
        Mmat33int(mrow,mcol)=Mco33int(Snum(mrow,1),Snum(mrow,2),Snum(mcol,1)...
            ,Snum(mcol,2),C11,C12,C13,C22,C23,C33,C44,C55,C66,medium);
    end
end

Mmattotalint=[Mmat11int,Mmat12int,Mmat13int;Mmat21int,Mmat22int,Mmat23int;Mmat31int,
    Mmat32int,Mmat33int];
%------------------------------
%Check that Mmattotal is hermitian
if isequal(Mmattotalint,ctranspose(Mmattotalint))==0
    %This is bad and needs to be fixed.
    disp('Mmattotalint is not hermitian!')
    return;
end
%------------------------------
%Calculate the eigenvalues and eigenvectors
[eigvecMint,eigMint]=eig(Mmattotalint);
end
```

F.6 Solution Determination Dode

This program searches for solutions to the determinant equal to zero for the intersection (Eqn. 6.193) for the intersection wave.

```
freq=1e6;%Set frequency to use (Hz)
velresolution=1e-12;%Resolution desired on velocity
scnt=1;%Counter
stcnt=1;%Start counter for stiffness
thcount=1;%Reset counter
firsttime=1;%Counter
finvel=[];%Make empty matrix
stiffness1a=[];%Make empty matrix
stiffness2a=[];%Make empty matrix
stiffness1b=[];%Make empty matrix
stiffness2b=[];%Make empty matrix
nextstiff=0;%Don't move stiffnesses yet.
```

```
nwloop=0;%Default setting
numsols=20;%Number of solutions to look for.
stpsize=0.005;%Stepsize in velocity (m/s)
%--------------------------
%Calculate the initial parameters.
for medium=1:4
    Q_calc_int;%run this program to calculate the Q matrices for use below in
    %----------------------
    %Label Qmat, Snum, eigenmat, rho, eigvecs, and the size of matrices
    if medium ==1
        Qmat1=Qmat_int;Qmat1p=Qmat_intp;Snum1=Snum;eigenmat1=eigenmat;nmax1=nmax;
        rho1=rho;eigvecs1=eigvecsint;jmax1=jmax;
        C11_1=C11;C12_1=C12;C13_1=C13;C23_1=C23;C22_1=C22;C33_1=C33;C44_1=C44;
        C55_1=C55;C66_1=C66;
        eigvalsint1=eigvalsint;
    elseif medium ==2
        Qmat2=Qmat_int;Qmat2p=Qmat_intp; Snum2=Snum;eigenmat2=eigenmat;nmax2=nmax
            ;
        rho2=rho;eigvecs2=eigvecsint;jmax2=jmax;
        C11_2=C11;C12_2=C12;C13_2=C13;C23_2=C23;C22_2=C22;C33_2=C33;C44_2=C44;
        C55_2=C55;C66_2=C66;
        eigvalsint2=eigvalsint;
    elseif medium ==3
        Qmat3=Qmat_int;Qmat3p=Qmat_intp;Snum3=Snum;eigenmat3=eigenmat;nmax3=nmax;
        rho3=rho;eigvecs3=eigvecsint;jmax3=jmax; C11_3=C11;C12_3=C12;C13_3=C13;C23_3=
            C23;C22_3=C22;C33_3=C33;C44_3=C44;
        C55_3=C55;C66_3=C66;
        eigvalsint3=eigvalsint;
    elseif medium==4
        Qmat4=Qmat_int;Qmat4p=Qmat_intp;Snum4=Snum;eigenmat4=eigenmat;nmax4=nmax;
        rho4=rho;eigvecs4=eigvecsint;jmax4=jmax;C11_4=C11;C12_4=C12;C13_4=C13;C23_4=
            C23;C22_4=C22;C33_4=C33;C44_4=C44;
        C55_4=C55;C66_4=C66;
        eigvalsint4=eigvalsint;
    else %There is some issue in the medium value if this occurs.
```

```
            disp('error in medium value')
            break;
        end
            %remove old labels to be used again later.
            clear Gmat; clear eigenmat; clear eigvecsint; clear Qmat_int;clear Qmat_intp;
            clear nmax;clear jmax; clear rho;
            disp(horzcat('Medium ',num2str(medium),' finished'));
end
%-------------------------
%Calculate the Gmat matrices. The matrix should be of size [3*(nmax+1) x 3*(nmax+1)];
Qmat1c=ctranspose(Qmat1);%take conjugate transpose of Q_n
Qmat1pc=ctranspose(Qmat1p);%take conjugate transpose of Q_p
Qmat2c=ctranspose(Qmat2);%take conjugate transpose of Q_n
Qmat2pc=ctranspose(Qmat2p);%take conjugate transpose of Q_p
Qmat3c=ctranspose(Qmat3);%take conjugate transpose of Q_n
Qmat3pc=ctranspose(Qmat3p);%take conjugate transpose of Q_p
Qmat4c=ctranspose(Qmat4);%take conjugate transpose of Q_n
Qmat4pc=ctranspose(Qmat4p);%take conjugate transpose of Q_p



%-------------------------
%Loop through stiffness
for stiff2a=logspace(log10(stiffstart),log10(stiffend),stiffstep)%define stiffness (Pa/m) range to look
    in.
    stiff2b=stiff2a;%Set value of stiffness
    stiff1a=stiff1a;%Set value of stiffness
    stiff1b=stiff1b;%Set value of stiffness
    while nextstiff==0 %until solution is found
        %----------------------
        %Setup velocity range info.
        scnt=1;%Reset counter
        if firsttime==1 %First time through
            if isempty(finvel)==1 %For first time through
                velstart=vstart;%Starting velocity point
            else%If one loop has been done already.
```

```
            velstart=finvel(stcnt-1,thcount)+stpsize;
        end
        velend=vend;%Ending search point
        velstep=stpsize;%Step size
    else %Redefine the limits
        velstep=stpsize;%Redefine stepsize
        if size(finvel,2)<thcount-1 %No previous solution was found
            velstart=finvel(1,1)-0.5;
        else
            if finvel(1,thcount-1)==0
                velstart=vstart;
            else
                velstart=finvel(1,thcount-1)-0.5;
            end
        end
    end
    %-----------------------------------
    while velstep>velresolution %Set the resolution desired on the velocity;
        clear Gmat1nq Gmat1np Gmat1mp Gmat1mq
        clear Gmat2nq Gmat2np Gmat2mp Gmat2mq
        clear Gmat3nq Gmat3np Gmat3mp Gmat3mq
        clear Gmat4nq Gmat4np Gmat4mp Gmat4mq
        clear velocity fmat fvalue locs pks;
        %-----------------------
        %Loop through velocity range desired.
        for veloc=velstart:velstep:velend
            velocity(scnt)=veloc;%store velocity.
            %Let matlab do the multiplication for calculating G.
            IL=eye(size(eigenmat1,1),size(eigenmat1,1));%make identity matrix
            Lam1=(eigvalsint1-(rho1*veloc^2)*IL)\IL;%1/(lambda-rho v^2)
            Gmat1nq(:,:,scnt)=Qmat1*Lam1*Qmat1c;
            Gmat1np(:,:,scnt)=Qmat1*Lam1*Qmat1pc;
            Gmat1mq(:,:,scnt)=Qmat1p*Lam1*Qmat1c;
            Gmat1mp(:,:,scnt)=Qmat1p*Lam1*Qmat1pc;
            Lam2=(eigvalsint2-(rho2*veloc^2)*IL)\IL;%1/(lambda-rho v^2)
```

```
Gmat2nq(:,:,scnt)=Qmat2*Lam2*Qmat2c;
Gmat2np(:,:,scnt)=Qmat2*Lam2*Qmat2pc;
Gmat2mq(:,:,scnt)=Qmat2p*Lam2*Qmat2c;
Gmat2mp(:,:,scnt)=Qmat2p*Lam2*Qmat2pc;
Lam3=(eigvalsint3-(rho3*veloc^2)*IL)\IL;%1/(lambda-rho v^2)
Gmat3nq(:,:,scnt)=Qmat3*Lam3*Qmat3c;
Gmat3np(:,:,scnt)=Qmat3*Lam3*Qmat3pc;
Gmat3mq(:,:,scnt)=Qmat3p*Lam3*Qmat3c;
Gmat3mp(:,:,scnt)=Qmat3p*Lam3*Qmat3pc;
Lam4=(eigvalsint4-(rho4*veloc^2)*IL)\IL;%1/(lambda-rho v^2)
Gmat4nq(:,:,scnt)=Qmat4*Lam4*Qmat4c;
Gmat4np(:,:,scnt)=Qmat4*Lam4*Qmat4pc;
Gmat4mq(:,:,scnt)=Qmat4p*Lam4*Qmat4c;
Gmat4mp(:,:,scnt)=Qmat4p*Lam4*Qmat4pc;
%--------------------------
%Clear variables
clear knum;clear K1bmat;clear K1amat;clear K2amat;
clear k2bmat;clear K1b;clear K1a;clear K2a; clear K2b;
%---------------------------
%Setup the stiffness matrices
 matsize=(p+1);%size of each portion of matrix (x,y,z)
 %Calculate k/K
 knum=(2*pi*freq)/veloc;%wavenumber
 nptzer=zeros(matsize,matsize);%make matrix of all zeros

 K1a=((eye(matsize,matsize))*(knum/stiff1a));
 K1amat=[x1a*K1a,nptzer,nptzer;nptzer,y1a*K1a,nptzer;nptzer,nptzer,z1a*K1a];

 K1b=((eye(matsize,matsize))*(knum/stiff1b));
 K1bmat=[x1b*K1b,nptzer,nptzer;nptzer,y1b*K1b,nptzer;nptzer,nptzer,z1b*K1b
      ];

 K2a=((eye(matsize,matsize))*(knum/stiff2a));
 K2amat=[x2a*K2a,nptzer,nptzer;nptzer,y2a*K2a,nptzer;nptzer,nptzer,z2a*K2a];
```

```
K2b=((eye(matsize,matsize))*(knum/stiff2b));
K2bmat=[x2b*K2b,nptzer,nptzer;nptzer,y2b*K2b,nptzer;nptzer,nptzer,z2b*K2b
    ];

%--------------------------
II=eye(3*matsize,3*matsize);%identity matrix
ZZ=II*0;%matrix of zeros
clear finmat;
finmat=[K1bmat+Gmat1nq(:,:,scnt)+Gmat2nq(:,:,scnt) Gmat1np(:,:,scnt) -
    Gmat2np(:,:,scnt) ZZ;...
    ZZ -Gmat4np(:,:,scnt) Gmat3np(:,:,scnt) K1amat+Gmat4nq(:,:,scnt)+
        Gmat3nq(:,:,scnt);...
    Gmat1mq(:,:,scnt) K2amat+Gmat1mp(:,:,scnt)+Gmat4mp(:,:,scnt) ZZ -
        Gmat4mq(:,:,scnt);...
    -Gmat2mq(:,:,scnt) ZZ K2bmat+Gmat2mp(:,:,scnt)+Gmat3mp(:,:,scnt)
        Gmat3mq(:,:,scnt)];

[~,EVAL]=eig(finmat);
EVAL=diag(EVAL);%diagonalize
for ev=1:size(EVAL,1)
    if isreal(EVAL(ev,1))==1
    else
        EVAL(ev,1)=77;
    end
end
cnst=1e7;%Multiply by constant to get away from small numbers.
fmat(scnt,1)=det(cnst*finmat);
if fmat(scnt,1)==0
    cnst=cnst*100;
    fmat(scnt,1)=det(cnst*finmat);
end
%--------------------------------
%Determine if solution is good enough or out of range.
if veloc>velstart+5*velstep %Don't do first 5 points.
  if velstep>stpsize
```

```
[pks,locs]=findpeaks(fmat,'minpeakdistance',4);
if isempty(locs)==1 %Not found yet.
    %Do nothing
    if stcnt>numsols %Only look at first 6 solutions
        disp('if loop 1');
        nextstiff=1;%Go to next stiffness
        velstep=1e-50;%Get out of the while loop
        break;
    end
    if veloc>velend-5*velstep %Reached end of velocity region
        disp('if loop 2');
        if isempty(finvel)==0 %Finvel exists
            if size(finvel,2)==thcount && size(finvel,1)>=stcnt && finvel(
                stcnt,thcount)~=0 %Only for this loop
                finvel(stcnt,thcount)=0;
                stiffness1b(stcnt,thcount)=stiff1b;
                stiffness1a(stcnt,thcount)=stiff1a;
                stiffness2b(stcnt,thcount)=stiff2b;
                stiffness2a(stcnt,thcount)=stiff2a;
            end
        end
        nextstiff=1;%Go to next stiffness
        velstep=1e-50;%Get out of the while loop
        break;
    end
    if velstep<stpsize %After first time through.
        if veloc>finvel(stcnt,thcount)+0.25 %If nothing is found within 0.25
            of starting point
            velstep=stpsize;
            velstart=finvel(stcnt,thcount)+0.25;
            disp('did not find solution here so using new range');
            break;
        end
    end
else
```

```
        abs(velocity(locs)-velocity(scnt));
      if abs(velocity(locs)-velocity(scnt))<1e-15 %Velocities are the same.
          %Do nothing
      elseif abs(velocity(locs)-velocity(1))<1e-15
          %Do nothing if solution is the first point


      else
          bcheck=0;
          nextstiff=0;%Stay at this stiffness still.
          firsttime=1;%Change parameter
          finvel(stcnt,thcount)=velocity(locs);%Store velocity
          velstart=veloc-2*velstep;%Change starting point
          velstep=velstep*0.01;%Change step size
          break;
      end
    end
    if stcnt>numsols %Only look at first 6 solutions
        disp('if loop 3');
          nextstiff=1;%Go to next stiffness
          velstep=1e-50;%Get out of the while loop
          break;
    end
    if velstart+5*velstep>velend-5*velstep %End of range reached.
        disp('if loop 4');
        nextstiff=1;
        velstep=1e-50;%Get out of the while loop
        break;
    end
  else %Look for zero crossings instead of peaks
    if stcnt>numsols %Only look at first 6 solutions
          nextstiff=1;%Go to next stiffness
          velstep=1e-50;%Get out of the while loop
          break;
    end
    if velstart+5*velstep>velend-5*velstep %End of range reached.
```

```
        nextstiff=1;
        velstep=1e-50;%Get out of the while loop
        break;
    end
    if veloc>velend-5*velstep %Reached end of velocity region
            disp('if loop 2');
            if isempty(finvel)==0 %Finvel exists
                if size(finvel,2)==thcount && size(finvel,1)>=stcnt && finvel(
                    stcnt,thcount)~=0 %On this loop
                    finvel(stcnt,thcount)=0;%no velocity found here, reached
                        max search range.
                    stiffness1b(stcnt,thcount)=stiff1b;%Store stiffnesses
                    stiffness1a(stcnt,thcount)=stiff1a;
                    stiffness2b(stcnt,thcount)=stiff2b;
                    stiffness2a(stcnt,thcount)=stiff2a;
                end
            end
            nextstiff=1;%Go to next stiffness
            velstep=1e-50;%Get out of the while loop
            break;
    end
    for cpt=2:size(fmat,1)
      if fmat(cpt-1,1)>0 && fmat(cpt,1)<0
            bradcheck=1;
            finsol(stcnt,thcount)=fmat(cpt,1)/(cnst^(size(finmat,1)));%Store
                determinant solution
            finvel(stcnt,thcount)=velocity(cpt);%Store velocity
            velstart=veloc-2*velstep;%Change starting point
            velstep=velstep*0.1;%Change step size
            nwloop=1;
            firsttime=1;
      end
      if fmat(cpt-1,1)<0 && fmat(cpt,1)>0
            finsol(stcnt,thcount)=fmat(cpt,1)/(cnst^(size(finmat,1)));%Store
                determinant solution
```

```
                finvel(stcnt,thcount)=velocity(cpt);%Store velocity
                velstart=veloc-2*velstep;%Change starting point
                velstep=velstep*0.1;%Change step size
                nwloop=1;
                firsttime=1;
            end
        end
        if nwloop==1 %Some solution found
                nwloop=0;
                break;
        end
        if isempty(finvel)==0 %Finvel exists
            if size(finvel,2)==thcount && size(finvel,1)>=stcnt && finvel(stcnt,
                thcount)~=0 %On this loop
                if veloc>finvel(stcnt,thcount)+1 %Did not find a solution where it
                    first appeared.
                    disp('step size was reset because no zero was near this peak');
                    velstep=stpsize;%Reset stepsize
                    velstart=finvel(stcnt,thcount)+1.005;%Change starting value
                    finvel(stcnt,thcount)=0;%Clear the old value
                    scnt=1;%Reset counter
                    clear fmat velocity
                    break;%Start new velocity search
                end
            end
        end


        end
    end
    scnt=scnt+1;%Advance counter
  end %Veloc loop
  %-----------------------------
end %While loop
%-------------------------------------
%Store values
```

```
        if nextstiff==1
            break;
        end
        %Store stiffness values
        stiffness1b(stcnt,thcount)=stiff1b;
        stiffness1a(stcnt,thcount)=stiff1a;
        stiffness2b(stcnt,thcount)=stiff2b;
        stiffness2a(stcnt,thcount)=stiff2a;
        stcnt=stcnt+1;%Advance counter;
    end %While nextstiff
    stcnt=1;%Reset counter;
    thcount=thcount+1;%Advance counter
    firsttime=0;%Done with loop through;
    nextstiff=0;%Go to next stiffness;
end %stiffness loop
```

F.7 Calculation of Stress and Displacement Matrices

Once the solutions are found from the above code, find the displacements and stresses at the intersection.

```
%Brad Abell 07/29/14
%Recalculate the Gmat matrices for each stiffness and velocity and use to
%calculate the displacement for every stiffness and velocity after running
%solution_int.m

%ovrnight=;%higher velocity points

 clear veloc stiff Gmat1 Gmat2 Ginvtotal1 Ginvtotal2;
 clear amn1 amn2 amn3 amn4 Um1 Um2 Um3 Um4
 clear Un1 Un2 Un3 Un4 tau1 gamma1 sigma1 H1
 clear HH1 TAU1 GAMMA1 SIGMA1 Unall finmat
 %
 for medium=1:4
    Q_calc_int;%run this program to calculate the Q matrices for use below in
```

```
%------------------------------
%Label Qmat, Snum, eigenmat, rho, eigvecs, and the size of matrices
if medium ==1
    Qmat1=Qmat_int;Qmat1p=Qmat_intp;Snum1=Snum;eigenmat1=eigenmat;nmax1=nmax;
    rho1=rho;eigvecs1=eigvecsint;jmax1=jmax;
    C11_1=C11;C12_1=C12;C13_1=C13;C23_1=C23;C22_1=C22;C33_1=C33;C44_1=C44;
    C55_1=C55;C66_1=C66;
    eigvalsint1=eigvalsint;
elseif medium ==2
    Qmat2=Qmat_int;Qmat2p=Qmat_intp; Snum2=Snum;eigenmat2=eigenmat;nmax2=nmax
        ;
    rho2=rho;eigvecs2=eigvecsint;jmax2=jmax;
    C11_2=C11;C12_2=C12;C13_2=C13;C23_2=C23;C22_2=C22;C33_2=C33;C44_2=C44;
    C55_2=C55;C66_2=C66;
    eigvalsint2=eigvalsint;
elseif medium ==3
    Qmat3=Qmat_int;Qmat3p=Qmat_intp;Snum3=Snum;eigenmat3=eigenmat;nmax3=nmax;
    rho3=rho;eigvecs3=eigvecsint;jmax3=jmax; C11_3=C11;C12_3=C12;C13_3=C13;C23_3=
        C23;C22_3=C22;C33_3=C33;C44_3=C44;
    C55_3=C55;C66_3=C66;
    eigvalsint3=eigvalsint;
elseif medium==4
    Qmat4=Qmat_int;Qmat4p=Qmat_intp;Snum4=Snum;eigenmat4=eigenmat;nmax4=nmax;
    rho4=rho;eigvecs4=eigvecsint;jmax4=jmax;C11_4=C11;C12_4=C12;C13_4=C13;C23_4=
        C23;C22_4=C22;C33_4=C33;C44_4=C44;
    C55_4=C55;C66_4=C66;
    eigvalsint4=eigvalsint;
else %There is some issue in the medium value if this occurs.
    disp('error in medium value')
    break;
end
    %remove old labels to be used again later.
    clear Gmat; clear eigenmat; clear eigvecsint; clear Qmat_int;clear Qmat_intp;
    clear nmax;clear jmax; clear rho;
```

```
end

%}
Snumsize=0.5*(p+1)*(p+2);%calculate the number of terms
Snum=zeros(Snumsize,2);%Make Snum that size
count=1;%start counter
for ncnt=0:p
    for mcnt=0:p
            Snum(count,1)=mcnt;
            Snum(count,2)=ncnt;
            count=count+1;%Advance counter
    end
end
mmax=max(Snum(:,1));%calculate the max m
nmax=max(Snum(:,2));%calculate the max n
jmax=3*(mmax+1)*(nmax+1);%calculate jmax

stsz=size(stiffness1a,1);%get size of stiffness matrix
stsz2=size(stiffness2a,1);%get size of stiffness matrix
vlsz=size(finvel,1);%get size of velocity matrix

if stsz==vlsz
else
    disp('stiffness and velocity are not the same size')
end
wcnt=1;%for waitbar
for ptcnt=1:vlsz
    wcnt=wcnt+1;
    finmatcanc=0;%case definition
    veloc=finvel(ptcnt,ovrnight);%pull out velocity
    stiff1a=stiffness1a(ptcnt,ovrnight);%pull out stiffness
    stiff1b=stiffness1b(ptcnt,ovrnight);
    stiff2a=stiffness2a(ptcnt,ovrnight);
    stiff2b=stiffness2b(ptcnt,ovrnight);
```

```
%calculating the G matrices
scnt=1;%start counter
%--------------------------------------
%Calculate the Gmat matrices. The matrix should be of size [3*(nmax+1) x 3*(nmax+1)];
Qmat1c=ctranspose(Qmat1);%take conjugate transpose of Q_n
Qmat1pc=ctranspose(Qmat1p);%take conjugate transpose of Q_p
Qmat2c=ctranspose(Qmat2);%take conjugate transpose of Q_n
Qmat2pc=ctranspose(Qmat2p);%take conjugate transpose of Q_p
Qmat3c=ctranspose(Qmat3);%take conjugate transpose of Q_n
Qmat3pc=ctranspose(Qmat3p);%take conjugate transpose of Q_p
Qmat4c=ctranspose(Qmat4);%take conjugate transpose of Q_n
Qmat4pc=ctranspose(Qmat4p);%take conjugate transpose of Q_p
clear Gmat1nq Gmat1np Gmat1mp Gmat1mq
clear Gmat2nq Gmat2np Gmat2mp Gmat2mq
clear Gmat3nq Gmat3np Gmat3mp Gmat3mq
clear Gmat4nq Gmat4np Gmat4mp Gmat4mq
IL=eye(size(eigenmat1,1),size(eigenmat1,1));%make identity matrix
Lam1=(eigvalsint1-(rho1*veloc^2)*IL)\IL;%1/(lambda-rho v^2)
Gmat1nq(:,:)=Qmat1*Lam1*Qmat1c;
Gmat1np(:,:)=Qmat1*Lam1*Qmat1pc;
Gmat1mq(:,:)=Qmat1p*Lam1*Qmat1c;
Gmat1mp(:,:)=Qmat1p*Lam1*Qmat1pc;
Lam2=(eigvalsint2-(rho2*veloc^2)*IL)\IL;%1/(lambda-rho v^2)
Gmat2nq(:,:)=Qmat2*Lam2*Qmat2c;
Gmat2np(:,:)=Qmat2*Lam2*Qmat2pc;
Gmat2mq(:,:)=Qmat2p*Lam2*Qmat2c;
Gmat2mp(:,:)=Qmat2p*Lam2*Qmat2pc;
Lam3=(eigvalsint3-(rho3*veloc^2)*IL)\IL;%1/(lambda-rho v^2)
Gmat3nq(:,:)=Qmat3*Lam3*Qmat3c;
Gmat3np(:,:)=Qmat3*Lam3*Qmat3pc;
Gmat3mq(:,:)=Qmat3p*Lam3*Qmat3c;
Gmat3mp(:,:)=Qmat3p*Lam3*Qmat3pc;
Lam4=(eigvalsint4-(rho4*veloc^2)*IL)\IL;%1/(lambda-rho v^2)
Gmat4nq(:,:)=Qmat4*Lam4*Qmat4c;
Gmat4np(:,:)=Qmat4*Lam4*Qmat4pc;
```

```
Gmat4mq(:,:)=Qmat4p*Lam4*Qmat4c;
Gmat4mp(:,:)=Qmat4p*Lam4*Qmat4pc;
%-----------------------------------
%clear variables
clear npttot14 npttot15 knum K1bmat K1amat K2amat;
clear k2bmat K1b K1a K2a K2b;
%-----------------------------------
    Gtotmat1nq(:,:,ptcnt)=Gmat1nq;
    Gtotmat1np(:,:,ptcnt)=Gmat1np;
    Gtotmat2nq(:,:,ptcnt)=Gmat2nq;
    Gtotmat2np(:,:,ptcnt)=Gmat2np;
    Gtotmat3nq(:,:,ptcnt)=Gmat3nq;
    Gtotmat3np(:,:,ptcnt)=Gmat3np;
    Gtotmat4nq(:,:,ptcnt)=Gmat4nq;
    Gtotmat4np(:,:,ptcnt)=Gmat4np;
    Gtotmat1mq(:,:,ptcnt)=Gmat1mq;
    Gtotmat1mp(:,:,ptcnt)=Gmat1mp;
    Gtotmat2mq(:,:,ptcnt)=Gmat2mq;
    Gtotmat2mp(:,:,ptcnt)=Gmat2mp;
    Gtotmat3mq(:,:,ptcnt)=Gmat3mq;
    Gtotmat3mp(:,:,ptcnt)=Gmat3mp;
    Gtotmat4mq(:,:,ptcnt)=Gmat4mq;
    Gtotmat4mp(:,:,ptcnt)=Gmat4mp;
    clear Gmat1nq Gmat1np Gmat1mp Gmat1mq
    clear Gmat2nq Gmat2np Gmat2mp Gmat2mq
    clear Gmat3nq Gmat3np Gmat3mp Gmat3mq
    clear Gmat4nq Gmat4np Gmat4mp Gmat4mq
%-----------------------------------
    %[Grow,Gcol]=size(Gmat1);%get size of G
     matsize=(p+1);%size of each portion of matrix (x,y,z)
     %Calculate k/K
     knum=(2*pi*freq)/veloc;%wavenumber
     nptzer=zeros(matsize,matsize);%make matrix of all zeros

     K1a=((eye(matsize,matsize))*(knum/stiff1a));
```

```
K1amat=[x1a*K1a,nptzer,nptzer;nptzer,y1a*K1a,nptzer;nptzer,nptzer,z1a*K1a];

K1b=((eye(matsize,matsize))*(knum/stiff1b));
K1bmat=[x1b*K1b,nptzer,nptzer;nptzer,y1b*K1b,nptzer;nptzer,nptzer,z1b*K1b];

K2a=((eye(matsize,matsize))*(knum/stiff2a));
K2amat=[x2a*K2a,nptzer,nptzer;nptzer,y2a*K2a,nptzer;nptzer,nptzer,z2a*K2a];

K2b=((eye(matsize,matsize))*(knum/stiff2b));
K2bmat=[x2b*K2b,nptzer,nptzer;nptzer,y2b*K2b,nptzer;nptzer,nptzer,z2b*K2b];

%--------------------------------
II=eye(3*matsize,3*matsize);%identity matrix
ZZ=II*0;%matrix of zeros

finmat(:,:,ptcnt)=[II ZZ ZZ ZZ ZZ ZZ ZZ ZZ Gtotmat1nq(:,:,ptcnt) Gtotmat1np(:,:,ptcnt)
    ZZ ZZ;...
    ZZ II ZZ ZZ ZZ ZZ ZZ ZZ -Gtotmat2nq(:,:,ptcnt) ZZ Gtotmat2np(:,:,ptcnt) ZZ;...
    ZZ ZZ II ZZ ZZ ZZ ZZ ZZ ZZ ZZ -Gtotmat3np(:,:,ptcnt) -Gtotmat3nq(:,:,ptcnt);...
    ZZ ZZ ZZ II ZZ ZZ ZZ ZZ ZZ -Gtotmat4np(:,:,ptcnt) ZZ Gtotmat4nq(:,:,ptcnt);...
    ZZ ZZ ZZ ZZ II ZZ ZZ ZZ Gtotmat1mq(:,:,ptcnt) Gtotmat1mp(:,:,ptcnt) ZZ ZZ;...
    ZZ ZZ ZZ ZZ ZZ II ZZ ZZ -Gtotmat2mq(:,:,ptcnt) ZZ Gtotmat2mp(:,:,ptcnt) ZZ;...
    ZZ ZZ ZZ ZZ ZZ ZZ II ZZ ZZ ZZ -Gtotmat3mp(:,:,ptcnt) -Gtotmat3mq(:,:,ptcnt)
        ;...
    ZZ ZZ ZZ ZZ ZZ ZZ ZZ II ZZ -Gtotmat4mp(:,:,ptcnt) ZZ Gtotmat4mq(:,:,ptcnt);...
    II -II ZZ ZZ ZZ ZZ ZZ ZZ -K1bmat ZZ ZZ ZZ;...
    ZZ ZZ -II II ZZ ZZ ZZ ZZ ZZ ZZ ZZ -K1amat;...
    ZZ ZZ ZZ ZZ II ZZ ZZ -II ZZ -K2amat ZZ ZZ;...
    ZZ ZZ ZZ ZZ ZZ II -II ZZ ZZ ZZ -K2bmat ZZ];

[fa,fb,fc]=size(finmat(:,:,ptcnt));
for fii=1:fa
    for fjj=1:fb
        if isnan(finmat(fii,fjj,ptcnt))==1
            disp('finmat is NaN');
```

```
            finmatcanc=1;%cancel calculation
        elseif isinf(finmat(fii,fjj,ptcnt))==1
            disp('finmat is Inf');
            finmatcanc=1;%cancel calculation
        end
    end
end

if finmatcanc==1 %not a number
    %need to end this loop
else
 [VEC,EVAL]=eig(finmat(:,:,ptcnt));
 EVAL=diag(EVAL);%diagonalize
 for ev=1:size(EVAL,1)
    if isreal(EVAL(ev,1))==1
    else
        EVAL(ev,1)=77;
    end
 end
 zpt=find(abs(EVAL)==min(abs(EVAL)));%find smallest eigenvalue position
 min(abs(EVAL))%display minimum eigenvalue.
 Unall(:,ptcnt)=VEC(:,zpt);%store the U_nˆ(alpha) terms. (Eqn. 14)

 Un1(:,ptcnt)=Unall(1:3*(p+1),ptcnt);
 Un2(:,ptcnt)=Unall(1*(3*(p+1))+1:2*(3*(p+1)),ptcnt);
 Un3(:,ptcnt)=Unall(2*(3*(p+1))+1:3*(3*(p+1)),ptcnt);
 Un4(:,ptcnt)=Unall(3*(3*(p+1))+1:4*(3*(p+1)),ptcnt);
 Um1(:,ptcnt)=Unall(4*(3*(p+1))+1:5*(3*(p+1)),ptcnt);
 Um2(:,ptcnt)=Unall(5*(3*(p+1))+1:6*(3*(p+1)),ptcnt);
 Um3(:,ptcnt)=Unall(6*(3*(p+1))+1:7*(3*(p+1)),ptcnt);
 Um4(:,ptcnt)=Unall(7*(3*(p+1))+1:8*(3*(p+1)),ptcnt);
 tau1(:,ptcnt)=Unall(8*(3*(p+1))+1:9*(3*(p+1)),ptcnt);%calculate tau for medium 1;
 gamma1(:,ptcnt)=Unall(9*(3*(p+1))+1:10*(3*(p+1)),ptcnt);
 sigma1(:,ptcnt)=Unall(10*(3*(p+1))+1:11*(3*(p+1)),ptcnt);
 H1(:,ptcnt)=Unall(11*(3*(p+1))+1:12*(3*(p+1)),ptcnt);
```

```
for cnt=1:(3*(p+1)^2)
    TAU1(cnt,ptcnt)=tau1(ceil(cnt/(p+1)),ptcnt);%this is phi_p(0)*tau1_q
    HH1(cnt,ptcnt)=H1(ceil(cnt/(p+1)),ptcnt);%This is phi_p(0)*H1_q
end

%Put gamma and sigma in correct form
count=1;%counter
for cnt=1:(3*(p+1)^2)
    if cnt<=(p+1)^2 %First few terms
        St=1:p+1;
        GAMMA1(cnt,ptcnt)=gamma1(St(count),ptcnt);
        SIGMA1(cnt,ptcnt)=sigma1(St(count),ptcnt);
        %adjust counter as needed
        if count==p+1
            count=1;
        else
            count=count+1;
        end
    else %rest of the terms
        St=1:p+1;
        GAMMA1(cnt,ptcnt)=gamma1(St(count)+(ceil(ceil(cnt/(p+1))/(p+1))-1)*(p
            +1),ptcnt);%this is phi_q(0)*gamma1_p
        SIGMA1(cnt,ptcnt)=sigma1(St(count)+(ceil(ceil(cnt/(p+1))/(p+1))-1)*(p+1),
            ptcnt);%this is phi_q(0)*sigma1_p
        if count==p+1
            count=1;
        else
            count=count+1;
        end

    end
end
```

```
        [Nmattotal1,Nmattotal2,Nmattotal3,Nmattotal4,mindex,nindex]=
            amn_calculation_intersection_aniso(p,veloc,C11_1,C12_1,C13_1,C22_1,C23_1,C33_1,
            C44_1,C55_1,C66_1,C11_2,C12_2,C13_2,C22_2,C23_2,C33_2,C44_2,C55_2,C66_2,C11_3,
            C12_3,C13_3,C22_3,C23_3,C33_3,C44_3,C55_3,C66_3,C11_4,C12_4,C13_4,C22_4,C23_4,
            C33_4,C44_4,C55_4,C66_4,rho1,rho2,rho3,rho4);
        amn1(:,ptcnt)=mldivide(Nmattotal1,-TAU1(:,ptcnt)-GAMMA1(:,ptcnt));%calculate
            amn for medium 1 (eqn. 9)
        amn2(:,ptcnt)=mldivide(Nmattotal2,TAU1(:,ptcnt)-SIGMA1(:,ptcnt));%calculate amn
            for medium 2 (eqn. 10)
        amn3(:,ptcnt)=mldivide(Nmattotal3,HH1(:,ptcnt)+SIGMA1(:,ptcnt));
        amn4(:,ptcnt)=mldivide(Nmattotal4,-HH1(:,ptcnt)+GAMMA1(:,ptcnt));

        %Check the sizes
        if size(amn1,1)==3*((p+1)^2)
            %correct size
        else
            disp('error in size of amn1')
        end


    end
end

clear Dcheck Uncheck alphacheck ncheck mcheck cnt zpt ypt wcnt
```

F.8 Coefficient Calculation ($a_{m,n}$)

```
%For calculating a_mn from eqn. 9 and 10 in Sokolova et al. 2012.
%Need to have parameters in the workspace for the number of expansion
%terms (p), the material parameters (rho and Cij) as well as the solution for the final velocity (
    finvel).
function [Nmattotal1,Nmattotal2,Nmattotal3,Nmattotal4,mindex,nindex]=
    amn_calculation_intersection_aniso(p,finvel,C11_1,C12_1,C13_1,C22_1,C23_1,C33_1,C44_1,
    C55_1,C66_1,C11_2,C12_2,C13_2,C22_2,C23_2,C33_2,C44_2,C55_2,C66_2,C11_3,C12_3,C13_3,
```

```
C22_3,C23_3,C33_3,C44_3,C55_3,C66_3,C11_4,C12_4,C13_4,C22_4,C23_4,C33_4,C44_4,C55_4,
C66_4,rho1,rho2,rho3,rho4)
clear mu lambda rho
    for medium=1:4
        veloc=finvel;
        %Define the parameters in the medium you wish to calculate
        if medium==1
            C11=C11_1;
            C12=C12_1;
            C13=C13_1;
            C22=C22_1;
            C33=C33_1;
            C23=C23_1;
            C44=C44_1;
            C55=C55_1;
            C66=C66_1;
            rho=rho1;
        elseif medium==2
            C11=C11_2;
            C12=C12_2;
            C13=C13_2;
            C22=C22_2;
            C33=C33_2;
            C23=C23_2;
            C44=C44_2;
            C55=C55_2;
            C66=C66_2;
            rho=rho2;
        elseif medium==3
            C11=C11_3;
            C12=C12_3;
            C13=C13_3;
            C22=C22_3;
            C33=C33_3;
            C23=C23_3;
```

```
        C44=C44_3;
        C55=C55_3;
        C66=C66_3;
        rho=rho3;
    elseif medium==4
        C11=C11_4;
        C12=C12_4;
        C13=C13_4;
        C22=C22_4;
        C33=C33_4;
        C23=C23_4;
        C44=C44_4;
        C55=C55_4;
        C66=C66_4;
        rho=rho4;
    else
        disp('medium not defined');
    end

%Create matrix of possible combinations of m,n,p (p is subscript in Mpqmn)
    clear Snum;
    count=1;%start counter
    for ncnt=0:p
        for mcnt=0:p
                Snum(count,1)=mcnt;
                Snum(count,2)=ncnt;
                count=count+1;%Advance counter
        end
    end
    %Define the indices which are summed over.
    mindex=Snum(:,1);
    nindex=Snum(:,2);
    %-----------------------------------------
    Msize=size(Snum,1);%get size
%Calculate M variables and use transformation from Maradudin et al. (1973).
```

```
i=sqrt(-1);%define imaginary number
for mrow=1:Msize;%sum over the rows
    for mcol=1:Msize %sum over the columns
        Mmat11(mrow,mcol)=Mco11int(Snum(mrow,1),Snum(mrow,2),Snum(mcol,1),...
            Snum(mcol,2),C11,C12,C13,C22,C23,C33,C44,C55,C66,medium);
        Mmat12(mrow,mcol)=i*Mco12int(Snum(mrow,1),Snum(mrow,2),...
            Snum(mcol,1),Snum(mcol,2),C11,C12,C13,C22,C23,C33,C44,C55,C66,medium)
                ;
        Mmat13(mrow,mcol)=i*Mco13int(Snum(mrow,1),Snum(mrow,2),...
            Snum(mcol,1),Snum(mcol,2),C11,C12,C13,C22,C23,C33,C44,C55,C66,medium)
                ;
        Mmat21(mrow,mcol)=-i*Mco21int(Snum(mrow,1),Snum(mrow,2),...
            Snum(mcol,1),Snum(mcol,2),C11,C12,C13,C22,C23,C33,C44,C55,C66,medium)
                ;
        Mmat22(mrow,mcol)=Mco22int(Snum(mrow,1),Snum(mrow,2),Snum(mcol,1)...
            ,Snum(mcol,2),C11,C12,C13,C22,C23,C33,C44,C55,C66,medium);
        Mmat23(mrow,mcol)=Mco23int(Snum(mrow,1),Snum(mrow,2),Snum(mcol,1)...
            ,Snum(mcol,2),C11,C12,C13,C22,C23,C33,C44,C55,C66,medium);
        Mmat31(mrow,mcol)=-i*Mco31int(Snum(mrow,1),Snum(mrow,2),...
            Snum(mcol,1),Snum(mcol,2),C11,C12,C13,C22,C23,C33,C44,C55,C66,medium)
                ;
        Mmat32(mrow,mcol)=Mco32int(Snum(mrow,1),Snum(mrow,2),Snum(mcol,1)...
            ,Snum(mcol,2),C11,C12,C13,C22,C23,C33,C44,C55,C66,medium);
        Mmat33(mrow,mcol)=Mco33int(Snum(mrow,1),Snum(mrow,2),Snum(mcol,1)...
            ,Snum(mcol,2),C11,C12,C13,C22,C23,C33,C44,C55,C66,medium);
    end
end

%Put matrix together.
Mmattotal=[Mmat11,Mmat12,Mmat13;Mmat21,Mmat22,Mmat23;Mmat31,Mmat32,
    Mmat33];
%Make sure the matrix is hermitian
if isequal(Mmattotal,ctranspose(Mmattotal))==0
    %This is bad and needs to be fixed.
    disp('Mmattotal is not hermitian!')
```

```
            return;
        end

        %calculate the rho*velocity^2 term.
        RV2=rho*(veloc^2)*eye(size(Mmattotal,1),size(Mmattotal,1));
        Nmattotal=Mmattotal-RV2;%calculate M-rho*v^2;

        %Store to output necessary matrix.
        if medium==1
            Nmattotal1=Nmattotal;
        elseif medium==2
            Nmattotal2=Nmattotal;
        elseif medium==3
            Nmattotal3=Nmattotal;
        elseif medium==4
            Nmattotal4=Nmattotal;
        else
            disp('Error in medium definition');
        end

    end


end
```

F.9 Wavelet Calculation

This program runs the wavelet analysis using the Nolte-Hilbert wavelet from Appendix E. Partially taken from code by D.D. Nolte.

```
function [Integral, Phase]=wavelet_nh(waveform,ti,tf,twi,twf,fmin,fmax,ntau,nfreq,Morletfact, i1)
%See Nolte et al, 2000 paper on wavlet and DD bc to see what is happening
%here.
%waveform is the original signal
%ti is the initial time of the signal (measured in sec)
% tf is the final time of the signal (measured in sec)
```

```
%twi use same values as ti
%twf use same values as tf
% fmin is the lowest frequency of the transform (in MHz)
% fmax is the highest frequency of the transform (in MHz)
% ntau is the number of time points in the transform
% nfreq is the number of frequency points in the transform
% Morletfact decides what kind of transform it will be:
% 0.5*sqrt(sqrt(2)/log(2)) is a traditional choice
% 1.0 is the minimal Morlet.
% 1/sqrt(2*pi)=0.3989 is the Nolte-Morlet
% 0.3 gives a good approximation to the 1-DOG and 2-DOG.
% Below approx. 0.3, the normalization falls off.
% 0.1 gives limiting 1-DOG and 2-DOG, but sub-unity normalization.
%-----------------------------------------
wsize = size(waveform);%Get size of waveform matrix
count = wsize(2);%set to size of count
y = waveform(1,:);%redefine as varible y.
y=y(1:count)-y(1);%Subtract the first element.
%-----------------------------------------
np=count; %The points collected in the sigal
np1=np-1; %Define a new counter.
dt=(tf-ti)/np1; %Sampling Rate
x=ti+(0:count-1)*dt; %Time axis of the signal
x=x(1:length(y));%select portion
%-----------------------------------------
minx = min(x); % ti initial time of the signal in seconds
maxx = max(x); %tf final time of the signal in seconds.
midx = (maxx-minx)/2.0;%Find the midpoints of the time.
delx = (twf-twi)/ntau; % Time interval chosen for transformation
%-----------------------------------------
freqmin=fmin;%Define minimum frequency in the transform.
freqmax=fmax;%Define the maximum frequency in the transform.
%-----------------------------------------
ralpmin = freqmin/Morletfact;%min
ralpmax = freqmax/Morletfact;%max
```

```
delralp = (ralpmax-ralpmin)/nfreq;%steps
%-----------------------------------------------
%Create empty matrices of the correct size.
IntR = zeros(ntau+1,nfreq+1);
IntI = zeros(ntau+1,nfreq+1);
Integral = zeros(ntau+1,nfreq+1);
Phase = zeros(ntau+1,nfreq+1);
freqcount = 0;%Start counter.
%-----------------------------------------------
for ralp = ralpmin:delralp:ralpmax;
  freqcount = freqcount + 1;%Advance counter.
  freq(freqcount) = Morletfact*ralp; %Store value.
  %-----------------------------------------------
% Calculate wavelet for this alpha
  ddx=(x(2)-x(1)); % here ddx equals to dt
  nxhalf=fix((maxx-minx)/ddx)+1;
  x0=ddx*(-nxhalf:nxhalf);
  DaughterR = morleta((x0).*ralp,Morletfact);
  DaughterI = HILBERTA(DaughterR);
  Daughter = sqrt(ralp)*(DaughterR - i*DaughterI);
  %-----------------------------------------------
  taucount = 0;%Set counter
  for x0 = twi:delx:twf;
   taucount = taucount + 1;%Advance counter.
   tau(taucount) = x0; %store value
   ny=size(y,2);
   ipos=round((taucount-1)*delx/ddx);
   istart=-ipos+nxhalf+1; iend=-ipos+ny+nxhalf;
   Product = Daughter(istart:iend).*y;
   temp = (x(2)-x(1))*sum(Product);
   Integral(taucount,freqcount) = abs(temp);%Wavelet result
   IntR(taucount,freqcount) = real(temp);%Only real porition
   IntI(taucount,freqcount) = imag(temp);%Only imaginary portion
   Phase(taucount,freqcount) = real(temp);%Phase portion
  end
```

```
 end
%-----------------------------------------
function y = morleta(x,f);
% Usage: Morlet(x,f), where f is related to the number
% of oscillations under the gaussian.
    y = (pi^(-0.25))*exp(-x.^2/2).*sin(2*pi*f*x);
return;



function y = HILBERTA(f); % f is a vector.
% Hilbert.m calculates the Hilbert transform of x
% by swaping the symmetric and asymmetric parts of the
% inverse Fourier transform that constructs the original function.
% Usage: Hilbert(f), where f is a row vector, ideally a power of two long.
% Caution: Data must be evenly spaced, and must vanish outside of
% the data range.
    D = size(f);
    max = D(2);
    ft = fft(f);
    Hft = ft;
    %Switch the symmetric and asymmetric parts
    Hft(round(max/2):max) = -Hft(round(max/2):max);
    temp = ifft(Hft);
    x = 1:max;
    y = -imag(temp);
return
```

Appendix G: Examples

G.1 CWW and Intersection Wave Example Calculation

As an example, a derivation of the $\bar{\mathbf{M}}$ matrix for media 1 with $\mu_L = \lambda_L = \rho = n_{max} = m_{max} = p_{max} = q_{max} = 1$ is shown. The same $\bar{\mathbf{M}}$ matrix for medium 1 works in both the CWW and interface wave derivation.

The elastic constants, using the above values, become

$$\begin{aligned} C_{11} &= \rho V_p^2 = \lambda_L + 2\mu = 3, \\ C_{22} &= C_{33} = C_{11} = 3, \\ C_{12} &= -2\rho V_s^2 + C_{11} = -2\mu_L + \lambda_L + 2\mu_L = 1, \\ C_{13} &= C_{23} = C_{12} = 1, \\ C_{44} &= \tfrac{1}{2}\left(C_{11} - C_{12}\right) = 1, \\ C_{55} &= C_{66} = C_{44} = 1. \end{aligned} \tag{G.1}$$

In matrix form this is

$$C_{ijkl} = \begin{pmatrix} 3 & 1 & 1 & 0 & 0 & 0 \\ 1 & 3 & 1 & 0 & 0 & 0 \\ 1 & 1 & 3 & 0 & 0 & 0 \\ 0 & 0 & 0 & 1 & 0 & 0 \\ 0 & 0 & 0 & 0 & 1 & 0 \\ 0 & 0 & 0 & 0 & 0 & 1 \end{pmatrix}. \tag{G.2}$$

The elastic constants are used to calculate $\bar{\mathbf{M}}$ according to the definition of $\bar{\mathbf{M}}$ from sections 5.3.4 and 6.4.4 above. $\bar{\mathbf{M}}$ is in the form

$$M_{pqmn}^{(\alpha,\beta,\eta)} = \begin{pmatrix} M_{0000}^{(1,1,\eta)} & M_{0010}^{(1,1,\eta)} & M_{0001}^{(1,1,\eta)} & M_{0011}^{(1,1,\eta)} & M_{0000}^{(1,2,\eta)} & \dots & M_{0011}^{(1,3,\eta)} \\ M_{1000}^{(1,1,\eta)} & M_{1010}^{(1,1,\eta)} & M_{1001}^{(1,1,\eta)} & \dots & & & M_{1011}^{(1,3,\eta)} \\ M_{0100}^{(1,1,\eta)} & M_{0110}^{(1,1,\eta)} & & & & & \vdots \\ M_{1100}^{(1,1,\eta)} & & \ddots & & & & \vdots \\ M_{0000}^{(2,1,\eta)} & & & & \ddots & & \vdots \\ \vdots & & & & & & \vdots \\ M_{1100}^{(3,1,\eta)} & \dots & \dots & \dots & \dots & & M_{1111}^{(3,3,\eta)} \end{pmatrix}, \quad \text{(G.3)}$$

and is size 12 x 12 for the parameters used in this example.

Now, calculate the first term (Eqn. 5.57), $M_{0000}^{(1,1,1)}$, and so forth with the rest. The first term is shown explicitly yielding

$$M_{0000}^{(1,1,1)} = C_{11}^{(1)}\delta_{00}\delta_{00} + C_{66}^{(1)}\{\delta_{00}\Gamma_{0,0}\} + C_{55}^{(1)}\{\delta_{00}\Gamma_{0,0}\}, \quad \text{(G.4)}$$

applying Eqn. G.2 leaves

$$\begin{aligned} M_{0000}^{(1,1,1)} &= (3)(1)(1) + (1)\left\{(1)\left[min(0,0) + \frac{1}{2} - \frac{\delta_{00}}{4}\right]\right\} + \\ &(1)\left\{(1)\left[min(0,0) + \frac{1}{2} - \frac{\delta_{00}}{4}\right]\right\} = \\ &(3) + (1)\left[(0) + \frac{1}{2} - \frac{1}{4}\right] + (1)\left[(0) + \frac{1}{2} - \frac{1}{4}\right] = \\ &(3) + (1)\left(\frac{1}{4}\right) + (1)\left(\frac{1}{4}\right) = 3.5. \end{aligned} \quad \text{(G.5)}$$

Repeating for the rest of the terms yields

$$\begin{aligned} M_{0000}^{(1,1,1)} &= 3 + 1(0 + 0.5 - 0.25) + 1(0 + 0.5 - 0.25) = 3.5, \\ M_{0010}^{(1,1,1)} &= 1(0 + 0.5) = 0.5, \\ M_{0001}^{(1,1,1)} &= 1(0 + 0.5) = 0.5, \\ M_{0011}^{(1,1,1)} &= 0, \\ &\vdots \end{aligned} \quad \text{(G.6)}$$

which results the final matrix of

$$M^{(\alpha,\beta,b)}_{pqmn} = \left(\begin{array}{cccc|cccc|cccc} 3.5 & 0.5 & 0.5 & 0 & 0 & i & 0 & 0 & 0 & 0 & i & 0 \\ 0.5 & 4.5 & 0 & 0.5 & -i & 0 & 0 & 0 & 0 & 0 & 0 & i \\ 0.5 & 0 & 4.5 & 0.5 & 0 & 0 & 0 & i & -i & 0 & 0 & 0 \\ 0 & 0.5 & 0.5 & 5.5 & 0 & 0 & -i & 0 & 0 & -i & 0 & 0 \\ \hline 0 & i & 0 & 0 & 2 & 1.5 & 0.5 & 0 & 0.5 & 0.5 & 0.5 & 0 \\ -i & 0 & 0 & 0 & 1.5 & 5 & 0 & 0.5 & 0.5 & 0.5 & 1 & 0.5 \\ 0 & 0 & 0 & i & 0.5 & 0 & 3 & 1.5 & 0.5 & 1 & 0.5 & 0.5 \\ 0 & 0 & -i & 0 & 0 & 0.5 & 1.5 & 6 & 0 & 0.5 & 0.5 & 0.5 \\ \hline 0 & 0 & i & 0 & 0.5 & 0.5 & 0.5 & 0 & 2 & 0.5 & 1.5 & 0 \\ 0 & 0 & 0 & i & 0.5 & 0.5 & 1 & 0.5 & 0.5 & 3 & 0 & 1.5 \\ -i & 0 & 0 & 0 & 0.5 & 1 & 0.5 & 0.5 & 1.5 & 0 & 5 & 0.5 \\ 0 & -i & 0 & 0 & 0 & 0.5 & 0.5 & 0.5 & 0 & 1.5 & 0.5 & 6 \end{array}\right), \quad \text{(G.7)}$$

where the lines have been inserted to help separate the α and β sections. Equation G.7 is the solution obtained after calculating $\bar{\mathbf{M}}$ for medium 1 with the above parameters but prior to the transformation to real coordinates (section 5.3.5).

After applying the transformation in section 5.3.5, Eqn. G.7 becomes

$$M^{(\alpha,\beta,b)}_{pqmn} = \left(\begin{array}{cccc|cccc|cccc} 3.5 & 0.5 & 0.5 & 0 & 0 & -1 & 0 & 0 & 0 & 0 & -1 & 0 \\ 0.5 & 4.5 & 0 & 0.5 & 1 & 0 & 0 & 0 & 0 & 0 & 0 & -1 \\ 0.5 & 0 & 4.5 & 0.5 & 0 & 0 & 0 & -1 & 1 & 0 & 0 & 0 \\ 0 & 0.5 & 0.5 & 5.5 & 0 & 0 & 1 & 0 & 0 & 1 & 0 & 0 \\ \hline 0 & 1 & 0 & 0 & 2 & 1.5 & 0.5 & 0 & 0.5 & 0.5 & 0.5 & 0 \\ -1 & 0 & 0 & 0 & 1.5 & 5 & 0 & 0.5 & 0.5 & 0.5 & 1 & 0.5 \\ 0 & 0 & 0 & 1 & 0.5 & 0 & 3 & 1.5 & 0.5 & 1 & 0.5 & 0.5 \\ 0 & 0 & -1 & 0 & 0 & 0.5 & 1.5 & 6 & 0 & 0.5 & 0.5 & 0.5 \\ \hline 0 & 0 & 1 & 0 & 0.5 & 0.5 & 0.5 & 0 & 2 & 0.5 & 1.5 & 0 \\ 0 & 0 & 0 & 1 & 0.5 & 0.5 & 1 & 0.5 & 0.5 & 3 & 0 & 1.5 \\ -1 & 0 & 0 & 0 & 0.5 & 1 & 0.5 & 0.5 & 1.5 & 0 & 5 & 0.5 \\ 0 & -1 & 0 & 0 & 0 & 0.5 & 0.5 & 0.5 & 0 & 1.5 & 0.5 & 6 \end{array}\right). \quad \text{(G.8)}$$

Eqn. G.8 is hermitian ($\bar{\mathbf{M}}$=$\bar{\mathbf{M}}^{\dagger}$) as required. Using a program like Matlab, the eigenvalues ($\lambda(j)$) and eigenvectors (V_{mn}) can be easily calculated. For this matrix, the eigenvalues are

$$\lambda(j) = \begin{pmatrix} 0.837154 \\ 0.927282 \\ 1.70091 \\ 2.50000 \\ 2.67227 \\ 3.93321 \\ 4.50000 \\ 4.68686 \\ 6.34187 \\ 6.50000 \\ 6.60198 \\ 8.79846 \end{pmatrix}, \quad \text{(G.9)}$$

and the eigenvectors are

$$V_{mn}(1) = \begin{pmatrix} 0 \\ -0.1896 \\ 0.1896 \\ 0 \\ 0.6197 \\ -0.2212 \\ -0.1595 \\ 0.0749 \\ -0.6197 \\ 0.1595 \\ 0.2212 \\ -0.0749 \end{pmatrix}, V_{mn}(2) = \begin{pmatrix} 0.1439 \\ 0.1249 \\ 0.1248 \\ -0.1439 \\ -0.5635 \\ 0.2475 \\ 0.2666 \\ -0.1177 \\ -0.5635 \\ 0.2666 \\ 0.2475 \\ -0.117 \end{pmatrix}, V_{mn}(3) = \begin{pmatrix} 00.0125 \\ -0.0125 \\ 0 \\ -0.2038 \\ -0.0535 \\ -0.6534 \\ 0.1687 \\ 0.2038 \\ 0.6534 \\ 0.0535 \\ -0.1687 \end{pmatrix}, \qquad \text{(G.10)}$$

$$V_{mn}(4) = \begin{pmatrix} 0.7500 \\ -0.2500 \\ -0.2500 \\ 0.2500 \\ 0 \\ 0.2500 \\ -0.2500 \\ 0 \\ 0 \\ -0.2500 \\ 0.2500 \\ 0 \end{pmatrix}, V_{mn}(5) = \begin{pmatrix} -0.2183 \\ 0.2982 \\ 0.2983 \\ 0.2183 \\ -0.2434 \\ 0.05879 \\ -0.4578 \\ 0.3018 \\ -0.2434 \\ -0.4578 \\ 0.0588 \\ 0.3018 \end{pmatrix}, V_{mn}(6) = \begin{pmatrix} 0 \\ 0.4739 \\ -0.4740 \\ 0 \\ 0.0135 \\ -0.4410 \\ -0.0318 \\ -0.2821 \\ -0.0135 \\ 0.0318 \\ 0.4410 \\ 0.2821 \end{pmatrix}, \qquad \text{(G.11)}$$

$$V_{mn}(7) = \begin{pmatrix} -0.5063 \\ -0.4143 \\ -0.4143 \\ 0.5063 \\ -0.1841 \\ 0.0460 \\ -0.0460 \\ -0.1841 \\ -0.1841 \\ -0.0460 \\ 0.0460 \\ -0.1841 \end{pmatrix}, V_{mn}(8) = \begin{pmatrix} 0 \\ 0.3308 \\ -0.3308 \\ 0 \\ 0.2619 \\ 0.5037 \\ -0.1682 \\ -0.2000 \\ -0.2619 \\ 0.1682 \\ -0.5037 \\ 0.2000 \end{pmatrix}, V_{mn}(9) = \begin{pmatrix} 0 \\ 0.3603 \\ -0.3603 \\ 0 \\ 0.0751 \\ 0.0032 \\ 0.1352 \\ 0.5885 \\ -0.0751 \\ -0.1352 \\ -0.0032 \\ -0.5885 \end{pmatrix}, \tag{G.12}$$

$$V_{mn}(10) = \begin{pmatrix} -0.2500 \\ -0.2500 \\ -0.2500 \\ -0.7500 \\ 0 \\ 0.2500 \\ -0.2500 \\ 0 \\ 0 \\ -0.2500 \\ 0.2450 \\ 0 \end{pmatrix}, V_{mn}(11) = \begin{pmatrix} 0.1584 \\ -0.3067 \\ -0.3067 \\ -0.1584 \\ -0.2532 \\ -0.3990 \\ 0.0661 \\ 0.3915 \\ -0.25320.0661 \\ -0.3990 \\ 0.3915 \end{pmatrix}, V_{mn}(12) = \begin{pmatrix} -0.1588 \\ -0.0692 \\ -0.0692 \\ 0.1588 \\ 0.1587 \\ 0.38604 \\ 0.2964 \\ 0.4560 \\ 0.1586 \\ 0.2964 \\ 0.3860 \\ 0.456 \end{pmatrix}. \tag{G.13}$$

Next, the calculation of $\bar{\mathbf{Q}}$ is made using Eqn. 5.91, which is size [3($n_{max}+1$) x j_{max}]=[6x12]. To calculate $\bar{\mathbf{Q}}$, the format for the first term is

$$Q_0^{(1)}(1) = V_{00}^{(1)}(1) + V_{10}^{(1)}(1). \tag{G.14}$$

The entire matrix representation of $\bar{\mathbf{Q}}$ is

$$\bar{\mathbf{Q}} = \begin{pmatrix} Q_0^{(1)}(1) & Q_0^{(1)}(2) & Q_0^{(1)}(3) & \dots & Q_0^{(1)}(12) \\ Q_1^{(1)}(1) & Q_1^{(1)}(2) & \dots & & \vdots \\ Q_0^{(2)}(1) & & \ddots & & \\ \vdots & & & & \\ Q_1^{(3)}(1) & & \dots & & Q_1^{(3)}(12) \end{pmatrix}. \tag{G.15}$$

Note that the entire matrix in Eqn. G.15 is not unitary, but that each column is. The result of calculating Eqn. G.15 yields

$$\bar{\mathbf{Q}} = \begin{pmatrix} -0.1896 & 0.2686 & 0.0125 & 0.5000 & 0.0800 & 0.4740 & -0.9206 & 0.3308 & 0.3603 & -0.5000 & -0.1483 & -0.2280 \\ 0.1896 & -0.0191 & -0.0125 & 0.0000 & 0.5166 & -0.4740 & 0.0921 & -0.3308 & -0.3602 & -1.0000 & -0.4650 & 0.0896 \\ 0.3986 & -0.3161 & -0.2573 & 0.2500 & -0.1846 & -0.4276 & -0.1381 & 0.7655 & 0.0783 & 0.2500 & -0.6521 & 0.5447 \\ -0.0846 & 0.1489 & -0.4847 & -0.2500 & -0.1560 & -0.3140 & -0.2301 & -0.3682 & 0.7236 & -0.2500 & 0.4576 & 0.7524 \\ -0.4603 & -0.2970 & 0.8572 & -0.2500 & -0.7012 & 0.0184 & -0.2301 & -0.0937 & -0.2102 & -0.2500 & -0.1871 & 0.4551 \\ 0.1463 & 0.1298 & -0.1152 & 0.2500 & 0.3606 & 0.7232 & -0.1381 & -0.3036 & -0.5917 & 0.2500 & -0.0075 & 0.8420 \end{pmatrix}. \tag{G.16}$$

The results from Eqn. G.16 as well as the eigenvalues from Eqn. G.9 are used to construct the $\bar{\mathbf{G}}$ matrix using

$$G_{nq}^{(\alpha,\beta)} = \sum_{j=1}^{j_{max}} \frac{Q_n^{(\alpha)}(j) Q_q^{(\beta)*}(j)}{\lambda(j) - \rho v^2}, \tag{G.17}$$

where ρ is the density, and v is the velocity of the wave.

When written out explicitly, the first term in $\bar{\mathbf{G}}$ is

$$\begin{aligned}
G_{00}^{(1,1)} &= \frac{Q_0^{(1)}(1) Q_0^{(1)*}(1)}{\lambda(1) - \rho v^2} + \frac{Q_0^{(2)}(1) Q_0^{(1)*}(2)}{\lambda(2) - \rho v^2} + \cdots + \frac{Q_0^{(1)}(12) Q_0^{(1)*}(12)}{\lambda(12) - \rho v^2}, \\
G_{10}^{(1,1)} &= \frac{Q_1^{(1)}(1) Q_0^{(1)*}(1)}{\lambda(1) - \rho v^2} + \frac{Q_1^{(2)}(1) Q_0^{(1)*}(2)}{\lambda(2) - \rho v^2} + \cdots + \frac{Q_1^{(1)}(12) Q_0^{(1)*}(12)}{\lambda(12) - \rho v^2}, \\
G_{00}^{(1,2)} &= \frac{Q_0^{(1)}(1) Q_0^{(2)*}(1)}{\lambda(1) - \rho v^2} + \frac{Q_0^{(2)}(1) Q_0^{(2)*}(2)}{\lambda(2) - \rho v^2} + \cdots + \frac{Q_0^{(1)}(12) Q_0^{(2)*}(12)}{\lambda(12) - \rho v^2}, \\
&\vdots
\end{aligned} \tag{G.18}$$

Appendix H: Tables

Table H.1: Location, scale, rock type, and reference for various geometries of fracture intersections.

Type	Location	Scale	Rock Type	Source
Orthogonal	UK	m	Sandstone	Dunne, 1990 [63]
	UT	m	?	Rives, 1994 [61]
	France	m	Sandstone	Rives, 1994 [61]
	France	m	Limestone	Rives, 1994 [61]
	UK	m	Limestone	Rives, 1994 [61]
	UK	cm	Limestone	Rives, 1994 [61]
	UK	cm	Shale	Rawnsley, 1992 [60]
	UK	m	Shale	Rawnsley, 1992 [60]
	CA	cm	?	Gross, 1992 [64]
	UK	cm	Limestone	Caputo, 1995 [22]
	UK	cm	Limestone	Caputo, 1995 [22]
	UK	cm	Limestone	Caputo, 1995 [22]
	Greece	cm	Oligo-Miocene Flysh	Caputo, 1995 [22]
	CA	dm	Carbonate	Bai, 2002 [38]
	Mars	km	?	Okubo, 2007 [45]
	Mars	m	?	Birnie, 2012 [46]
	UK	m	Limestone	Olson, 2007 [28]
	WY	m	Sandstone	Olson, 2007 [28]
	UT	m	Sandstone	Olson, 2007 [28]
	Italy	cm	Carbonate	Agosta, 2010 [31]
	Syria	cm	Lava Rock	Ozkaya, 2003 [29]
X-Shape	Africa	km	Bedrock	Hast, 1973 [44]
	UK	m	Sandstone	Dunne, 1990 [63]

continued on next page

Table H.1: *continued*

Type	Location	Scale	Rock Type	Source
X-Shape	France	m	Limestone	Rives, 1994 [61]
	UK	cm	Limestone	Rives, 1994 [61]
	UK	cm	Shale	Rawnsley, 1992 [60]
	Australia	km	Sandstone	Memarian, 2003 [65]
	UT	?	Sandstone	Pollard, 1988 [42]
	Mars	m	?	Birnie, 2012 [46]
	Sweden	m	Granite	Davy, 2013 [27]
	CA	cm	Dolomite	Olson, 2007 [28]
	Italy	cm	Carbonate	Agosta, 2010 [31]
T-Shape	Laboratory	mm	Varnish	Rawnsley, 1992 [60]
	UK	cm	Shale	Rawnsley, 1992 [60]
	CA	cm	?	Gross, 1992 [64]
	UK	cm	Limestone	Caputo, 1995 [22]
	CA	dm	Carbonates	Bai, 2002 [38]
	UT	cm	Sandstone	Agosta, 2010 [31]
	Italy	cm	Carbonate	Agosta, 2010 [31]
	Italy	cm	Mudstone	Larsen, 2010 [30]
Star Shape	Moon	km	?	Hast, 1973 [44]
	Greece	cm	Oligo-Miocene Flysh	Caputo, 1995 [22]
	Australia	mm	Sandstone	Memarian, 2003 [65]
	Mars	km	?	Okubo, 2007 [45]
	Sweden	m	Granite	Davy, 2013 [27]
	UK	m	Limestone	Olson, 2007 [28]
	NV	m	Sandstone	Aydin, 2000 [49]
Y-Shape	Greece	cm	Oligo-Miocene Flysh	Caputo, 1995 [22]

continued on next page

Table H.1: *continued*

Type	**Location**	**Scale**	**Rock Type**	**Source**
Y-Shape	CA	dm	Carbonate	Bai, 2002 [38]
	Australia	m	Sandstone	Memarian, 2003 [65]
	UT	cm	Sandstone	Pollard, 1988 [42]
	CA	cm	Mud	Pollard, 1988 [42]
	Italy	cm	Mudstone	Larsen, 2010 [30]
	CA	cm	Lava Rock	Aydin, 1988 [43]
	HI	cm	Lava Rock	Aydin, 1988 [43]
	AK	m	Tundra (frozen)	Leffingwell, 1915 [233]
	AK	m	Ice	Plug, 2001 [71]
	Syria	cm	Lava Rock	Ozkaya,2003 [29]

Table H.2
Sample sizes in the directions indicated. All sizes have an uncertainty of ± 0.3 mm.

Direction	Aluminum Cubes (m)	Aluminum bars (m)	Hexagonal Aluminum (m)
x (m)	0.302514	0.297840	0.100
y (m)	0.302514	0.076175	0.075
z (m)	0.302514	0.076175	0.075

Table H.3
Aluminum parameters used in the numerical analysis that were based on experimental measurements. The first parenthesis is the direction the velocity was measured in, the second is the unit.

Parameter	Aluminum Cubes	Aluminum Bars	Hexagonal Aluminum
ρ $(\frac{kg}{m^3})$	2700	2717	2700
C_{11} (Pa)	1.0332x10^{11}	8.8750x10^{10}	9.1814x10^{10}
C_{12} (Pa)	5.1960x10^{10}	4.1460x10^{10}	4.3344x10^{10}
C_{13} (Pa)	5.1960x10^{10}	3.7000x10^{10}	4.3344x10^{10}
C_{33} (Pa)	1.0332x10^{11}	1.0545x10^{11}	9.1814x10^{10}
C_{44} (Pa)	2.5680x10^{10}	2.5607x10^{10}	2.4235x10^{10}
C_{66} (Pa)	2.5680x10^{10}	2.3645x10^{10}	2.4235x10^{10}
$n_{max} = m_{max}$	15	15	n/a
S-Wave Velocity (x) $(\frac{m}{s})$	3084.5 $\pm$ 2.5	3070.0 $\pm$ 2.5	2996.0 $\pm$ 1.0
S-Wave Velocity $(y,\ z)$ $(\frac{m}{s})$	3084.5 $\pm$ 2.5	2950.0 $\pm$ 2.5	2996.0 $\pm$ 1.0
Rayleigh Velocity (x) $(\frac{m}{s})$	2890.0 $\pm$ 10.0	2900.0 $\pm$ 1.0	2813.2 $\pm$ 1.0
Rayleigh Velocity $(y,\ z)$ $(\frac{m}{s})$	2890.0 $\pm$ 10.0	2780.0 $\pm$ 1.0	2813.2 $\pm$ 1.0
Wedge Velocity $(\frac{m}{s})$	2815.0 $\pm$ 5	2840.0 $\pm$ 10.0	2770.6 $\pm$ 8.4
P- Velocity (x) $(\frac{m}{s})$	6185.6 $\pm$ 2.5	6230.0 $\pm$ 2.5	5831.4 $\pm$ 5.3
P- Velocity $(y,\ z)$ $(\frac{m}{s})$	6185.6 $\pm$ 2.5	5715.3 $\pm$ 2.5	5831.4 $\pm$ 5.3

VITA

VITA

Bradley Charles Abell was raised in Elk River, Minnesota, by his parents Alan and Carol Abell. He graduated top 20 in his class from Elk River High School in 2006 and began his studies in physics at Gustavus Adolphus College in St. Peter, Minnesota, the same year. Bradley began experimental physics research under the advisement of Professor Thomas Huber while at Gustavus and found his passion for experimental acoustics research. He graduated Magna Cum Laude from Gustavus in 2010, with a bachelor of arts degree in Honors Physics. His honors thesis was entitled, *Non-contact imaging with a broadband air-coupled transducer and soft-edge fixing.*

Bradley enrolled at Purdue University in West Lafayette, Indiana, as a graduate student in the physics department in August of 2010. In January 2011 he began conducting research for Professor Laura Pyrak-Nolte in the rock physics group, studying the effects of fracture intersections on elastic waves and micromodel fabrication. In the spring of 2015, Bradley graduated with a Doctor of Philosophy degree in physics for his work on elastic waves propagating along fracture intersections.